Landscape Evolution Modeling and Quantitative Provenance Analysis Across Scales and Time for Mineral Exploration

Beatriz Hadler Boggiani
ORCID: 0000-0002-4553-6955

A thesis submitted to fulfil the requirements of the degree of
Doctor of Philosophy

October 2025

Faculty of Science
School of Geosciences
The University of Sydney
Australia

Supervisor: A/Prof. Tristan Salles

Co-Supervisor: Dr. Claire Mallard

Declaration

I, Beatriz Hadler Boggiani, certify that the intellectual content of this thesis is the product of my own work, and that all assistance received in preparing this thesis and all sources have been acknowledged. This thesis has not been submitted for any other degree or purpose.

Copilot was used for the purposes of text enhancement. The use of this generative AI tool includes spelling corrections, minor sentence restructuring, and clarity enhancement. I confirm that where text was modified by generative AI, the content was reviewed for possible errors, inaccuracies, and bias. I take full responsibility for the submitted thesis, confirm the work is my own, and have used generative AI in accordance with University guidelines and policies.

Signature:
Name: Beatriz Hadler Boggiani
Date: 14/08/2025

Acknowledgments

This work is dedicated to:

First and foremost, my supervisor A/Prof Tristan Salles. Thank you for your intellectual generosity, guidance, and constant encouragement to think independently while providing grounded and consistent support. To my co-supervisor Dr. Claire Mallard, thank you for your insights, enthusiasm, and encouragement throughout this project. I am also grateful to Nicholas Atwood for his valuable inputs and scientific guidance.

To my family: Your belief in me, even from afar, kept me grounded during the hardest times. Thank you for always reminding me of the power of curiosity, perseverance, resilience and the meaning of "familia".

To Lachie (the soon Dr. Lachlan Arthur Perris):

"Coauthor of my daily mess,
From home food to sailing quests,
Late night rambles, coffee dawns,
Shared glances across calm lawns.

House friend, office partner, love(r) true,
Bike trails chased and oceans in view
You held each part with calm and keen,
And made the world our home within

My steady star when paths ran wide,
My secret spark, my sneaky guide.
Through all the noise, you stayed art,
The quiet riot in my heart."

To Patrice, Vasilis, Sam, Sara, Ana VC, Ana Paula, and all the lecturers who kept me grounded in the field, both literally and academically. Thank you for your patience with my endless questions (including "is that a boudin?") and for the laughs over my mysterious rock samples. Field trips were more than a break from my desk, they kept me sane and reminded me why I love geology.

To Sinan, for the friendship nourished by countless catch-ups, laughs, scientific and silly conversations, and incredible meals shared. To Andres, for the Victoria Park departures. To Mugabo, for always finding me at conferences and making even the most unfamiliar places feel like home. To Jono and Joe, for the good days in the field, the cold beers after, and the crash course in Aussie culture. To my friends Vili, Rayila, Lian, Estevão, and Pedro. Thank you for enriching my life with culture, laughter, good food, and great company. You made Australia feel much closer to home. A heartfelt thanks to Room 446 colleagues and the Geocoastal Research Group for your camaraderie.

To the Perris family, thank you for your generosity and kindness throughout these years, specially for introducing me to "sailing the oceans", a gift I will never forget.

I acknowledge the financial support from funding agencies: National Computational Infrastructure (NCI), supported by the Australian Government, and from Artemis HPC Grand Challenge supported by the Sydney Informatics Hub at the University of Sydney; the School of Geosciences for the "Completion Scholarship"; and the STELLAR Project, an industry collaboration supported by BHP. This research was supported by an Australian Government Research Training Program (RTP) Scholarship.

Australia taught me far more than landscape evolution modeling. The generosity, support, and spirit of everyone I met along the way turned this challenging chapter into a joyful and deeply transformative journey. Thank you.

Authorship Attribution

This thesis is based on the following three articles:

ARTICLE 1: Hadler Boggiani, B., Mallard, C., Salles, T., Atwood, N., Sweet, M.L., Snedden, J., Xu, J., Whiteaker, L. and Virdell, W. (2025): Quantitative provenance analysis of the Miocene Gulf of Mexico using high-resolution Landscape Evolution Modeling. *(Submitted to the Journal of Geophysical Research: Earth Surface on 15/10/2025)*
I co-designed the study with C.M. and T.S., interpreted the model data, and led the manuscript writing with feedback from all co-authors. B.H.B., C.M., and T.S. developed the post-processing tools.

ARTICLE 2: Hadler Boggiani, B., Mallard, C., Salles, T. and Atwood, N. (2025): Evolution and provenance of the Polish Rotliegend in the Southern Permian Basin. *(Resubmitted on the 21/09/2025, following revision, to the Journal of Geophysical Research: Earth Surface)*
I conceived the study, conducted the numerical experiments, and analyzed the sediment provenance with T.S. and C.M. I wrote the initial draft; all co-authors reviewed the manuscript.

ARTICLE 3: Hadler Boggiani, B., Salles, T., Mallard, C., & Atwood, N. (2025). The roles of surface processes in porphyry copper deposit preservation. Earth Surface Dynamics, 13(4), 683-704. *(Published on 07/08/2025)* DOI: 10.5194/esurf-13-683-2025
I co-designed the study, conducted the numerical experiments with T.S., analyzed exhumation rates, and wrote the initial draft. All co-authors reviewed the manuscript.

Two co-authored articles are included as appendices for further reference:

APPENDIX A: Salles, T., Husson, L., Rey, P., Mallard, C., Zahirovic, S., Boggiani, B.H., Coltice, N. and Arnould, M. (2023): Hundred million years of landscape dynamics from catchment to global scale. *Science, 379(6635), 918–923.* DOI: 10.1126/science.add2541.

APPENDIX B: Salles, T., Husson, L., Lorcery, M. and Hadler Boggiani, B. (2023): Landscape dynamics and the Phanerozoic diversification of the biosphere. *Nature, 624(7990), 115–121.* DOI: 10.1038/s41586-023-06777-z.

In addition to the authorship attribution statements above, in cases where I am not the corresponding author of a published item, permission to include the published material has been granted by the corresponding author.

Beatriz Hadler Boggiani, August 2025

As supervisor for the candidature upon which this thesis is based, I can confirm that the authorship attribution statements above are correct.

Tristan Salles, August 2025

Abstract

The search for economically viable copper deposits is becoming increasingly urgent in the context of a global transition toward net-zero carbon emissions. Although traditional mineral exploration methods have proven to be effective, they are no longer sufficient to meet the growing demand. Conventional techniques fall short in reconstructing the long-term surface dynamics of ore bodies, often neglecting their histories of preservation, exposure, and remobilization. To identify frontier deposits, we need innovative approaches. This thesis presents novel frameworks by applying a Landscape Evolution Model (LEM), *goSPL*, to address these limitations. Designed for deep-time, large-scale simulations, *goSPL* integrates paleo-elevation, paleoclimate, tectonics, and sea-level change to model and quantify sediment transport from source to sink. This research contributes to bridging the gap between climate dynamics and ore body evolution, offering new insights into sediment remobilization and exhumation histories.

The objectives of this thesis are to: (1) develop and apply a method for quantitative provenance analysis using well-constrained landscape evolution models and workflows that extract provenance-relevant data; and (2) investigate the role of climate in the exhumation, remobilization, and preservation of ore bodies by comparing landscape evolution models subjected to different forcing conditions (elevation and climate) against present-day data.

In this thesis, three case studies illustrate the applicability of goSPL to mineral exploration. These progress from a relatively recent and well-constrained region (the Miocene Gulf of Mexico), to a deep-time interpretative model (the Southern Permian Basin), and finally to a long-term global model (the Cenozoic). The first case presents regional-scale models of the mid-Miocene Gulf of Mexico, assessing how different initial conditions influence sediment routing and volumetric provenance. The results are compared with present-day observations and geological records for validation. The post-processed quantitative provenance analysis matches well with traditional provenance tools. The second case examines volumetric sediment accumulation in the red beds of the intracontinental European Southern Permian Basin, focusing not only on sediment origin, but also on evaluating their copper potential based on paleolithological reconstructions. This addresses whether the red beds (from the Upper Rotliegend stage) could be the sedimentary source rock for copper in overlying layers (the Kupferschiefer shale). The third case builds on a global landscape evolution model covering the Cenozoic to the present, evaluating porphyry copper preservation by linking tectonic exhumation rates to known emplacement depths.

Together, these chapters demonstrate that landscape evolution modeling offers a quantitative, scalable, and reproducible framework for mineral systems analysis. By integrating goSPL with provenance analysis and mineral systems thinking, this thesis represents one of the first applications of LEMs to directly inform copper exploration. It underscores the relevance of Earth surface processes over geological time and positions LEMs as a powerful tool to support mineral prospectivity in frontier terrains.

Contents

Authorship Attribution ii

Abstract iii

1 Introduction 2

2 ARTICLE 1 15

Hadler Boggiani, B., Mallard, C., Salles, T., Atwood, N., Sweet M. L., Snedden, J., Xu, J., Whiteaker T. L., Virdell, J. W. (2025). Quantitative provenance analysis for the Miocene Gulf of Mexico using high-resolution Landscape Evolution Modeling *(Submitted to the Journal of Geophysical Research: Earth Surface)*

3 ARTICLE 2 57

Hadler Boggiani, B., Mallard, C., Salles, T., Atwood, N. (2025). Evolution and provenance of the Polish Rotliegend in the Southern Permian Basin *(Re-submitted, following revision, to the Journal of Geophysical Research: Earth Surface)*

4 ARTICLE 3 101

Hadler Boggiani, B., Salles, T., Mallard, C., Atwood, N. (2025). The roles of surface processes in porphyry copper deposits preservation*(Published at EGU - ESurf on 07/08/2025)*

5 Discussion 124

6 Conclusion 133

A| APPENDIX

Salles, T., Husson, L., Rey, P., Mallard, C., Zahirovic, S., Boggiani, B.H., Coltice, N. and Arnould, M. (2023). Hundred million years of landscape dynamics from catchment to global scale. *Science* 135

B| APPENDIX

Salles, T., Husson, L., Lorcery, M. and Hadler Boggiani, B. (2023). Landscape dynamics and the Phanerozoic diversification of the biosphere. *Nature* 143

1 | Introduction

As global temperatures rise, the demand for critical metals like copper grows, driven by the push for sustainable energy solutions. In response, the Australian Government has revised its National Science and Research Priorities, emphasizing research that supports the transition to a net zero future and builds a secure and resilient economy. Meeting the material demands of this energy transition will require nearly doubling the global copper production over the next 25 years (International Energy Agency 2025; Guj and Schodde 2025). Meanwhile, conventional copper exploration methods are reaching their limits. As a result, there is a growing interest in predictive modeling frameworks that move beyond traditional geophysical and geochemical methods, incorporating deep learning and big data analytics (Xiao et al. 2024).

Despite these advances, many approaches overlook a critical dimension: the dynamic evolution of Earth's surface under the influence of climate and tectonics. This thesis argues that integrating landscape evolution modeling (LEM) into mineral exploration fills a crucial gap in understanding ore deposit formation, preservation, and redistribution over geological time. A key challenge to testing this gap is the lack of tools capable of quantitatively simulate surface dynamics across geologic timescales while linking them to mineral systems in a replicable way. To address this gap, I apply the landscape evolution model *goSPL* (Salles et al. 2020), which integrates tectonic and climatic variations to simulate surface processes from recent to deep time, and across spatial scales from local to global. By resolving the interplay between climate and tectonic, *goSPL* provides a quantitative framework to address limitations in traditional regional database geological approaches, including their frequent neglect of climate's role in ore deposit exhumation, preservation and remobilization.

Building on this foundation, this Thesis leverages landscape evolution modeling to address long-standing questions about source-to-sink dynamics and mineral system processes, such as: What is the total volume of sediment transported from a given source over time? (Chapter 2); To what extent do tectonic changes influence sediment provenance? (Chapter 2); How likely is it that copper in sediment-hosted provinces originates from underlying red-bed layers, which are commonly associated with such systems? (Chapter 3); If the provenance and composition of sediments are known, can we estimate the copper potential of the basin where they accumulate? (Chapter 3); What role does climate play in the exhumation history of porphyry bodies, and can such exhumation completely remove the mineralized system? (Chapters 3 and 4); and Is it possible to estimate the copper content within the remobilized sediments? (Chapters 3 and 4).

The remainder of this chapter begins with a review of traditional mineral exploration methods (Section 1.1), followed by a discussion of how surface processes influence ore systems and why these dynamics are often overlooked (Section 1.2). I then outline the rationale for applying LEMs in this context, with a focus on *goSPL* (section 1.3). This is followed by the introduction of a revised method for quantifying sediment provenance based on LEM output, and demonstrate its relevance to copper mineral systems. Finally, I define the scope and structure of this Thesis (section 1.4).

This Thesis advances landscape evolution modeling by developing new post-processing routines, including a volumetric provenance analysis method that extracts detailed sediment sourcing and accumulation histories directly from *goSPL* outputs. These methodological innovations extend the role of LEMs beyond traditional surface process simulation, positioning them as powerful tools within mineral systems science to better understand ore deposit preservation and redistribution over geological timescales. By integrating *goSPL* into mineral exploration workflows, I aim to demonstrate how landscape evolution modeling could provide crucial insights for the discovery of future copper resources.

1.1 Traditional methods in mineral exploration

The emergence of Geographic Information Systems (GIS), combined with the abundance of data generated during mineral exploration, has transformed the way we understand mineral deposits. The field has shifted from qualitative reasoning about geological processes to the quantitative, three-dimensional prediction of ore deposit models (Xiao et al. 2024). This shift has enabled a focus on deeper, more concealed, and technically challenging deposits beyond the shallow and surface-accessible ones.

Three-dimensional models integrate data such as topography, geological mapping, borehole logs, cross-sections, geophysical surveys, and geochemical analyses to infer the structure and distribution of ore bodies (Xiao et al. 2024). Traditional geostatistical methods, such as kriging, help fill gaps in these datasets, which are then used to construct digital deposit models using software platforms such as *Lynx*, *Suka*, *GOCAD*, *EarthVision*, *RockWare*, *GeoModeller*, and *Leapfrog*. Yet, despite increasing sophistication with extensive datasets, these methods remain largely site-specific and static, offering limited insight into Earth's evolving surface.

More recently, with increasing computational power, the growing availability of landscape evolution datasets (*e.g.* paleoclimatic and paleotopographic reconstructions), and advances in artificial intelligence have enabled the application of big data techniques to mineral prospectivity (*e.g.* Alfonso et al. 2024. Machine learning and deep learning algorithms are now used to build predictive models, employing methods such as random forests, support vector machines, artificial neural networks, and convolutional neural networks (Sun et al. 2020; Prado et al. 2020; Rodriguez-Galiano et al. 2015; Diaz-Rodriguez et al. 2021). These data-driven approaches have revolutionized mineral exploration by facilitating intelligent prospectivity models that can identify and prioritize mining exploration targets (Xiao et al. 2024).

While interpreting mineral deposits using subsurface and geochemical data has proven effective, such predictive models induce important extrapolation and often neglect the direct influence of climate and surface processes in ore formation,

preservation and concentration. In the next sections, I argue for the importance of integrating climate and tectonics into mineral deposit models, presenting both the rationale for this broader perspective and recent advancements in LEMs that allow us to quantify the role of these external forcing mechanisms.

These traditional approaches, while powerful, remain blind to the landscape scale processes that redistribute, weather and erode ore bodies over millions of years. The lack of integration between surficial processes and ore system modeling represents a critical gap, one that LEMs are uniquely positioned to address.

1.2 The role of climate and tectonics in mineral deposit history

Climate, in conjunction with tectonics, is among the most influential factors shaping the history of mineral deposits (Wang et al. 2024; Yanites and Kesler 2015). These forces drive landscape evolution through cycles of erosion, transport, and deposition. Although most mineral systems initiate due to geodynamic and tectonic processes, surface processes (often influenced by climate) are frequently critical to the final accumulation, redistribution, or preservation of ore (Fig. 1).

For example, well-known diamond-rich kimberlite orthomagmatic systems typically date from 50 - 250 million years ago (Mather et al. 2023; Arndt et al. 2017), while the diamonds themselves may be much older. These diamonds often concentrate as re-worked clasts in paleo-fluvial (paleo-placer) deposits and may date back to the Paleoproterozoic ($\approx$ 2.5 Ga) (Carvalho et al. 2016). In some cases, the primary kimberlite source has not yet been identified, as it may have been completely eroded (Chaves et al. 1998).

Similarly, porphyry Cu-Au-Mo deposits, associated with arc-related magmatism and generally placed between 2 and 5 km depth (Singer 1995; Sillitoe 2010), are typically not economically viable until they have been exhumed to, or near, the surface over geological time. However, older porphyry deposits with prolonged exhumation histories may be entirely eroded. The sediments produced through erosion can be redeposited and reburied, forming primary or enriching diagenetic red beds deposits, which may later act as source for sediment-hosted stratiform deposits. These deposits can then be further enriched by meteoric waters, resulting in supergene mineralization (Zientek et al. 2014; Hitzman et al. 2010).

Although three-dimensional ore deposit models are becoming increasingly sophisticated, interpretations of the surface processes shaping their post-formational history remain underdeveloped. For instance, identifying catchment reorganizations resulting from basin inversions could offer valuable insights into the transport and re-deposition of metal enriched sediments, particularly relevant in the context of paleo-placer and stratiform deposits.

Significant progress has also been made in the reconstruction of regional paleo-elevation maps, one of the main inputs for starting a LEM, constrained by thermochronological data such as denudation rates from cosmogenic ^{10}Be (Ruetenik et al. 2023), or apatite fission track analysis. Additionally, the growing availability of global paleoclimate models, built from diverse datasets including fossil record and

stable isotopes, offers new opportunities to quantify the co-evolution of climate, topography and ore system preservation over geological time.

These examples highlight that the processes responsible for ore preservation and enrichment often occur long after primary formation and are strongly modulated by surface dynamics. Understanding such a long-term evolution requires innovative tools capable of linking tectonic, climatic, and geomorphic processes across geological timescales, such as the LEM *goSPL* applied in this Thesis.

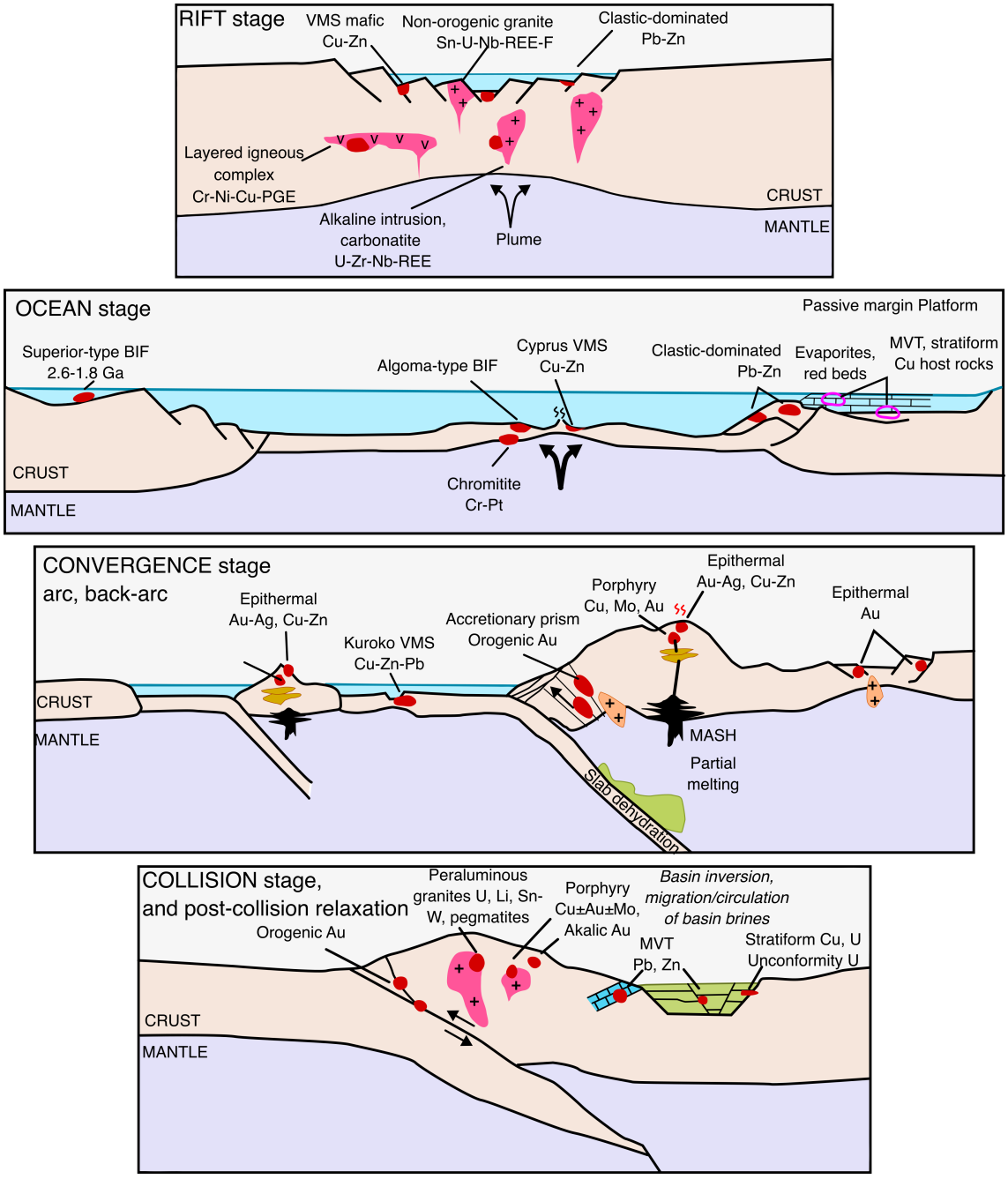

Figure 1: Ore deposits within their plate tectonic settings (adapted from (Arndt et al. 2017)). Note that most deposit types, regardless of their tectonic setting, are emplaced at depth and need to be exhumed to the surface to become economically viable.

1.3 Landscape evolution modeling

The origins of landscape evolution theory can be traced back to the late 19th century, notably to Gilbert's (1877) pioneering work on the geology of the Henry Mountains. In addition to describing the region's geological structures, Gilbert provided early hypothesis on the mechanics of weathering, erosion and sediment transport, offering a conceptual framework for understanding landscape forming processes (Gilbert 1877; Tucker and Hancock 2010). These early ideas remained largely qualitative until the 1960s, when researchers began formalizing them through mathematical equations and quantitative testing (Pazzaglia 2003). These developments laid the foundation for modern landscape evolution modeling (LEM).

Landscape evolution models are defined by mathematical equations that describe how geomorphic processes interact with and drive topographic change over time (Tucker and Hancock 2010; Pazzaglia 2003; Willgoose 2018). At the core of LEMs is the continuity of mass equation, expressed through geomorphic transport laws (stream power law) that describe and simulate hillslope processes dynamics, runoff generation, and erosion and sediment transport by water (Tucker and Hancock 2010; Pazzaglia 2003).

LEM frameworks vary in how they formulate and implement these governing equations. The specific continuity of mass equation determines which geomorphic processes and environmental conditions the model can realistically represent (Tucker and Hancock 2010; Willgoose 2018; Pazzaglia 2003) (Fig. 2). For example, models such as *SIBERIA* (Hancock et al. 2000) and *Landlab* (Hobley et al. 2017) focus on relatively small spatial scales over short time-frames. Others, such as *LECODE* (Salles and Duclaux 2012), *CAESAR* (Coulthard et al. 2002) and *FastScape* (Braun and Willett 2013), simulate longer-term evolution at similar spatial scale. Meanwhile, models like *BadLands* (Salles 2016; Salles et al. 2018a) are designed to handle large-scale, deep-time landscape dynamics. Only a few models, including *eSCAPE* (Salles 2019), and *goSPL* (Salles et al. 2020), are capable of simulating global-scale landscape evolution over geological timescales.

Despite their widespread application in geomorphology, LEMs remain underutilized in the field of mineral exploration. Some studies have applied LEMs to simulate post-mining landscape evolution (*e.g.* Hancock et al. 2000; Moliere et al. 2002; Hancock et al. 2008; Hancock et al. 2016; Hancock et al. 2017; Hancock et al. 2025), but to date, no recorded applications have used LEMs explicitly to support mineral prospectivity. This thesis represents a first step toward integrating LEMs (specifically *goSPL*) into mineral exploration research.

As with any modeling framework, LEMs involve trade-offs. These include simplifications of geomorphic processes, computational limitations, and challenges in validating model output with empirical data (Tucker and Hancock 2010; Dietrich et al. 2003). However, each model includes design choices to address specific challenges, often at the expense of others. The strength of *goSPL* lies in its ability to handle large, complex datasets while simulating surface processes across vast temporal and spatial scales, making it particularly well-suited for the mineral systems approach explored in this research.

This thesis is among the first efforts to demonstrate the potential of a global-scale

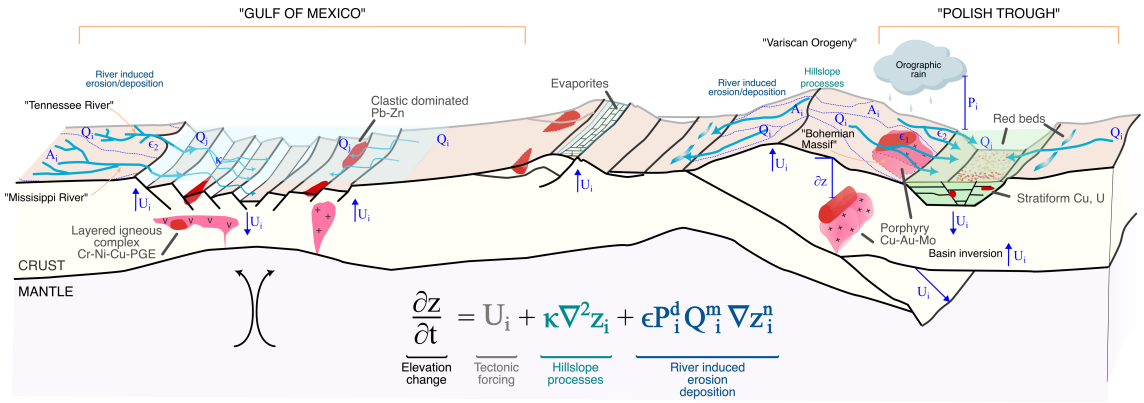

Figure 2: Schematic illustration of the mass continuity equation underpinning the *goSPL* landscape evolution model, highlighting two contrasting case studies from this thesis: the rift setting of the Gulf of Mexico and the passive margin setting of the Polish Trough. Despite differing tectonic regimes, both systems are shaped by comparable surface processes, including hillslope diffusion, fluvial erosion and deposition, and dynamic uplift and subsidence. In the equation, z represents the surface elevation (m) changing over time t (yr), U is the tectonics (vertical land motion) in m/yr. The hillslope processes are simulated with a diffusion equation, were κ is the diffusion coefficient for soil creep (Salles et al. 2018b). Fluvial processes are based on the stream power law (SPL) by quantifying the rate of incision from local slope and amount of water passing through a cell, where m and n represent dimensionless empirically constants, the erodibility coefficient (ϵ) is scalable with local mean annual precipitation rate (P_i), which is a positive exponent (d) obtained from field-based relationships, the flow discharge (Q_i) accounts for the upstream total area (A_i) and local precipitation (P_i) that combines to form the water flux ($P_i A_i$) with added upstream flow discharge (Q_j).

LEM (*goSPL*) to inform mineral prospectivity, by reconstructing and tracking the long-term surface dynamics that govern ore body exposure, burial, and remobilization (Fig. 2).

1.3.1 The *goSPL* model and why it is appropriate

goSPL simulates upstream erosion linked to downstream fluvial deposition in depressions, endorheic basins and marine environments using a multiple flow algorithm that routes both sediment and water flux. Unlike many landscape evolution models, *goSPL* is uniquely designed for large-scale, deep-time simulations. Its capability to model landscape dynamics across vast spatial and temporal domains offers valuable insights into long-term geomorphic processes, making it particularly relevant to the challenges of mineral exploration. In contrast to models such as *eSCAPE* (Salles 2019), *goSPL* incorporates plate motion advection, multi-lithology stratigraphic layering, and sediment compaction, enabling the reconstruction of landscape and sedimentary evolution through deep time within a consistent tectonic and climatic framework.

A key advantage of *goSPL* lies in its increased model stability and runtime scalability across hundreds of CPUs (Central processing unit). These capabilities are achieved through the use of implicit, parallel equation solvers implemented via Portable,

Extensible Toolkit for Scientific computing (PETSc) libraries (Smith et al. 2012), which efficiently handle both linear and non-linear constitutive equations.

What differentiates *goSPL* from other LEMs is not only its scalability and computational stability, but also its ability to assimilate paleoenvironmental data into predictive, global-scale models of surface evolution. This makes *goSPL* best suited to assess where and how copper deposits may have been exhumed, buried, or reworked over geological time, offering a novel layer of information to guide mineral exploration strategies, particularly in the context of a net-zero transition.

Like many other LEMs, *goSPL* currently simplifies sediment dynamics using a single grain-size class. It also does not account for the influence of biota, mass movements processes (*e.g.* debris flow, scarp retreat), or the complex physical, chemical, and biological controls on process rate coefficients. Moreover, *goSPL* is sensitive to uncertainties in paleoelevation and paleoclimatic reconstructions, meaning that inconsistencies in these inputs can propagate through the simulation.

Nonetheless, *goSPL* stands out for its demonstrated ability to generate robust, global-scale datasets, like the studies presented by Salles et al. (2023b) and Salles et al. (2023a) for the Phanerozoic. By assimilating spatially and temporally variable paleoelevation and paleoclimate histories, it enables a comprehensive quantification of source-to-sink sediment fluxes at the global scale (Fig. 2). This makes *goSPL* uniquely capable of capturing the influence of surface processes on long-term landscape dynamics.

1.3.2 LEM and provenance analysis

Traditional sediment provenance studies aim to identify sediment source areas, reconstruct transport pathways from source to sink, and assess the compositional influences on sedimentary rocks (Haughton et al. 1991). These analyses are also critical for constraining paleogeographic reconstructions, detecting lateral displacements in orogens, testing tectonic models, monitoring crustal evolution and assessing hydrocarbon reservoirs quality (Haughton et al. 1991). Early approaches, relying on paleo-current data and petrographic analysis, have since been complemented by geochemical and isotopic techniques, enabling more precise source reconstructions and inter-basin correlations. However, despite these advances over the past three decades, such methods are often constrained by spatial and temporal sampling limitations, leading to biased interpretations.

To address these limitations, this Thesis integrates *goSPL* simulations to reconstruct sediment provenance over geological timescales, as presented in Chapter 2. This chapter focuses on a specific regional case study (the Miocene Gulf of Mexico), but it is conceptually central to the thesis because it develops and tests the quantitative provenance method later applied to other basins. By simulating erosion, transport, and deposition within a physically-based, quantitative framework, *goSPL* enables extraction of provenance histories directly from model outputs. This approach not only overcomes key sampling biases and, but also and more importantly, introduces a novel quantitative post-processing routine tool for mineral exploration, particularly within sediment-hosted systems (Lovell-Kennedy et al. 2023).

By tracking flow paths, erosion rates, and basin fill histories, this method enhances

the resolution and scope of provenance analysis beyond what is typically possible with field-based datasets alone. The result is a more holistic understanding of sediment sourcing and accumulation processes, validated by traditional provenance analysis datasets (*e.g.* detrital zircon) and directly tied to the broader geodynamic and climatic controls modelled by *goSPL*.

1.3.3 LEM and copper deposits

Currently, global copper production originates from two main deposit types: sediment-hosted stratiform deposits and intrusive porphyry systems (Fig. 1, and 2). These two deposit types are vastly governed by different post-formation processes, yet the accumulation of ore in both is shaped by Earth's surface dynamics over deep time (Fig. 2).

For porphyry copper systems, most of the easily accessible deposits have been mined. The lack of new world-class porphyry discoveries since the early 2000s (Wood and As 2024) underscores the growing challenge in identifying frontier economically viable resources. While in intrusive porphyry systems copper is typically sourced from magmatic-hydrothermal fluids leaching metals from surrounding host rocks, in sediment-hosted stratiform copper ore systems, the origin of copper transported into the enriched stratiform layers remains a subject of ongoing debate (Hitzman et al. 2005; Sillitoe 2010). Some studies suggest that underlying red beds, which commonly occur beneath copper-bearing strata, may serve as the primary source of copper in theses systems (Hitzman et al. 2010). However, this hypothesis remains difficult to conclusively demonstrate.

In Chapter 3, I introduce a novel quantitative provenance analysis approach that reconstructs sediment accumulation histories in sediment-hosted stratiform copper provinces. In Chapter 4, I demonstrate how exhumation rates driven by climate and tectonics, when combined with emplacement depth data, can support the targeting of new porphyry copper systems. These methods enable estimation of copper mass contained in underlying red beds and the likely preservation state of porphyry copper deposits, providing new insights into their potential as copper sources.

1.4 Thesis Overview

In this Thesis, I apply the numerical code *goSPL* to simulate landscape evolution over deep geological time. I investigate the interplay between paleoelevation, climate, lithology and sea level to model sediment transport from source to sink, developing new post-processing methods to quantify sediment provenance and accumulation in a volumetric framework. The results of these models are evaluated against traditional datasets (*e.g.* cosmogenic nuclide analysis, detrital zircon studies). These methodological advances allow for a more rigorous integration of landscape evolution modeling into mineral systems science, enabling new insights into ore deposit exposure, burial, and remobilization that go beyond traditional surface process modeling.

In Chapter 2, I present nine well constrained landscape evolution models of the Gulf of Mexico for the mid-Miocene, with a spatial resolution of approximately 2.5 km. This chapter explores how variations in initial boundary conditions of a

well constrained paleo-environment and *goSPL* parameters affect sediment delivery and provenance from source regions to the Gulf of Mexico (the sink). With post-processing workflows developed for this project, I quantify water and sediment fluxes over time for major contributing rivers. Model outputs are compared to modern day river fluxes and marine depositional patterns, and they show to agree with present-day observations. While discrepancies emerge in provenance predictions when compared with traditional techniques, the chapter introduces a volumetric provenance method in a well constrained system and evaluates how different input scenarios influence these results.

Chapter 3 builds on this framework by presenting, for the first time, LEM simulations of the sag phase of the Southern Permian Basin system, focusing on the Polish Trough. There, I reconstruct the basin's sedimentation history under two tectonic subsidence scenarios and calculate corresponding erosion/deposition rates. Major contributing catchments to the Polish Trough are identified, revealing new potential provenance areas that have not yet been described by traditional provenance analysis methods. A parallel workflow incorporated a paleolithology map developed in this thesis to target potential copper enrichment sources, such as surrounding mafic rocks, enabling a novel estimate of the copper content within the sediments deposited in the Polish Trough.

In Chapter 4, I broaden the scope to a global scale, using the landscape evolution dataset of (Salles et al. 2023b) spanning the Cenozoic to the present day. This chapter presents modelled exhumation rates across the Earth's surface, with a particular focus on subduction zones known to host porphyry copper deposits. By integrating a global porphyry deposit database with emplacement depth estimates, I propose a new tool to assess the preservation state and potential exhumation levels of porphyry systems worldwide.

Appendices A and B include peer-reviewed publications I co-authored, which illustrate additional applications of LEMs to Phanerozoic sediment transport modeling. Appendix A introduces a 100-million-year global model that resolves a conundrum in sedimentology: why periods of apparent marine sediment starvation occur? The model outputs suggest that sediments were entrapped in evolving endorheic basins (such as the Andean retroarc foreland basin, and the Himalayan foreland basin). Appendix B presents a global correlation between sediment flux to the oceans and how diversification rates in both marine fauna and terrestrial vegetation is enhanced by the larger aport of sediments.

The Discussion and Conclusion chapters synthesize the main findings and contributions of this thesis. It highlights the potential of LEMs not only as tools for reconstructing basin scale provenance and sediment histories, but also for revealing exhumation patterns on a global scale, offering a valuable new framework for future mineral exploration strategies.

References

Alfonso, C. P., R. D. Müller, B. Mather, and M. Anthony (2024). "Spatio-temporal copper prospectivity in the American Cordillera predicted by positive-unlabeled

machine learning". In: *GSA Bulletin* 137.1-2, pp. 702–711. DOI: 10.1130/B37614.1.

Arndt, N., L. Fontboté, J. Hedenquist, S. Kesler, J. Thompson, and D. Wood (2017). *Future global mineral resources, Geochem. Perspect., 6, 1–171.* DOI: 10.7185/geochempersp.6.1.

Braun, J. and S. D. Willett (2013). "A very efficient $O(n)$, implicit and parallel method to solve the stream power equation governing fluvial incision and landscape evolution". In: *Geomorphology* 180-181, pp. 170–179. DOI: 10.1016/j.geomorph.2012.10.008.

Carvalho, L. D. V. d., J. Schnellrath, S. R. de Medeiros, and F. F. Vieira (2016). "Aspectos mineralógicos dos diamantes de Andaraí, Chapada Diamantina – BA". In: *IV Simpósio de Minerais Industriais do Nordeste*. Apresentado no IV Simpósio de Minerais Industriais do Nordeste, 10 a 13 de abril de 2016. João Pessoa, PB, Brasil.

Chaves, M. L. d. S. C., J. Karfunkel, and D. P. Svisero (1998). "Sobre a polêmica da origem do diamante na Serra do Espinhaço (Minas Gerais): um enfoque mineralógico". In: *Revista Brasileira de Geociências* 28.3, pp. 285–294.

Coulthard, T., M. Macklin, and M. J. Kirkby (2002). "A cellular model of Holocene upland river basin and alluvial fan evolution". In: *Earth Surface Processes and Landforms* 27.3, pp. 269–288. DOI: 10.1002/esp.318.

Diaz-Rodriguez, J., R. D. Müller, and R. Chandra (2021). "Predicting the emplacement of Cordilleran porphyry copper systems using a spatio-temporal machine learning model". In: *Ore Geology Reviews* 137, p. 104300. DOI: 10.1016/j.oregeorev.2021.104300.

Dietrich, W. E., D. G. Bellugi, L. S. Sklar, J. D. Stock, A. M. Heimsath, and J. J. Roering (2003). "Geomorphic Transport Laws for Predicting Landscape form and Dynamics". In: *Prediction in Geomorphology*. American Geophysical Union (AGU), pp. 103–132. DOI: https://doi.org/10.1029/135GM09.

Gilbert, G. K. (1877). *Report on the geology of the Henry Mountains*. English. Report. Washington, D.C., p. 212. DOI: 10.3133/70039916.

Guj, P. and R. Schodde (2025). "Will future copper resources and supply be adequate to meet the net zero emission goal?" In: *Geosystems and Geoenvironment* 4.1, p. 100320. DOI: 10.1016/j.geogeo.2024.100320.

Hancock, G. R., K. G. Evans, G. R. Willgoose, D. R. Moliere, M. J. Saynor, and R. J. Loch (2000). "Medium-term erosion simulation of an abandoned mine site using the SIBERIA landscape evolution model". en. In: *Soil Research* 38.2, p. 249. DOI: 10.1071/SR99035.

Hancock, G. R., J. B. C. Lowry, D. R. Moliere, and K. G. Evans (2008). "An evaluation of an enhanced soil erosion and landscape evolution model: a case study assessment of the former Nabarlek uranium mine, Northern Territory, Australia". en. In: *Earth Surface Processes and Landforms* 33.13. _eprint: https://onlinelibrary.wiley.com/doi/pdf/10.1002/esp.1653, pp. 2045–2063. DOI: 10.1002/esp.1653.

Hancock, G. R., J. B. C. Lowry, and M. J. Saynor (2016). "Early landscape evolution — A field and modelling assessment for a post-mining landform". In: *CATENA* 147, pp. 699–708. DOI: 10.1016/j.catena.2016.08.015.

Hancock, G. R., D. Verdon-Kidd, and J. B. C. Lowry (2017). "Soil erosion predictions from a landscape evolution model – An assessment of a post-mining landform

using spatial climate change analogues". In: *Science of The Total Environment* 601-602, pp. 109–121. DOI: 10.1016/j.scitotenv.2017.04.038.

Hancock, G., L. Nicolson, J. Purtill, and J. Dunlop (2025). "Applying erosion and Landscape Evolution Models to assess post-mining landform stability: Technical Paper". In: *Brisbane, Office of the Queensland Mine Rehabilitation Commissioner, Queensland Government*. DOI: 10.13140/RG.2.2.34671.34729.

Haughton, P. D. W., S. P. Todd, and A. C. Morton (1991). "Sedimentary provenance studies". en. In: *Geological Society, London, Special Publications* 57.1, pp. 1–11. DOI: 10.1144/GSL.SP.1991.057.01.01.

Hitzman, Kirkham, Broughton, Thorson, and Selley (2005). "The Sediment-Hosted Stratiform Copper Ore System". In: *One Hundredth Anniversary Volume*. Society of Economic Geologists. DOI: 10.5382/AV100.19.

Hitzman, M. W., D. Selley, and S. Bull (2010). "Formation of Sedimentary Rock-Hosted Stratiform Copper Deposits through Earth History". en. In: *Economic Geology* 105.3, pp. 627–639. DOI: 10.2113/gsecongeo.105.3.627.

Hobley, D. E., J. M. Adams, S. S. Nudurupati, E. W. Hutton, N. M. Gasparini, E. Istanbulluoglu, and G. E. Tucker (2017). "Creative computing with Landlab: an open-source toolkit for building, coupling, and exploring two-dimensional numerical models of Earth-surface dynamics". In: *Earth Surface Dynamics* 5.1, pp. 21–46. DOI: 10.5194/esurf-5-21-2017.

International Energy Agency (2025). *Copper*. Licence: CC BY 4.0. Paris.

Lovell-Kennedy, J., E. Roquette, S. Schröder, and J. Redfern (2023). "'I hate sand … it gets everywhere'—Phanerozoic sedimentary recycling from NW Africa". en. In: *Basin Research* 35.1, pp. 187–213. DOI: 10.1111/bre.12709.

Mather, B. R., R. D. Müller, C. P. Alfonso, M. Seton, and N. M. Wright (2023). "Kimberlite eruptions driven by slab flux and subduction angle". eng. In: *Scientific Reports* 13.1, p. 9216. DOI: 10.1038/s41598-023-36250-w.

Moliere, D., K. Evans, and G. Willgoose (2002). "Temporal trends in erosion and hydrology for a post-mining landform at Ranger Mine". In: *Research Institute* 31.

Pazzaglia, F. J. (2003). "Landscape evolution models". In: *Developments in Quaternary Sciences*. Vol. 1. The Quaternary Period in the United States. Elsevier, pp. 247–274. DOI: 10.1016/S1571-0866(03)01012-1.

Prado, E. M. G., C. R. De Souza Filho, E. J. M. Carranza, and J. G. Motta (2020). "Modeling of Cu-Au prospectivity in the Carajás mineral province (Brazil) through machine learning: Dealing with imbalanced training data". en. In: *Ore Geology Reviews* 124, p. 103611. DOI: 10.1016/j.oregeorev.2020.103611.

Rodriguez-Galiano, V., M. Sanchez-Castillo, M. Chica-Olmo, and M. Chica-Rivas (2015). "Machine learning predictive models for mineral prospectivity: An evaluation of neural networks, random forest, regression trees and support vector machines". en. In: *Ore Geology Reviews* 71, pp. 804–818. DOI: 10.1016/j.oregeorev.2015.01.001.

Ruetenik, G. A., J. D. Jansen, P. Val, and L. Ylä-Mella (2023). "Optimising global landscape evolution models with^{10} Be". en. In: *Earth Surface Dynamics* 11.5, pp. 865–880. DOI: 10.5194/esurf-11-865-2023.

Salles, T. (2016). "Badlands: A parallel basin and landscape dynamics model". en. In: *SoftwareX* 5, pp. 195–202. DOI: 10.1016/j.softx.2016.08.005.

Salles, T. and G. Duclaux (5, 2012). "3D Stratigraphic and geomorphic modelling from source to sink". In: *Proceedings of the 34th International Geological Congress*. Invited presentation. Brisbane, Australia.

Salles, T. (2019). "eSCAPE: Regional to Global Scale Landscape Evolution Model v2.0". en. In: *Geoscientific Model Development* 12.9, pp. 4165–4184. DOI: 10.5194/gmd-12-4165-2019.

Salles, T., X. Ding, and G. Brocard (2018a). "pyBadlands: A framework to simulate sediment transport, landscape dynamics and basin stratigraphic evolution through space and time". en. In: *PLOS ONE* 13.4. Ed. by Borazjani, I., e0195557. DOI: 10.1371/journal.pone.0195557.

– (2018b). "pyBadlands: A framework to simulate sediment transport, landscape dynamics and basin stratigraphic evolution through space and time". In: *PLoS ONE* 13, e0195557. DOI: 10.1371/journal.pone.0195557.

Salles, T., L. Husson, M. Lorcery, and B. Hadler Boggiani (2023a). "Landscape dynamics and the Phanerozoic diversification of the biosphere". In: *Nature* 624.7990, pp. 115–121. DOI: 10.1038/s41586-023-06777-z.

Salles, T., L. Husson, P. Rey, C. Mallard, S. Zahirovic, B. H. Boggiani, N. Coltice, and M. Arnould (2023b). "Hundred million years of landscape dynamics from catchment to global scale". en. In: *Science* 379.6635, pp. 918–923. DOI: 10.1126/science.add2541.

Salles, T., C. Mallard, and S. Zahirovic (2020). "gospl: Global Scalable Paleo Landscape Evolution". In: *Journal of Open Source Software* 5.56, p. 2804. DOI: 10.21105/joss.02804.

Sillitoe, R. H. (2010). "Porphyry copper systems". In: *Economic geology* 105.1, pp. 3–41. DOI: 10.2113/gsecongeo.105.1.3.

Singer, D. (1995). "World Class Base and Precious Metal Deposits—A Quantitative Analysis". In: *Economic Geology* 90, pp. 88–104. DOI: 10.2113/gsecongeo.90.1.88.

Smith, B., L. C. McInnes, E. Constantinescu, M. Adams, S. Balay, J. Brown, M. Knepley, and H. Zhang (2012). "PETSc's software strategy for the design space of composable extreme-scale solvers". In: *Preprint ANL/MCS-P2059-0312, Argonne National Laboratory*, pp. 16–18.

Sun, T., H. Li, K. Wu, F. Chen, Z. Zhu, and Z. Hu (2020). "Data-Driven Predictive Modelling of Mineral Prospectivity Using Machine Learning and Deep Learning Methods: A Case Study from Southern Jiangxi Province, China". en. In: *Minerals* 10.2, p. 102. DOI: 10.3390/min10020102.

Tucker, G. and G. Hancock (2010). "Modeling landscape evolution". In: *Earth Surface Processes and Landforms* 35, pp. 28–50. DOI: 10.1002/esp.1952.

Wang, Y., Z. He, K. Bian, C. Zhao, L. Chen, R. Dong, J. Zhang, Z. Zhu, and G. Liu (2024). "Tectonic controls on ore deposit exhumation and preservation: A case study of the Handan-Xingtai iron-skarn district". In: *Geoscience Frontiers* 15.6, p. 101924. DOI: 10.1016/j.gsf.2024.101924.

Willgoose, G. (2018). *Principles of soilscape and landscape evolution*. Cambridge University Press.

Wood, D. and A. van As (2024). "Discovery and Underground Mining of Large Deposits: Essential Training to Ensure Copper Supply". In: *SEG Discovery* 139, pp. 11–23. DOI: 10.5382/Geo-and-Mining-25.

Xiao, K., C. Li, M. Fan, L. Sun, R. Tang, N. Li, and X. Song (2024). "Quantitative prediction methods and applications of digital ore deposit models". In: *Ore Geology Reviews* 168, p. 106049. DOI: 10.1016/j.oregeorev.2024.106049.

Yanites, B. J. and S. E. Kesler (2015). "A climate signal in exhumation patterns revealed by porphyry copper deposits". en. In: *Nature Geoscience* 8.6, pp. 462–465. DOI: 10.1038/ngeo2429.

Zientek, M. L., J. D. Bliss, D. W. Broughton, M. Christie, P. Denning, T. S. Hayes, M. W. Hitzman, J. D. Horton, S. Frost-Killian, D. J. Jack, et al. (2014). *Sediment-hosted stratabound copper assessment of the Neoproterozoic Roan Group, central African copperbelt, Katanga Basin, Democratic Republic of the Congo and Zambia.* Tech. rep. US Geological Survey. DOI: 10.3133/sir20105090T.

2| ARTICLE 1
Quantitative provenance analysis for the Miocene Gulf of Mexico using high-resolution Landscape Evolution Modeling

Beatriz Hadler Boggiani[1], Claire Mallard[2], Tristan Salles[1], Nicholas Atwood[3], Michael L. Sweet[4], John Snedden[4]

[1]School of Geosciences, The University of Sydney, Sydney, Australia
[2]BHP Metal Global Endowment Team, BHP, Adelaide, SA, Australia
[3]BHP Metal Global Endowment Team, BHP, Tucson, Arizona, USA
[4]IJackson School of Geosciences, Institute for Geophysics, University of Texas at Austin, USA

- Using LEM, we reproduce the sedimentary architecture of the Gulf of Mexico;
- Our method enables provenance analysis under realistic geological scenarios simulated with LEMs;
- Climate was the primary driver of sediment transport into the Paleo-Mississippi catchment during the Mid-Miocene.

Abstract

Understanding source-to-sink dynamics is critical for reconstructing sediment transport pathways and the evolution of sedimentary basins. Here, we apply the landscape evolution model *goSPL* to simulate and quantify source-to-sink system dynamics in the well-documented Mid-Miocene of the Gulf of Mexico (GoM) basin. We produce landscape evolution models at a 2.5 km resolution to assess sediment transport over a 3-million-year period using paleo-elevation and paleo-climate models. We perform a series of sensitivity tests to highlight how climate and tectonic changes impact sediment provenance and deposition. The modelled sedimentation is compared against offshore sedimentation with regional stratigraphic records and provenance data, including detrital zircon and heavy mineral analysis. We track and quantify the volumes of sediment eroded from potential sources and compare it to the volume of sediment deposited in the GoM. Our results show that the provenance of sediments deposited in the Gulf of Mexico during the Middle Miocene remains largely stable despite variations in precipitation and tectonic uplift, and that high-elevation provenance regions are more sensitive to these changes due to changes in the slope/erodibility ratio. Our provenance studies show that traditional methods of provenance analysis tend to underestimate the contribution of older sources (*e.g.* Yavapai-Mazatzal) while overestimating the contribution of younger sources (*e.g.* Western Cordillera). Finally, we propose a novel and robust approach to quantify provenance analysis, minimizing reliance on traditional detrital mineral analyses.

Plain Language Summary

Sediment moves from its source, where it erodes, to its final destination, where it is deposited. Understanding this process, known as a source-to-sink, is essential for studying how landscapes evolve and how sediment accumulates over time. In this study we produce and evaluate landscape evolution models, using goSPL, to simulate and quantify the source-to-sink systems of the Mid-Miocene Gulf of Mexico (GoM), such as the paleo-Mississippi river. We analyzed how the landscape and sediment transport changed over a 3-million-year period in response to precipitation and tectonic uplift variations. To test the accuracy of our model, we compared its results with geological records and sediment depositional histories, incorporating data like detrital zircon and apatite fission track analyses. Our findings indicate that climate plays the most significant role in sediment transport, with high-elevation areas being more sensitive to climate changes. Additionally, we developed a new method to track and quantify sediment sources, reducing dependence on traditional detrital mineral (zircon) analyses that can be biased by sampling techniques. Our study provides new insights into sediment movement and offers an improved approach for analyzing past landscapes and sedimentary deposits.

1 Introduction

The Middle Miocene Gulf of Mexico (GoM) source-to-sink system is a well-known region for oil and gas exploration (Gutiérrez Paredes et al. 2018). The gulf is characterized by relatively young sedimentary systems and a well-documented sediment sink, supported by published literature, well data, and seismic interpretations (Snedden and Galloway 2019; Towoju and Gani 2024; Villagómez et al. 2022). We use the landscape evolution model goSPL (Salles et al. 2020) to evaluate the relationships between the various components of this continental-scale source-to-sink system. The abundance of available data in the region allows for a quantitative calibration of model accuracy and for potential frontier studies in mineral exploration.

We quantify the relationships between the Middle Miocene Gulf of Mexico sedimentary basin formation and the evolution of North America hinterland drainage network informing the provenance of our sediments. Our numerical approach is validated using this well-documented system, with focus on the processes that explain present-day accumulation, to support future global-scale modeling applications, including the possibility of assessing the GoM metallogenic potential (*e.g.* Lithium).

1.1 Geological settings

The Gulf of Mexico Basin initiated during the Triassic to Jurassic rifting phase which occurred between the Yucatan microplate and the North American plate, followed by seafloor spreading until the Early Cretaceous (Marton and Buffler 1994; Pindell and Kennan 2009; Filina and Hartford 2021; Curry et al. 2024). Throughout the Mesozoic, this basin evolved from non-marine deposits, to shallow marine carbonates, to a deep-marine sedimentary system. During the Paleogene, large rivers drained much of the North American continent and delivered sediments into the basin (Blum and Pecha 2014).

The variability of depositional environment found in the basin is mostly attributed to regional tectonics and climatic evolution, both of which modify sediment routing system and erosional intensity in the upstream regions (Galloway 2008). Fourteen depositional episodes have been defined for the Cenozoic gulf filling history, with at least five different tectono-climatic events (Galloway et al. 2011). As an example, drainage reorganization and enhanced sediment discharge during the Paleocene were contemporary to the growth of the Laramide orogenic front and increased precipitation conditions (Blum and Pecha 2014). During the Oligocene, the combination of small catchments shaped due to local tectonics and a more arid climate in the Western Interior resulted in a significant decrease in marine sediment accumulation in the deepest part of the basin despite a global sea-level fall.

During the Miocene, the Gulf of Mexico catchment entered an arid extensional era characterised by North-South regional extensions including the Basin and Range and the Rio Grande rift (Galloway et al. 2011). The associated depositional episode formed a single genetic sequence modulated by the interplay of sea-level changes, sediment supply, and salt-controlled subsidence (Liro et al. 2000; Hall 2002). Sediment supply increased concomitantly to the expansion of the Tennessee catchment and more humid condition in eastern North America (Snedden et al. 2018a). It then shifted from West to East as the result of (1) the subsidence of the Rockies, (2) drier

conditions extending across the western gulf margin and throughout the western interior and (3) the unroofing of the Appalachian uplands triggered by epeirogenic uplift and/or wet climatic conditions both of which enhancing sediment delivery to the gulf (Bentley et al. 2015). These tectonic and climatic forcing favoured the development of large and thick submarine fans as well as the resurgence of slope and deep-water deposition (Ferrari et al. 2005; Ferrari et al. 2012; Fernandes et al. 2019), (Fig. 1A & B).

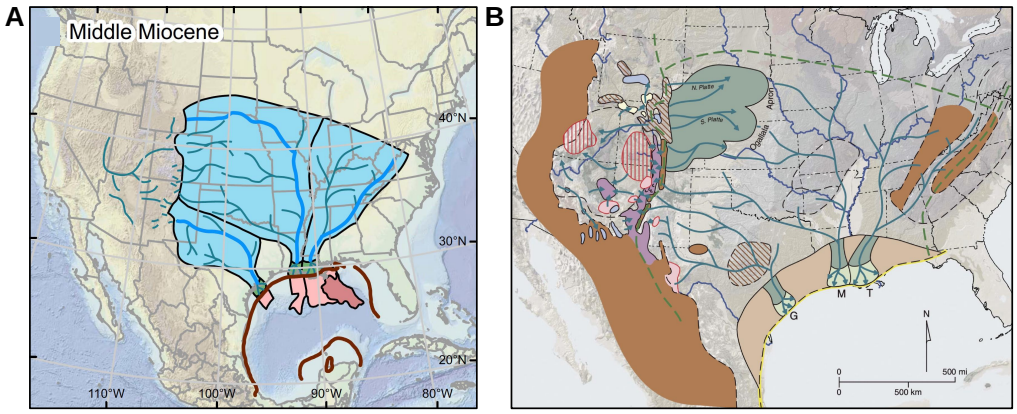

Figure 1: **A.** Catchment areas of the longest rivers (dark blue lines) directly draining into the Gulf of Mexico during the Mid-Miocene (Snedden et al. 2018b). **B.** Corresponding paleogeographic reconstruction highlighting the central plains tributaries and surrounding high-relief uplands, from the Greenville area in the east to the Western Cordillera in the west(Galloway et al. 2011).

Upstream paleo-catchment reconstruction for the Miocene indicates the contribution of at least five main rivers (i.e., Mississippi, Tennessee, Rio Bravo, Guadalupe, Rio Grande - Fig. 1A & B) that supplied large volumes of sediment into the basin (up to 100×10^3 km^3/Myr, Galloway et al. (2011)), and which individual importance into the total sedimentary budget varied significantly from Upper to Lower Miocene. For example, provenance analysis shows an increase in sediment influx from an emerging Tennessee drainage system which expanded and fully developed over the Middle and Late Miocene (Xu et al. 2022), reflecting both in wetter climate in eastern North America and tectonic rejuvenation of the Appalachians.

2 Methods

2.1 Simulated processes and model overview

Forward modeling of landscapes and sedimentary systems has proven to be a valuable avenue to integrate source-to-sink concepts into a process-based framework that considers sedimentation, eustatic sea level, climatic and geodynamic forcing (Granjeon and Joseph 1999; Syvitski and Hutton 2001; Adams et al. 2017; Salles et al. 2018b; Yuan et al. 2019; Salles et al. 2023a; Salles et al. 2023b; Hadler Boggiani et al. 2025).

Here, we use goSPL (Salles et al. 2020) an open-source scalable parallel numerical model available on GitHub (`https://github.com/Geodels/gospl`, last access

08/10/2025) that simulates landscapes and sedimentary basins reconstruction from regional to global scale over unstructured grids. It is based on a simplified mathematical representation of several physical processes: river incision, hillslope processes in both marine and terrestrial domains computed by stream power and creep laws, and marine deposition, sediment compaction, stratigraphic layering and porosity change. Finally, it can be forced with spatially and temporally varying tectonics (horizontal and vertical displacements), climatic conditions (precipitation) and sea-level fluctuations.

goSPL simulates sediment supply and routing from source to sink in a self-consistent process-based manner. In other words, the erosion occurring in upstream catchments is linked to basin sedimentation through sediment routing resulting from a combination of channeling and hillslope processes (Fig. 2). The routing implementation for both water and sediment fluxes depends on a multiple flow direction algorithm, which prevents erosion pathways from becoming locked along a single direction and enable fluxes to be routed across flat regions into multiple branches (Tucker and Hancock 2010). The model's main equation, the continuity of mass, is expressed by:

$$\frac{\partial z}{\partial t} = U_i + \kappa \nabla^2 z_i + \epsilon P_i^d Q_i^m \nabla z_i^n \tag{3.1}$$

where the flow discharge Q_i in cell i is given by:

$$Q_i = P_i A_i + \sum_{j \in \text{up}} Q_j \tag{3.2}$$

where z represents the change in surface elevation (m) over time t (yr), U is the tectonics (vertical land motion) in m/yr and κ the diffusion coefficient for soil creep (Salles et al. 2018a). The last term in the right-hand side of Eq. 3.1 represents fluvial processes based on a stream power law with ϵ describing the precipitation-independent component of erodibility, m and n representing dimensionless empirically constants set to 0.5 and 1. The proposed stream power law incorporates the effect of local mean annual precipitation rate and d is a positive exponent that has been estimated from field-based relationships to 0.42 (Murphy et al. 2016). In the flow discharge equation (Eq. 3.2, Q_i), the upstream total area (A_i) and local precipitation (P_i) are combined to form the water flux ($P_i A_i$) with added upstream flow discharge (Q_j, in Equation 3.2).

In goSPL, the flow discharge ($P_i A_i$) in m^3/yr and the net precipitation rate P are computed on unstructured grids using a parallel implicit drainage area method (Salles 2019; Richardson 1911). The number of flow directions has been assigned to its maximum value (6) for this study. In this study, we neglect transport-limited behavior and instead account only for detachment-limited behavior using a stream power law to simulate the erosion rate function of river discharge, precipitation and slope (Howard et al. 1994).

Our landscape evolution models include source to sink transfers, inland and marine sedimentation as well as erosion in complex catchments dynamics, so we have to account for draining and filling of inland depressions. The depression filling approach used in goSPL is based on the implementation of the priority-flood algorithm (Barnes et al. 2014) which removes flat surfaces and creates gradient allowing flow in multiple directions as well as calculation of each depression volume through time.

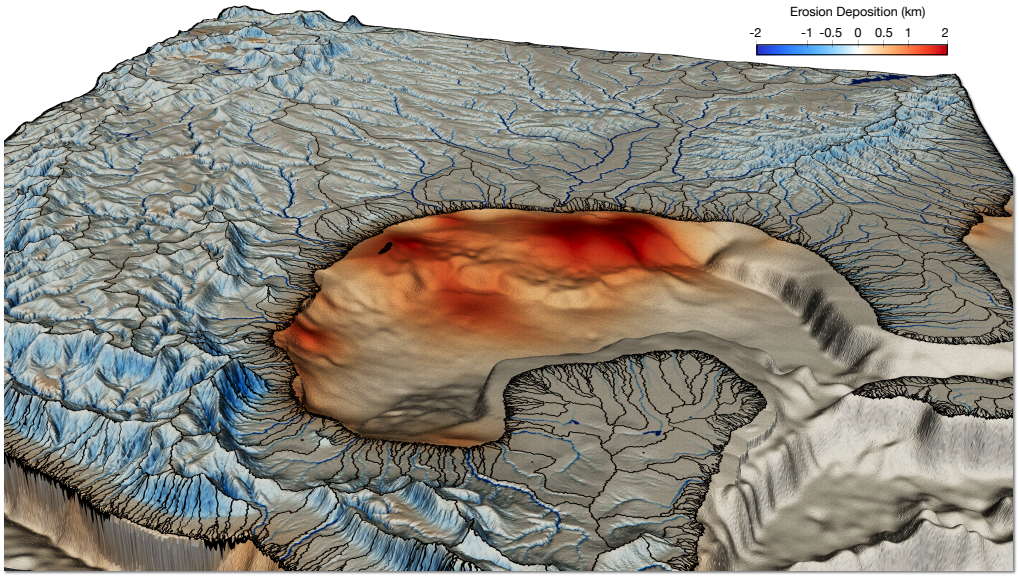

Figure 2: Source-to-sink perspective of Gulf of Mexico Mid Miocene evolution from drainage catchments to offshore basin sedimentation. The cumulative, from 15.6 to 12 Ma, erosion-deposition map highlight regions dominated by erosion in blue and deposition in red. The black lines represent drainage basin divides and the deep blue ones show the major river systems.

Sediment fills depressions based on availability: if erosion products are lower than the available depression volume, all material is deposited, raising the depression floor; the volume of incoming sediment is higher than the depression volume available, depressions fill, elevation increases, and overflow continues downstream at the pour point overflowing into the next catchment. This process repeats until all sediment is deposited inland or in marine areas. The final depression-filled elevation is used to compute the flow accumulation.

A more detailed description of the physical processes and algorithmic approaches is available in (Salles 2019) and from the following link `https://gospl.readthedocs.io` (last access 08/10/2025). The main advantages of the model lie in its design of implicit and parallel solutions for the constitutive linear and non-linear equations, making it possible (1) to increase the model stability even with large time steps, and (2) to scale the simulation runtime over hundreds of CPUs when grids of several millions of vertices are considered (Salles et al. 2020).

2.2 Additional simulation parameters

We built our simulation mesh at an average 2.5 km resolution (representing about 1.6×10^6 vertices and 3×10^6 triangular cells) covering an area of about 4000 km (W-E) by 4500 km (N-S). The simulations are run from 15.6 Ma to 12 Ma with a time step of 5 kyr (used to solved the implicit formulation of Eq. 3.1). Stratigraphic architecture is recorded every 25 kyr and outputs generated every 200 kyr.

We tested different erodibility coefficients (ϵ) during the calibration phase (Fig. S3 and Tab. S1). Based on total sediment accumulation within the basin, we decide for an erodibility coefficient ϵ set to 2.1 x 10^{-7} /yr. The diffusion coefficient κ is given

Structure	Parameters	Values
Domain	flowdir	6
Time	start	-15.6 Myr
	end	-12.0 Myr
	outputs timestep	200 kyr
	tectonic timestep	5 kyr
	stratigraphy timestep	25 kyr
SPL - Stream Power Law	ϵ	2.1 x 10^{-7} /yr
	d	0.42
Diffusion	κ_a	0.02 m^2/yr
	κ_m	0.02 m^2/yr
	clinSlp	5.0 x 10^{-6}
	smthS	1.0 x 10^{-3} m^2/yr
	smthD	1.0 x 10^{6} m^2/yr
	offset	10
	oFill	-2.5 x 10^{3}
Sea	curve	Figure 4C, (Haq et al. 1987)
Tectonic	maps	Figure 4A
Climate	map	Figure 4B

Table 1: goSPL parameters used to simulate mid-Miocene Gulf of Mexico source-to-sink system.

a value of 0.02 m^2/yr, and d, m, and n exponents in Eq. 3.1 are set to 0.42, 0.5, and 1 respectively, other parameters are available in Tab. 1. The nine simulations are then run on a super-computer using 128 CPUs with a run-time of up to 4 hours for each simulation.

Figure 3 shows the results for one of these simulations and illustrates the basic outputs produced by goSPL: (1) landscape temporal evolution, (2) associated catchments and rivers network, and (3) spatial distribution of cumulative erosion/deposition patterns. We then analyze these outputs in detail using post-processing notebooks discussed previously and evaluate the controls of our different forcing on the Gulf of Mexico source-to-sink system focusing initially on the continental domain (evaluating water and sediment flux), and then on the marine region (analyzing predicted sediment accumulations, provenance data and stratigraphy within the offshore basins).

2.3 Designing initial conditions and temporal forcing

In order to simulate the source-to-sink system for the Middle Miocene, we build an initial topography at 2.5 km resolution deemed representative of the Upper to Middle Miocene transition. To do so, we rely on present-day topography that is then adjusted with available information provided by the Gulf Basins Depositional System (GBDS) industrial associates program datasets (Fig. S4A). We chose this option instead of using a paleo-elevation reconstruction models (e.g. the ones from Scotese and Wright (2018) at 0.1°, 0.2° and 1°, from Frigola et al. (2018) at 0.2° and 0.5° and from Straume et al. (2020) at 0.2° and 0.5°) after observing unrealistic

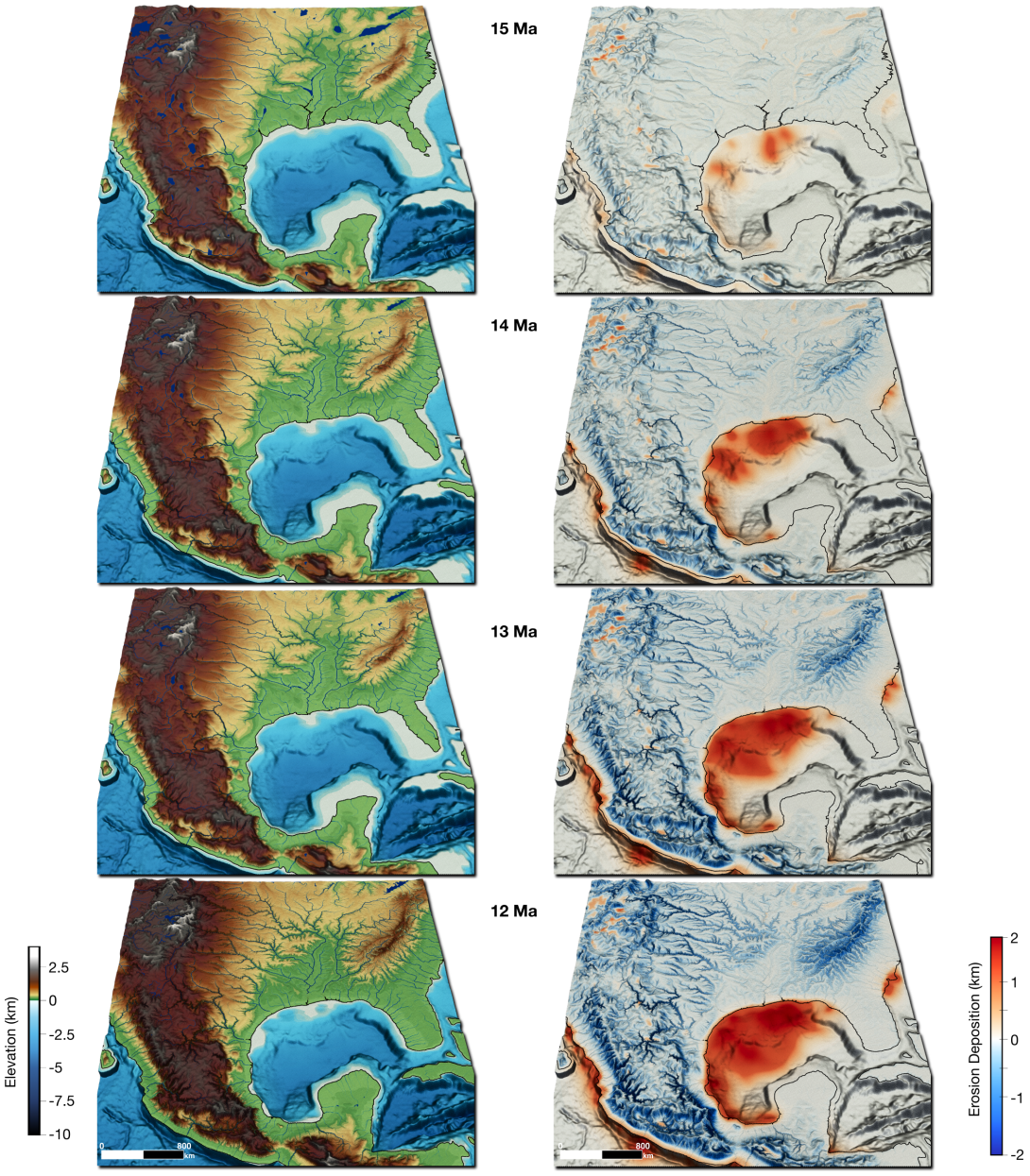

Figure 3: Simulation outputs when considering maximum uplift and rainfall conditions. Left views show predicted elevation over time for every 1 Myr with major rivers positions. Right views present the associated cumulative erosion deposition distribution across the landscape, with incision along the mountain ranges and sediment accumulation across the Gulf of Mexico continental shelf and offshore regions.

landscape and associated tectonic interpretation, resulting in improbable drainage pattern and main depocenter locations. These poor results are also linked with the inherent coarse resolution of available reconstructed paleo-elevations (above 0.1°). We observed that resolutions of at least 0.05° are needed to reasonably model earth-like regional drainage geometries and depositional systems. Nevertheless, the long-wavelength of the paleo-elevations from Scotese and Wright (2018) at 20, 15, and 10 Ma have been sporadically compared with the elevational range produced in our simulations.

In terms of GBDS dataset, we mostly rely on maximum flooding surface boundary, paleo-shorelines, continental shelf limits, regional catchments extent, and paleo-river positions to adjust our initial surface (Fig. S4A). In addition, we also account for rates of vertical land motions (both isostatic and dynamic - Sup. Fig. S1 & S5) inferred from our current understanding of the regional geological context, especially using geomorphological indicators, stratigraphic, and seismic data (Paredes et al. 2017; Hentz and Zeng 2003).

The first backward step, integrating Middle Miocene paleo-rivers drainage, shorelines and tectonic rates yields a series of paleo-elevation maps that are subsequently modified and refined to fit observations. As an example, the Mississippi paleo-drainage from Fig. 1A & B defines a North-South trending paleo-Mississippi river cutting through the Ozark Plateau, which seems at odds with existing observations for the region. Instead, we modified the paleo-drainage to force a North-East connection with the paleo-Missouri River that resembles present-day conditions (Fildani et al. 2018) while keeping the proposed paleo-Arkansas River route between Ouachitas Mountains and the Ozark Plateau.

We compared obtained elevations with previous studies (Galloway 2008; Galloway et al. 2011; Snedden et al. 2018a) and did several readjustments to the initial surface based on catchments extension, shore-face slopes and upstream elevations. We did not test uncertainties associated with the initial simulated paleo-drainage network morphology as we used rich GBDS and detrital zircon/apatite studies reducing uncertainty on the initial drainage network.

Instead, we assume that tectonic subsidence/uplift and precipitation represent the two largest uncertainties in the model and global understanding of the regional dynamic. To mitigate the inherent uncertainties in the temporal forcing, we select deterministic low, mid and high case scenarios to evaluate three uplift (Fig. 4A, Fig. S5) and three precipitation (Fig. 4B) cases convolving these together to get the nine scenarios. Additional tests were performed to constrain the erodibility and marine diffusion parameters and are presented in Fig. S3.

Each pair of scenarii is then ran one after another (totalizing nine simulations) not only to estimate the likelihood of a specific combination of climate and tectonic regime to reproduce sediment flux and basin stratigraphy, but more importantly to understand their role, contribution, and impact on the regional evolution of the Gulf of Mexico during the simulated period.

2.3.1 Precipitation and sea-level

For the climate, we initially rely on the paleo-precipitations reconstruction from Valdes et al. (2021) and then perform a series of adjustments to account for orographic effects and regional variabilities based on previous work (Retallack 2007; Blakey and Ranney 2017). The corresponding rainfall maps (Fig. 4B) allow to test three distributions: (1) a *dry*-climate with low precipitation over the Sierra Nevada, Great Basin, and Coastal Plains region and moderate rainfall for the Appalachian Mountains (up to 1.1 m/yr); (2) a case with the same dryer conditions in the Sierra Nevada but globally higher rainfall on the northern part of the Gulf of Mexico catchment in particular for The Rocky Mountains, the Great Plains area and the Appalachians. This induces average rainfall of 1.7 m/yr in the Appalachians, as well as an increased orographic effect on the eastern side of the Sierra Madres; and (3) an overall increased in Miocene rainfall regime over the entire region with up to 2.5 m/yr over the Appalachians, 1.5 m/yr in the Chiapanecan orogeny and >1 m/yr for the Colorado Plateau.

In addition to rainfall, we also force the model with a long-wavelength sea-level curve (Fig. 4C). As eustatic variations directly influence the volume of sediments stored in the coastal plain and shelf, we tested different curves (Fig. S2A) to evaluate their impacts on stratigraphic evolution and sediment accumulation.

We set on the curve from Haq et al. (1987) which takes into account the influence of glacio-eustasy in the gulf (Galloway et al. 2000) and seems the more accurate in terms of sediment volume, maximum transgression timing and long-term sea-level fall in the region. This curve shows an initial lowering (down 75 m from its relative position) followed by a rise back to its initial position over the first 300 kyr. These sea-level variations preserve the shoreline in the most reasonable positions, avoiding an overly flooded continent, in accordance with GBDS dataset and previous studies (Galloway et al. 2000). The subsequent Middle Miocene sea-level evolution can then be described as a long-term decrease in relative position due to the expansion of the west Antarctic ice sheet (Abreu and Anderson 1998). This induced an overall regressive cycle and sea-level fall after a major flooding event in lower Middle Miocene. Here, we define three distinct stages each lasting approximately 1 Myr and corresponding to successive $\simeq$50 m fall. On top of this large frequency signal, we add small wavelength variations of up to 50 m amplitude based on Miller et al. (1998) high-frequency curve (Fig. S2A).

2.3.2 Tectonic conditions

For the tectonic regime, we evaluate the importance of Middle Miocene tectonic regimes (Miall and Blakey 2019) on sedimentation by forcing the model with different conditions for The Rocky Mountains, southern Sierra Madres, and Appalachians regions as well as for the Central Plains.

We first modulate the amplitude of the greater Colorado Plateau region to provide different conditions for erosion, drainage reorganization, and landscape evolution. Lacustrine deposits (Lake Mead - western Colorado Plateau) record several major pulses of mid-Miocene extensions between 24 and 16 Ma, as well as a post-Miocene uplift (11 to 6 Ma) (Huntington et al. 2010). The spatial and temporal extension

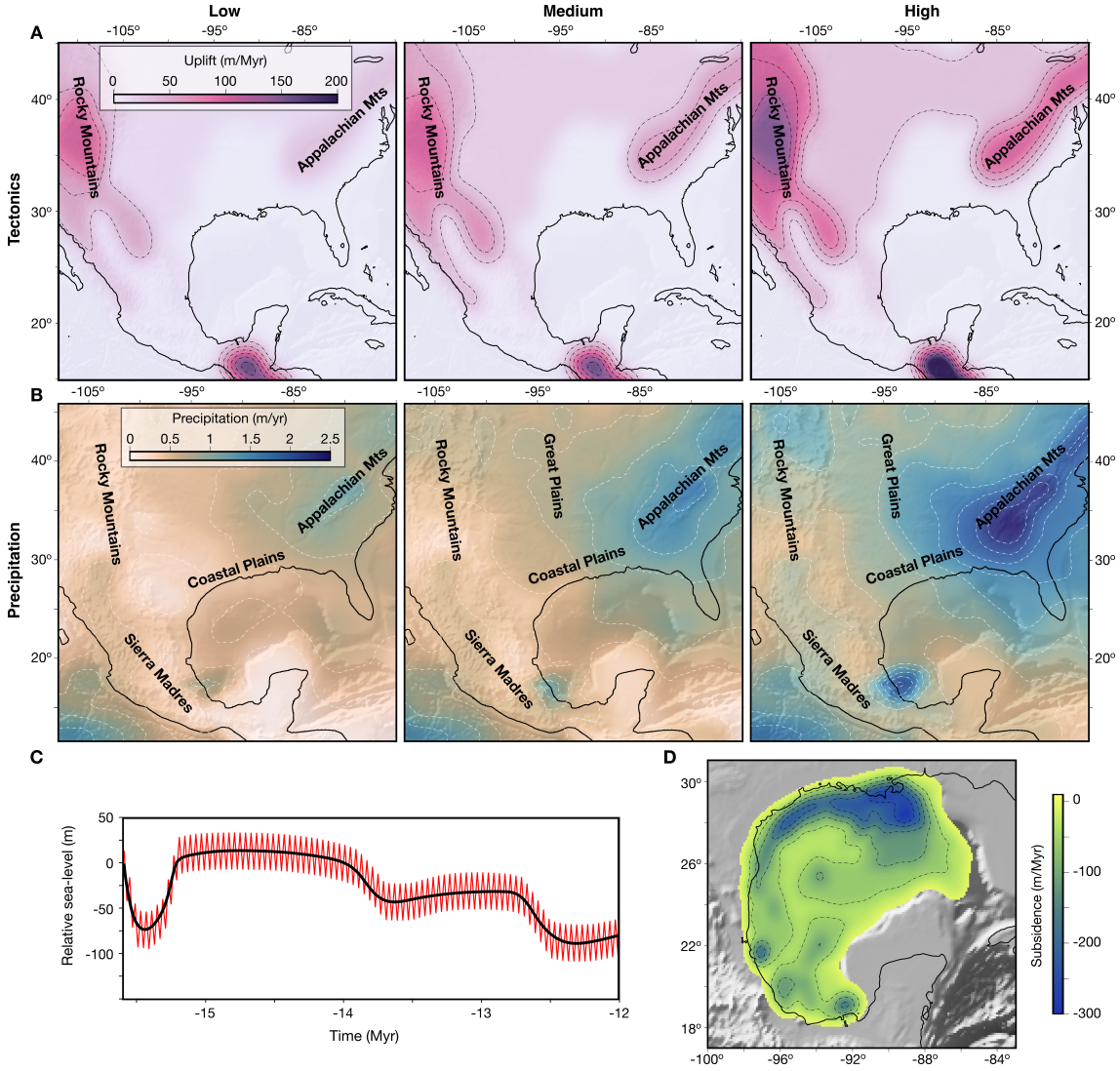

Figure 4: **Lower to Mid Miocene forcing conditions. A.** Evaluated tectonic scenarios with rates up to 200 m/Myr (Fig. SS5): The first panel (left panel) corresponds to the low tectonic uplift scenario with small uplift along the Appalachians. Medium scenario (central panel) has an increase in uplift rate along the Rockies and Appalachians. Right panel represents high tectonic uplift scenario with accrued uplift for all mountain ranges, the Great Plains and Mississippi River catchment. **B.** Precipitation maps based on paleo-climate reconstructions (Valdes et al. 2021), adjusted for local variability beyond the spatial resolution of the general circulation model. From left to right, the maps show an increase on precipitation referred to as low (mean value: 0.5 m/yr), mid (mean value: 0.73 m/yr), and high (mean value: 1.1 m/yr) precipitation, respectively. **C.** Relative eustatic curve (black line) after Haq et al. (1987). With the initial elevations of our simulation defined relative to the position of the coastline at 15.6 Ma, the sea-level curve is set to 0.0 m at that time. Higher frequencies in the sea-level signal were simulated with a 50 m amplitude fluctuation centered on the low frequency curve (red line). **D.** Extracted sediment volume from the GBDS dataset for the simulated period (15.6 to 12 Ma) is used to define an offshore subsidence rate that is added to the uplift rate (**A**) to build the tectonic forcing in the simulation.

of these pulses is still debated, and we define values ranging from 60 m/Myr (*low case*) to 100 m/Myr (*mid case*) (Roberts et al. 2012; Miall and Blakey 2019) to 170 m/Myr (*high case*) which falls within the calculated rock uplift rates between 25 and 10 Ma (150 to 200 m/Myr) based on longitudinal river profile analysis (Stephenson et al. 2014) (Fig. 4A).

As mentioned previously, evidence for a Miocene rejuvenation of the Appalachian Mountains has been described from provenance analysis of marine sediments collected on the northeastern part of the gulf (Pazzaglia et al. 2000; Liu 2014). Convergent measurements of erosion rates determined from cosmogenic ^{10}Be (Miller et al. 2013) point to an ongoing wave of 100-150 m of incision that has been propagating upstream since at least 3.5 Ma, and possibly since 15 Ma, suggesting relief growth over the region. These values correspond to an average uplift rate of 20 to 50 m/Myr and have been used to build the Middle Miocene tectonic forcing for the Appalachians in our simulation (Fig. 4A: low case - <25 m/Myr, high case - 70 to 100 m/Myr, Fig. S5).

In the South, uplift in eastern Mexico is associated with the Middle Miocene Chiapanecan orogeny. From low-temperature thermochronological data of the Chiapas Massif, uplift rates of up to 700 m/Myr were estimated in this region (Villagomez and Pindell 2021; Gray et al. 2021). Age-elevation profiles from zircon (U-Th)/He ages across the Caribbean-North America plate boundary document more conservative values of up to 170 m/Myr assuming a steady vertical rock uplift (Simon-Labric et al. 2013). Based on these studies, the Sierra Madres Oriental and Sierra Madres de Chiapas mountain ranges have been defined with the highest tectonic uplift rates in our scenarii (Fig. 4A) with values ranging from 120 m/Myr (*low case*) up to 300 m/Myr (*high case*).

Finally, we impose a subsidence rate in the offshore region (Fig. 4D) based on reconstructed sediment thickness for the Middle Miocene interval compiled by the GBDS (Fig. S4). These datasets have been edited to eliminate mini-basins created by salt tectonics after discussion with BHP and GBDS experts.

3 Sediment fluxes through space and time

We first focus on the continental domain and quantify sediment transfer by major rivers across the landscape. This analysis is a pre-requisite before one can start evaluating the simulated marine sedimentation.

3.1 Predicted continental water and sediment fluxes

To do so, we extract the top fifty largest sediment fluxes and monitor predicted water discharges for the Middle Miocene period (Fig. 5A & B). The distribution of the water discharge depends on the size of the river catchments and on the amount of rainfall they receive. We find that a few major catchments dominate the regional water distribution to the gulf (main ones being the Mississippi, Tennessee, and Rio Grande drainage basins). Overall, the extension of these catchments fits with previous studies (Galloway et al. 2011; Xu et al. 2022). At regional scale, we notice that except for a large drainage capture of the southern headwaters of the

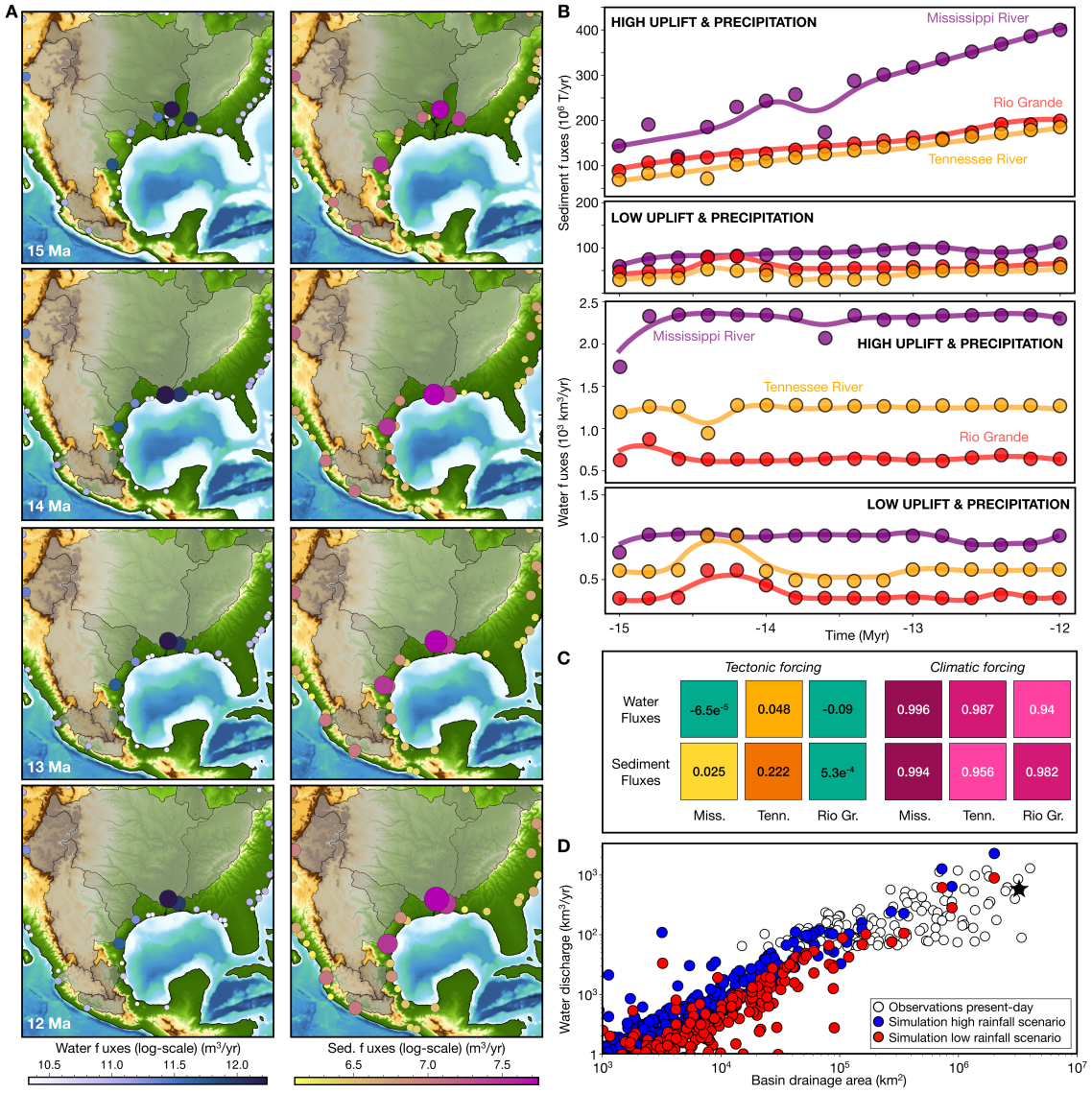

Figure 5: **Analyzing water and sediment flux. A.** Distribution of top 10 largest catchment areas from 15 to 12 Ma and their drainage divides are shown in light gray. Position of the 50 largest simulated river water (left) and sediment (right) fluxes based on surface morphologies resulting from tectonics, imposed paleo-climates, and riverine processes. **B.** Temporal distribution of sediment and water fluxes for the three major contributors of sediment within the Gulf of Mexico (i.e. Mississippi, Rio Grande and Tennessee rivers) under (1) high uplift and precipitation forcing, and (2) low uplift and precipitation forcing. **C.** Summary of correlations between water and sediment fluxes for the 3 rivers showing correlation coefficients with uplift and climatic forcing based on Table 2. **D.** Log-log plot of modelled water discharge against basin drainage area for 2 forcing scenarios (red and blue circles) at 12 Ma. White circles correspond to present-day river values only considering rivers whose discharge is more than 2000 m^3/s (~63 km^3/yr). Black star represents Mississippi River values.

paleo-Mississippi river by the paleo-Guadalupe basin (Fig. 5A - between 15 and 14 Ma), most of these drainage basins remain remarkably stable throughout the Miocene. We also found a plethora of smaller size watersheds draining waters from the surrounding mountain ranges (the Rockies Appalachians, and Sierra Madres).

Generally the highest sediment flux corresponds to the largest river water discharges (Fig. 5A). However, this relationship does not always hold because the physiography of the watershed plays a crucial role in modulating sediment flux. For example, small catchments adjacent to high mountain ranges, such as the ones on both sides of the Sierra Madres, have low water discharges but deliver significant volumes of sediments to the Gulf of Mexico or the Pacific Ocean. Conversely, large water flux do not necessarily convey larger sediment flux. As an example for the high uplift and precipitation scenario, there is a two-fold increase in water fluxes between the Tennessee and Rio Grande rivers but their respective sediment fluxes are of a similar order (Fig. 5B). This is attributed to high-precipitation rates over the relatively flat landscape of the downstream paleo-Tennessee basin and to the erosional unroofing and the storage of Appalachians-sourced sediments in upstream depocenters (Pazzaglia et al. 2000).

Extracted drainage networks from the modelled landscapes and the corresponding water discharge for each catchment (Fig. 5D) show an expected increase of the water discharge with drainage area and indicate a nearly linear relationship (log-log scaling). We also see a clear dependency of water discharge with rainfall regime (red *vs* blue circles in Fig. 5D) and a comparison with modern river values shows that the simulated range fits well with observations both for the low and high precipitation scenario.

In our simulation, the continental-scale Mississippi River system resembles the modern one, integrating drainages from the Appalachian Mountains in its eastern side to the northern and central Rocky Mountains on the west. When compared to present-day Mississippi basin drainage area and discharge (star in Fig. 5D), the Miocene Mississippi basin drainage area is of the same order but delivers more water.

Simulated major river positions and their associated catchment areas conform with interpreted representation for that time (Snedden et al. (2018a); Fig. 5A). Looking at the distribution of sediment fluxes draining from North America (i.e. The Rocky Mountains, Central Plains, and the Appalachians), the ancestral Mississippi River is the dominant sediment contributor throughout the Middle Miocene (e.g., 52% by 12 Ma in Fig. 5B) and its delta is the principal extra basinal fluvial/delta axis in the Louisiana coastal plain with a sediment load of up to 100×10^3 km/yr which is in accordance with estimates from previous studies (Ricardo 2003; Galloway et al. 2011). The contributions of the Tennessee and Rio Grande rivers are substantial and relatively similar (equivalent sediment volume corresponding to around 24% of the total North America sediment budget delivered to the gulf). These results are of the same order as the ones derived from detrital zircon geochronology analysis (Bentley et al. 2015; Xu et al. 2022).

Precipitation	Uplift	Rio Grande water flux (km^3/yr)	Rio Grande sediment flux (10^6 T/yr)	Mississippi water flux (km^3/yr)	Mississippi sediment flux (10^6 T/yr)	Tennessee water flux (km^3/yr)	Tennessee sediment flux (10^6 T/yr)
high	*high*	712	135	2347	246	1285	118
high	*mid*	829	138	2325	237	1299	113
high	*low*	836	134	2374	245	1253	97
mid	*high*	457	83	1612	155	926	76
mid	*mid*	462	81	1586	148	910	68
mid	*low*	480	80	1561	143	851	57
low	*high*	378	51	1003	80	633	45
low	*mid*	366	55	1016	81	680	44
low	*low*	354	55	1027	81	648	39

Table 2: Estimates of average sediment and water fluxes for the Rio Grande, Mississippi, and Tennessee rivers for the period ranging from 15 to 12 Ma obtained for each of tested uplift and precipitation scenarios. Highest and lowest values have been underlined.

3.2 Correlations and statistical analysis

Independent evaluation of the influences of tectonic uplift and precipitation on the geomorphology and continental fluxes evolution can be performed statistically from systematic extraction of the results presented above for each scenario (i.e. combined pair of forcing - Tab. 2). From this, correlation matrices can be derived and are summarized using correlation coefficient values (Fig. 5C). First, these correlation values show that Middle Miocene precipitation, more than tectonic uplift (based on the chosen forcing), drives sediment transport and delivery to the Gulf of Mexico, with correlation values above 0.9 in all cases. This is not surprising as we expect precipitation to control water discharge (more precipitation would increase river discharge). However, over geological time scale and when combined to tectonics, it could also trigger drainage reversal or reorganization that might actually change the overall geometry of a basin and result in a decrease in water flux induced by shrinking and splitting of specific catchments. Here, this is not the case for the Mississippi, Tennessee, and Rio Grande as shown in Fig. 5A where all these basins remain stable from 15 to 12 Ma.

For the tectonic uplift forcing conditions, we find no significant relationship except for the Tennessee River where the uplift of the Appalachian Mountains statistically increases the sediment supply into the gulf (highest value in the correlation matrix for sediment flux: 0.22 and lowest value for the precipitation: 0.95 - Fig. 5C). Those results do not imply that increased uplift across the different regions has no effect on the capacity of these rivers to erode and transport sediment into the gulf (as shown in Tab. 2). Rather, they show that, within the range of input conditions tested, tectonic uplift forcing plays a secondary role compared to precipitation, and has a lesser influence than precipitation over the Middle Miocene sediment dynamics in the region. This conclusion is regionally-dependent and can be induced by the low tectonic uplift rates in the gulf catchment as areas experiencing higher tectonic uplift rates may have more relation of tectonic rates to sediment fluxes.

4 Assessing sedimentation and regional stratigraphic history

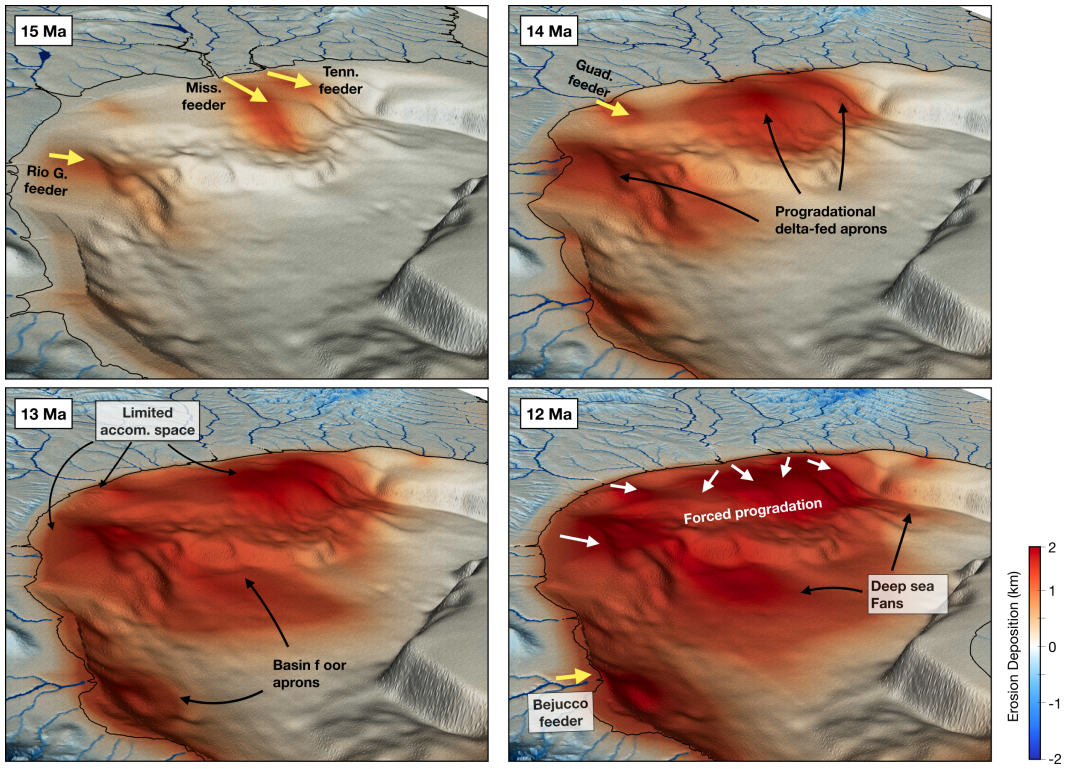

Figure 6: Predicted evolution of Gulf of Mexico marine deposition during the Mid Miocene for the high precipitation and uplift scenario. The main feeders across the northern shelf (Rio Grande, Mississippi, and Tennessee rivers) form large deltaic systems that prograde on the continental shelf following (Snedden et al. 2018a). Additional feeders are activated later on during the simulation, first from the Guadalupe River around 14 Ma, then from the Sierra Madres mountain range directly to the eastern Mexican Shelf (across the Bejuco Canyon). Fast sedimentation rate over the shelf, for this specific scenario, quickly fills the accommodation. As a result, it forces sediment progradation on the continental slopes and creates large delta-fed and basin floor aprons. By 12 Ma, sediments transferred from the Rio Grande, Mississippi and Tennessee rivers accumulate in the deepest part of the Gulf of Mexico forming large deep sea fans.

4.1 History of marine sediment accumulation

We first start by analyzing the general trends in depositional patterns over the entire region (Fig. 6). We see that the coastal and deep-water sediment accumulation over the Middle Miocene creates an extensive central Gulf of Mexico composite delta system fed largely by the Mississippi River and the Tennessee River (Fig. 5A & B). The large influx of sediment combined with relative sea-level fall from 15 to 12 Ma (Fig. 4C) is not counterbalanced by the imposed offshore subsidence rate (Fig. 4D) and the available space gets filled rapidly. Similar trends happen on the western side of the gulf where the Rio Grande feeder quickly builds a prograding delta during the first 1 Myr. This is in accordance with well datasets (Cristelaria I MFS datum,

Ricardo (2003)) that show the formation of an early depocenter on the western side of the gulf over this time period. Reduced accommodation and continuous sediment influx forces the development of slope aprons across the entire region with more notable ones on the southeast and southwest of the Mississippi-Tennessee large coastal delta and on the slope facing the Rio Grande catchment (Fig. 6). The central depocenter is filled with off-lapping delta lobes over the ancestral Mississippi delta and Tennessee delta front (Fig. 6). It is in accordance with the sedimentation record showing a central fluvial-dominated delta that prograded rapidly on the shelf margin. However, it is worth noting that delta fed aprons on the eastern side of the gulf are wave-dominated with along-strike reworked sediments delivered parallel to the continental platform (Galloway et al. 2000; Galloway 2008). This mechanism is not accounted for in our simulation.

By 14 Ma, several smaller drainage basins, such as the Guadalupe River, also accumulate significant deposits with the formation of noticeable deltas (Galloway et al. 2011). It suggests that several major terrestrial-to-marine delivery conduits existed simultaneously throughout the Middle Miocene and is in accordance with previously described incised channels cutting into prodelta/muddy shelf facies in the region (Hentz and Zeng 2003; Combellas-Bigott and Galloway 2006).

These provided the foundation for later shelf-edge progradation around 13 Ma (Fig. 6), and large basinal accumulation in the central and western Gulf of Mexico. The central depocenter is partially influenced by both the ancestral Mississippi and Tennessee deltas and a relatively thin basin floor apron fed by the Rio Grande system.

By 12 Ma, major deep-water depocenters have been created with the development of basin floor aprons and deep sea fans on the eastern and central regions and to a lesser extent on the western side of the basin (i.e. the thick McAVLU submarine plain fan, Snedden et al. (2018a); Fig. 7A). This is in accordance with previous studies defining a renewed and increased influence of the ancestral Tennessee delta in the central and eastern depocenters at the end of Mid Miocene. The maximal deposited sediment thickness reaches 1.8 km in the central depocenter facing the Mississippi River. It corresponds to an averaged deposition rate of 500 m/Myr in this area (Fig. 7 and 8). Overall the history of sediment accumulation and marine depositional features reproduced by the different simulations matches observations (Snedden et al. 2018a) (Tab. S2).

4.2 The roles of forcing conditions on offshore sedimentation

To evaluate the impact of our forcing conditions, we first extract the cumulative deposition in the offshore region for the nine scenarii (pairs of precipitation and tectonic uplift forcing conditions - each left panels in Fig. 7A & C and Fig. 8). Then we compare predicted accumulation with observations derived from seismic surveys and wells dataset (shown in Fig. 7A and S4).

We already noted that the predicted locations of the main feeders match to the first-order ones defined in the GBDS dataset (Galloway 2008; Snedden et al. 2018a) (Fig. 1B and S4). We now focus on the three main depocenters in the southern part of the Louisiana coastal plain (western, central and eastern - Fig. 7A) (Galloway 2008; Combellas-Bigott and Galloway 2006). The western depocenter initiated during the

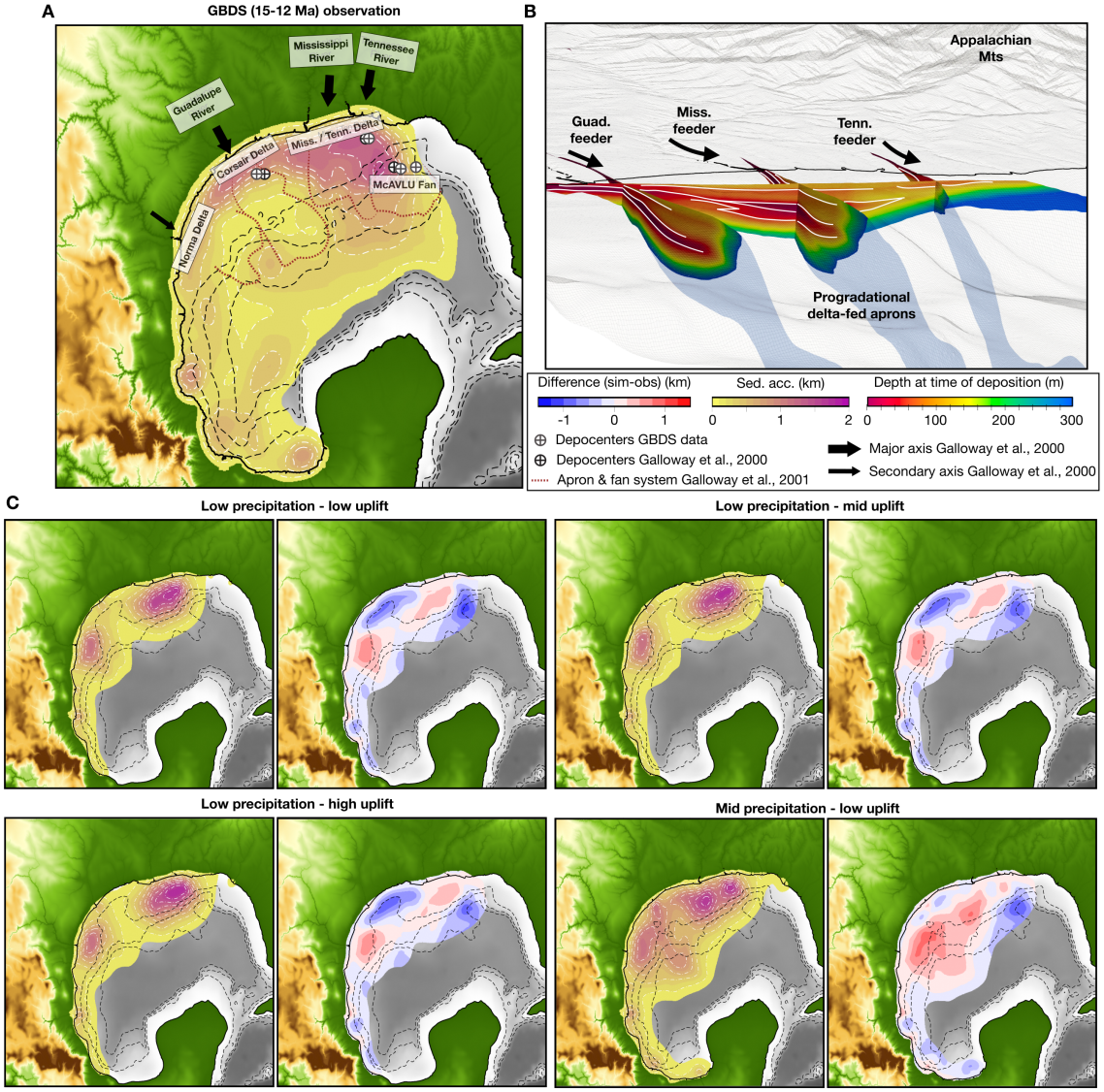

Figure 7: **Evaluation of predicted sediment accumulation within the Gulf of Mexico for the different forcing scenarios. A.** Estimated sediment accumulation for the Mid Miocene period from the GBDS dataset. **B.** Stratigraphic view of the thicker depocenters across the northern continental shelf coloured by water depth at time of deposition. Main transgressive and erosional surfaces are displayed with white lines. **C.** For each specific forcing conditions, distribution of simulated marine sediments are presented on the left panel and corresponding thickness differences with the GBDS dataset are mapped on the right panels. White dashed lines on each left panels are sediment thickness contours at 200 m intervals. Black dashed lines correspond to bathymetric contours at 1, 2, and 3 km depth.

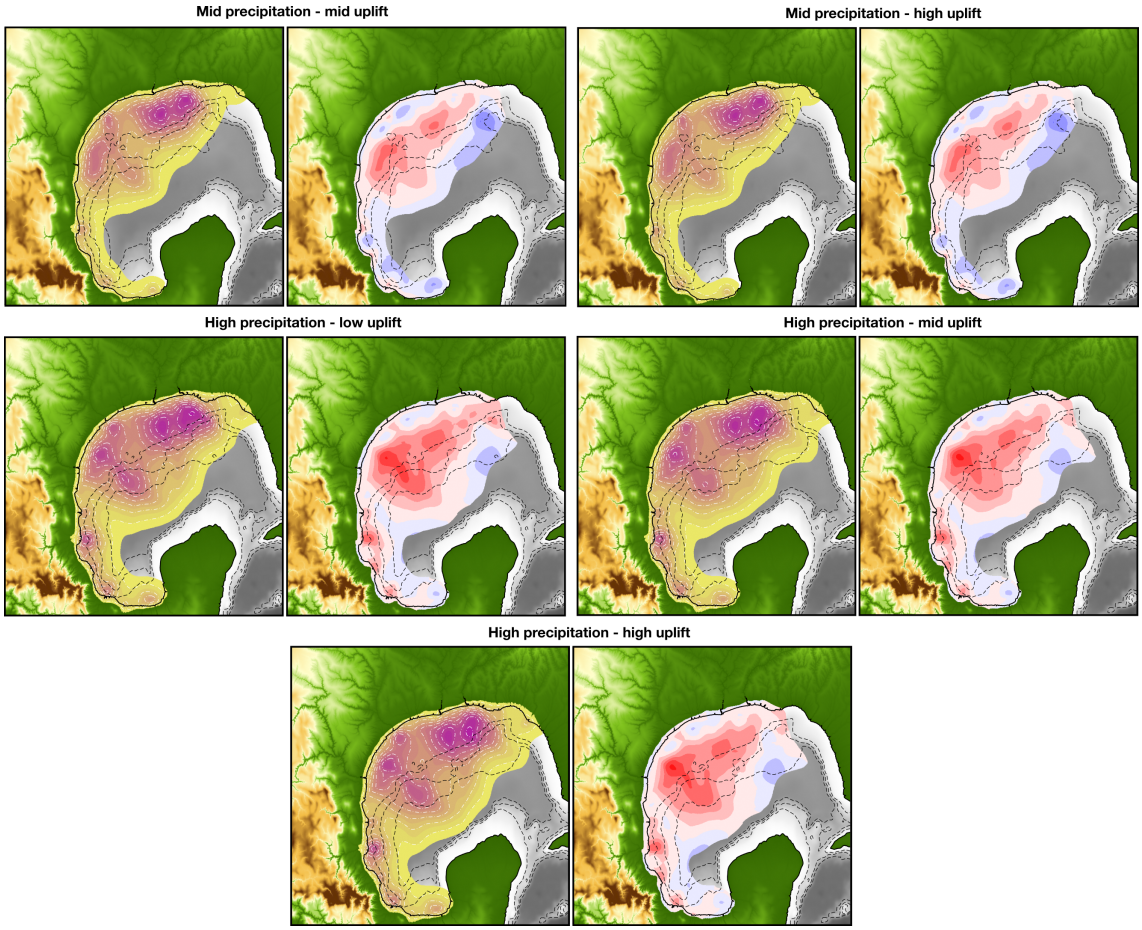

Figure 8: **Evaluation of predicted sediment accumulation within the Gulf of Mexico for the remaining forcing scenarios.** Similar description as Fig. 7C).

Precipitation	Uplift	Sed. acc. shelf (km^3/yr)	Sed. acc. slope (km^3/yr)	Sed. acc. <3 km (km^3/yr)	Ratio shelf sed. acc.	Ratio slope sed. acc.	Ratio deep sed. acc.	Ratio total sed. acc.	Ave. diff. sed. acc. (m)
high	*high*	8673	2931	5256	1.64	1.73	1.25	1.52	123.7
high	*mid*	8715	2752	4905	1.63	1.67	1.14	1.48	110.4
high	*low*	8877	2931	**4460**	1.64	1.73	**1.07**	1.46	108.2
mid	*high*	6502	1808	2949	1.33	1.22	0.56	1.02	5.9
mid	*mid*	6462	1848	2827	1.31	1.20	0.53	**1.01**	**3.5**
mid	*low*	6088	**1579**	2847	1.27	**1.15**	0.49	0.95	-11.56
low	*high*	**3800**	1301	1108	**0.98**	0.67	0.18	0.60	-94.2
low	*mid*	3848	1192	1097	0.98	0.63	0.17	0.58	-97.4
low	*low*	3821	1160	1120	0.97	0.63	0.17	0.58	-98.9

Table 3: Offshore marine sedimentation for all tested tectonic uplift and precipitation scenarios. Sediment accumulation in km^3/yr for the continental shelf (<1 km depth), the continental slope (<2.5 km depth), and the ocean floor (≥2.5 km) are provided. Ratios for each region (shelf, slope, deep ocean, and total) are calculated using the corresponding estimates from the GBDS dataset, with values >1.0 showing a surplus of sediment in the simulation and values <1.0 a deficit. Last column shows the average difference per cell area (2.5 km size) over the entire Gulf of Mexico for the 3 Myr in sediment accumulation (metres) when compared to the GBDS dataset (here, positive values represent surplus of sediment and negative values a deficit). Underlined values represent closer match with observations.

early Miocene, its predicted geometry is radial and it progrades on the shelves with a final thickness that varies from 1.7 to 1.9 km. The central depocenter is the most prominent and reaches up to 1.8 km thick in 3.5 million-years (Fig. 8). These two regions are impacted by salt tectonic deformations either via a series of East-West salt related roller faults (North Cameron detachment province) or induced by the Roho salt system. Even though salt mini-basins are not simulated here and their local subsidence histories not accounted for, we observe similar locations and extensions for both depocenters when compared to GBDS dataset (Fig. S4). Yet, the elongated shape of the eastern deposit is not reproduced in our simulations potentially because salt tectonics (salt-withdrawal mini-basins) might have a bigger control on its local evolution when compared to the two other depocenters.

We note several differences between each scenario both in terms of thicknesses of cumulative deposits and positions of the main sedimentary locus (Fig. 7 and 8). We also see, when comparing the difference maps, that rainfall is the main upstream forcing impacting on the offshore deposition. Based on our statistical analysis of continental sediment flux (Fig. 5C), this result is not surprising.

Overall, we notice that all scenarii tend to overestimate the accumulation on the western side of the shelf (facing the Rio Grande feeder) and to underestimate eastern deep sea deposits (with the exception of the high rainfall forcing conditions) and fail to reproduce the geometry of the eastern submarine plain fans (the McAVLU Fan - Fig. 7A). In all cases, the simulations under predict the relationship between river length and submarine fan dimension compared to published values for the region (Snedden et al. 2018a), which generally show run out lengths of 0.1 to 0.5 times the river length (Sømme et al. 2009). However, these empirical scaling relationships represent first order predictions, so discrepancies are unsurprising when applying more physically robust modeling, such as the one presented in this study. We also find a surplus of sediments for the Mississippi Delta and a deficit on the western side directly adjacent to the coast. This, however, changes when applying different climatic scenarii. It suggests that a shift in preferential supply towards the west is likely induced by precipitation variations (Hessler et al. 2018) rather than by tectonic uplift forcing.

Those mismatches between predicted and observed sediment accumulations are first related to limitations in goSPL ability to simulate mass wasting and gravity dominated flows (therefore not able to fully reproduce deep sea sediment transfer known to be important in the region, Combellas-Bigott and Galloway (2006)). In addition, goSPL does not account for secondary transport processes induced by alongshore currents and waves, both of which are known to actively redistribute sediments in the nearshore environment (Mullins et al. 1987; Welsh and Inoue 2000; Syvitski and Hutton 2001; Xu et al. 2022). A last limitation is associated with the architecture of the entire Cenozoic fan system, including shelf storage, which is subject to local failure events (margin collapse). Indeed, structural displacements, especially induced by salt tectonic, affect the depositional continuity and sediment dispersal across the margin (Snedden et al. 2018a). These complex interactions between salt deformation and sediment load shaped different structural provinces that have not been included in our forcing conditions. As our sediment fluxes for the Mississippi River are in accordance with previous work (Galloway et al. 2011; Bentley et al. 2015), improvements would consist in refining both the subsidence regime and the sea-level

curve in order to force the accommodation to follow the incoming sedimentary flux, and also implement sediment redistribution by waves along shore.

To better quantify those results and evaluate goSPL performance, we compile in Table 3 a summary of predicted and observed offshore sedimentation rates (km^3/yr) for three regions across the Gulf of Mexico: the *continental shelf*, the *continental slope* and the *deep sea floor*. To discuss those results, we focus on the ratio (predicted *vs.* observed) rather than the raw accumulation values. We find that low climatic conditions are the ones successfully reproducing estimated accumulations on the shelf (with a remarkable ratio of 0.98). Shelf deposits are the more difficult to match and are better represented with the mid climatic scenario with sedimentation rate exceeded by an average of 17% over the entire region (from Fig. 7C and Fig. 8, we note that the excess is mostly distributed on the western side of the central slope). Finally, deep sea sedimentation rates are better reproduced by the highest climatic conditions for which we find an averaged excess of around 14%, yet with a particular simulation (i.e. high precipitation and low tectonic uplift conditions) much closer to observations ($\sim$7%). The role of tectonics, while secondary, allows to modulate these values and better fits are obtained when considering the lower tectonic uplift scenario and evaluating the shelf and deep sea predicted sediments accumulation.

When interpreting those ratios for the entire Gulf of Mexico, we find that the simulation with mid precipitation and mid tectonic uplift conditions has the best ratio between predicted and observed of 1.01. It corresponds to an average difference between the model and the data of 3.5 m per cell (each cell being 2.5 km in length). Based on the resolution of our model and the underlying assumptions in regards to the physics and processes that are simulated, this result is exceptionally good. One might be tempted to conclude that this specific simulation is the preferred one, however our analysis shows that even though it nicely reproduces the overall depositional trend in the gulf, it scores lower than many of the other forcing pairs when assessing the fit against more specific parts of the gulf. More than being capable to match with observations, the power of these simulations lies in their ability to quantify how the main drivers that shaped the landscapes over geological time-scales have influenced the observed marine depositional patterns.

4.3 Provenance analysis

The relatively stable topography of the North American hinterland during the Middle Miocene sustained long-lived drainage networks flowing into the Gulf of Mexico. These drainage patterns remain largely unchanged over the simulation time, as discussed in section 3.1. Using model outputs, we extract the maximum volume of sediment eroded from the continent that ultimately reached the GoM and analyze their crustal provenance. While this approach offers valuable insights into sediment routing across the continent, provenance classification is based on interpretative paleo-geotectonic maps (Xu et al. 2017; Fildani et al. 2016). Although these maps provide a robust regional framework, they are subject to inherent spatial and temporal uncertainties. We defined our source provinces using crustal terrains and orogenic belt boundaries adapted by Xu et al. (2017) and Fildani et al. (2016) (Fig.9). Additional uncertainty stems from the exclusion of sediment reworking and redistribution

in the marine environment, which falls outside the scope of this analysis.

Our simulations identify the Western Cordillera, the youngest tectonic province in the source region (< 280 Ma), and the much older Grenville province (0.95–1.3 Ga) as the two largest sediment contributors to the Gulf of Mexico, each supplying approximately 20% of the total volume. Previous provenance estimates by Xu et al. (2022) and Morton et al. (2024) used detrital zircon and heavy mineral analyses to estimate source contributions. Compared to our results, we find that these methods tend to overestimate contributions of provinces of younger ages. For instance, the contribution of the Western Cordillera is overestimated by 11% in Xu et al. (2022), while the Grenville province contributions are overestimated by 6% in Xu et al. (2022) and by 20% in Morton et al. (2024). Similarly, both studies overestimate the contributions from the Appalachian-Oucahita and Mid-Continent provinces. In contrast, older and more distal provinces such as the Yavapai-Mazatzal, Superior-Wyoming, and Amarillo-Wichita, are consistently underestimated or entirely absent in detrital zircon datasets, as seen in the case of the Amarillo-Wichita (Fig. 9).

Our results show that detrital zircon and heavy mineral analyses often underestimate or omit contributions from older provinces, likely due to limited sample availability, while overestimating input from younger, more proximal sources. Although detrital zircon and heavy minerals remain powerful tools for identifying sediment provenance, given their reliance on sampling, using these methods alone to estimate proportions of sediment contributions remains questionable (Lovell-Kennedy et al. 2023). The workflow designed in this study has proven efficient in overcoming the key limitations of conventional sediment provenance analysis, which include limited sampling coverage and availability, and lengthy and costly analysis times. By providing a quantitative assessment of provenance in the Gulf of Mexico, we establish a framework that can be applied for investigating metallogenic potential of these sediments over time based on their protolith.

4.4 How forcing conditions affect sediment provenance

We perform a series of sensitivity tests to evaluate how the imposed changes in precipitation and tectonic uplift influence sediment volumes across provenance areas. This approach is essential for testing alternative simulation scenarios aimed at replicating observed patterns and improving model calibration. We focus on the paleo-Mississippi catchment, which alone delivers ∼52% of the sediments to the Gulf of Mexico. Using the catchment boundaries defined by Xu et al. (2022), we compare sediment volumes under three scenarios: high uplift and precipitation forcing (HUP), mid (MUP), and low (LUP) (Figs. 9 and 10).

The paleo-Mississippi catchment spreads over nine geologic provinces, defined by Xu et al. (2017) and Fildani et al. (2016). These provinces reflect the final elevation and, concurrently, the climate across the paleo-Mississippi catchment (Fig. 9). We analyze the contribution of each province to the total sediment accumulation in the Gulf of Mexico, accounting for how changes in elevation and climate across scenarios affect their sediment supply.

The Yavapai-Mazatzal province is the largest contributor of sediments to the paleo-Mississippi river (51%), and reaches elevations characteristic from a mountain base

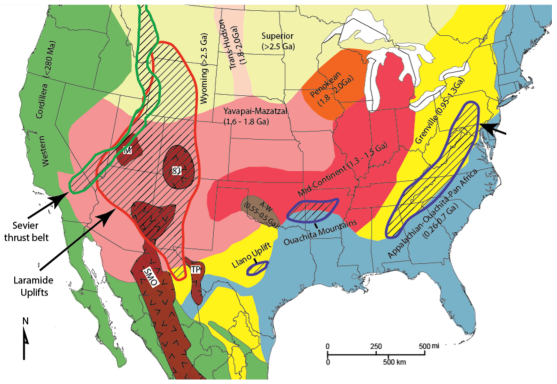

Modified from Xu et al., 2017

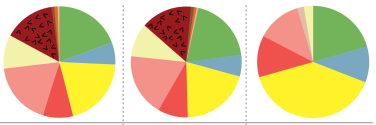

Age	Province	LEM	Xu et al., 2022	Morton et al., 2024
1.8-2.0 Ga	Trans-Hudson	0.4%	N/A	2%
0.55-0.5 Ga	Amarillo Wichita	1%	N/A	N/A
1.8-2.0 Ga	Penokean	1%	N/A	N/A
0.26-0.7 Ga	Appalachian-Ouachita	6%	9%	10%
1.3-1.5 Ga	Mid-Continent	9%	12%	12%
>2.5 Ga	Superior Wyoming	10%	5%	3%
	Mid-Cenozoic volcanic fields	15%	N/A	N/A
1.6-1.8 Ga	Yavapai-Mazatzal	18%	12%	13%
0.95-1.3 Ga	Grenville	20%	26%	40%
<280Ma	Western Cordillera	20%	31%	20%

Figure 9: **Provenance analysis of sediments in the Gulf of Mexico**. On the left hand side we have the North American crustal terrains and orogenic belts (provenance provinces) adapted from Xu et al. (2017) and Fildani et al. (2016). The table shows the percentages of sediment provenance derived from our simulation (LEM), the values from Xu et al. (2022) which are based on robust detrital zircon analysis ($n > 100$), and the Miocene average values from Morton et al. (2024), which are based on heavy mineral and detrital zircon data (with n commonly below 100). The reference provinces are considered as similar among all authors.

to a mountaintop. The Appalachian-Ouachita has the lowest mean elevations, although geologically young in age and ∼4% sediment contribution. The Mid-Continent is geologically the oldest province, but still sustains intermediate mean elevations and contributes ∼24% of the sediment volume.

Elevation differences of up to 600 m between scenarios are observed due to variations in forcing conditions, with the more pronounced changes occurring in the northwestern portion of the Yavapai-Mazatzal province. This localized amplification is likely a response to the non-uniform tectonic uplift forcing applied to areas of pre-existing topographic highs (Fig. 10B and D). By uplifting elevated mountaintops (Yavapai-Mazatzal), the relationship of hillslope and soil creep processes is more affected than in the mountain base (Appalachian-Ouachita). The non-uniform distribution of uplift and precipitation helps to steepen the slopes and enhance erosion, though at the cost of reducing depositional surfaces, and enlarging sediment run-off (Fig. 10C and E). This effect is particularly noticeable in the Yavapai-Mazatzal region, where absolute volume variations of up to 30.6 km^3 are observed relative to the regional average (Fig. 10A).

Despite the large variance in volumes and the more pronounced changes in tectonic uplift forcing for the Yavapai-Mazatzal province compared to Mid-Continent and Appalachian-Ouachita regions, the percentage variation around the mean for the sediment provenance from this area remains relatively stable across scenarii. This stability is due to its small fluctuations around a large average percentage contribution, with a maximum deviation of 1.4% from the mean. In contrast, the

Appalachian-Ouachita province has a much smaller volume variation around the average contribution, which is almost ten times lower than that of the Yavapai-Mazatzal. Hence, even small variations in volume result in larger percentage deviations, reaching up to 2.7%, with larger deviations from the norm appearing for the Mid-Continent province, up to 4.9% (Fig. 10A). Nonetheless, percentual distribution show that the final sediments contribution per province remain largely unaffected by changes in uplift or precipitation, although their absolute volume vary, and is strongly linked to the initial elevation.

We found that forcing conditions will impact more strongly the elevated regions (mountaintops), while lowlands are less affected. Although tectonic uplift forcing amplifies the final erosion, precipitation forcing remains the dominant factor influencing the final volume delivery, with a similar pattern observed for the Paleo-Tennesse river (see Fig. S6).

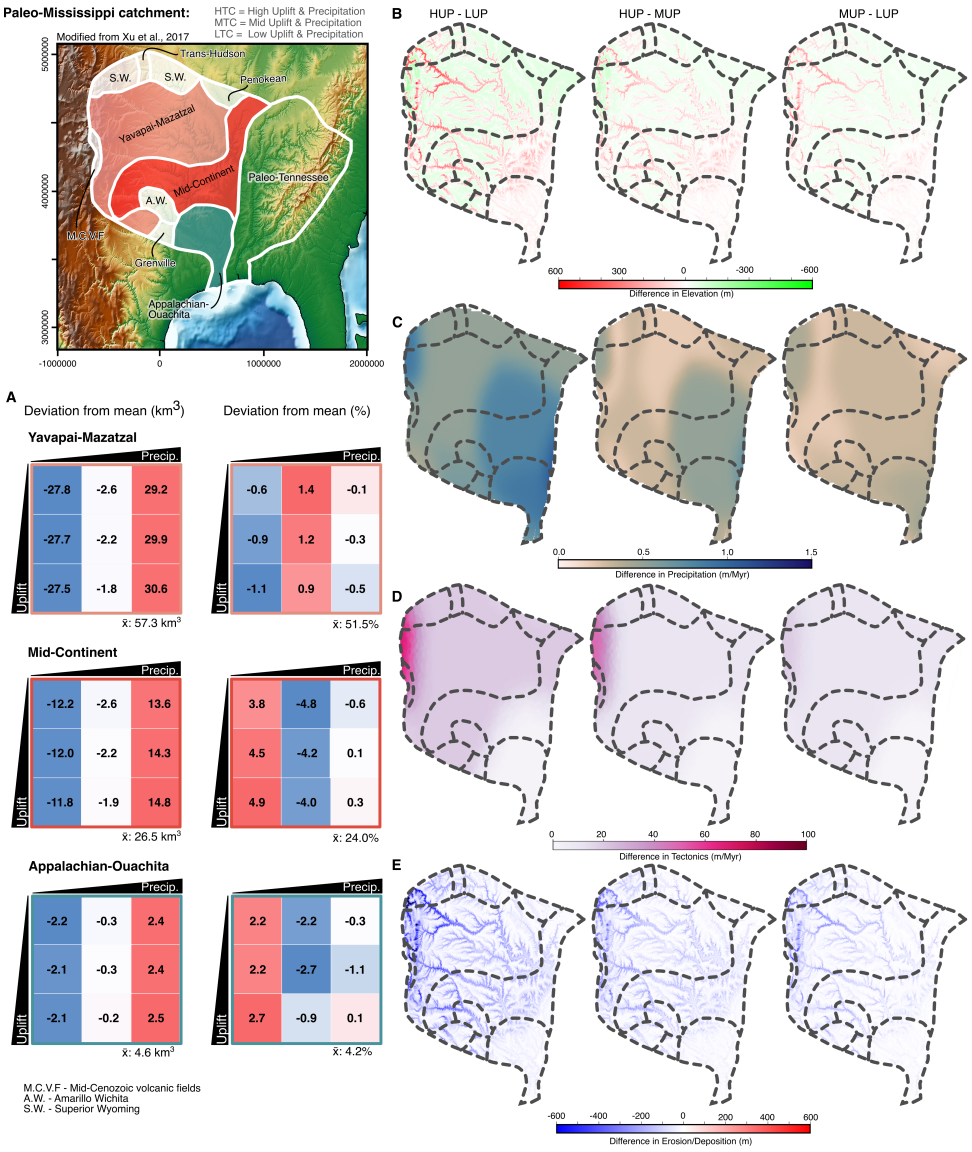

Figure 10: **Differences in forcing conditions across modeled scenarios. A**. Sensibility tests for volume (in km^3) and percentage deviation for each of the provinces that belong to the paleo-Mississippi catchment in comparison to the mean ($\bar{x}$) . Difference in **B**. elevation, **C**. precipitation, **D**. tectonic uplift and **E**. erosion and deposition. Comparisons are made between scenarios (i) high uplift and high precipitation (HUP) vs. low uplift and low precipitation (LUP), (ii) high uplift and high precipitation (HUP) vs. mid uplift and mid precipitation (MUP) and (iii) mid uplift and mid precipitation (MUP) vs. low uplift and low precipitation (LUP).

5 Conclusion

We conducted a series of experiments to simulate the offshore sediment accumulation of the Gulf of Mexico using available datasets (GBDS) and regional geological observations for validation. Our focus was on evaluating the roles the two primary forcings known to be the main drivers controlling sediment delivery into the gulf during that period: (1) the climate (through precipitation regimes) and (2) the tectonics (through the uplift of the Rocky, Appalachian, Sierra Madres and Great Plains). We characterized sediment dynamics from upstream to downstream across the North American hinterlands into the gulf basin, and quantified contributions from the main feeders (Mississippi, Tennessee and Rio Grande rivers). Analyzes of metric variations between modelled scenarios indicate that Middle Miocene climate was likely the main driver of upstream sediment flux changes, with tectonics playing a secondary role. We further quantified sediment accumulation across basin components (shelf, slope, deep sea regions) assessing their provenance. Our predicted delta fed apron broadly aligns with previous studies (Galloway et al. 2000; Galloway 2008; Galloway et al. 2011), and total sediment volumes in the gulf correspond well with observations (Ricardo 2003; Snedden et al. 2018a; Snedden and Galloway 2019). Different scenarios influenced the position of the three main depocenters and sediment distribution from the shelf to the deep sea basins. It is important to note that our simulation do not account for localized subsidence triggered by sediment loading and salt deformation in the marine environment. Comparisons with detrital zircon and heavy mineral provenance analysis from Xu et al. (2022) and Morton et al. (2024) reveal that these methods tend to overestimate contributions from younger sources (*e.g.* Western Cordillera and Grenville), while underestimating those from older, more distal sources (*e.g.* Yavapai-Mazatzal and Superior-Wyoming). Additionally, we quantified how forcing conditions (precipitation and uplift) impact sediment accumulation per source area, finding that regions at higher-elevation are more sensitive to changing forcing conditions than areas with moderate to low elevation, whereas tectonic forcing remaining as a secondary influence. Overall, these simulations demonstrate the ability of the goSPL model to test and quantify the complex interactions between sediment fluxes (driven by precipitation and tectonic uplift), shelf and slope physiographies (constrained by marine subsidence rates), and accommodation space (controlled by sea-level fluctuations balanced against sediment supply and tectonics). Furthermore, we highlight the relevance of the framework developed here as a complementary tool to traditional provenance analysis methods, offering quantitative estimates of sediment volumes and overcoming common limitations of traditional methods, and providing a foundation for future metallogenic characterization of Gulf sediments, based on their protolith composition.

SUP. 1: Extracted dynamic topography.

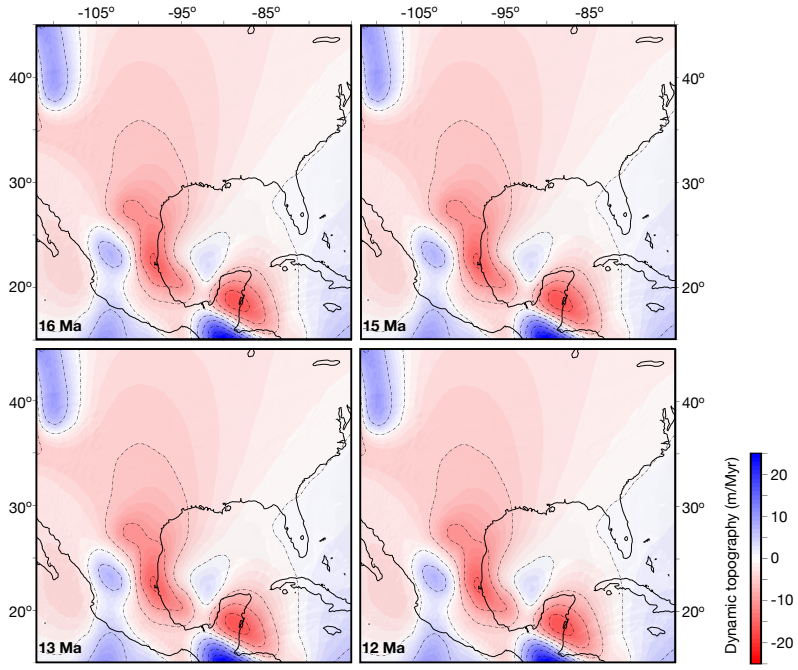

Figure S1: **Extracted dynamic topography rates in m/Myr from model M1 (Müller et al. 2017)**. This small amplitude, long wavelength signal is added to the tectonic forcing defined in Fig. 4A and D.

SUP. 2: Evaluation of input conditions on marine sedimentation along specific cross-sections.

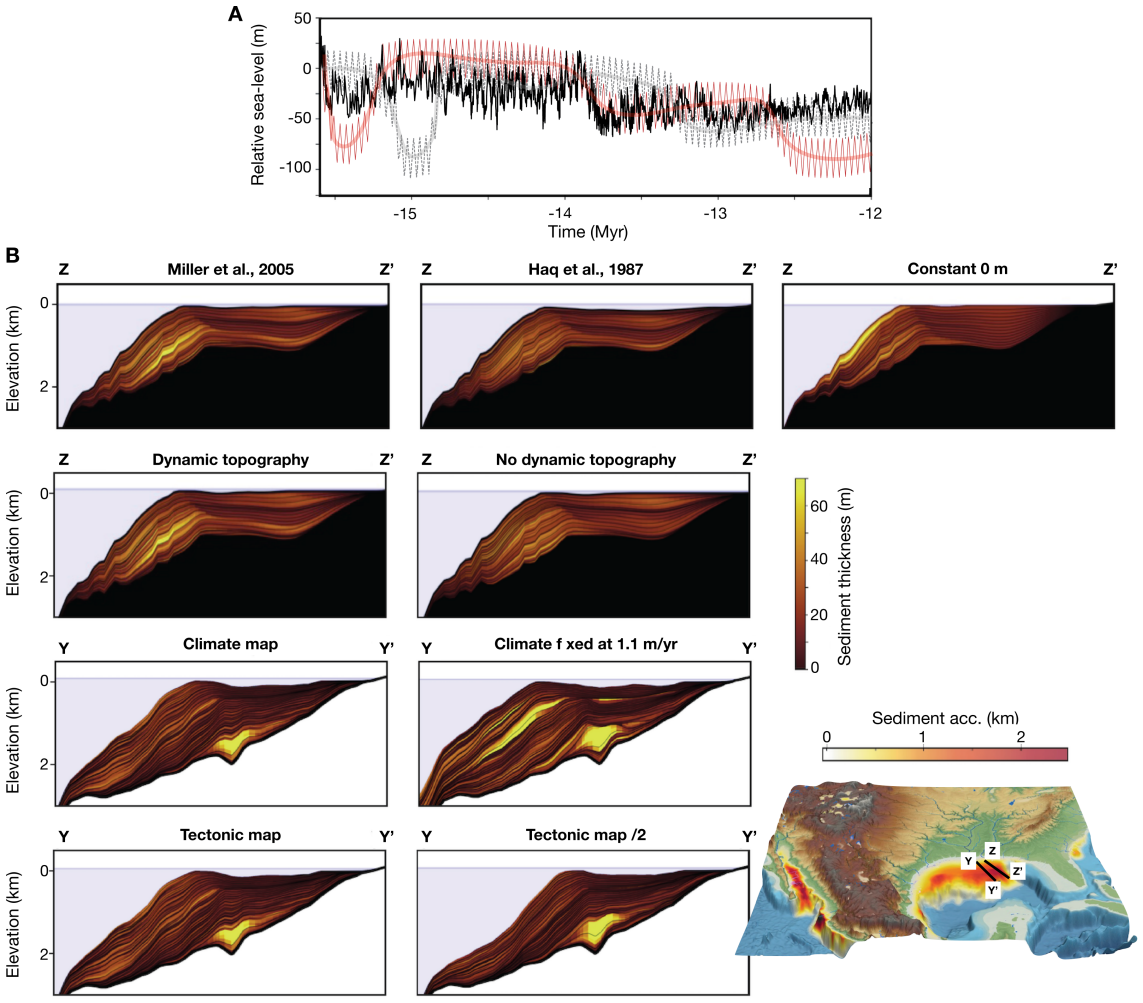

Figure S2: **Example of additional tests performed during the calibration process. A.** Relative eustatic sea-level curves after Haq et al. (1987) (red), and 2 curves from Miller et al. (gray Miller et al. (2005) and black Miller et al. (2020)). With the initial elevations of our simulation defined relative to the position of the coastline at 15.6 Ma. To account for higher frequencies in the sea-level signal, a 50 m amplitude fluctuation centered on the low frequency curve is added. **B.** Stratigraphic sections of the thicker depocenter under different forcing conditions (sea-level, vertical displacements and climate) for the simulated period (15.6 to 12 Ma). Bottom right panel: positions of the 2 cross-sections are shown (Y-Y' and Z-Z').

SUP. 3: Impact of goSPL parameters on marine sedimentation.

	Value	**Margin**	**Shelf**	**Basin**	**Comment**
clinSlp	1 x 10^{-8}	+	+	+	This parameter mostly influences the volume of deposited material.
clinSlp	1 x 10^{-6}	-	-	-	
offset	50	-	-	++	Low values push deposits away from the coastline; higher values allow more proximal accumulation.
offset	200	+	+	-	
offset	500	++	++	–	
smthD	50	+	+	o	Low smoothing forms angular shapes; high values induce smoother deposits.
smthD	5 x 10^{3}	+	++	o	
smthD	5 x 10^{5}	-	-	++	
smthS	1 x 10^{3}	+	+	+	Higher values smooth surface roughness, reducing overall deposition.
smthS	1 x 10^{5}	-	-	-	
smthS	1 x 10^{7}	–	–	—	
oFill	-50	–	–	o	Lower values concentrate sediment near coast; higher values push sediment distally.
oFill	-100	-	-	–	
oFill	-500	+	++	+	
ϵ	3 x 10^{-7}	+	+	-	Higher erodibility increases sediment volume; thickness remains similar.
ϵ	6 x 10^{-7}	++	++	+	

Table S1: Tested goSPL parameters for marine deposition and erosion with their impact of the accumulated sediments on the margin, the shelf and the deep basin areas (+ indicates important deposition, - for reduced deposition and o for no deposition). A list of goSPL parameters and their definitions is provided in the readthedocs website `https://gospl.readthedocs.io/en/latest/user_guide/inputfile.html`.

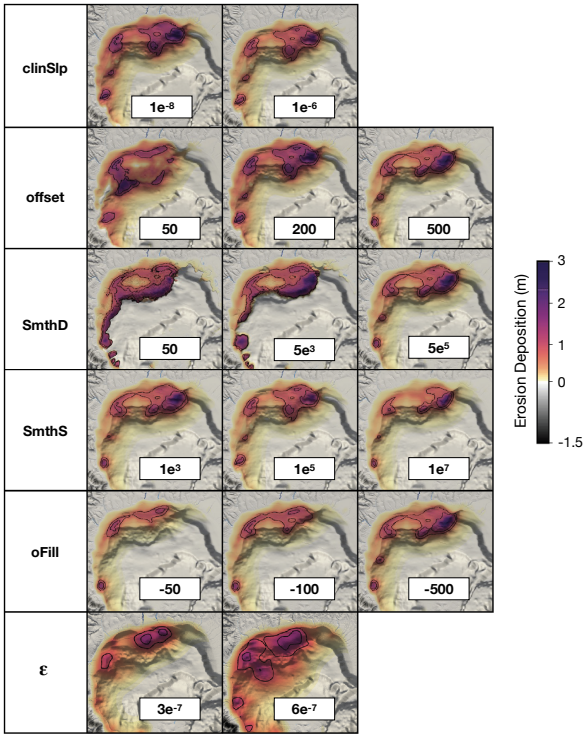

Figure S3: Sensitivity tests performed to evaluate marine sedimentation showing simulated erosion deposition distribution for different goSPL parameters.

SUP. 4: Main datasets for the marine environment.

Environment	**Total Grain Volume (km^3)**	**Sand Grain Volume (km^3)**	**Shale Grain Volume (km^3)**
Deepwater	2.48 x 10^5	2.634 x 10^4	2.217 x 10^5
Shallow/non-marine	9.76 x 10^4	4.8 x 10^4	4.956 x 10^4
Total	3.456 x 10^5	7.44 x 10^4	2.71 x 10^5

Table S2: Total sediment volumes and sand/shale distribution for deep and shallow environments.

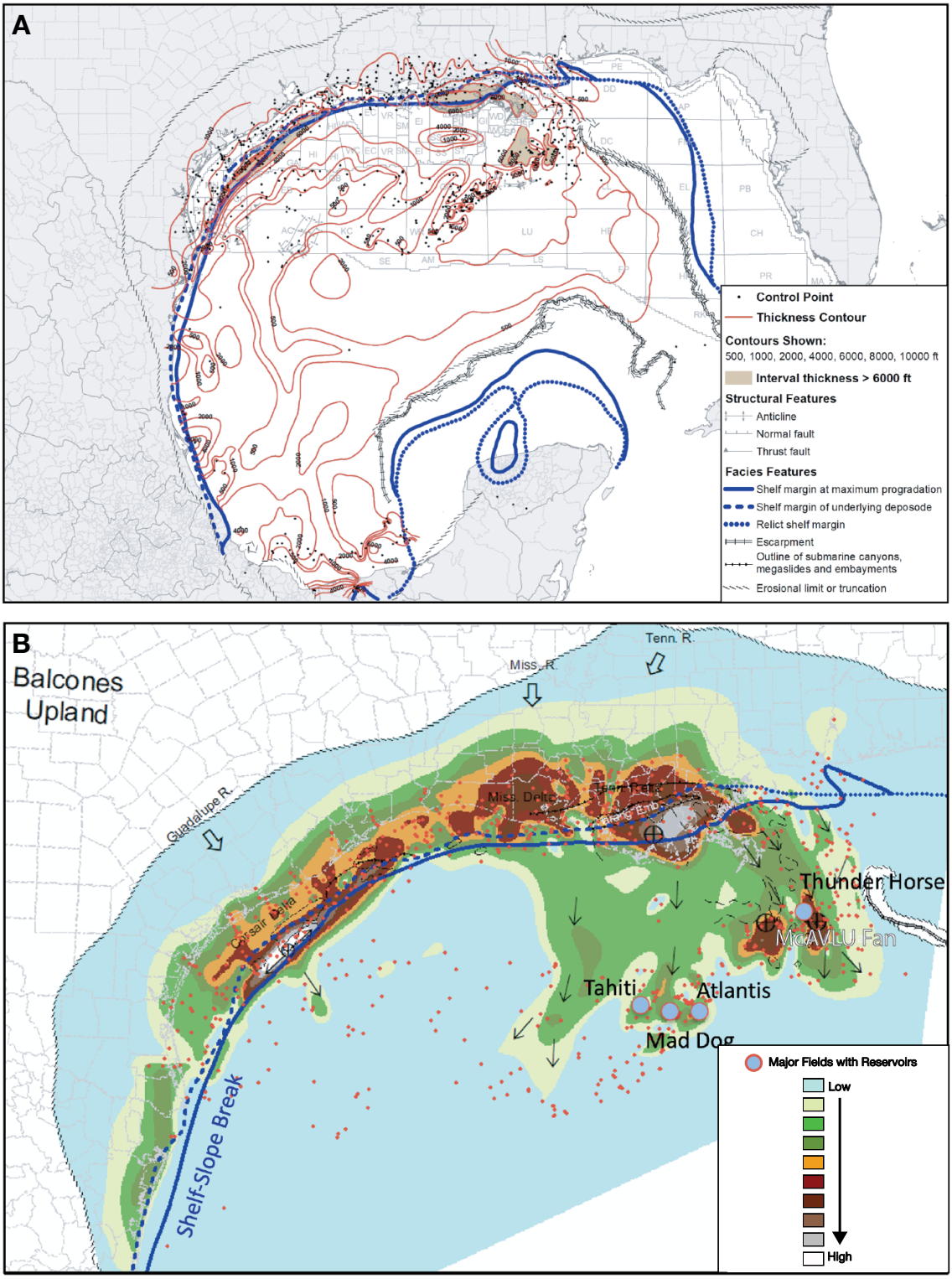

Figure S4: **GBDS datasets. A.** Contour map showing the Middle Miocene deposits (in feet). The thickness contours are in red, the areas where thickness is >6000 feet are in light brown. The blue line shows the shelf margin at maximum progradation and the dot line shows the relict shelf margin. **B.** Volume of sediment accumulated on the northern part of the Gulf of Mexico, location of the major depocenters and reservoirs.

SUP. 5: Miocene tectonic forcing conditions used for the region.

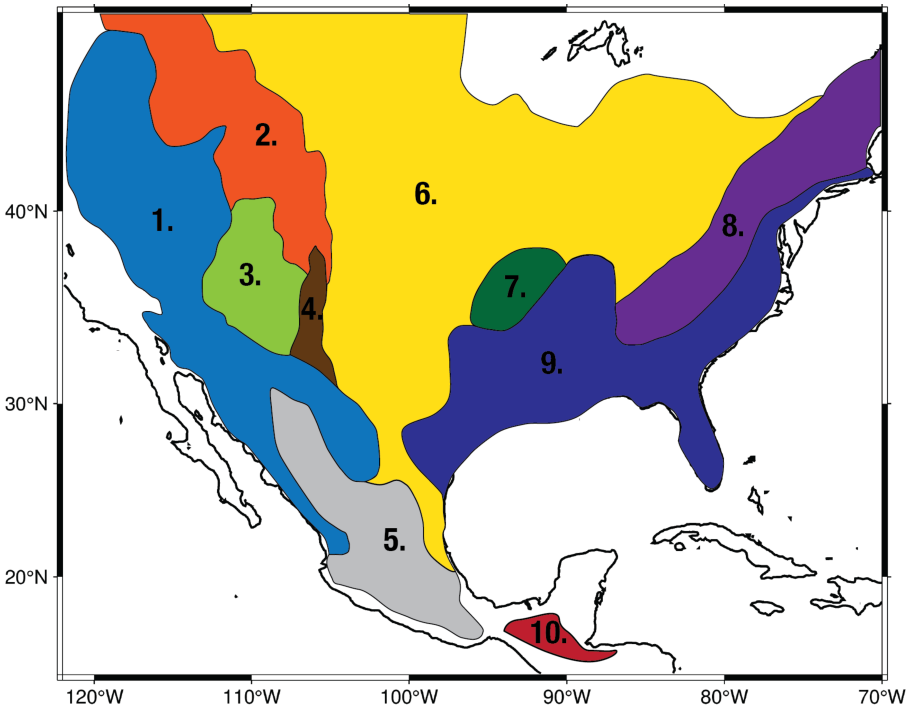

Figure S5: Map showing the different tectonic provinces used to add vertical displacement in the simulations. Corresponding tectonic conditions for each scenario are provided in Tab. S3.

High	**Mid**	**Low**	**References**
100	75	50	Aslan et al. (2010), Chapin (2008), Colgan et al. (2010), and Morgan (2003)
100	50	30	Aslan et al. (2010), Chapin (2008), Gregory and Chase (1994), McMillan et al. (2006), Molnar and England (1990), Rosenberg et al. (2014), and Wolfe et al. (1998)
150	100	90	Aslan et al. (2010), Crow et al. (2019), McMillan et al. (2006), Morgan (2003), and Rosenberg et al. (2014)
15	10	5	Bentley et al. (2015), Chapin (2008), Galloway et al. (2000), Galloway et al. (2011), McMillan et al. (2006), Morgan (2003), and Xu et al. (2022)
3	0	0	Snedden and Galloway (2019)
30	20	10	Chapin (2008) and Snedden and Galloway (2019)
0	0	0	Snedden and Galloway (2019)
100	60	25	Boettcher and Milliken (1994), Gallen et al. (2013), Pazzaglia et al. (2006), and Xu et al. (2022)
0	0	0	Snedden and Galloway (2019)
350	200	200	Villagómez and Pindell (2020)

Table S3: Values and references used to define the High, Mid and Low tectonic uplift scenario for the Cordillera region (1), the Rockies/Eastern Cordillera (2), Colorado Plateau (3), Rio Grande catchment (4), Mexican highlands (5), Great Plains and Interior lowlands (6), Ozark Dome (7), the Appalachians (8), the Coastal plains (9), and the Chiapas Massif (10). These values are in m/Myr and have been defined after discussion with the BHP and GBDS teams.

SUP. 6: Effects of forcing conditions in the Paleo-Tennessee region.

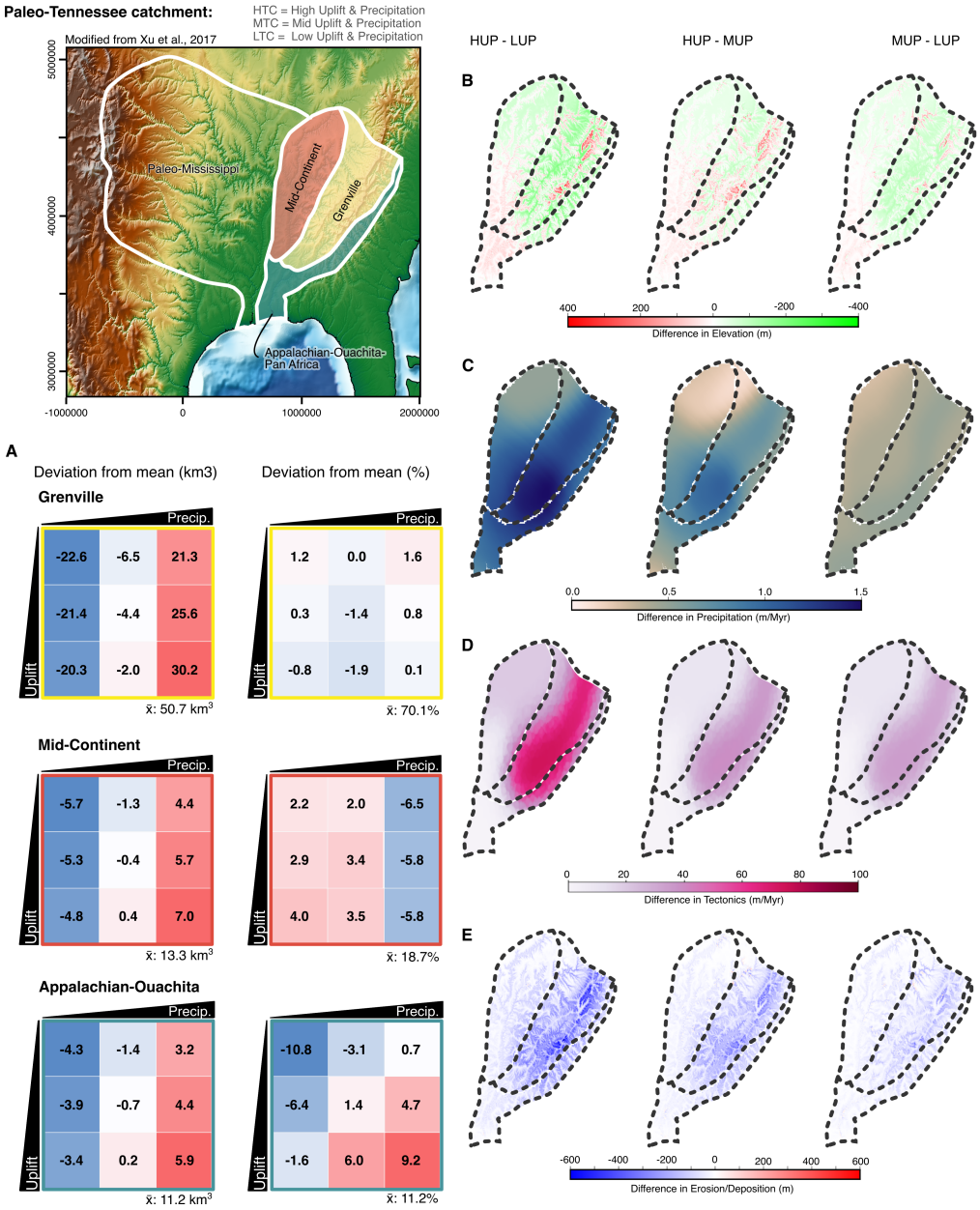

Figure S6: **Differences in forcing conditions across modelled scenarios. A**. Sensibility tests for volume (in km^3) and percentage deviation for each of the provinces that belong to the paleo-Tennessee catchment in comparison to the mean ($\bar{x}$) . Difference in **B**. elevation, **C**. precipitation, **D**. tectonic uplift and **E**. erosion and deposition. Comparisons are made between scenarios (i) high uplift and high precipitation (HUP) vs. low uplift and low precipitation (LUP), (ii) high uplift and high precipitation (HUP) vs. mid uplift and mid precipitation (MUP) and (iii) mid uplift and mid precipitation (MUP) vs. low uplift and low precipitation (LUP).

Open Research Section

Code Data Availability: The scientific software used in this study, *goSPL* (Salles et al. 2020), is available from `https://github.com/Geodels/gospl` and the software documentation can be found at `https://gospl.readthedocs.io`. We also provide a series of Jupyter notebooks used for processing the data sets and model outputs that can be followed to reproduce some of the figures presented in the paper and can be accessed `https://github.com/Geodels/paleoPhysiography` and `https://github.com/biahadler/Provenance_analysis`.

Author Contribution: B.H.B, C.M and T.S conceived the study and conducted the numerical experiments, B.H.B, T.S & C.M analyzed the sediment provenance. B.H.B, C.M and T.S wrote the initial draft, and all co-authors (N.A, M.L.S, J.S.) reviewed the manuscript.

Competing Interests: The authors declare no competing interests.

Acknowledgments: This work was undertaken through STELLAR (Spatio-temporal exploration for resources) industry collaboration supported by BHP. This research was undertaken with the assistance of resources from the National Computational Infrastructure (NCI), which is supported by the Australian Government and from Artemis HPC Grand Challenge supported by Sydney Informatics Hub at the University of Sydney.

References

Abreu, V. and J. Anderson (1998). "Glacial eustacy during the Cenozoic: Sequence stratigraphic implications". In: *AAPG bulletin* 82, pp. 1385–1400.

Adams, J., N. Gasparini, D. Hobley, G. Tucker, E. Hutton, S. Nudurupati, and E. Istanbulluoglu (2017). "The Landlab v1.0 OverlandFlow component: A Python tool for computing shallow-water flow across watersheds". In: *Geoscientific Model Development* 10, pp. 1645–1663. DOI: 10.5194/gmd-10-1645-2017.

Aslan, A., K. Karlstrom, L. Crossey, S. Kelley, R. Cole, G. Lazear, and A. Darling (2010). "Late Cenozoic evolution of the Colorado Rockies: Evidence for Neogene uplift and drainage integration". In: vol. 18. GSA, pp. 21–54. DOI: 10.1130/2010.0018(02).

Barnes, R., C. Lehman, and D. Mulla (2014). "Priority-flood: An optimal depression-filling and watershed-labeling algorithm for digital elevation models". In: *Computers & Geosciences* 62, pp. 117–127. DOI: https://doi.org/10.1016/j.cageo.2013.04.024.

Bentley, S., M. Blum, J. Maloney, L. Pond, and R. Paulsell (2015). "The Mississippi River source-to-sink system: Perspectives on tectonic, climatic, and anthropogenic influences, Miocene to Anthropocene". In: *Earth-Science Reviews* 153. DOI: 10.1016/j.earscirev.2015.11.001.

Blakey, R. C. and W. D. Ranney (2017). *Ancient landscapes of western North America: A geologic history with paleogeographic maps*. Springer. DOI: https://doi.org/10.1007/978-3-319-59636-5.

Blum, M. and M. Pecha (2014). "Mid-Cretaceous to Paleocene North American drainage reorganization from detrital zircons". In: *Geology* 42.7, pp. 607–610. DOI: https://doi.org/10.1130/G35513.1.

Boettcher, S. S. and K. L. Milliken (1994). "Mesozoic-Cenozoic unroofing of the southern Appalachian Basin: Apatite fission track evidence from Middle Pennsylvanian sandstones". In: *The Journal of Geology* 102.6, pp. 655–668. DOI: 10.1086/629710.

Chapin, C. E. (2008). "Interplay of oceanographic and paleoclimate events with tectonism during middle to late Miocene sedimentation across the southwestern USA". In: *Geosphere* 4.6, pp. 976–991. DOI: https://doi.org/10.1130/GES00171.1.

Colgan, J. P., K. A. Howard, R. J. Fleck, and J. L. Wooden (2010). "Rapid middle Miocene extension and unroofing of the southern Ruby Mountains, Nevada". In: *Tectonics* 29.6. DOI: https://doi.org/10.1029/2009TC002655.

Combellas-Bigott, R. I. and W. E. Galloway (2006). "Depositional and structural evolution of the middle Miocene depositional episode, east-central Gulf of Mexico". In: *AAPG bulletin* 90.3, pp. 335–362. DOI: 10.1306/10040504132.

Crow, R. S., K. A. Howard, L. S. Beard, P. A. Pearthree, P. K. House, K. E. Karlstrom, L. Peters, W. McIntosh, C. Cassidy, T. J. Felger, et al. (2019). "Insights into post-Miocene uplift of the western margin of the Colorado Plateau from the stratigraphic record of the lower Colorado River". In: *Geosphere* 15.6, pp. 1826–1845. DOI: 10.1130/GES02020.1.

Curry, M. E., M. R. Hudec, F. J. Peel, N. Fernandez, G. Apps, and J. W. Snedden (2024). "Structural Restorations of the Complete Conjugate US-Mexico Eastern

Gulf of Mexico Margin". en. In: *Tectonics* 43.1, e2023TC007897. DOI: 10.1029/2023TC007897.

Fernandes, V., G. Roberts, N. White, and A. Whittaker (2019). "Continental-Scale Landscape Evolution: A History of North American Topography". In: *Journal of Geophysical Research: Earth Surface* 124. DOI: 10.1029/2018JF004979.

Ferrari, L., T. Orozco-Esquivel, V. Manea, and M. Manea (2012). "The dynamic history of the Trans-Mexican Volcanic Belt and the Mexico subduction zone". In: *Tectonophysics* 522, pp. 122–149.

Ferrari, L., T. Tagami, M. Eguchi, M. T. Orozco-Esquivel, C. M. Petrone, J. Jacobo-Albarrán, and M. López-Martínez (2005). "Geology, geochronology and tectonic setting of late Cenozoic volcanism along the southwestern Gulf of Mexico: The Eastern Alkaline Province revisited". In: *Journal of volcanology and geothermal research* 146.4, pp. 284–306. DOI: https://doi.org/10.1016/j.jvolgeores.2005.02.004.

Fildani, A., M. P. McKay, D. Stockli, J. Clark, M. Dykstra, L. Stockli, and A. Hessler (2016). "The ancestral Mississippi drainage archived in the late Wisconsin Mississippi deep-sea fan". In: *Geology* 44.6, pp. 479–482. DOI: https://doi.org/10.1130/G37657.1.

Fildani, A., A. M. Hessler, C. C. Mason, M. P. McKay, and D. F. Stockli (2018). "Late Pleistocene glacial transitions in North America altered major river drainages, as revealed by deep-sea sediment". In: *Scientific reports* 8.1, pp. 1–8. DOI: https://doi.org/10.1038/s41598-018-32268-7.

Filina, I. and L. Hartford (2021). "Subsurface structures along western Yucatan from integrated geophysical analysis". In: *Marine and Petroleum Geology* 127, p. 104964. DOI: 10.1016/j.marpetgeo.2021.104964.

Frigola, A., M. Prange, and M. Schulz (2018). "Boundary conditions for the middle Miocene climate transition (MMCT v1. 0)". In: *Geoscientific Model Development* 11.4, pp. 1607–1626. DOI: https://doi.org/10.5194/gmd-11-1607-2018.

Gallen, S. F., K. W. Wegmann, and D. Bohnenstiehl (2013). "Miocene rejuvenation of topographic relief in the southern Appalachians". In: *GSA Today* 23.2, pp. 4–10. DOI: 10.1130/GSATG163A.1..

Galloway, W. E. (2008). "Depositional evolution of the Gulf of Mexico sedimentary basin". In: *Sedimentary basins of the world* 5, pp. 505–549. DOI: 10.1016/S1874-5997(08)00015-4.

Galloway, W. E., P. E. Ganey-Curry, X. Li, and R. T. Buffler (2000). "Cenozoic depositional history of the Gulf of Mexico basin". In: *AAPG bulletin* 84.11, pp. 1743–1774. DOI: 10.1306/8626C37F-173B-11D7-8645000102C1865D.

Galloway, W. E., T. L. Whiteaker, and P. Ganey-Curry (2011). "History of Cenozoic North American drainage basin evolution, sediment yield, and accumulation in the Gulf of Mexico basin". In: *Geosphere* 7.4, pp. 938–973. DOI: 10.1130/GES00647.1.

Granjeon, D. and P. Joseph (1999). "Concepts and Applications of A 3-D Multiple Lithology, Diffusive Model in Stratigraphic Modeling". In: *Numerical Experiments in Stratigraphy: Recent Advances in Stratigraphic and Sedimentologic Computer Simulations*. SEPM Society for Sedimentary Geology. DOI: 10.2110/pec.99.62.0197.

Gray, G. G., D. Villagomez, J. Pindell, R. Molina-Garza, P. O'Sullivan, D. Stockli, W. Farrell, D. Blank, and J. Schuba (2021). "Late Mesozoic and Cenozoic thermotectonic history of eastern, central and southern Mexico as determined through

integrated thermochronology, with implications for sediment delivery to the Gulf of Mexico". In: *Geological Society, London, Special Publications* 504.1. Publisher: The Geological Society of London, pp. 255–283. DOI: 10.1144/SP504-2019-243.

Gregory, K. M. and C. G. Chase (1994). "Tectonic and climatic significance of a late Eocene low-relief, high-level geomorphic surface, Colorado". In: *Journal of Geophysical Research: Solid Earth* 99.B10, pp. 20141–20160. DOI: 10.1029/94JB00132.

Gutiérrez Paredes, H. C., O. Catuneanu, and U. Hernández Romano (2018). "Controls on the quality of Miocene reservoirs, southern Gulf of Mexico". In: *Journal of South American Earth Sciences* 81, pp. 45–65. DOI: 10.1016/j.jsames.2017.10.007.

Hadler Boggiani, B., T. Salles, C. Mallard, and N. Atwood (2025). "The roles of surface processes in porphyry copper deposit preservation". en. In: *Earth Surface Dynamics* 13.4, pp. 683–704. DOI: 10.5194/esurf-13-683-2025.

Hall, S. (2002). "The role of autochthonous salt inflation and deflation in the northern Gulf of Mexico". In: *Marine and Petroleum Geology* 19.6, pp. 649–682. DOI: 10.1016/S0264-8172(02)00025-9.

Haq, B., J. Hardenbol, and P. Vail (1987). "Chronology of fluctuating sea levels since the Triassic (250 million years ago to present)". In: *Science* 235, pp. 1159–1167. DOI: 10.1126/science.235.4793.1156.

Hentz, T. F. and H. Zeng (2003). "High-frequency Miocene sequence stratigraphy, offshore Louisiana: Cycle framework and influence on production distribution in a mature shelf province". In: *AAPG bulletin* 87.2, pp. 197–230. DOI: 10.1306/09240201054.

Hessler, A. M., J. A. Covault, D. F. Stockli, and A. Fildani (2018). "Late Cenozoic cooling favored glacial over tectonic controls on sediment supply to the western Gulf of Mexico". In: *Geology* 46.11, pp. 995–998. DOI: 10.1130/G45528.1.

Howard, A. D., W. E. Dietrich, and M. A. Seidl (1994). "Modeling fluvial erosion on regional to continental scales". In: *Journal of Geophysical Research* 99, pp. 13971–13986. DOI: 10.1029/94JB00744.

Huntington, K. W., B. P. Wernicke, and J. M. Eiler (2010). "Influence of climate change and uplift on Colorado Plateau paleotemperatures from carbonate clumped isotope thermometry". en. In: *Tectonics* 29.3. DOI: 10.1029/2009TC002449.

Liro, L., M. Lahr, K. Cline, J. Young, M. Kadri, P. Montecchi, H. Gerke, B. Bankhead, M. Murphy, B. Skinner, et al. (2000). "Application of 3-D visualization to integrated geophysical and geologic model building: A prestack, subsalt depth migration project, deepwater Gulf of Mexico". In: *The Leading Edge* 19.5, pp. 466–472. DOI: 10.1190/1.1438628.

Liu, L. (2014). "Rejuvenation of Appalachian topography caused by subsidence-induced differential erosion". en. In: *Nature Geoscience* 7.7. Publisher: Nature Publishing Group, pp. 518–523. DOI: 10.1038/ngeo2187.

Lovell-Kennedy, J., E. Roquette, S. Schröder, and J. Redfern (2023). "'I hate sand … it gets everywhere'—Phanerozoic sedimentary recycling from NW Africa". en. In: *Basin Research* 35.1, pp. 187–213. DOI: 10.1111/bre.12709.

Marton, G. and R. T. Buffler (1994). "Jurassic Reconstruction of the Gulf of Mexico Basin". In: *International Geology Review* 36.6. Publisher: GSA Website, pp. 545–586. DOI: 10.1080/00206819409465475.

McMillan, M. E., P. L. Heller, and S. L. Wing (2006). "History and causes of post-Laramide relief in the Rocky Mountain orogenic plateau". In: *Geological Society of America Bulletin* 118.3-4, pp. 393–405. DOI: 10.1130/B25712.1.

Miall, A. D. and R. C. Blakey (2019). "The Phanerozoic tectonic and sedimentary evolution of North America". In: *The Sedimentary Basins of the United States and Canada*. Elsevier, pp. 1–38. DOI: 10.1016/B978-0-444-63895-3.00001-2.

Miller, K. G., J. V. Browning, W. J. Schmelz, R. E. Kopp, G. S. Mountain, and J. D. Wright (2020). "Cenozoic sea-level and cryospheric evolution from deep-sea geochemical and continental margin records". In: *Science advances* 6.20, eaaz1346. DOI: 10.1126/sciadv.aaz1346.

Miller, K. G., M. A. Kominz, J. V. Browning, J. D. Wright, G. S. Mountain, M. E. Katz, P. J. Sugarman, B. S. Cramer, N. Christie-Blick, and S. F. Pekar (2005). "The Phanerozoic record of global sea-level change". In: *science* 310.5752, pp. 1293–1298. DOI: 10.1126/science.1116412.

Miller, K. G., G. S. Mountain, J. V. Browning, M. Kominz, P. J. Sugarman, N. Christie-Blick, M. E. Katz, and J. D. Wright (1998). "Cenozoic global sea level, sequences, and the New Jersey transect: results from coastal plain and continental slope drilling". In: *Reviews of Geophysics* 36.4, pp. 569–601.

Miller, S., P. Sak, E. Kirby, and P. Bierman (2013). "Neogene rejuvenation of Central Appalachian topography: Evidence for differential rock uplift from stream profiles and erosion rates". In: *Earth and Planetary Science Letters* 369–370, pp. 1–12. DOI: 10.1016/j.epsl.2013.04.007.

Molnar, P. and P. England (1990). "Late Cenozoic uplift of mountain ranges and global climate change: chicken or egg?" In: *nature* 346.6279, pp. 29–34. DOI: 10.1038/346029a0.

Morgan, P. (2003). "Colorado Plateau and southern Rocky Mountains uplift and erosion". In: *Cenozoic Systems of the Rocky Mountain Region*. Robert G. Raynolds, Ed. Rocky Mountain Section (SEPM). DOI: 10.1130/1052-5173(2002)012<0004:CPUAEE>2.0.CO;2.

Morton, A. C., M. E. Strickler, and C. M. Fanning (2024). "Heavy Mineral and Zircon Age Constraints on Provenance of Cenozoic Sandstones in the Gulf of Mexico Subsurface". en. In: *Minerals* 14.8, p. 779. DOI: 10.3390/min14080779.

Müller, D., R. Hassan, M. Gurnis, N. Flament, and S. Williams (2017). "Dynamic topography of passive continental margins and their hinterlands since the Cretaceous". In: *Gondwana Research* 53, pp. 225–251. DOI: 10.1016/j.gr.2017.04.028.

Mullins, H. T., A. F. Gardulski, S. W. WISE Jr, and J. Applegate (1987). "Middle Miocene oceanographic event in the eastern Gulf of Mexico: implications for seismic stratigraphic succession and Loop Current/Gulf Stream circulation". In: *Geological Society of America Bulletin* 98.6, pp. 702–713. DOI: 10.1130/0016-7606(1987)98<702:MMOEIT>2.0.CO;2.

Murphy, B., J. Johnson, N. Gasparini, and L. S. Sklar (2016). "Chemical weathering as a mechanism for the climatic control of bedrock river incision". In: *Nature* 532, pp. 223–227. DOI: 10.1038/nature17449.

Paredes, H. C. G., O. Catuneanu, and U. H. Romano (2017). "Sequence stratigraphy of the Miocene section, southern Gulf of Mexico". In: *Marine and Petroleum Geology* 86, pp. 711–732. DOI: 10.1016/j.marpetgeo.2017.06.022.

Pazzaglia, F. J., D. D. Braun, M. Pavich, P. Bierman, N. Potter, D. Merritts, R. Walter, and D. Germanoski (2006). "Rivers, glaciers, landscape evolution, and active tectonics of the central Appalachians, Pennsylvania and Maryland". In: *Excursions in Geology and History: Field Trips in the Middle Atlantic States: Geological Society of America Field Guide* 8, pp. 169–197. DOI: 10.1130/2006.fld008(09).

Pazzaglia, F. J., T. W. Gardner, and M. Summerfield (2000). *Late Cenozoic landscape evolution of the US Atlantic passive margin: insights into a North American Great Escarpment*. Wiley: Chichester.

Pindell, J. L. and L. Kennan (2009). "Tectonic evolution of the Gulf of Mexico, Caribbean and northern South America in the mantle reference frame: An update". In: *The Origin and Evolution of the Caribbean Plate*. Ed. by James, K. H., Lorente, M. A., and Pindell, J. L. Vol. 328. Geological Society of London. DOI: 10.1144/SP328.1.

Retallack, G. (2007). "Cenozoic Paleoclimate on Land in North America". In: *Journal of Geology* 115, pp. 271–294. DOI: 10.1086/512753.

Ricardo, C.-B. (2003). "Depositional and Structural Evolution of the Middle Miocene Depositional Episode, East-Central Gulf of Mexico". PhD thesis. The University of Texas.

Richardson, L. F. (1911). "IX. The approximate arithmetical solution by finite differences of physical problems involving differential equations, with an application to the stresses in a masonry dam". In: *Philosophical Transactions of the Royal Society of London. Series A, Containing Papers of a Mathematical or Physical Character* 210.459-470, pp. 307–357. DOI: 10.1098/rsta.1911.0009.

Roberts, G., N. White, G. Martin-Brandis, and A. Crosby (2012). "An uplift history of the Colorado Plateau and its surroundings from inverse modeling of longitudinal river profiles". In: *Tectonics* 31.4. DOI: 10.1029/2012TC003107.

Rosenberg, R., E. Kirby, A. Aslan, K. Karlstrom, M. Heizler, and W. Ouimet (2014). "Late Miocene erosion and evolution of topography along the western slope of the Colorado Rockies". In: *Geosphere* 10.4, pp. 641–663. DOI: 10.1130/GES00989.1.

Salles, T. (2019). "eSCAPE: Regional to Global Scale Landscape Evolution Model v2.0". In: *Geoscientific Model Development* 12, pp. 4165–4184. DOI: 10.5194/gmd-12-4165-2019.

Salles, T., X. Ding, and G. Brocard (2018a). "pyBadlands: A framework to simulate sediment transport, landscape dynamics and basin stratigraphic evolution through space and time". In: *PLoS ONE* 13, e0195557. DOI: 10.1371/journal.pone.0195557.

Salles, T., X. Ding, J. Webster, A. Vila-Concejo, G. Brocard, and J. Pall (2018b). "A unified framework for modelling sediment fate from source to sink and its interactions with reef systems over geological times". In: *Scientific Reports* 8. DOI: 10.1038/s41598-018-23519-8.

Salles, T., L. Husson, M. Lorcery, and B. Hadler Boggiani (2023a). "Landscape dynamics and the Phanerozoic diversification of the biosphere". en. In: *Nature* 624.7990, pp. 115–121. DOI: 10.1038/s41586-023-06777-z.

Salles, T., L. Husson, P. Rey, C. Mallard, S. Zahirovic, B. H. Boggiani, N. Coltice, and M. Arnould (2023b). "Hundred million years of landscape dynamics from catchment to global scale". en. In: *Science* 379.6635, pp. 918–923. DOI: 10.1126/science.add2541.

Salles, T., C. Mallard, and S. Zahirovic (2020). "gospl: Global Scalable Paleo Landscape Evolution". In: *The Journal of Open Source Software* 5, p. 2804. DOI: 10.21105/joss.02804.

Scotese, C. and N. Wright (2018). *PALEOMAP Paleodigital Elevation Models (PaleoDEMS) for the Phaerozoic PALEOMAP Project*.

Simon-Labric, T., G. Brocard, C. Teyssier, P. Beek, M. Fellin, P. Reiners, and C. Authemayou (2013). "Preservation of contrasting geothermal gradients across the Caribbean-North America plate boundary (Motagua Fault, Guatemala)". In: *Tectonics* 32. DOI: 10.1002/tect.20060.

Snedden, J., W. Galloway, K. Milliken, J. Xu, T. Whiteaker, and M. Blum (2018a). "Validation of empirical source-to-sink scaling relationships in a continental-scale system: The Gulf of Mexico basin Cenozoic record". In: *Geosphere* 14. DOI: 10.1130/GES01452.1.

Snedden, J. W. and W. E. Galloway (2019). *The Gulf of Mexico sedimentary basin: Depositional evolution and petroleum applications*. Cambridge University Press. DOI: 10.1017/9781108292795.

Snedden, J. W., W. E. Galloway, K. T. Milliken, J. Xu, T. Whiteaker, and M. D. Blum (2018b). "Validation of empirical source-to-sink scaling relationships in a continental-scale system: The Gulf of Mexico basin Cenozoic record". In: *Geosphere* 14.2, pp. 768–784. DOI: 10.1130/GES01452.1.

Sømme, T. O., W. Helland-Hansen, O. J. Martinsen, and J. B. Thurmond (2009). "Relationships between morphological and sedimentological parameters in source - to - sink systems: a basis for predicting semi-quantitative characteristics in subsurface systems". en. In: *Basin Research* 21.4, pp. 361–387. DOI: 10.1111/j.1365-2117.2009.00397.x.

Stephenson, S. N., G. G. Roberts, M. J. Hoggard, and A. C. Whittaker (2014). "A Cenozoic uplift history of Mexico and its surroundings from longitudinal river profiles". In: *Geochemistry, Geophysics, Geosystems* 15.12, pp. 4734–4758. DOI: 10.1002/2014GC005425.

Straume, E. O., C. Gaina, S. Medvedev, and K. H. Nisancioglu (2020). "Global Cenozoic paleobathymetry with a focus on the Northern Hemisphere oceanic gateways". In: *Gondwana Research* 86, pp. 126–143. DOI: 10.1016/j.gr.2020.05.011.

Syvitski, J. and E. Hutton (2001). "2D SEDFLUX 1.0C:: an advanced process-response numerical model for the fill of marine sedimentary basins". In: *Computers & Geosciences* 27, pp. 731–753. DOI: 10.1016/S0098-3004(00)00139-4.

Towoju, V. O. and M. R. Gani (2024). "Spatiotemporal distribution of sediment waves in the northern Gulf of Mexico Basin, USA". In: *Sedimentary Geology* 471, p. 106729. DOI: 10.1016/j.sedgeo.2024.106729.

Tucker, G. E. and G. R. Hancock (2010). "Modelling landscape evolution". en. In: *Earth Surface Processes and Landforms* 35.1. _eprint: https://onlinelibrary.wiley.com/doi/pdf/10.1002/esp.1952, pp. 28–50. DOI: 10.1002/esp.1952.

Valdes, P., C. Scotese, and D. Lunt (2021). "Deep ocean temperatures through time". In: *Climate of the Past* 17, pp. 1483–1506. DOI: 10.5194/cp-17-1483-2021.

Villagomez, D. and J. Pindell (2021). "Cooling and uplift history of the Chiapas Massif and its influence on sedimentation and deformation in the adjacent Sierra de Chiapas Basin". In: *Southern and Central Mexico: Basement Framework, Tectonic Evolution, and Provenance of Mesozoic–Cenozoic Basins*. Geological Society of America. DOI: 10.1130/2020.2546(17).

Villagómez, D., C. Steffensen, J. Pindell, R. S. Molina-Garza, G. Gray, R. Graham, P. O'Sullivan, D. Stockli, and R. Spikings (2022). "Tectono-sedimentary evolution of Southern Mexico. Implications for Cretaceous and younger source-to-sink systems in the Mexican foreland basins and the Gulf of Mexico". In: *Earth-Science Reviews* 231, p. 104066. DOI: 10.1016/j.earscirev.2022.104066.

Villagómez, D. and J. Pindell (2020). "Cooling and uplift history of the Chiapas Massif and its influence on sedimentation and deformation in the adjacent Sierra de Chiapas Basin". In: *Southern and Central Mexico: Basement Framework, Tectonic Evolution, and Provenance of Mesozoic–Cenozoic Basins. Geological Society of America, Special Papers* 546. DOI: 10.1130/2020.2546(17).

Welsh, S. E. and M. Inoue (2000). "Loop Current rings and the deep circulation in the Gulf of Mexico". In: *Journal of Geophysical Research: Oceans* 105.C7, pp. 16951–16959. DOI: 10.1029/2000JC900054.

Wolfe, J. A., C. E. Forest, and P. Molnar (1998). "Paleobotanical evidence of Eocene and Oligocene paleoaltitudes in midlatitude western North America". In: *Geological Society of America Bulletin* 110.5, pp. 664–678. DOI: 10.1130/0016-7606(1998)110<0664:PEOEAO>2.3.CO;2.

Xu, J., J. Snedden, F. Craig, D. Stockli, W. Galloway, and Z. Sickmann (2022). "Quantifying the relative contributions of Miocene rivers to the deep Gulf of Mexico using detrital zircon geochronology: Implications for the evolution of Gulf Basin circulation and regional drainage". In: *Basin Research*. DOI: 10.1111/bre.12653.

Xu, J., D. F. Stockli, and J. W. Snedden (2017). "Enhanced provenance interpretation using combined U–Pb and (U–Th)/He double dating of detrital zircon grains from lower Miocene strata, proximal Gulf of Mexico Basin, North America". In: *Earth and Planetary Science Letters* 475, pp. 44–57. DOI: https://doi.org/10.1016/j.epsl.2017.07.024.

Yuan, X., J. Braun, L. Guerit, B. Simon, B. Bovy, D. Rouby, C. Robin, and R. Jiao (2019). "Linking continental erosion to marine sediment transport and deposition: A new implicit and O(N) method for inverse analysis". In: *Earth and Planetary Science Letters* 524, p. 115728. DOI: 10.1016/j.epsl.2019.115728.

3| ARTICLE 2
Evolution and provenance of the Polish Rotliegend in the Southern Permian Basin

Beatriz Hadler Boggiani[1], Claire Mallard[2], Tristan Salles[1], Nicholas Atwood[3]

[1]School of Geosciences, The University of Sydney, Sydney, Australia
[2]BHP Metal Global Endowment Team, BHP, Brisbane, QLD, Australia
[3]BHP Metal Global Endowment Team, BHP, Tucson, Arizona, USA

- Using *goSPL*, we reconstruct for the first time a Landscape Evolution Model for the Permian source-to-sink system of the Polish Trough;
- We suggest that the Fenno-Scandian Shield and the Carpathian Massifs contribute with more sediments into the basin than previously described;
- We quantify sediment volume per provenance area to estimate copper mass in Upper Rotliegend red beds, highlighting their source potential.

Abstract

The Southern Permian Basin (SPB) has been extensively explored for ore deposits. However, a comprehensive evaluation of the remaining copper potential, specifically for sediment-hosted stratiform copper system, remains lacking. This study applies goSPL, an open-source landscape and stratigraphic evolution model, to reconstruct the Permian rift-phase sedimentary evolution of the Polish Trough, in the southeastern SPB. We integrate open-source datasets with key tectonic events that shaped the paleogeography, sediment provenance and accumulation of the region. We reconstruct the basin sediment deposits from 285-256 Ma, and evaluate (1) six tectonic regimes under different tectonic and climate forcing, (2) their impact on the Upper Rotliegend red beds provenance and (3) the copper potential of these red beds. Two models best align with the literature, showing distinct subsidence regimes that produced similar sediment volumes (≈19,000 km^3). One model, featuring variable subsidence, better captures the ≈ 15 million year hiatus, sedimentation rates (≈ 200 m/Myr), and depositional depth, particularly when the basin subsided below sea level. The primary sources infilling the Polish Basin (Bohemian and Carpathian Massifs) remain stable across models. Alongside known sources (East European Craton, Małopolska Massif, and Bohemian Massif), our findings suggest that the Fenno-Scandian Shield and Carphatian Massifs contributed ≈50% of the Permian sediments entering the Polish Basin. We estimate that around 1,000 km^3 of red-bed sediments contained significant copper mass, between 50 -155 MT, suggesting the Upper Rotliegend red beds are a significant, if not the primary copper source to the overlaying Kupferschiefer shale, although further investigation into the contribution from interlayered volcanic rocks is needed.

Plain Language Summary

The Southern Permian Basin (SPB) is known for its sediment-hosted copper deposits, but how these formed over time is not fully understood yet. This study uses a numerical model called goSPL to explore the Permian source-to-sink evolution of the Polish Trough, part of the southeastern SPB. We looked at existing open-source data and key tectonic events to understand sediment provenance, deposition, and their potential to be the source of copper for the mineral system. Out of six tectonic scenarios tested, two showed similar sediment volumes (about 19, 000 km^3). The model with changing subsidence rates better matched real-world sedimentation patterns, including a 15 million year gap in sedimentation and realistic deposition rates. This model indicates that the main sources of sediment were the Bohemian and Carpathian Massifs, with smaller contributions from nearby regions like the East European Craton and Fenno-Scandian Shield. We estimate that the Upper Rotliegend red beds may contain 1, 000 km^3 of copper-bearing sediment containing between 50 and 155 MT of copper. This makes them an important source of copper for the famous overlying Kupferschiefer ore shale.

1 Introduction

The Polish Rotliegend Basin (or Polish Trough), located in the eastern part of the greater Southern Permian Basin (SPB), began forming in the Late Carboniferous (Karnkowski 1999). The SPB extends west-to-east through northern Europe, from the North Sea, across northern Germany, to Poland (Fig. 1). The Polish Trough shares many similarities with the central and western parts of the SPB, particularly in sedimentation style, which is influenced by syn-sedimentary block faulting and a shift to an arid to semi-arid climate in the Mid-Permian (Kiersnowski and Buniak 2006).

The Permian Upper Rotliegend red beds, together with the overlaying Kupferschiefer shale, form a sediment-hosted stratiform copper mineral system of significant economic value. While it is generally believed that sediment-hosted stratiform copper systems form in restricted sedimentary basins, the nature and origin of the source of copper to the host reductants remain debated. Theories suggest that copper may originate from very low-grade oxidized mafic siliciclastic sediments found in the early rift strata, such as the Upper Rotliegend red beds (Vaughan et al. 1989; Hitzman et al. 2005; Hitzman et al. 2010). Alternatively, acidic volcanics and other igneous rocks associated with rifting systems or subduction zones are often identified as the primary copper source for these deposits (Sillitoe 2010). Other hypotheses suggest that the copper source might originate from wall rock leaching by the dehydrating brines from the serpentinized lower crust (Keith et al. 2018).

Although numerous studies have been conducted over the last century for the Southern Permian Basin, due to its importance in oil, gas and copper exploration, to our knowledge there has been no published numerical modeling focusing on the landscape evolution of the basin and its associated stratigraphy. In this study, we use the landscape evolution model goSPL (Salles et al. 2020), which can be applied to sedimentary basin reconstructions at both regional and global scales, to develop the first landscape evolution model of the Southern Permian Basin. We begin by reassessing the initial paleo-topography to (1) better constrain the active tectonic events during the evolution of the Southern Permian Basin, such as the collapse of the Variscan Orogeny, and (2) to calibrate the paleoprecipitation conditions. Six different simulations are proposed, from model 1 to model 6, with varying tectonic scenarios, paleoprecipitation and sea level. Most models produced a sediment budget that accurately reproduces the thicknesses of the Permian Upper Rotliegend red beds between 285 and 256 Ma, and we identify and quantify the volume of sediment from each of the main sources that fed the Polish basin. In addition to determining sediment sources, we aim to use landscape evolution modeling to test how much of these sediments originated from red-bed sediments with likely copper-source potential. To achieve this, we created a paleo-lithology map to account for regional sediment sources and quantitatively estimate the copper potential of the basin.

2 Geological background

2.1 General settings

The Southern Permian Basin is bordered in the north by the vast uplands of the Fennoscandian Plateau and the lowlands of the East European Craton (Baltica), and the Ringkøbing-Fyn High (Fig. 1). To the west, it is bordered by the Mid-North Sea High and the London Brabant Massif (Kiersnowski et al. 1995). In the southwest and southeast, the Variscan and Caledonian orogenies have exposed rocks from the Rhenish and Bohemian Massif. To the east, the Southern Permian Basin is flanked by the Teisseyre Terrane Assemblage, which includes the Małopolska Massif (Karnkowski 1999; Pharaoh et al. 2010) (Fig. 1).

The eastern portion of the SPB, the Polish Trough, is framed within the narrow Teisseyre-Tornquist structural zone (TTSZ), while the remaining southern basins, North German and Danish Basins, developed within the Elbe Fault System (Scheck-Wenderoth and Lamarche 2005). The TTSZ marks the northeastern boundary of the Trans-European Suture Zone (TESZ), the later is oriented NW-SE, and divides the Palaeozoic lithosphere of western Europe from the Precambrian East European Craton. The basement of the Polish Trough to the north is along the boundary between the Gondwana-derived East Avalonia Terrane Assemblage at the North German/North Polish Caledonides highlands and the Precambrian Baltica crust of Denmark.

The Rhenish and Bohemian Massifs, marked by a succession of parallel horsts and grabens that generate basement highs and graben basins, define the southern portion of the Polish Basin. The TESZ, thickened in Poland during the Caledonian ($\approx$ 500 - 400 Ma) and Variscan ($\approx$ 300 Ma) orogenies, comprises a system of Gondwana-derived continental terranes (Ziegler 1990; Pożaryski 1990; Pharaoh et al. 2006), and some Baltica-derived blocks (Nawrocki and Poprawa 2006). Both massifs expose the Variscan orogenic belt.

2.2 Tectonic history

The crust underlying the SPB reflects a long tectonic history, with Gondwana-derived terranes amalgamated to Baltica during the Caledonian and Variscan orogenies, culminating in the formation of Laurussia in the Late Carboniferous. These events, involving the closure of oceanic basins, collisions, crustal shortening, and post-orogenic collapse, created the foreland setting in which the SPB later developed (Pharaoh et al. 2010).

By the late Early Permian, thermal subsidence and post-orogenic collapse of the Variscan Orogeny triggered wrench faulting and alkaline volcanism. Rifting associated with Pangea's breakup led to the formation of the Viking Graben (Pharaoh et al. 2010), while the Polish Trough, atop the Teisseyre-Tornquist Zone, recorded both compressional and extensional tectonic activity (Bayer et al. 2002; Kutek 2001).

This study focuses on the Permian Period, when the Polish Basin experienced bimodal intrusive and extrusive magmatic activity associated with extensional rift faulting as a result of the thermal destabilization of the Variscan Orogeny (Ziegler

1990; Rey et al. 2001; Wilson et al. 2004; Heeremans et al. 2004; Krawczyk et al. 2008; Kroner et al. 2008; Borg et al. 2012) . During the mid-to-late Early Permian, lithospheric thermal subsidence began as asthenospheric temperatures normalized (Ziegler et al. 2004). Concurrently, wrench-faulting, deep crustal fracturing, magmatic activity, and erosion occurred north of the Variscan Mountains (Ziegler et al. 2004). By the Mid-Permian (Altmark tectonics), volcanism and wrench tectonics had ceased, leading to thermal contraction and basin subsidence (Ziegler 1990; Bachmann and Hoffmann 1995; Wees et al. 2000). As thermal anomalies decayed, the Polish and North German basins subsided significantly, coinciding with the deposition of aeolian and fluvial sandstones of the Upper Rotliegend stage (Gast (1988) and Bachmann and Hoffmann (1995)).

The Late Permian was characterized by continued thermal subsidence, driven by

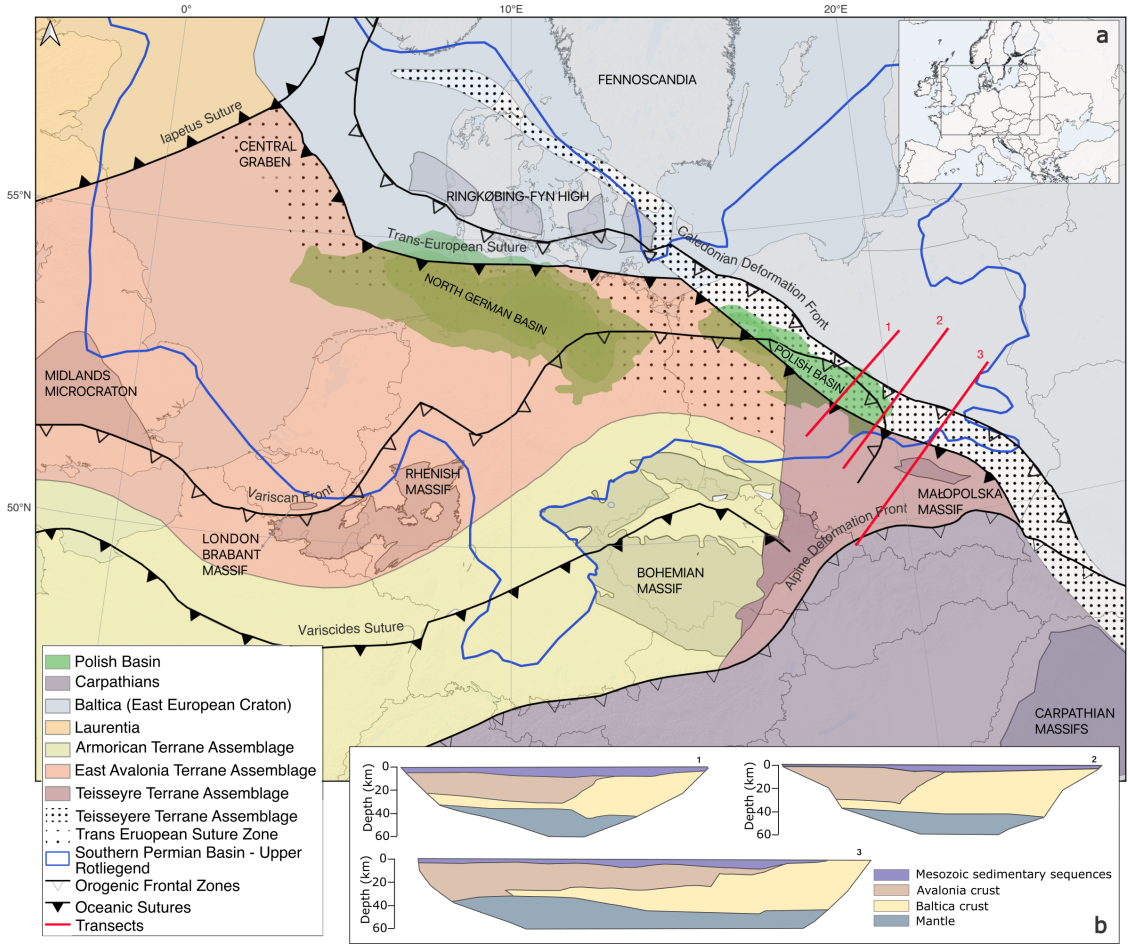

Figure 1: **Main tectonic blocks and suture zones marking the basement of the Southern Permian Basin**. **a.** The map shows the Polish Trough/Basin highlighted in green, with the main regional tectonic structures and geological units. The Southern Permian Basin contour is equivalent to the extension of the Zechstein Basin during the Upper Permian. **b.** Cross-sections summarizing the crustal structure of the region, based on seismic-refraction/wide-angle reflection data (adapted from Pharaoh et al. 2010). Seismic line locations and their endpoints are indicated by the red lines and corresponding numbers in **a**. This map represents the modeled domain in present-day coordinates.

thermal decay and rifting, which contributed to the formation of the Viking and Central grabens (Stampfli and Borel 2002). Marine transgressions, such as the Zechstein/Barents transgression, resulted from the flooding of depressions by the Boreal Sea (Glennie and Buller 1983; Bachmann et al. 2008a). Zechstein Sequence sediments were deposited over Upper Rotliegend red beds amid ongoing thermal subsidence and cyclical eustatic sea level fluctuations, resulting in the deposition of evaporite cyclothems and the Kupferschiefer shale - a 0.5 m thick black, bituminous, carbonaceous marine shale or marl, deposited in anoxic, euxinic bottom waters during a quiet tectonic phase (Ziegler 1990).

2.3 Climate and paleo-environments

For much of the Paleozoic, the Southern Permian Basin terranes were dominated by marine shelf to deep-water clastic sediments deposition. Humid conditions prevailed during the Late Carboniferous and Early Permian, transitioning to arid climates by the Late Permian (Kiersnowski et al. 1995).

The first deposition of sediments in the SPB occurred during the Devonian. The deepest part of the SPB, the North German basin, was characterized by shallow-marine sediments with occasional volcanic deposits. Coarse-grained eolian and fluvial clastic sediments filled other regions (Pharaoh et al. (2010), and references therein). During the early Carboniferous, most of the basin was covered by open marine shelf sediments, with occasional fluvio-lacustrine sediments interfingering. The deepest part of the basin retained a fully marine environment until the Late Carboniferous. The regression of the North Sea shifted the environment to pro-delta and fluvio-lacustrine deposits in the North German basin, while red beds were deposited in the more marginal portions of the Southern Permian Basin (Pharaoh et al. 2010).

The Permian sedimentary sequences that makes up the Rotliegend Group began with increased explosive volcanic activity (between $\approx$ 300 and 285 Ma) forming a thick layer of volcanic rocks (evolving from rhyolites to basalts - of the Lower Rotliegend stage Benek et al. (1996)). This was followed by a 20 million year hiatus, known as the Saalian Unconformity (McCann 1998a) or the Pangea Gap (Menning et al. 2022), during which proximal alluvial sediments were deposited in the North German Basin and Polish Trough (Müritz Subgroup and Kórnik Formation, respectively; Pharaoh et al. (2010)). In the early Late Permian (Upper Rotliegend stage), a larger area of the basin was covered by a thick layer of sediments deposited under arid and semi-arid, oxidizing climate conditions, in environments as alluvial fans, ephemeral rivers and aeolian dunes (Kiersnowski et al. 2010).

2.4 Basin lithology evolution and its main stratigraphic units

The Southern Permian Basin constitutes an intracontinental basin that extends NW-SE for over 2000 km and is up to 100 km in the N-S direction. The entire sedimentary sequence deposited in the basin from the Devonian until the Permian varies in thickness from 7 to 9 km. The Permian red beds, part of the Upper Rotliegend stage, reach depths of up to 2500 m in North Germany, and 1300 m in the Polish portion of the SPB (Pharaoh et al. 2010). The lateral correlation

between stratigraphic units has been explored by various authors (Menning 1995; Wees et al. 2000; Kiersnowski and Buniak 2006; Kiersnowski et al. 2010; Pharaoh et al. 2010) . Here, we adopt the lithostratigraphic framework of Pharaoh et al. (2010), which identifies the main units for the Upper Rotliegend stage from lower to upper Permian are Altmark, Müritz, Havel and Elbe Subgroups in the North German basin. The correlative units in the Polish basin include the Dolsk/Swiniec, Wiellkopolska, Kórnik, Drawa Subgroups and Upper/Lower Notec Formations (Fig. 2). We assume later in this manuscript that lithostratigraphic units broadly correlate to chronostratigraphic units for a temporal correlation.

The pre-Permian basement (before 298 Ma) consisted of schist, greywacke, hornfels, granodiorite, and gneiss, reflecting complex geological events from the Proterozoic to the Late Paleozoic, along with Devonian argillaceous limestone and black shale deposits (Kłapciński and Sachanbiński 1975; Tomaszewski 1978). Early Carboniferous volcanic activity and granite porphyry intrusions thermally contributed to Late Carboniferous coal formation, as part of a magmatic arc linked to subduction during Variscan Orogeny. During the Late Carboniferous, intense volcanic activity spanned the region from the Oslo Graben to the Variscan Mountains, marked by significant andesite and ignimbrite deposits (Neumann et al. 2002; Heeremans and Faleide 2004; Wilson et al. 2004; Awdankiewicz et al. 2025).

Conspicuous vertical lithofacies changes and/or erosional boundaries mark the depositional cycles, with the Upper Rotliegend stages I and II distinguished by the onset of the Altmark tectonic events (Kiersnowski et al. 1995; Kiersnowski and Buniak 2006). Upper Rotliegend I sediments were confined to rift basins and grabens, locally governed by cyclic fluctuations between arid and less-arid conditions (Fig. 2, Kiersnowski et al. (1995)). In contrast, the Upper Rotliegend II stage comprises nine successive depositional cycles, involving alluvial fan, fluvial, lacustrine, playa-lake and aeolian deposits (Fig. 2). Recent research highlights the importance of the equatorial Variscan mountain chain as a significant topographic barrier during Carboniferous and Permian times (Kiersnowski 2013).

Basal Clastic and Volcanic Rocks of the Lower Rotliegend Stage (298 - 290 Ma): The Lower Rotliegend stage represents the initial phase of basal clastic rocks deposition, which comprised two sequences of reddish-brown conglomerate-sandstone-mudstone, with thicknesses reaching up to 150 meters. Concurrently, intense bi-modal volcanic activity occurred, evidenced by the deposition of volcanic rocks varying from a few meters to over 1500 meters in thickness were deposited (Kucha and Piestrzynski 1995; Pharaoh et al. 2010; Maliszewska et al. 2016).

Upper Rotliegend Stage Red-Bed Clastic Rocks (290 - 258 Ma): The deposition of Upper Rotliegend clastic rocks marked a pivotal development, originating from isolated, fault-controlled basins that evolved into a series of northwest-trending, partially interconnected horsts and grabens. These basins predominantly hosted clastic facies, including red oxidized sandstones and conglomerates, deposited across various environments such as alluvial fans, braided rivers, meandering streams, aeolian dunes, and saline lake (Blundell et al. 2003). This stratigraphic sequence differs from the underlying Lower Rotliegend stage by an unconformity. While the Lower Rotliegend stage is distinguished by its coarser composition, higher conglomerate content and large volcanic content, the Upper Rotliegend stage, typically over 1000

meters thick but extending up to 2500 meters in places, features a finer-grained sedimentary rock, predominantly composed of sandstones, with minor interfingered volcanic rocks (Kiersnowski et al. 1995; Karnkowski 1999; Pharaoh et al. 2010).

Weissliegend and Grauliegend Formations (Terminal Phases - 258 - 257 Ma): The Weissliegend Formation, typically between 1 and 50 m thickness, primarily composed of aeolian, fluvial, and locally marine sandstones, exhibits a lack of oxidation and diagenetic hematitic reddening, retaining a white to grey coloration before being capped by the Kupferschiefer shale (Glennie and Buller 1983). The Grauliegend Formation conglomerates, in contrast, underwent terrestrial oxidation and hematitic reddening, followed by chemical reduction due to interactions with overlying euxinic conditions and reducing fluids, producing a light grey to grey-pink coloration.

Zechstein Sequence (257- 252 Ma): This sequence records a rapid transgression correlating with increased regional subsidence. This event resulted in the Kupferschiefer Sea due to rift-induced subsidence and glacio-eustatic sea level rise, flooding the basin and cyclically depositing evaporites with occasional shale interbedded. This sequence is usually between 1500 to 2000 m thickness (Peryt 1978; Oszczepalski 1986; Kiersnowski 2013; Pharaoh et al. 2010).

2.5 Provenance history

The provenance of the 2500 m thick Upper Rotliegend stage red beds in the German Basin and the equivalent 1300 m sequence in the Polish Trough has been investigates by a range of authors (*e.g.* McCann 1998b; Kiersnowski and Buniak 2006; Doornenbal and Stevenson 2010; Mazur et al. 2010). McCann (1998b) correlates the quartz-rich sediments of the Upper Rotliegend II stage to cratonic or recycled sedimentary sources, while compositionally immature sediments are attributed to volcanic and sedimentary rock fragments. Zircon and trace element analyses by Zieger et al. (2023) further suggest that the Upper Rotliegend II stage comprise a mix of repeatedly recycled material and bedrock-derived sediments.

For the Polish Basin, Kiersnowski et al. (2010) interpreted the sediment routing of the Upper Rotliegend II stage using 3D seismic data. Weak water supply and poor drainage characterized the southwestern highlands (Variscides, near the Bohemian Massif), while prevailing winds transported aeolian sediments from the lowlands of Baltica (East European Craton) and the Małopolska Massif (Kiersnowski et al. 2010). A later study by Kiersnowski (2013) identified six aeolian lithostratigraphic units (ERU, ERBU 1, EBYU, ERBU 2, ECU 1 and ECU 2) and one fluvial unit (FIU) in the Polish Upper Rotliegend Basin. The Lower Drawa Formation (ERU) received sediment from Cambrian and Carboniferous sandstones, with winds from the S-SE. Subsequent aeolian units (ERBU1, EBYU, ERBU 2) were influenced by winds from the east, south, north and northwest, with sources along the basin margin and the Małopolska Upland (Kiersnowski 2013).

The fluvial Notec Formation (FIU) sourced its sediments from the East European Craton. The final aeolian units, (ECU 1 and ECU 2) also included fluvial input, with sediments contributions from the Precambrian Platform and from the Małopolska Massif/Upland (Kiersnowski 2013). Paul et al. (2008) suggested that the sandy

deposits from the southeastern margin of the Zechstein Sequence likely originated from the Bohemian Massif.

2.6 Sedimentation rates and volumes

Several maps constraining the paleothickness of the Southern Permian Basin have been inferred from seismic data and boreholes (*e.g.* Pharaoh et al. 2010; Kiersnowski 2013; Krzywiec et al. 2019). While sediment volume can be derived from these maps, few studies have attempted to quantify the total volume for the Southern Permian Basin or its smaller units, such as the Polish basin. Scheck and Bayer (1999) estimated a sediment volume of 340,000 km^3 for the Northeast German Basin on its subsidence history, excluding erosion processes. Approximately one-third of this volume was deposited during the initial thermal subsidence phase, corresponding to Upper Rotliegend stage Mirrow Formation and Elbe subgroup, with a deposition rate of 1,700 km^3/Myr (Scheck and Bayer (1999), Fig. 1).

Scheck and Bayer (1999) outlined five main phases of subsidence throughout the basin's evolution, from the Late Carboniferous to the Cenozoic. The initial ther-

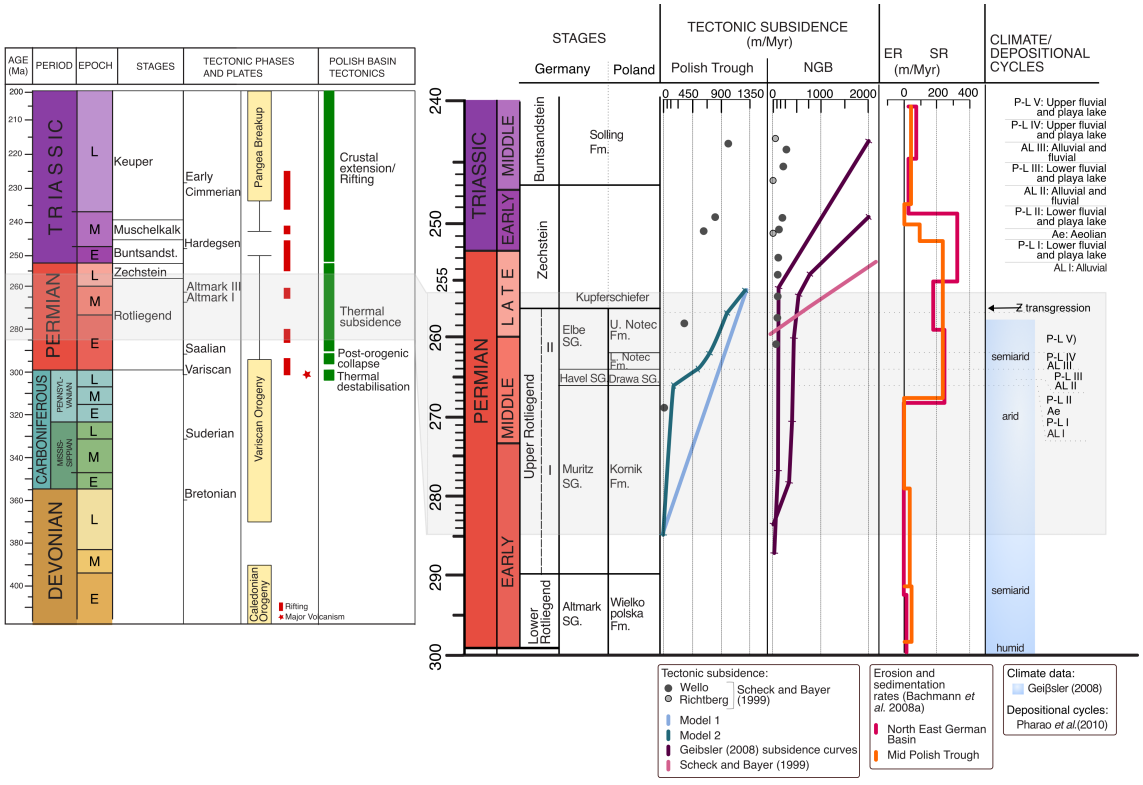

Figure 2: **Chronostratigraphy of the Southern Permian Basin**. Left: The chart illustrates the major tectonic events that shaped the landscape of the Southern Permian Basin from Devonian to Triassic. Right: key events during the Permian are shown, with the shaded grey area representing the time of our simulations. The stratigraphy is based on Pharaoh et al. (2010), tectonic subsidence rates are from Scheck and Bayer (1999) and Gast and Gundlach (2006), the erosion/deposition record is from Bachmann et al. (2008b), depositional cycles are from Pharaoh et al. (2010) and climate data is from Geißler et al. (2008). NGB refers to the North German Basin, ER and SR denote erosion and sedimentation rates, respectively.

mal subsidence phase, driven by rifting, occurred from the Late Carboniferous to the Early Permian. However, most of the subsidence resulted from thermal relaxation, possibly linked to slab break-up from the Variscan Orogeny. This subsidence was oriented NW-SE during the Early Permian (Rotliegend sediments) and Middle Triassic (Scheck and Bayer 1999).

For the Middle Permian Upper Rotliegend II stage (Mirow Formation and Elbe Subgroup) in the North German Basin, subsidence rates of 30 m/Myr were sustained over 12 million year (Scheck and Bayer 1999). Additional estimates provided by Wees et al. (2000), presenting subsidence rates for the Northeast German Basin during the Upper Rotliegend stage (264 to 258 Ma), ranging from 130 to 50 m/Myr. In the Polish Trough, subsidence rates were generally lower, varying between 130 to 15 m/Myr, with higher rates observed in the basin center compared to the margins (Wees et al. 2000).

3 Methodology

3.1 Landscape evolution model (LEM)

In this study, we aim to estimate the volume of sediments deposited in the Polish Trough during its Permian evolution (285 to 256 Ma) by understanding how the interplay between precipitation and tectonics influences sediment transport, driven by surface processes and landscape dynamics. To achieve this, we used the landscape evolution model *goSPL* (Salles et al. 2020), which simulates upstream erosion, sediment transport, and basin deposition driven by riverine processes based on multiple flow direction algorithm.

The equation governing landscape evolution over time is as follow:

$$\frac{\partial z}{\partial t} = U_i + \kappa_{hl}\nabla^2 z_i + \epsilon P_i^d (P_i A_i + \sum_{j \in \text{up}} Q_j)^m \nabla z_i^n \tag{3.1}$$

where the changes in elevation (z in meters) over time (t in years) are influenced by the three terms on the right-hand side of the equation : the tectonic forcing U (m/yr); a linear diffusion law (soil creep) for hillslope transport (Salles 2016; Salles et al. 2018); and the stream power law (SPL), respectively. In this simplified formulation, continental deposition occurs in depressions and endorheic basins. In term (**2**), κ_{hl} is the diffusion coefficient, defined separately for marine and land environments. In this study, it is set to 0.8 m^2/yr for marine environments and 0.4 m^2/yr for land environments. In term (**3**), m and n are dimensionless empirical constants in which default formulation values were assumed, set to 0.5 and 1, respectively (Salles et al. 2018; Salles et al. 2023). The precipitation-independent component of erodibility (ϵ) was initially set as a spatially uniform value of 7.0×10^{-8} m/yr and 8.0×10^{-8} m/yr, changing from model to model. This component remains constant throughout the simulation time. The erodibility coefficient is scaled with the local mean annual precipitation rate (P), using a positive exponent (d) set to 0.42 (Murphy et al. 2016). The upstream total area (A) and local precipitation (P) are combined to form the water flux (PA) (Salles et al. 2018).

3.2 Model setup

3.2.1 Initial conditions

We developed regional models with 2.5 km average cell resolution, which corresponds to approximately 1.5×10^6 triangular cells. The simulated domain spans approximately 3,000 km east-west, from the London-Brabant Massif to the Carpathian Massifs, and 2,000 km north-south, from the Variscan Mountains in the south to the Fennoscandian Shield in the north (Fig. 1). This coverage encompasses all major sediment sources that could influence deposition in the Polish Trough. The simulations were run from 285 Ma to 256 Ma, with time steps (dt) of 10,000 years, and outputs every 1 million year. The time span covers the end of the major volcanism in the Southern Permian Basin (SPB) up to the Zechstein marine transgression, ensuring in this way that the sedimentation prior to the final marine transgression is captured. The stratigraphic architecture (strata), when activated, is recorded every 100,000 years.

For our initial paleogeography, we used the PALEOMAP paleo-elevation maps (Scotese and Wright 2018), which provide global grids at 0.1°. The climatic forcings (precipitation) were extracted from paleo-climate simulations outputs run on the paleogeographies, from the HadCM3BL-M2.1aD29 model (Valdes et al. 2020), with a resolution of 3.75°×2.5°. Since both datasets (paleo-elevation and paleo-precipitation) are global, we adjusted the initial conditions as shown in Fig. 3, and Figures S1 and S2 in the Appendix. We acknowledge that limitations to our model are tied to inaccuracies in interpreted paleo-elevation and modeled paleo-precipitation datasets.

During the calibration phase, we ran approximately 30 simulations on 128 cores, with each simulation taking up to 10 hours to complete. The analysis performed in this manuscript consists of six models. The main points of calibration and validation for the six presented scenarios can be found in Figures S4 and S5. Figure S3 shows the results for the best fitting model (model 2), with the corresponding tectonic forcings outlined in Fig. S1. Figure S3 illustrates the basic outputs produced by goSPL, including landscape evolution, associated river networks, and spatial distribution of cumulative erosion and deposition patterns. To access to the full evolution of all six models, refer to the figures available in the Zenodo repository (Hadler Boggiani 2024).

3.2.2 Refining forcing conditions

Each model is constrained by a specific combination of tectonic changes, precipitation, sea level curves and a uniformly distributed erodibility (Fig. 3a).

Models 1 to 5 account for the tectonic evolution of the Variscan Orogeny, which developed from initial convergence to post-convergence collapse between the Devonian and Late Carboniferous/Early Permian (Rey et al. 1997; Vacek and Žák 2019). This post-convergence collapse results from the break-off of the subducting slab beneath Laurussia. However, due to limited available data, and to identify which model better replicate these conditions, we tested different subsidence rates in the Variscides, ranging from 0 and 7 m/Myr, applied at different periods during the simulation

(Fig. S1a, VM).

The final evolution of the Variscan Orogeny in the early Permian marks the end of the collisional stage between the Laurussia and Gondwana supercontinents and corresponding to beginning the disintegration of Pangea (Glennie 1995). From the Late Carboniferous to the Jurassic, the post-tectonic E-W extension of the Proto-Atlantic Ocean propagated southward, initiating the rifting observed in the Viking Graben (Glennie 1995). To simulate this effect, we applied a subsidence rate of 3 to 4 m/Myr over in the Viking Graben area, while assuming an uplift of 2 to 8 m/Myr along the rift shoulders, based on literature values (Pharaoh et al. 2010). This forcing was applied during the first 15 million years of the simulation (Fig. S1a, VG and RS) where it modulated the sea level changes.

Model 6 does not incorporate tectonic changes in the Variscan Mountains nor the Viking Graben and its initial paleo-elevation at 285 Ma is similar to the original paleo-elevation map from Scotese and Wright (2018) (Fig. 3d, S1a).

The Southern Permian Basin subsidence evolution was simulated using data from paleo-thickness maps (Karnkowski 1999; Scheck-Wenderoth and Lamarche 2005; Kiersnowski and Buniak 2006; Karnkowski 2007; Pharaoh et al. 2010; Krzywiec et al. 2019) . Two subsidence rates were applied in the basin. The first, used in models 1, 3, 4, 5 and 6, assumes a linear subsidence rate through the entire modeling period, with uniform deposition of the Upper Rotliegend II stage (Geißler et al. 2008; Doornenbal and Stevenson 2010) (Fig. 3a). For these models, we assumed that over 29 million years, the maximum preserved sediment thickness in the Polish Trough is 1300 m ($\approx$ 45 m/Myr), and is set to 2200 m (75 m/Myr) for the German Basin (Fig. S1a). These thicknesses align with those proposed by Wees et al. (2000).

The second subsidence rate, tested in model 2 (Fig. 3a), is a non-linear rate accounting for the deposition of the five main stratigraphic subgroups of the Polish Basin (Wielkopolska/Altmark, Kórnik/Muritz, Drawa/Havel, Lower Notec/Dethlingen Formations, Upper Notec/Lower Hannover Formation). In this case, we used the maximum sediment thickness predicted for each of these units (based on Hug and Gaupp (2006), Doornenbal and Stevenson (2010), and Kiersnowski et al. (2010)) and considered the deposition timescales based on Pharaoh et al. (2010). This corresponds to five distinct subsidence steps, consistent with literature data from Wees et al. (2000) and Bachmann et al. (2008b) (Fig 3b).

For the paleoprecipitation, we adjust for orographic effects by adjusting precipitation rates based on elevation and regional variability, reflecting how precipitation patterns are influenced by topography (Fig. S2). Additionally, we imposed a progressively drier climate across all models, as suggested by Kiresnowski (1997) and Kiersnowski et al. (2010), with model 5 representing the driest scenario (Fig. S2). Model 6 considers the paleoprecipitation without adjustments.

3.3 Deriving data from LEM outputs

We generated netCDF grids from the *goSPL* outputs (every million years) containing the following information: latitude and longitude, elevation (m), cumulative erosion/deposition (m), catchment ID, water flux discharge accounting for lakes

(m^3/yr), water flux in rivers excluding lakes (m^3/yr), sediment flux in rivers (m^3/yr) and rainfall (m/yr).

Using this series of grids, we first estimate the sediment volume deposited in the Polish Trough over time, specifically for the Upper Rotliegend II stage red beds. Then we identified the main catchments feeding into the basin. To calculate the sediment volume from upstream regions, we extracted data from the 500 major catchments whose outlets (major discharge point) were located in or near the subsiding basin.

To track the provenance of sediments deposited in the Polish Trough, we divided the region in eight key polygons of interest. These were delineated based on paleo-elevation, regional tectonic and structural domains, as well as the age and the main lithology of the topographically elevated regions (Fig. 4). The polygons were named after main geological formations in the area they represent: (1) Anglo-London Bra-

Model Setup - Forcing conditions:

a	Model 1	Model 2	Model 3	Model 4	Model 5	Model 6
Sea level curve	set to zero	set to zero	set to zero	set to zero	varying curve based on Smith (1979)	set to zero
Subsidence rate changes	no	yes	no	no	no	no
Erodibility	$\epsilon = 8.0\ e^{-8}$	$\epsilon = 8.0\ e^{-8}$	$\epsilon = 7.0\ e^{-8}$	$\epsilon = 8.0\ e^{-8}$	$\epsilon = 7.0\ e^{-8}$	$\epsilon = 7.0\ e^{-8}$
Paleo-elevation changes	yes, similar changes in the surroundings as Model 2, but with constant subsidence rate in the SPB	yes, similar changes in the surroundings as Model 1, but with varying subsidence rates in the SPB	yes, similar to Model 4	yes, similar to Model 3	yes, highest subsidence on the Variscan Mountains	none, considers initial paleo-geographhy
Paleo-precipitation changes	yes	yes	yes	yes	yes - dryer climate	none, considers initial paleo-precipitation

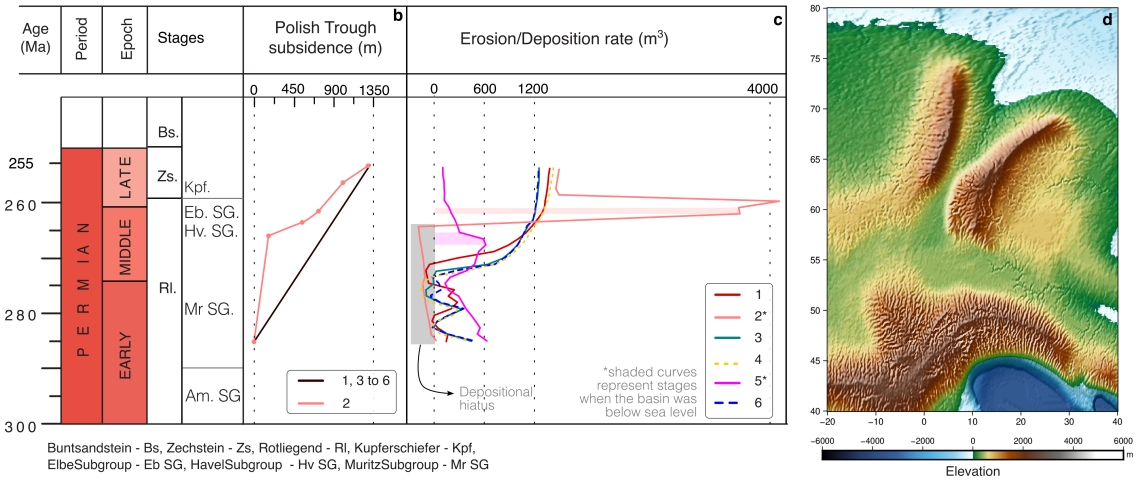

Figure 3: **Main changes in forcing conditions between models, with equivalent erodibility value (ϵ). a**. Table summarizing the main changes between models. Note that in model 6 no changes to the initial paleo-elevation or paleo-climate were imposed (for rates of changes in tectonic and precipitation conditions per model, please refer to Figures S1 and S2 in the appendix). **b.** A plot showing the changes in subsidence rate that distinguish model 2 (in salmon) from the other models (in black). **c**. Erosion/deposition recorded in the basin after the simulation, with models 2 and 5 reaching elevations below sea level at times, as indicated by the shaded area under the erosion/deposition curve. A marine incursion is observed in model 5. **d.** Initial paleo-elevation of the modeled domain prior to any forcing conditions.

bant Massif, (2) Variscides Rhenish Massif, (3) Variscides Bohemian Massif, (4) Carpathian Massifs, (5) Holly Cross Mountains/Małopolska Massif, (6) Precambrian Platform/East European Mid to Lowlands, (7) Fenno-Scandian Shield/high lands and (8) the German and Danish basins (highlighted in Fig. 5).

4 Basin forcing and sedimentary response

4.1 Influence of temporal forcing and sea level on basin's evolution

From the six models discussed above, model 1 and 2 provide a good fit in terms of final sediment volume and basin architecture, with identifiable horsts and grabens (Fig. 8). Models 1 and 2 yield similar sediment volumes of $19,594$ km^3 and $19,807$ km^3, respectively (Fig. 6). Although model 1 and 2 consider similar forcing conditions, the key difference lies in the subsidence regimes imposed within the Southern Permian Basin, which strongly influence the sedimentation history in the Polish Trough. Model 2, however, better captures periods of hiatuses in sedimentation, when the basin subsided below sea level, followed by renewed sediment accumulation. The resulting sediment volumes and erosion/deposition rates are consistent with published estimates (for correlation see the appendix Fig. S5), leading us to consider model 2 as the best fit scenario.

In model 6, we tested an initial uniform erodibility value $\epsilon = 7.0$ x 10^{-8} m/yr over the entire modeled area, and obtained sediment accumulation of about 20,000 km^3. This model exhibits a significant erosion in the Variscan Mountains, with peaks of elevation of around 2 km only observed on the deformation front of the Variscan Orogeny (Figures 3a, 3c, 7, and Figure S1a in the Appendix, supplementary videos are available from the Zenodo repository (Hadler Boggiani 2024)).

Upon testing model 6, we identified the absence of marine incursion from the Viking Graben. Model 5 addresses this with imposed sea level variation based on previous studies (Smith 1979; Legler and Schneider 2008), forcing subsidence in both the Viking Graben and the Variscan Mountains (Fig. 3b and Fig. S1a). This resulted in an under-filled basin, that accumulated less than 10,000 km^3 of sediments over the simulation period (Fig. 7), with fully marine conditions established around 265 Ma, persisting until the end of the simulation (Fig. 3c). In this model, the final elevation of the Variscan Mountains did not exceed 1 km, which makes this model unrealistic based on the known evolution of the region (Hillenbrand and Williams 2022). Nevertheless, model 5 is still valuable for constraining the tectonic evolution of the area.

For the next calibration, we simulated marine incursion by imposing subsidence in the Viking Graben to account for active rifting, while also uplifting the shoulders of this system to calibrate isostatic changes in potential source areas (Fig. S1a). Small adjustments to the subsidence rate and different durations for the orogenic collapse were applied to the Variscan Mountains (Rey et al. 1997; Pharaoh et al. 2010; Vacek and Žák 2019) in models 3 and 4, compared to model 1. We shortened the subsidence time for the Variscan Mountains in order to maintain more realistic elevations at the end of the simulation, and increased the precipitation in these

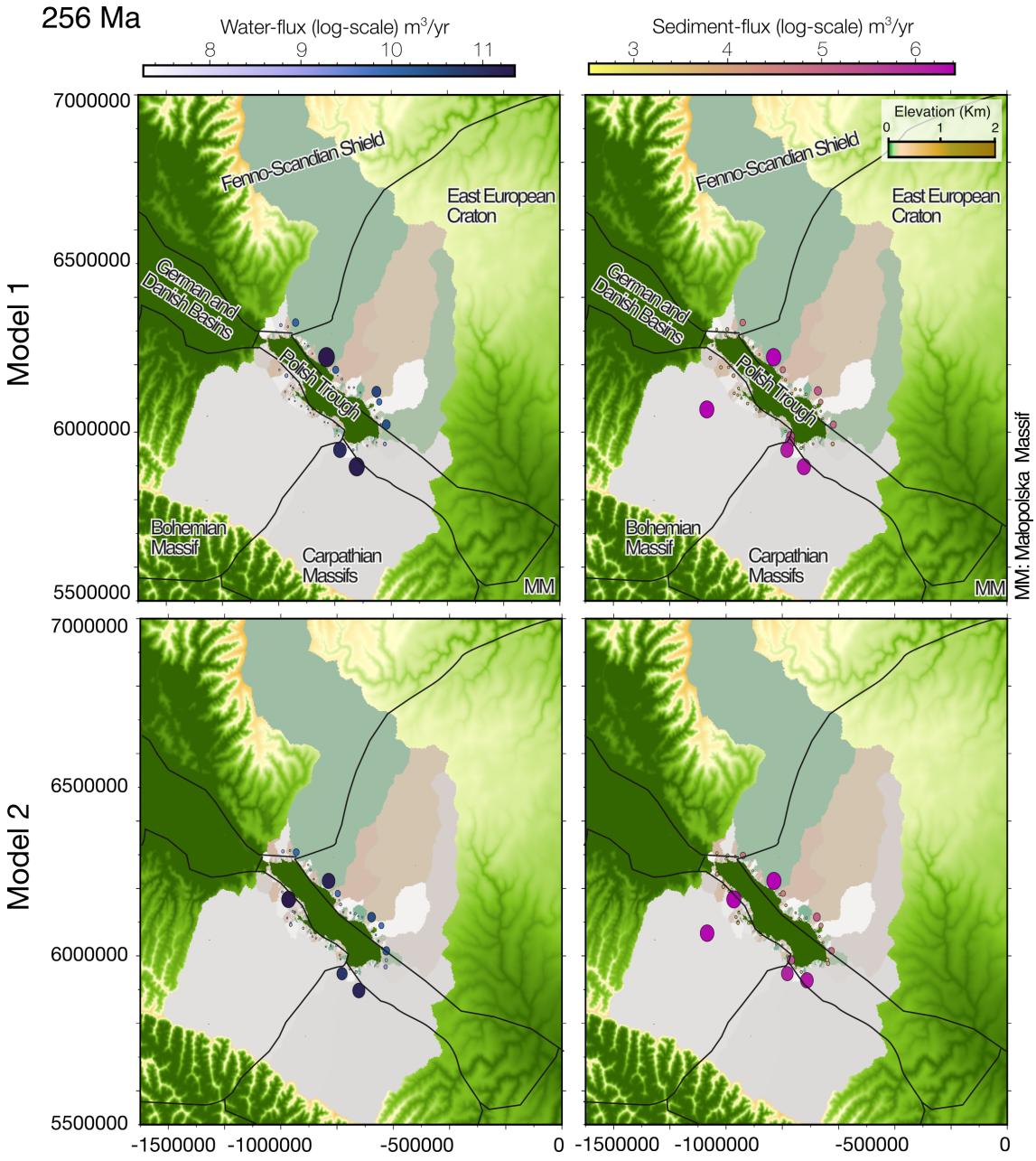

Figure 4: **Example of water and sediment flux from the 100 major catchments draining to the Polish Trough at 256 Ma, comparing outputs from the two best-fit models (1 and 2)**. Each circle represent the major outlet for sediment and water, and their size indicate the volumes of water or sediment flux, the larger circles represent the largest volumes and vice-versa. The pale green to light brown color represent each individual catchment that drained to the Polish Trough at 256 Ma. The differences, despite subtle, are observed between water fluxes, particularly in the northwest (NW) and southwest (SW) corners of the Polish Trough. These variations highlight the influence of different tectonic, climatic, and erosional conditions on the water and sediment fluxes distribution across the basin. For a representation of all the six models, please refer to the Zenodo repository (Hadler Boggiani 2024)

.

models (Fig. S1b). Models 3 and 4 resulted in a better approximation of the final cumulative sediment volume in the Polish Basin, both overfilled with final sediment volumes of approximately 20,000 and 19,000 km^3, respectively (Fig. 6).

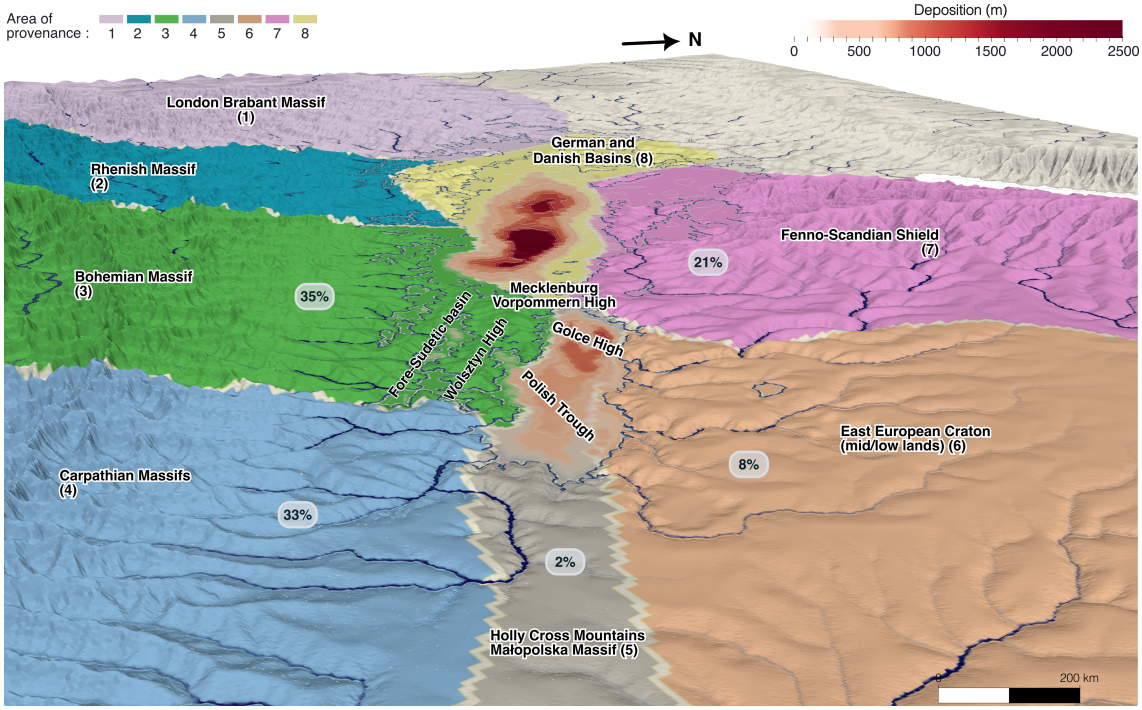

Figure 5: **3D view of the modeled region at 256 Ma.** The colored polygons delineate the provenance areas used to track sediment origin. Red shading represents the thickness of the sediment package deposited in the Polish Trough. Blue lines indicate the main drainage systems in the region during this period. The grey boxes display the percentage of sediments provided by each source to the Polish Basin, based on the results from model 2

4.2 Influence of subsidence on basin evolution

Following the description in section 3.2.2, we tested two subsidence rates in the Southern Permian Basin (Fig. 3). Results from both simulations are presented to contrast how these two subsidence rates affect the basin's infilling history.

Despite the similar final cumulative volumes, the differing subsidence rates lead to distinct sediment accumulation patterns over time (Fig. 6, first column). In model 1, accumulation is initially slow but continuous at a gradual rate until 277 Ma, followed by a 4-million-year period of no deposition. After this, the rate of sediment accumulation steadily increases until the end of the simulation (Figs. 3d, and 6 middle column). For the first two million years, less than 220 km^3 of sediment were deposited. Between 284 and 276 Ma, sediment deposition fluctuates, peaking at 390 km^3 before dropping to zero over a 3-million-year period of no deposition. After 273 Ma, sediment deposition increases sharply and becomes more evenly distributed. The maximum net sediment volume deposited per time step in model 1 is $\approx 1,400$ km^3 (after 263 Ma, Fig. 6).

In contrast, model 2 shows a small initial sediment accumulation at 285 Ma (≈ 5.8 km^3), followed by a depositional hiatus until 268 Ma (Fig. 6, first column). After

this period, three main net sediment accumulation phases occur, each with rates higher than those simulated in model 1 (Figs. 3d, and 6, middle column). In model 2, after a brief phase of initial deposition, no sediment accumulation occurs until 268 Ma. Then, 750 km^3 of sediment is deposited at 264 Ma, followed by large sediment volumes (between 3,500 and 4,000 km^3) deposited over the next 3 million years. From 262 Ma to the end of the simulation, $\approx 1,700$ km^3 of sediment is deposited per million years in this model (Fig. 6, first column). The deposited sediment volume is of similar order of magnitude as those presented for the North German Basin (Scheck and Bayer 1999).

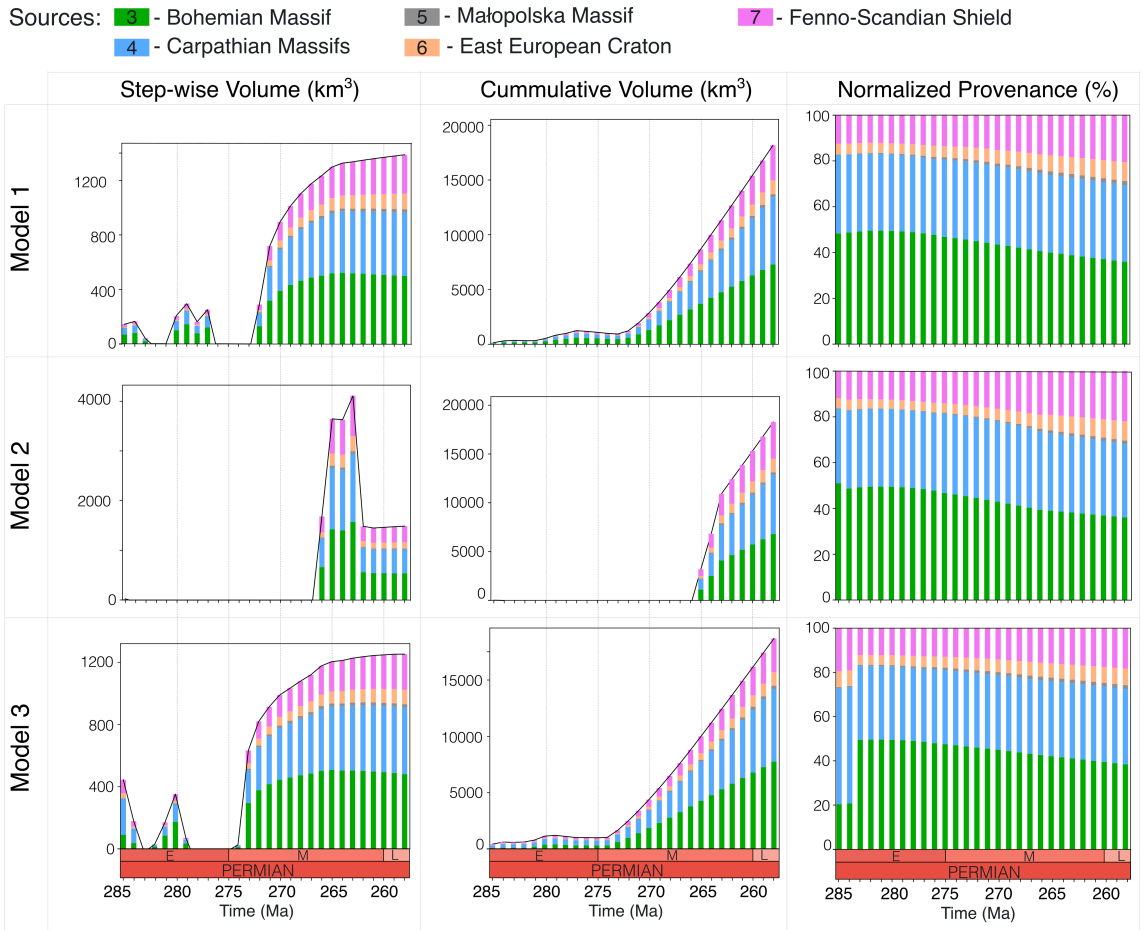

Figure 6: **Characterization of the volume of sediment deposited in the Polish Basin based on each source polygon for all models.** First column: Volume of sediment deposited at each time step. Notable periods of no deposition (hiatus) are observed in models 1 to 4. Middle column: Cumulative sediment volume per time-step for each source. Right column: Percentual distribution of sediments contribution from each to the basin, highlighting changes in the dominant source polygons over time. The source regions include : 1 - London Barbant Massif, 2 - Rhenish Massif, 3 - Bohemian Massif, 4 - Carpathian Massifs, 5 - Małopolska Massif, 6 - East European Craton, 7 - Fenno-Scandian Shield, 8 - German and Danish basins. Note that sources 1, 2 and 8 do not contribute sediment to the Polish Basin.

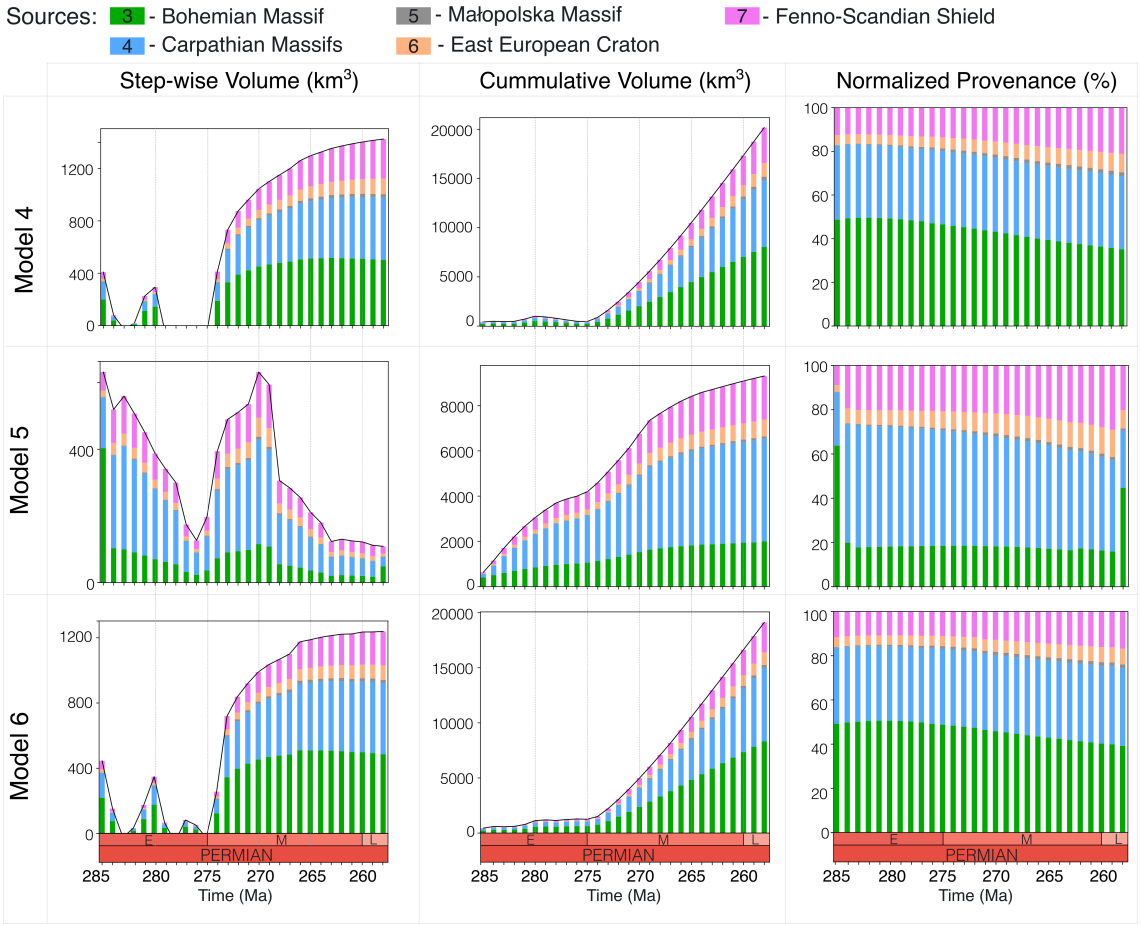

Figure 7: **Continued from Fig. 6.**

4.3 Provenance analysis

4.3.1 Predicted water and sediment flux

Here we extract the sediment provenance areas infilling the Polish Trough for all models. The water and sediment flux provided per catchment to the Polish basin (Fig. 4) are the ones used to calculate the provenance volumes per source region (Figs. 6 and 7). We observe that for models 1, 2, 3, 4 and 6 these catchments are generally constant, with smaller variations to model 5. We estimate for the largest catchment on the north side of the basin (Fig. 4), which partially contains the Fenno-Scandian Shield source area, an area of approximately $580,000$ km^2, and a sediment flux of 7.3 MT/year. These values are comparable to fluxes observed in the modern Upper Mekong river basin, which share similar precipitation and elevation records (Sok et al. 2020).

We observe that the source areas 1 (London Barbant Massif), 2 (Rhenish Massif) and 8 (German and Danish basins) do not contribute sediments to the Polish Basin in any of the presented models despite their close spatial proximity. Source areas 1, 2 and 8, are not overlapped by catchments that feed to the Polish Trough (Fig. 4), explaining their absent contribution. Source 8, though in contact with the Polish Trough, functions as an even deeper depocenter (the German and Danish basins), where sediments are more likely to be transported to, rather than from. Source area 5 (Małopolska Massif) sediment proportion increases for all modeled scenarios, although its contribution is usually smaller than 2%.

Models 1, 2, 3, 4 and 6, which do not account for sea level variations, show a general dominance of sediment provenance from source 3 (Bohemian Massif), with a decrease of up to 15% in contribution over time (Figs. 6 and 7). For most of the models, the primary sources of sediment flux are the southern margins of the basin, primarily from the Bohemian Massif (source 3) and Carpathian Massifs (source 4). There are notable contributions from the Fennoscandia highs (source 7) and the East European Craton (source 6) in all models. As the simulation progresses, the contributions from these two latter areas increase, and by around 270 Ma, the sediment input from the southern sources becomes more balanced with contributions from the Fennoscandian highs and the East European Craton (Figs. 6, 7 and 4).

Only model 5 shows a clear dominance of sediments sourced from the Carpathian Massifs (source 4), with the Bohemian Massif (source 3) and the Fennoscandian highs (source 7) contributing secondary amounts. Between 270 and 265 Ma, the Fennoscandian Shield surpass the Bohemian Massif as the dominant source. In this model, much of the sediment derived from the Bohemian Massif is trapped behind the Wolsztyn High in the Fore-Sudetic basin, which isolated the Polish Basin from this source. The more pronounced elevation of the Wolsztyn High in this second group effectively reduces sediment contribution from the Bohemian Massif, altering the sediment provenance pattern (Figs. 5, 6, 7, and videos for elevation and sediment flux, available from the Zenodo repository Hadler Boggiani (2024)).

4.3.2 Sediment accumulation

goSPL also records the architecture and depth of sedimentary layers at time of deposition, along with stratigraphic layer thickness (Fig. 8). Since this increases considerably the simulation time, we activated the stratigraphic layer recording only for the two best models that best fit the constraining data available (models 1 and 2).

The evolution of sediment thickness differs between the two models (Fig. 8a). In model 1, steady deposition rates are observed, starting at 1 - 4 m per 100,000 yrs for the first 10 million years, and increasing to 3 - 4 m for the remaining 19 million years (Fig. 8a). If we account for deposition in Myrs, we estimate that for the first 10 million years, between 200 and 400 m of sediments were deposited (between 20 and 40 m/Myr). The remaining 900 - 1100 m of sediments deposited in the last 19 million years ($\approx$ 52 m/Myr).

In contrast, model 2 starts with no sediment deposition for the first 17 million years, then increases to 5 m per 100,000 years (50 m/Myr), spiking to 40 m at 19 million years (400 m/Myr). The deposition rates stabilizes between 10 to 25 m for the next 3 million years (100 to 250 m/Myr), before slowing to 5 m during the final 7 million years as subsidence declines (350 m/Myr). The initial 1 million-year sediment accumulated in this model, characterized by varying layer thickness between 2 to 40 m, totals nearly 300 m of sediments deposited around 267 Ma. Until 260 Ma, four sediment packages of about 200 m each are deposited per million years. The final 5 million years contribute an additional 250 m of sediment (Fig. 8a).

Figure 10 shows cross-sections coloured by stratigraphic units. In model 1, a thick layer of Kórnik Formation is present, while in model 2, it is barely visible. The thickness of the Drawa Formation differs significantly, reaching 300 m in model 1 and up to 700 m in model 2. The Lower and Upper Notec Formations have similar thickness in both cases, approximately 500 m (Fig. 10). We also note that horsts and grabens are observed in our models, closely resembling the interpreted stratigraphy from Pharaoh et al. (2010) (Fig. 10). The cross-sections provided in Figures 8 and 10 also show smaller structures, such as Piaski, Golce and Roktenica Highs, as well as the Czaplinek sub-basins as observed in Fig. 8c.

5 Basin dynamics and resource implications

5.1 Comparison between initial temporal forcing conditions

The final accumulated sediment volume and the changes in provenance observed across the different models highlight how variations in surrounding topography, erodibility, and climate influence sedimentation patterns. Model 5, which incorporates sea level fluctuations and the lowest precipitation rates, reveals that basin deposition does not exceed erosion, resulting in an under-filled basin by the end of the simulation. In contrast, for models 1, 3, 4 and 6 erosion exceeds deposition until a maximum of 13 million years into the simulation, however some time steps (varying between models) still present a positive net accumulation. For model 2, erosion exceeds deposition until 17 million years into the simulation (Fig. 6 and 7).

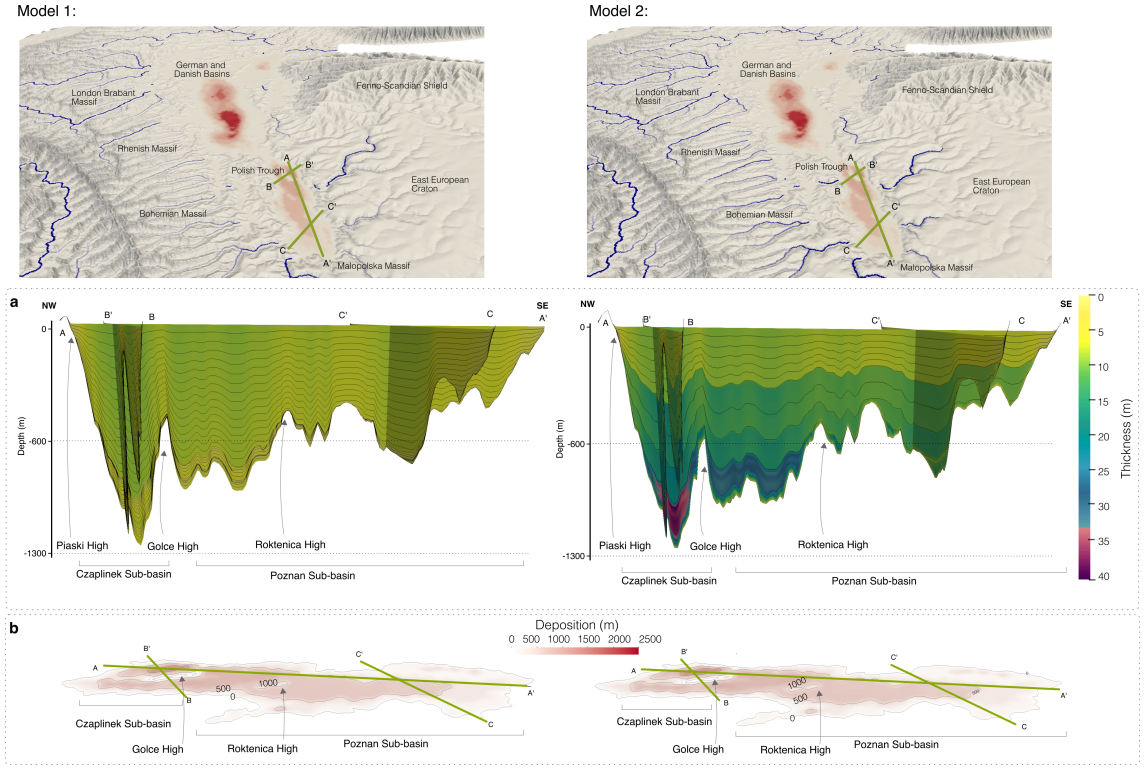

Figure 8: **Cross sections of the Polish Basin with black lines marking a 1 Ma time step.** The map above shows the location of the three representative cross-sections A-A', B-B' and C-C'. In red shades, the figure indicates the simulated thickness of sediments deposited in the Polish Trough along with the North German Basin (not studied in this manuscript). **a.** In this panel, the varying colors illustrate the thickness of sediments deposited over each 100,000-year time step. Yellow shades represent sediment thickness not exceeding 10 m, while the green to purple tones represent thickness greater than 10 m. The sedimentation over a 1 million year can be calculated by adding the thickness between two contour lines.

In model 5, the under-filled basin recorded the largest sediment volumes derived from the East European Craton. This model indicates the Carpathian Massifs as the most significant source of sediment in the basin. We suggest that this outcome relates to the pronounced elevations of the Wolsztyn High in this model (Fig. 5), effectively separating the Fore-Sudeic basin from the Polish Basin. The Fore-Sudeic basins then acts as a sediment trap for material coming from the Bohemian Massif. Furthermore, one could suggest as well that such outcome is a response of the initial paleotopography (in combination with model 5 parameters), which lacks smaller scale details (small wave-length topography), reflecting on how the catchments are distributed with time, with an effect on the sediment provenance.

Model 5 features higher erodibility, and larger subsidence rates applied to the Variscan Mountains. As a result, the final landscape in model 5 seldom reaches elevations above 1 km, and remains fully marine since around 270 Ma, which is incongruent considering Dusséaux et al. (2021) simulations, as well as what has been observed in regards to the depositional environment evolution (Geißler et al. 2008).

5.2 Comparison between subsidence scenarios

The two best fitting models, models 1 and 2, yield similar final sediment volumes and remain similar in their setup parameters with the only exception being the subsidence rate through time. To compare the subsidence regimes, we extract the architecture of the sediment deposits in the basin. We acknowledge the limitations of correlating lithostratigraphic units interpreted from sequence stratigraphy data for the Polish Trough (Pharaoh et al. 2010; Kiersnowski 2013) with its chronostratigraphic units generated from the LEM, such as heterogeneity of sedimentary facies, diachronism of lithological boundaries and the discontinuity of continental deposition. The lithostratigraphic units may be diachronous and thus not perfectly equivalent to chronostratigraphic unis of constant time.

When compared to interpreted sequence stratigraphy/lithostratigraphy, (Wees et al. 2000; Bachmann et al. 2008b; Kiersnowski 2013), we find that model 2 better captures the evolution of the sedimentary layers of the Polish Basin (Figs. 7 and 8). Specifically, it reproduces the proposed hiatus observed in the basin architecture, between 284 - 263 Ma (Hug and Gaupp 2006; Kiersnowski and Buniak 2006; Pharaoh et al. 2010). This hiatus is an important feature of the sedimentary record interpreted in other studies (Pharaoh et al. 2010; Kiersnowski 2013). Additionally, the volume of sediment deposited per time step in model 2 is consistent with rates observed in the North East German Basin, which are generally around to 1,600 km^3/Myr (see section 2.6, Scheck and Bayer 1999).

Likewise, vertical accumulation rates also vary significantly between the two best fitting models 1 and 2 (Fig. 8). For instance, the Kórnik Formation (Müritz Subgroup), which spans from 290 to 266 Ma, shows distinct patters. In model 1, it reaches 600 m in thickness, followed by 100 m of Lower Drawa Formation and 200-300 m of Upper Drawa Formation. In model 2, however, the Kórnik Formation is barely represented, with only 10 meters of thickness. Model 2 exhibits a more balanced deposition: 300 m for Lower Drawa Formation, 400 m of Upper Drawa Formation, followed by 400 m and 150 m of Lower and Upper Notec Formations, respectively (Figs. 3 and 10).

While neither models perfectly match the sediment thickness distributions described by Pharaoh et al. (2010), model 2, accounting for a more constrained regional tectonic evolution, provides a better fit. It effectively captures the low subsidence rates and deposition hiatus of the Kórnik Formation. The sediment thickness for the subsequent units, although not exact, are more consistent with published data (Pharaoh et al. 2010, Fig. 9).

The vertical distribution of sediments in the basin (as shown in cross-section, Figs. 8 and 10) is strongly impacted by the different subsidence rates. While model 1 has deposition rates between 20 to 52 m/Myr, model 2 shows variable sedimentation rates, reaching up to 300 m/Myr. When compared to sedimentation rate values from (Bachmann et al. 2008b, Fig. 1), we note that model 2 shares similar orders of magnitude for those rates. These sedimentation rates are evident in the cross-sections shown in Fig. 8, which better correlate with the chronostratigraphy of the basin. In model 2, the thickness of the Lower Drawa Formation is slightly thinner than that interpreted from seismic data (Fig. 10), while the Upper Drawa Formation is thicker than predicted. However, the thicknesses of the Lower and Upper Notec Formations in model 2 are consistent with those reported in the literature.

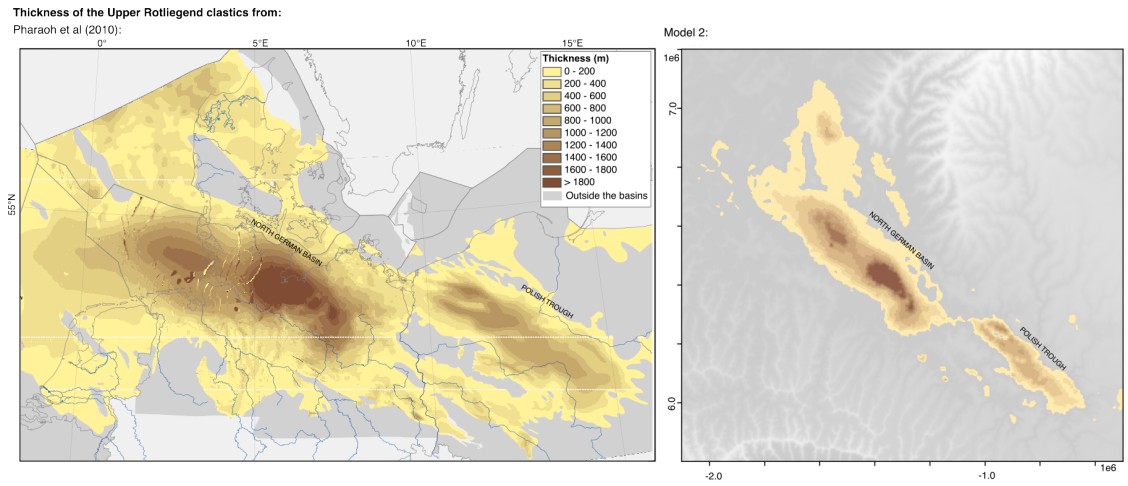

Figure 9: **Thickness of the Upper Rotliegend clastics.** On the left is the sediment thickness map from Pharaoh et al. (2010), which guided the subsidence conditions of the basin in our model. On the right is the final thickness map from Model 2 for the same Upper Rotliegend clastics. Overall, the maps display similar large-scale thickness patterns, demonstrating good agreement with the literature dataset. Both figures share the same color bar but are projected in different datum. The figure from Model 2 is rotated to match the plate configuration at the time of simulation, and the map from Pharaoh et al. 2010 represents the paleothickness using present day coordinates.

5.3 Basin Evolution

5.3.1 Deposition history

At the beginning of the simulation (285 Ma), the basin is nearly flat, with an elevation of around 500 m. By 280 Ma, model 1 shows the formation of a depocenter

in the Polish Trough, with elevations dropping to 0 - 100 m, a product of the constant subsidence rates. In model 2, elevations remain around 400 - 500 m, reflecting low initial subsidence rates. Both models show similar drainage patterns supplying sediments to the basin, however in model 1 subsidence begins to confine sediment deposition into the basin, whereas in model 2, sediments take longer to start accumulating in the Polish Trough (Supplementary figure S3 and additional figures in the Zenodo repository, Hadler Boggiani (2024)).

At 275 Ma, the Polish Trough in model 1 has subsided to elevations between 0 - 100 meters. In model 2, river valleys have been incised, but there is still limited accommodation space for sediments deposition. The drainage patters are similar in both models (Supplementary figure S3).

From 275 to 265 Ma, continued subsidence and sediment deposition in model 1 result in an overfilled and generally flat basin, with a complex upstream drainage system feeding the depocenter. In model 2, river-incised patterns develop more quickly. However, by 265 Ma, subsidence peaks, and the basin sinks slightly below global sea level for about 4 million years (Supplementary figure S3). Between 260 Ma and the end of the simulation (256 Ma), both models show similar elevations and drainage systems (Supplementary figure S3).

Regarding depositional environments, model 1 exhibits a linear progression, with the basin steadily lowering and transitioning from alluvial fan deposits to more fluvial or lacustrine environments (Geißler et al. 2008). By 267 Ma, as the basin fills and the climate dries, the deposition of sediments in playa lakes become more common (Glennie (1995), Figs. 10 and S3).

In contrast, model 2 starts with a basin that remains at moderate elevations, potentially undergoing a phase of autophagy (autogenic erosion), where it reworks its own sediments. Alluvial and fluvial deposits dominate until 265 Ma, after which subsidence drops the basin below sea level, forming a hydrologically closed, endorheic basin (Geißler et al. 2008; Kiersnowski et al. 2010). Lacustrine deposits likely follow, transitioning into playa lakes as the climate continues to dry (McCann 1998a; Kiersnowski et al. 2010). Toward the end of the simulation, the basin becomes overfilled, with a balance between sedimentation and erosion (Figs. 10 and S3).

5.3.2 Provenance data interpreted

We have outlined the primary sediment provenance regions for the Southern Permian Basin. The Upper Rotliegend stage in the Polish basin shows a significant contribution of sediments from aeolian transport (Kiersnowski 2013). However, sediments of alluvial and fluvial origins are primarily sourced from the southwestern highlands (Variscides - Bohemian Massif), the northeast (Pre-Cambrian Platform and basin margin) and east (Małopolska Massif) (Fig. 5 and 11).

Our results indicate that different initial tectonic forcings affect the main sediment source to the basin. The Bohemian Massif is the dominant source in models 1, 2, 3, 4 and 6, while the Carpathian Massifs becomes the main source in model 5.

Despite variations in the tectonic settings across models, we find that the main sediment source areas remain consistent over time in models 1 and 2. The key

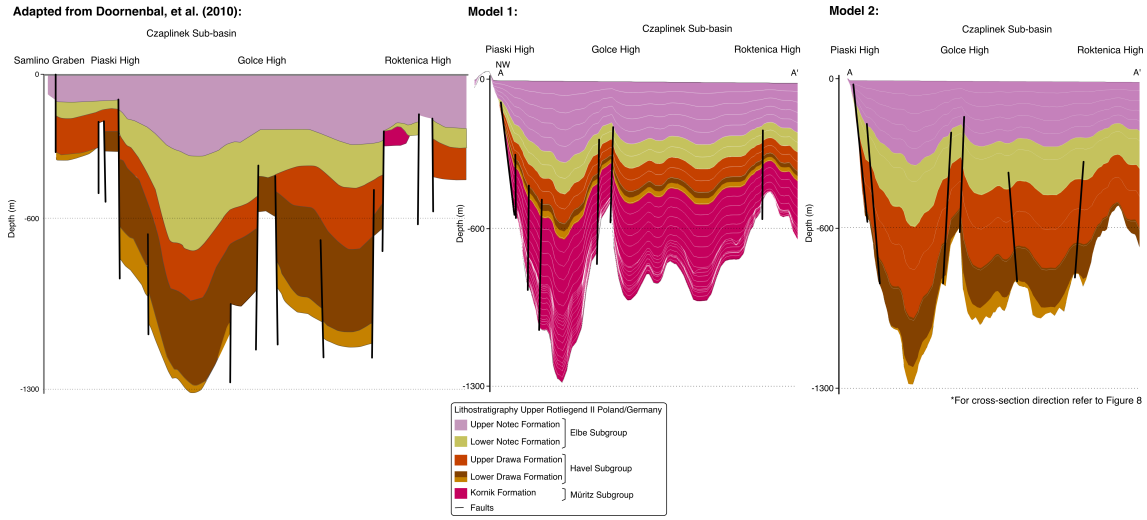

Figure 10: **Comparison between A-A' cross-sections for both modeling scenarios, showing different stratigraphic units from the Upper Rotliegend sediments based on Pharaoh et al. (2010)**. The cross-sections in this figure are aligned with the same direction as those shown in Fig. 8. The comparison includes the modeled sediment distribution from models 1 and 2, highlighting differences in sediment thickness and stratigraphy. The figure also shows the corresponding cross-section from Doornenbal and Stevenson (2010), providing a validation of the modeled stratigraphy against observed data.

sources, in order of significance are from the Bohemian Massif, the Carpathian Massifs, the Fenno-Scandian Shield, the East European Craton and the Małopolska Massif (Fig. 6).

Our interpretation of sediment provenance is consistent with several key sources identified in the literature, including the East European Craton, Małopolska Massif, and Bohemian Massif (McCann (1998b), Kiersnowski and Buniak (2006), Doornenbal and Stevenson (2010), and Mazur et al. (2010)). Additionally, our findings highlight the importance of previously unconsidered source areas for the Polish basin, such as the Fenno-Scandian Shield and the Carphatian Massifs, which together account for approximately 50% of the sediments supplied to the basin over time. We reinforce that one novelty in this study is in providing volumetric constraints for provenance analysis, taking into account the entire tectonic and climatic evolution of the sediments that are deposited in the Polish Trough, enabling future discussions in terms of ore content in the basin.

It is important to note that some sediments are eroded from the basin throughout its evolution, as observed in models 1, 2, 3, 4 and 6, possibly due to limited accommodation space or infilling process. For an overfilled basin, sediments bypass or erode as excess material is transported out of the system. This erosion likely facilitated the re-transportation of sediments from the Fenno-Scandian Shield and Carphatian Massifs outside of the Polish Basin area.

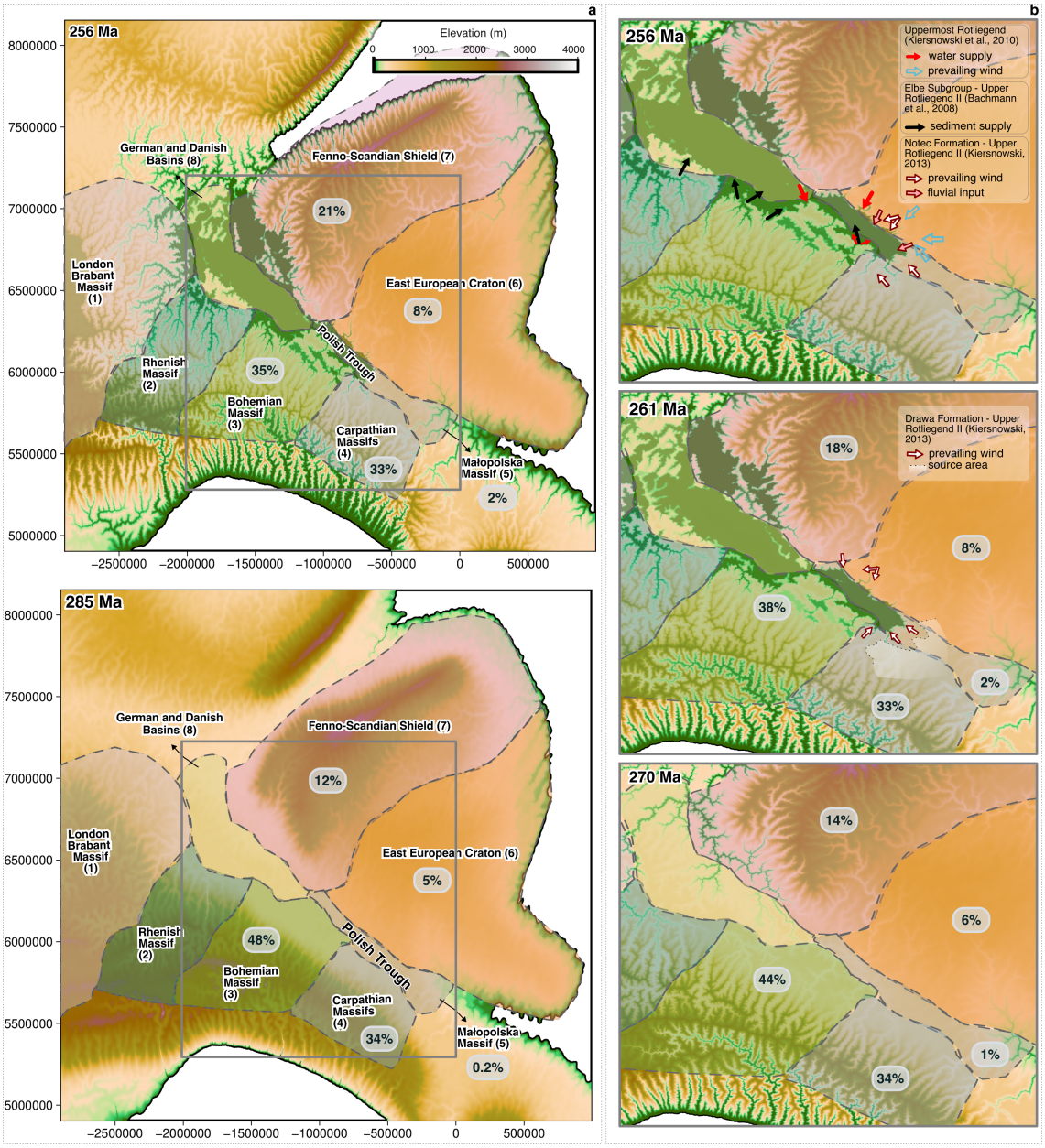

Figure 11: **Provenance areas described by the model and in the literature. a.** The first and last time step of the simulation are shown, with the percentage of sediments eroded from each source that ended up in the Polish Basin. **b.** Inside the white-shaded polygon, the arrows refer to the main provenance areas as mapped in the literature by (Bachmann et al. 2008b; Kiersnowski et al. 2010; Kiersnowski 2013) for their respective period. For the time step at 270 Ma, no corresponding data was available for comparison. The percentages shown represent values from model 1, but differences between models are not emphasized here.

5.4 Polish Rotliegend potential as the main copper source for the Kupferschiefer layer

This section aims to provide a broad preliminary estimate for the Rotliegend stage red beds to act as the main copper source for the overlying sediment-hosted copper systems and demonstrate how landscape evolution modeling can assist targeting new exploration fronts. The results presented above quantify the volume of sediments removed from all provenance areas, thus providing a valuable tool for estimating the potential mass of copper delivered within oxidized red bed sediments. Although low concentrations, these large volume red bed sediments could supply copper to the overlying Kupferschiefer ore shale.

The Kupferschiefer shale, deposited during the Barents Sea transgression (Pharaoh et al. 2010), lies above the red beds of the Upper Rotliegend II stage. Despite the Kupferschiefer shale hosting some of the largest sedimentary-hosted copper deposits globally, the original source of the copper to the reductant layer remains uncertain.

The most accepted theory is that large volumes of low-grade copper red bed sediments are deposited in the early rift strata (Hitzman 2000; Hitzman et al. 2010). The protolith for such sediments are likely acidic volcanics and igneous rocks originated in rifting systems or subduction zones (Sillitoe 2010). The main hypotheses for the transport of the metalliferous brines from the red beds to the reductant trap (Kupferschiefer shale) are: (i) syn-sedimentary metallogeny in an euxinic environment, and (ii) epigenetic mineralization from ascending metalliferous fluids through the Rote Faule (Borg et al. 2012).

Here we identify protolith lithologies in the basin provenance areas that likely contained elevated (although still very sub-economic) copper during the basin formation such as mafic composition basement rocks and igneous complexes. Considering that these lithologies were part of the catchment areas feeding the Polish Trough, with some assumptions on approximate original copper concentrations we can assess their potential as copper sources for the Upper Rotliegend red beds.

Prior to the basin formation, two significant periods of convergent tectonics and subsidence occurred. The first phase involved the collision of Baltica and Laurentia plates during the Early Devonian, forming the Caledonides (Caledonian Orogeny) in an east-west oriented subduction zone (Pharaoh et al. 2010). The second phase, during the Carboniferous to Permian, involved the nearly north-south convergence of Baltica and Gondwana along with the collision of Avalonia, which led to the formation of the Variscan Orogen/Belt. This collision altered the tectonic regime, resulting in a transform plate boundary (Rey et al. 2001; Pharaoh et al. 2010).

The shear created by this tectonic regime shift opened pathways for magma intrusions and volcanic rock extrusions (Borg et al. 2012). These mafic volcanics are suggested to be a significant copper-bearing protolith. Their erosion and deposition in an arid or desert environment (Upper Rotliegend I and II) may create oxidized conditions which can later support metal leaching with circulation of hot brines (Jowett 1986).

Using the paleo-lithology map (Fig. 11), we estimate sediment volumes from copper-bearing source rock provenance areas for the two best-fit models (1 and 2). We iden-

tify five primary provenance domains with copper potential: Fennoscandia, Eastern European Craton/Baltic-Lublin Igneous Province, Bohemian Massif, Rhenish Massif, and Carpathian Massifs. Together, these regions contribute 55–62% of sediments in the Polish red beds, equivalent to $10,000$ to $10,300$ km^3. The Bohemian Massif is the largest contributor, supplying up to 45% of sediments between 285 - 274 Ma, while the Rhenish Massif contributes none. Fennoscandia, followed by the Baltic-Lublin Igneous Province, accounts for up to 10%, and the Carpathian Massifs represents contributing around 2%.

Within these domains, polygons were assigned copper potential based on their composition and assumption that certain lithologies may have elevated low-concentration copper potential (mafic rocks with elevated amphibole and pyroxene copper content, magmatic arc intermediate composition igneous rock with porphyry copper system potential - see 6, Table S1). We assume the highest copper concentrations are found in mafic rocks of the Baltic-Lublin Igneous Province and the Bohemian Massif, with sediment volumes ranging from $1,000$ and $1,031$ km^3 (Fig. 12). Considering the modeled porosity of sediments within the Polish Trough, a final sediment volume between 550 and 567 km^3 is estimated. Assuming that lithologies such as basalts, gabbros, granitoids and syenites - mapped as high significance copper sources - have concentrations ranging from 0.01 to 0.03 % (100 to 300 ppm) (Alexander and Thomas 2011; Naldrett 2013; Gill and Fitton 2022), we estimate final copper volumes between 8.91 to 26.7 km^3 which equates to 51 to 153 MT of copper in the basin.

Cathles III et al. (1993) presents a simplified volume estimate of 5,760 km^3 for Rotliegend red beds (Lubin Basin), with a total estimated copper content of 350 MT based on copper grades in composite samples. Estimates of remobilized copper into the Kupferschiefer shale range from 165 to 230 MT (Cathles III et al. 1993; Oszczepalski et al. 2019), suggesting that the Upper Rotliegend red beds could provide sufficient copper to the Kupferschiefer shale (Hitzman et al. 2005).

We note that the initial volume estimation by Cathles III et al. (1993) is four times smaller than that predicted using goSPL. Yet, their copper estimations are nearly twice as high as those calculated for the high-significance copper sources presented here. Since the purpose of this manuscript is to introduce a new methodology rather than characterize a deposit, we do not include tonnage calculations for medium copper potential sediments. However, it is important to mention that these sediments represent 50% more volume than the high copper potential (Fig. 12). Despite their lower copper concentrations, their increased volume suggests they could be a significative copper source for the Kupferschiefer layer.

While the Upper Rotliegend red beds may represent a major contributor of copper to the Kupferschiefer shale, they alone seem insufficient. Apart from considering the copper transported from surroundings areas into the Polish Trough, we need to consider as well the vertical transport of copper from the thick volcanic-rock layers (over 1500 m thick) that are present in the Lower Rotliegend stage, as well as smaller interfingered volcanics in portions of the Upper Rotliegend stage. Although goSPL is limited to modeling sediment deposition decurrent from erosion, we know there is occurrence of volcanic rocks in portions of the basin (Fig. 2). Therefore, to estimate the ultimate expelled copper potential of these beds, one need to take into account

the copper leached from these volcanic layers to the Upper Rotliegend red beds. Nonetheless, we show here that high copper significance sediments deposited in the Polish Trough are likely to be providing more than half of the copper that is today observed in the Kupferschiefer shale.

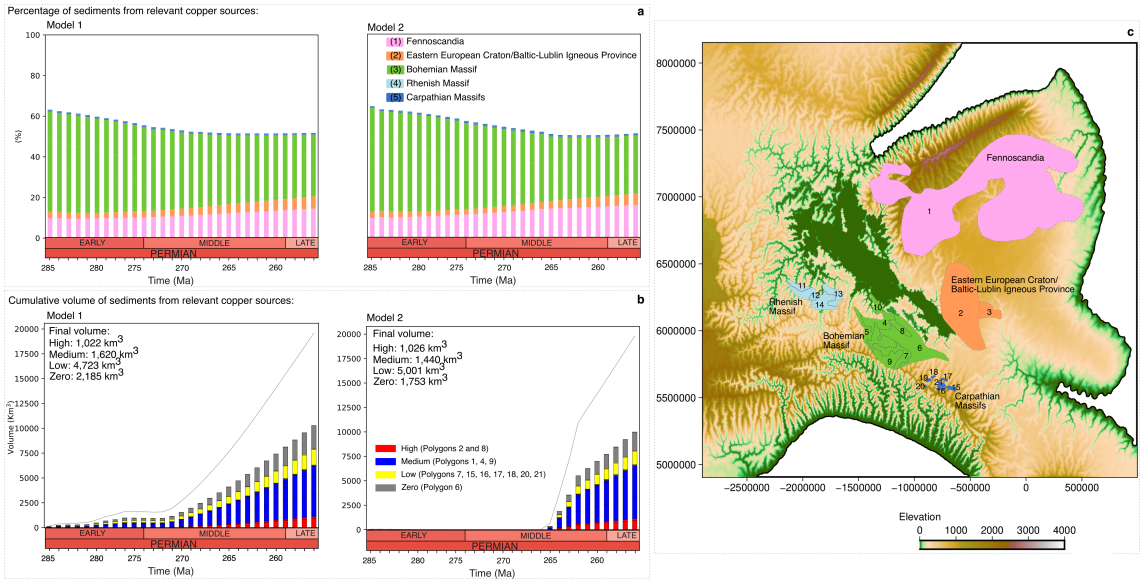

Figure 12: **Paleolithology map with relevant regions were possible copper sources could be tracked before the Permian**. **a.** The percentage of sediment transported into the Polish Trough, considering only the lithological polygons mapped **b.** The volume of sediments divided by the significance of copper content within each source region. **c.** Paleolithology map with the location of possible copper sources that existed prior to the deposition of the Upper Rotliegend red beds

6 Conclusions

We modeled the evolution of the Southern Permian Basin during the deposition of the Upper Rotliegend stage red beds, calculating sediment volumes and provenance in the Polish Trough under six modeling scenarios. These models combined varying tectonic forcing settings, precipitation regimes, and two subsidence forcing (*i.e.* constant subsidence and subsidence reflecting the basin main sedimentary cycles). The resulting sediment volumes for the models ranged from approximately $9,000$ km^3 to $20,000$ km^3. The best fitting scenario, model 2, with variable subsidence rate, yielded an accumulation of $19,800$ km^3 of sediment.

Our models confirmed previously proposed sediment provenance areas, including the Małopolska Massif, Bohemian Massif and the East European Craton, while also identifying two additional significant sources: the Carpathian Massifs and the Fenno-Scandian Shield. By the end of our simulation, sediment contributions for model 2 were as follow: Bohemian Massif (35%), Carpathian Massifs (33%), Fenno-Scandian Shield (21%), East European Craton (8%) and the Małopolska Massif (2%).

The landscape evolution for model 2 reproduces the migration to an arid climate, characterized by early alluvial fans and fluvial deposits transitioning to lacustrine or playa-lake deposits, and culminating in a nearly flat, overfilled basin.

The simulations produced with goSPL are valuable for improving the accuracy of volume calculations throughout a basin's evolution. They also enable the estimation of the effects of different tectonic and climatic scenarios to help constrain the subsidence history of a basin. We emphasize that our methodology can be broadly applied to other sediment-hosted ore systems with similar sourcing of metals from clastic sedimentary rocks, providing insights into sediment provenance and future resource discovery potential.

SUP. A: Model evolution figures

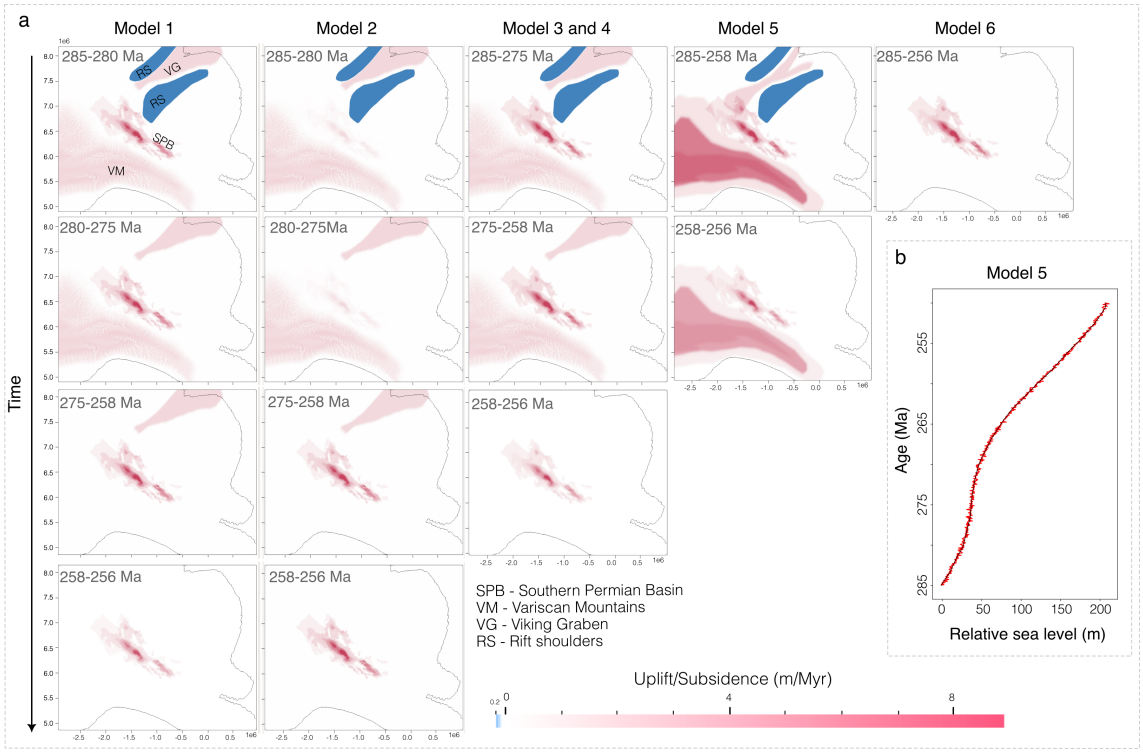

Figure S1: **Tectonic conditions for modeled scenarios**. **a**. The frames show the evolution of the forcing conditions for all the modeled scenarios, where blue represents uplift rates applied to rift shoulders (RS) of the Viking Graben (VG), and the red shades are subsidence rates applied to the Viking Graben (VG), the Variscan Mountains (VM) and the Southern Permian Basin (SPB) **b**. is the sea level curve applied in model 5, based on (Smith 1979), where the sea level change during the simulation time is of 200 meters.

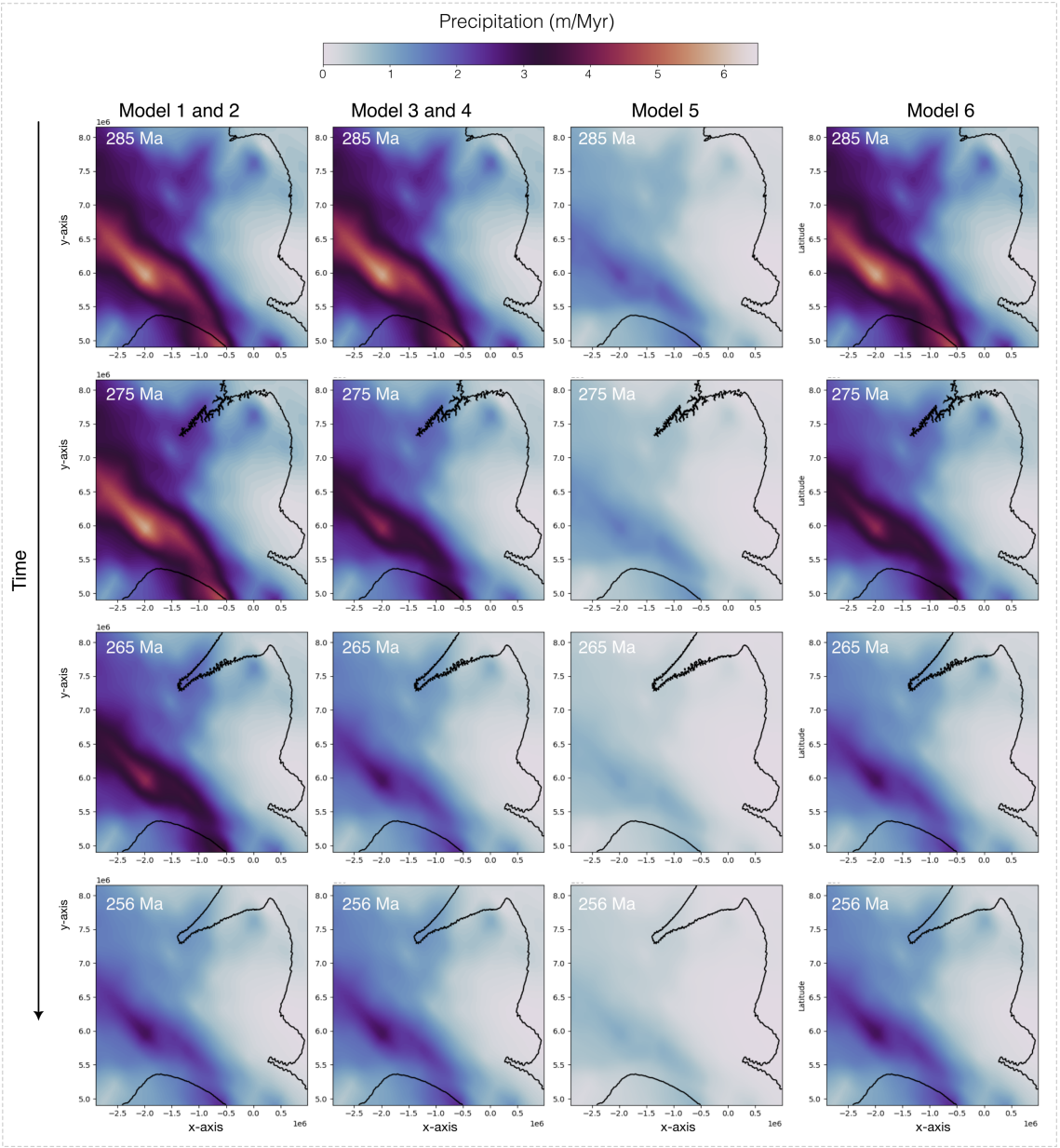

Figure S2: **Forcing climate conditions for modeled scenarios**. The frames represent the changing conditions in precipitation over time, characterizing an increasingly arid environment. We note that model 5 has the lowest precipitation values, while models 1 and 2 have the higher values with increased precipitation where the Variscan Mountains are located (bright orange/yellow shades).

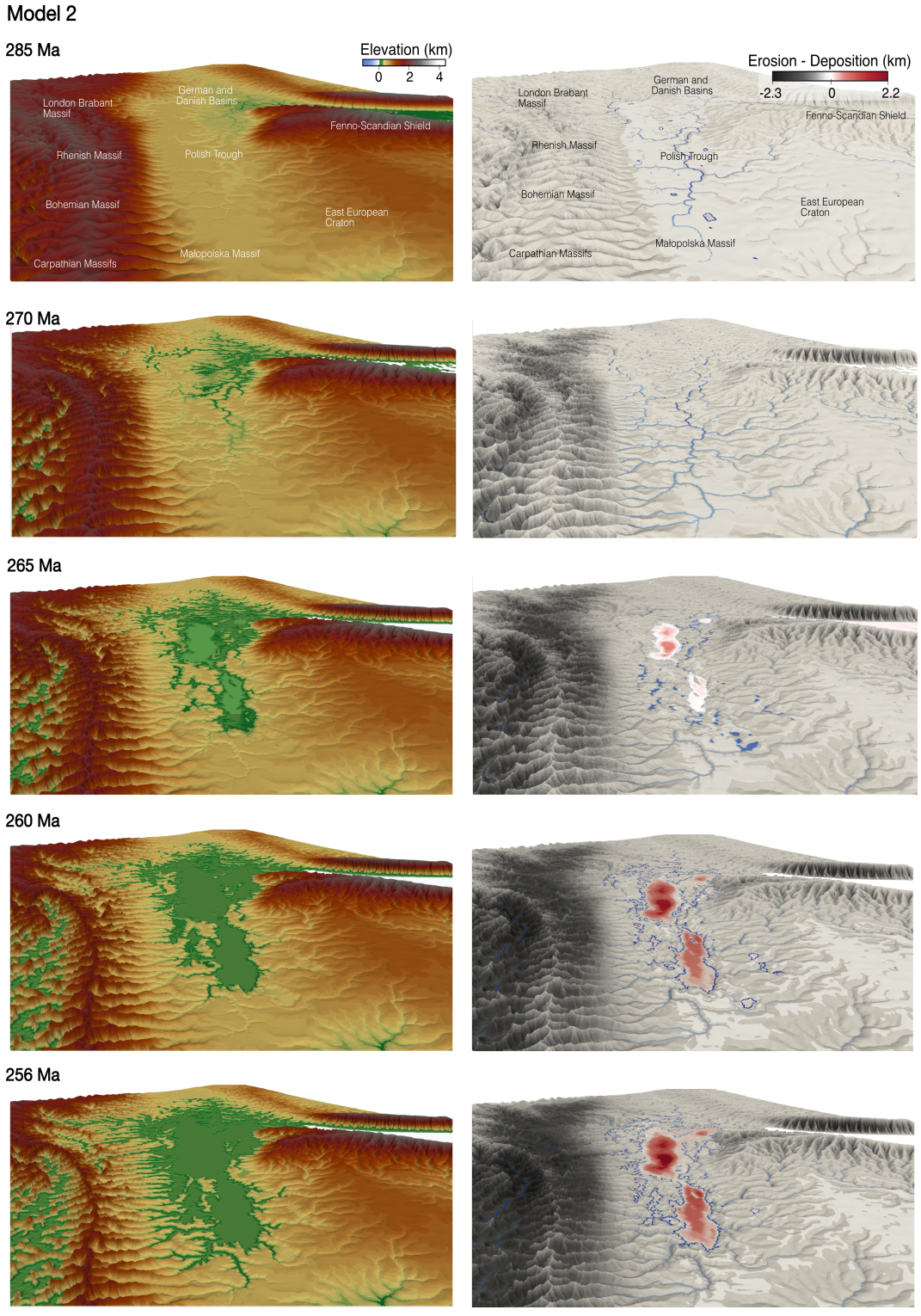

Figure S3: **Evolution over time for model 2, which represents the best fitting model**. To the left we represent changes in elevation, and to the frames on the right show the accumulated deposition (in red) and erosion (in shades of black).

SUP. B: Model calibration and validation parameters

Calibration points:

Parameter	Model 1	Model 2	Model 3	Model 4	Model 5	Model 6
Erodibility	$\epsilon = 8.0\ e^{-8}$	$\epsilon = 8.0\ e^{-8}$	$\epsilon = 7.0\ e^{-8}$	$\epsilon = 8.0\ e^{-8}$	$\epsilon = 7.0\ e^{-8}$	$\epsilon = 7.0\ e^{-8}$
Sea level curve	Sea level balanced by subsidence of the Viking Graben				While Smith (1979) reports sea level variations between 250 and 300 m, we impose a conservative estimate of 200 m	No changes, sea level is at zero, thus testing a simplified scenario
Subsidence rate changes *see section 2.2 and 2.6*	A constant subsidence rate was applied to evaluate the varying conditions in the surroundings of the Polish Trough.	Variable subsidence rates were imposed following the basin evolution history in Scheck and Bayer (1999).	A constant subsidence rate was applied to evaluate the varying conditions in the surroundings of the Polish Trough.			
Paleo-elevation *The time span of the Variscan collapse is poorly constrained in the literature, so we tested different scenarios (see section 2.2)*	Different timings of the Variscan Mountains orogenic collapse and associated subsidence rates were tested to mimic this event, while the Viking Graben rifting was also incorporated into the calibration				Imposed subsidence to replicate geological events (*e.g.*, Variscan orogenic collapse) and forced marine incursions through Viking Graben subsidence and rising sea level.	Considers original paleo-elevation
Paleo-precipitation *see section 2.3*	Adjusted paleo-precipitation to account for orographic effects and variations in rainfall					Considers original paleo-precipitation
Basin architecture *see Figure 8*	The architecture of the modeled cross-sections is consistent with that described in the published literature	Not evaluated				

Figure S4: **The table summarizes the main parameters assessed during the calibration of each model.** Model 6 represents the initial test of this process, followed by Models 5, 4, 3, and 1, with Model 2 developed as the final scenario.

Validation points: NGB - North German Basin; PT - Polish Trough; SPB - Southern Permian Basin

Parameter	Vaildation value	Model 1	Model 2	Model 3	Model 4	Model 5	Model 6
Subsidence rates *see section 2.2 and 2.6*	5 main phases NGB: 130 - 50 m/Myr PT: 130 - 15 Myr	Constant at 45 m/Myr	10 m/Myr 150 m/Myr 110 m/Myr 60 m/Myr 175 m/Myr	Constant at 45 m/Myr	Constant at 45 m/Myr	Constant at 45 m/Myr	Constant at 45 m/Myr
Erosion and deposition rate *see section 4.3*	NGB: 0 - 200 - 300 m/Myr; PT: 10 - 0 - 210 m/ Myr	20–52 m/Myr, smaller than values reported by Bachmann et al. (2008a).	0 - 300 m/Myr, of similar order of magnitude to Bachmann et al. (2008a)	Not evaluated	Not evaluated	Not evaluated	Not evaluated
Paleo-elevation evolution *see section 5.1*	See section 2.2	Surrounding topography provides a valid scenario, however the basin subsidence is not representative of basin evolution	SPB sinks below sea level with considered induced subsidence	Adjusted to test varying erodibility values and tectonic forcing conditions	Adjusted to test varying erodibility values and tectonic forcing conditions	The model incorporates the largest subsidence in the Variscan Mountains; however, despite low precipitation and erodibility, it produces very low relief in the surroundings and an underfilled basin.	None, considers initial paleo-geographhy
Depth of basin/ Sediment thickness *see section 2.4*	1300 m in the Polish Trough see section 2.4	Reaches close to 1300 m	Reaches close to 1300 m	Not evaluated	Not evaluated	Not evaluated	Not evaluated
Sediment volume *Poorly constrained in the literature, see section 2.6*	NGB: 1,700 km^3	Maximum 1,400 km^3, otherwise lower	Maximum 4,000 km^3, otherwise varying between 1,500 - 1,700 km^3	Maximum 1,400 km^3, otherwise lower	Maximum 1,400 km^3, otherwise lower	Maximum 600 km^3	Maximum 1,400 km^3, otherwise lower
Chronostratigraphic sequence *see section 2.4*	See section 2.4 and Fig. 7.25 from Pharao et al, (2010)	The Kornik Formation shows unrealistic thickness when cross-sections are assessed according to published data	Lithostratigraphic thicknesses match published values	Not evaluated	Not evaluated	Not evaluated	Not evaluated
Saalian Unconformity *see section 2.3*	20 Myr hiatus, see section 2.3	Hiatus observed, but its timing and duration do not match published data	Hiatus can be observed with a 19 Myr no deposition	Hiatus observed, but its timing and duration do not match published data	Hiatus observed, but its timing and duration do not match published data	Not observed, constant sedimentation	Not observed, constant sedimentation

Figure S5: **The table presents the main validation points used to constrain the best-fitting scenario after the calibration process.**We emphasize that, to the best of our knowledge, all available data were incorporated into the validation of the presented scenarios. However, values such as erosion and sedimentation rates, final sediment volume, and sediment volume through time remain poorly constrained in the literature, and are in some cases unavailable.

SUP. C: Copper Sources

Table S1: **Summary of lithologies mapped as possible copper sources to the Polish Basin. Were given copper grades/estimations only for regions with high chances of copper prospectivity, since the intent of this publication is not to attempt on calculating copper reserves, but to show the applicability of the software**. For "Map ID" location, please refer to Fig. 12. For literature references, please refer to: Alexander and Thomas (2011), Járóka et al. (2021), Villaseñor et al. (2021), Barros et al. (2020), Poprawa (2019), Nádaskay et al. (2019), Gill and Fitton (2022), Kraft et al. (2023), and Járóka et al. (2023)

Map ID	Location	Age	Lihology	Cu Significance	Cu Grade	Rock history	References
1	Fennoscandia - Western East European Craton	Mesoproterozoic/ Paleoproterozoic	Anorogenic and sin/post/late orogenic intrusions - schists and volcanics, granulites, granites, migmatites.	Low	-	Old collisional setting	Lahtinen (2012), Poprawa (2019), Alexander and Thomas (2011)
2	Fennoscandia - South Western/Baltic Basin/Baltic Sea	Lower Carboniferous (Mississipain)	Lublin Baltic Mississippian Igneous Province (LBMIP) - flood basalts, gabbro and syenites	High	0.05% Cu (Deccan Basalts) - high end	Igneous province	Poprawa (2019)
3	Fennoscandia - South Western/Baltic Basin/Baltic Sea	Lower Carboniferous (Mississipain)	Lublin Baltic Mississippian Igneous Province (LBMIP) - geophysical anomalies - no proven lithology	Low	-	Igneous province	Poprawa (2019)
4	Bohemian Massif - Saxo - Thuringian Zone	Neoproterozoic to Lower Paleozoic	Volcano sedimentary units (tiilites, sandstones/quartzites, iron ore horizons), low grade to unmetamorphosed	Low	-	Cadomian history. Sediments deposited in shallow marine facies, higher altitudes/cold climate (tiilite)	Nádaskay et al. (2019), Kraft et al. (2023)
5, 6, 10	Bohemian Massif	-	Sediments - Cretaceous basin	Zero	-	-	Nádaskay et al. (2019), Kraft et al. (2023)
7	Bohemian Massif - Moldanubian Zone/ Complex	Neoproterozoic to Early Paleozoic	Metamorphic rocks - metasedimentary/metavolcanic, granulite bodies. Ultrapotassic melasyenites.	Medium	-	Exhumed high grade orogenic root. High grade rocks for heavy minerals	Jaroka et al. (2021), Jaroka et al. (2023), Kraft et al. (2023)
8	Bohemian Massif - Lausitz Block	Middle Devonian to Early Carboniferous	Mafic-ultramafic/Gabbroic rocks. Cadomian granodiorites (moderate alkaline basaltic parental magmas with high volatile content)	High	0.01% to 0.3% (100 to 3,000 ppm)	Magmatic sulfide, accumulation in a sub-vertical gabbroic dike. Late stage hydrothermal overprint	Naldrett et al., (2013) Gill et al. (2011), Jaroka et al. (2021), Jaroka et al. (2023)
9	Bohemian Massif - Central Bohemian Plutonic Complex/ Moldanubian batolith/ Bavarian Forest granitoids	Carboniferous	Granites and associated migmatites - Variscan igneous rocks	Low	-	Syn-colisional/arc related; syn to post-colisional; post-colisional	Jaroka et al. (2021), Jaroka et al. (2023), Kraft et al. (2023)
11-13	Rhenish Massif	Lower Carboniferous	Black-shale/Basic volcanic. Basalts - Marsberg copper,clastic, chemoclastic, volcanoclastic and chemical sediments	Medium	-	Deposited in the vicinity of submarine exhalative volcanic centers. Quiet marine, temporary anoxic. Small scale deposits (Cu, Au, Barite, Ag, Pb, Zn)	Barros et al. (2020)
14	Rhenish Massif	Upper Devonian	Clayshales, Siltstones, Sandstones, Carbonate	Medium	-		Barros et al. (2020)
15	Western Carpatians	Devonian to Carboniferous	Acid intermediate volcanics, gabbrodiorite, metabasalt	Medium	-		Villaseñor et al. (2021)
16	Western Carpatians	Devonian to Permian	Granite - Granidoirite, Granitoids, Micaschist, two mica granite	Medium	-		Villaseñor et al. (2021)
17-21	Carpatians	Meso-Variscan	S and I granitoids	Medium	-		Ondrejka et al. (2021)

Open Research Section

Code Data Availability: The scientific software used in this study, *goSPL* (Salles et al. 2020), is available from `https://github.com/Geodels/gospl` and the software documentation can be found at `https://gospl.readthedocs.io`. We also provide a series of Jupyter notebooks used for processing the data sets and model outputs that can be followed to reproduce some of the figures presented in the paper and can be accessed from `https://doi.org/10.5281/zenodo.17118081` (Hadler Boggiani 2025).

Video Supplements: The animated gifs from all the six simulations representing the evolution of elevation, erosion/deposition, sediment flux and water flow can be seen in the repository `https://doi.org/10.5281/zenodo.14126216` (Hadler Boggiani 2024).

Author Contribution: B.H.B conceived the study and conducted the numerical experiments, B.H.B., T.S. & C.M. analyzed the sediment provenance. B.H.B wrote the initial draft, and all co-authors reviewed the manuscript.

Competing Interests: The authors declare no competing interests.

Acknowledgments: This work was undertaken through STELLAR (Spatio-temporal exploration for resources) industry collaboration supported by BHP. This research was undertaken with the assistance of resources from the National Computational Infrastructure (NCI), which is supported by the Australian Government and from Artemis HPC Grand Challenge supported by Sydney Informatics Hub at the University of Sydney.

References

Alexander, P. O. and H. Thomas (2011). "Copper in Deccan basalts (India): review of the abundance and patterns of distribution". In: *Boletín del Instituto de Fisiografía y Geología*. DOI: ISSN1666-115X.

Awdankiewicz, M., M. Pańczyk, I. Ploch, P. Raczyński, H. Awdankiewicz, A. Górecka-Nowak, W. Pawlak, and T. Peryt (2025). "Timing of post-orogenic silicic volcanism in the eastern part of the European Variscides: constraints from SHRIMP U–Pb zircon study of the Permo-Carboniferous Góry Suche Rhyolitic Tuffs (the Intra-Sudetic Basin)". In: *International Journal of Earth Sciences* 114.1, pp. 75–98. DOI: 10.1007/s00531-024-02474-y.

Bachmann, G. H., B.-C. Ehling, R. Eichner, and M. Schwab (2008a). "Geologie von Sachsen-Anhalt". In: *Zeitschrift zur Geschichte des Berg-und Hüttenwesens* 14, pp. 53–55. DOI: ISBN978-3-510-65240-2.

Bachmann, G. and N. Hoffmann (1995). "Formation and development of the North German Rotliegend Basin". In: *Stratigraphy of Germany I; North German Rotliegend Basin—Rotliegend Monograph Part II. Courier Forsch.-Inst. Senckenberg* 183, pp. 156–169.

Bachmann, G., T. Voigt, U. Bayer, H. von Eynatten, B. Legler, and R. Littke (2008b). "Depositional history and sedimentary cycles in the Central European Basin System". In: *Dynamics of Complex Intracontinental Basins: the Example of the Central European Basin System*. Springer, pp. 156–172.

Barros, R., A. Defourny, A. Collignon, P. Jobe, A. Dassargues, K. Piessens, and K. Welkenhuysen (2020). "A review of the geology and origin of CO2 in mineral water springs in east Belgium". en. In: *Geologica Belgica* 24.1-2, pp. 17–31. DOI: 10.20341/gb.2020.023.

Bayer, U., M. Grad, T. Pharaoh, H. Thybo, A. Guterch, D. Banka, J. Lamarche, A. Lassen, B. Lewerenz, M. Scheck, et al. (2002). "The southern margin of the East European Craton: new results from seismic sounding and potential fields between the North Sea and Poland". In: *Tectonophysics* 360.1-4, pp. 301–314. DOI: 10.1016/S0040-1951(02)00359-1.

Benek, R., W. Kramer, T. McCann, M. Scheck, J. Negendank, D. Korich, H.-D. Huebscher, and U. Bayer (1996). "Permo-Carboniferous magmatism of the Northeast German Basin". In: *Tectonophysics* 266.1. Dynamics of Extensional Basins and Inversion Tectonics, pp. 379–404. DOI: https://doi.org/10.1016/S0040-1951(96)00199-0.

Blundell, D., P. Karnkowski, D. Alderton, S. Oszczepalski, and H. Kucha (2003). "Copper mineralization of the Polish Kupferschiefer: a proposed basement fault-fracture system of fluid flow". In: *Economic Geology* 98.7, pp. 1487–1495. DOI: 10.2113/gsecongeo.98.7.1487.

Borg, G., A. Piestrzynski, G. Bachmann, W. Püttmann, S. Walther, and M. Fiedler (2012). "An Overview of the European Kupferschiefer Deposits". In: *Economic Geology Special Publication* 16, pp. 455–486. DOI: 10.5382/SP.16.18.

Cathles III, L., S. Oszczepalski, and C. Jowett (1993). "Mass balance evaluation of the late diagenetic hypothesis for Kupferschiefer Cu mineralization in the Lubin basin of Southwestern Poland". In: *Economic Geology* 88, pp. 948–956. DOI: 10.2113/gsecongeo.88.4.948.

Doornenbal, H. and A. Stevenson (2010). *Petroleum geological atlas of the Southern Permian Basin area*. EAGE.

Dusséaux, C., A. Gébelin, G. Ruffet, and A. Mulch (2021). "Late Carboniferous paleoelevation of the Variscan Belt of Western Europe". en. In: *Earth and Planetary Science Letters* 569, p. 117064. DOI: 10.1016/j.epsl.2021.117064.

Gast, R. (1988). "Rifting im Rotliegenden Niedersachsens". In: *Geowissenschaften (Weinheim, Zeitschrift)* 6.4, pp. 115–122.

Gast, R. and T. Gundlach (2006). "Permian strike slip and extensional tectonics in Lower Saxony, Germany". en. In: *Zeitschrift der Deutschen Gesellschaft für Geowissenschaften* 157.1, pp. 41–55. DOI: 10.1127/1860-1804/2006/0157-0041.

Geißler, M., C. Breitkreuz, and H. Kiersnowski (2008). "Late Paleozoic volcanism in the central part of the Southern Permian Basin (NE Germany, W Poland): facies distribution and volcano-topographic hiati". en. In: *International Journal of Earth Sciences* 97.5, pp. 973–989. DOI: 10.1007/s00531-007-0288-6.

Gill, R. and G. Fitton (2022). *Igneous rocks and processes: a practical guide*. John Wiley & Sons. DOI: ISBN:978-1-119-45568-4.

Glennie, K. W. (1995). "Permian and Triassic rifting in northwest Europe". In: *Geological Society, London, Special Publications* 91.1. Publisher: The Geological Society of London, pp. 1–5. DOI: 10.1144/GSL.SP.1995.091.01.01.

Glennie, K. W. and A. T. Buller (1983). "The Permian Weissliegend of NW Europe: The partial deformation of aeolian dune sands caused by the Zechstein transgression". en. In: *Sedimentary Geology* 35.1, pp. 43–81. DOI: 10.1016/0037-0738(83)90069-6.

Hadler Boggiani, B. (2024). "Polish Rotliegend Basin". In: Publisher: Zenodo. DOI: 10.5281/ZENODO.14126215.

– (2025). *Quantitative provenance analysis from goSPL outputs*. Version goSPL_QuantitativeProvenanceAnalysis. DOI: 10.5281/zenodo.17118081.

Heeremans, M. and J. I. Faleide (2004). "Late Carboniferous-Permian tectonics and magmatic activity in the Skagerrak, Kattegat and the North Sea". en. In: *Geological Society, London, Special Publications* 223.1, pp. 157–176. DOI: 10.1144/GSL.SP.2004.223.01.07.

Heeremans, M., M. J. Timmerman, L. A. Kirstein, and J. I. Faleide (2004). "New constraints on the timing of late Carboniferous-early Permian volcanism in the central North Sea". In: *Geological Society, London, Special Publications* 223.1, pp. 177–193. DOI: 10.1144/GSL.SP.2004.223.01.08.

Hillenbrand, I. W. and M. L. Williams (2022). "Geochemical evidence for diachronous uplift and synchronous collapse of the high elevation Variscan hinterland". In: *Geophysical Research Letters* 49.21, e2022GL100435. DOI: 10.1029/2022GL100435.

Hitzman, Kirkham, Broughton, Thorson, and Selley (2005). "The Sediment-Hosted Stratiform Copper Ore System". In: *One Hundredth Anniversary Volume*. Society of Economic Geologists. DOI: 10.5382/AV100.19.

Hitzman, M. W. (2000). "Source basins for sediment-hosted stratiform Cu deposits: Implications for the structure of the Zambian Copperbelt". In: *Journal of African Earth Sciences* 30.4, pp. 855–863. DOI: 10.1016/S0899-5362(00)00056-7.

Hitzman, Selley, and Bull (2010). "Formation of sedimentary rock-hosted stratiform copper deposits through Earth history". In: *Economic Geology* 105.3, pp. 627–639. DOI: 10.2113/gsecongeo.105.3.627.

Hug, N. and R. Gaupp (2006). "Palaeogeographic reconstruction in red beds by means of genetically related correlation: results from the upper Zechstein (Late Permian)". en. In: *Zeitschrift der Deutschen Gesellschaft für Geowissenschaften*. Publisher: Schweizerbart'sche Verlagsbuchhandlung, pp. 107–120. DOI: 10.1127/1860-1804/2006/0157-0107.

Járóka, T., J. A. Pfänder, T. Seifert, F. Hauff, B. Sperner, S. Staude, T. Stephan, and B. Schulz (2023). "Age and petrogenesis of Ni-Cu-(PGE) sulfide-bearing gabbroic intrusions in the Lausitz Block, northern Bohemian Massif (Germany/Czech Republic)". en. In: *Lithos* 444-445, p. 107090. DOI: 10.1016/j.lithos.2023.107090.

Járóka, T., S. Staude, T. Seifert, J. A. Pfänder, M. E. Bauer, J. Krause, and B. Schulz (2021). "Mineralogical and geochemical constraints on the origin of the Sohland-Rožany Ni-Cu-(PGE) sulfide mineralization (Lausitz Block, Bohemian Massif, Germany/Czech Republic)". In: *Ore Geology Reviews* 133, p. 104055. DOI: 10.1016/j.oregeorev.2021.104055.

Jowett, E. C. (1986). "Genesis of Kupferschiefer Cu-Ag deposits by convective flow of Rotliegendes brines during Triassic rifting". en. In: *Economic Geology* 81.8, pp. 1823–1837. DOI: 10.2113/gsecongeo.81.8.1823.

Karnkowski, P. H. (1999). "Origin and evolution of the polish rotliegend basin". EN. In: *Polish Geological Institute Special Papers* Vol. 3, pp. 1–93.

Karnkowski, P. H. (2007). "Permian Basin as a main exploration target in Poland". In: *Przegląd Geologiczny* 55.12/1, pp. 1003–1015.

Keith, M., K. M. Haase, R. Klemd, D. J. Smith, U. Schwarz-Schampera, and W. Bach (2018). "Constraints on the source of Cu in a submarine magmatic-hydrothermal system, Brothers volcano, Kermadec island arc". In: *Contributions to Mineralogy and Petrology* 173, pp. 1–16. DOI: 10.1007/s00410-018-1470-5.

Kiersnowski, H. (2013). "Late Permian aeolian sand seas from the Polish Upper Rotliegend Basin in the context of palaeoclimatic periodicity". In: *Geological Society, London, Special Publications* 376.1. Publisher: The Geological Society of London, pp. 431–456. DOI: 10.1144/SP376.20.

Kiersnowski, H. and A. Buniak (2006). "Evolution of the Rotliegend Basin of northwestern Poland". In: *Geological Quarterly* 50, pp. 119–138.

Kiersnowski, H., J. Paul, T. M. Peryt, and D. B. Smith (1995). "Facies, Paleogeography, and Sedimentary History of the Southern Permian Basin in Europe". en. In: *The Permian of Northern Pangea: Volume 2: Sedimentary Basins and Economic Resources*. Ed. by Scholle, P. A., Peryt, T. M., and Ulmer-Scholle, D. S. Berlin, Heidelberg: Springer, pp. 119–136. DOI: 10.1007/978-3-642-78590-0_7.

Kiersnowski, H., T. M. Peryt, A. Buniak, and Z. Mikołajewski (2010). "From the intra-desert ridges to the marine carbonate island chain: middle to late Permian (Upper Rotliegend–Lower Zechstein) of the Wolsztyn–Pogorzela high, west Poland". en. In: *Geological Journal* 45.2-3, pp. 319–335. DOI: 10.1002/gj.1189.

Kiresnowski, H. (1997). "Depositional development of the Polish Upper Rotliegend Basin and evolution of its sediment source areas". In: *Geological Quarterly* 41.4, pp. 433–456.

Kłapciński, J. and M. Sachanbiński (1975). "New data on geology of the Fore-Sudetic crystalline basement". In: *Geol Sudet* 10.2, pp. 7–46.

Kraft, P., U. Linnemann, M. Mergl, J. Bruthansová, L. Laibl, and G. Geyer (2023). "Ordovician of the Bohemian Massif". en. In: *Geological Society, London, Special Publications* 532.1, pp. 433–464. DOI: 10.1144/SP532-2022-191.

Krawczyk, C. M., T. McCann, L. R. M. Cocks, R. W. England, J. H. McBride, and S. Wybraniec (2008). "Caledonian tectonics". In: *The Geology of Central Europe: Volume 1: Precambrian and Palaeozoic*. Ed. by McCann, T. Geological Society of London. DOI: 10.1144/CEV1P.7.

Kroner, U., J.-L. Mansy, S. Mazur, P. Aleksandrowski, H. P. Hann, H. Huckriede, F. Lacquement, J. Lamarche, P. Ledru, T. C. Pharaoh, H. Zedler, A. Zeh, and G. Zulauf (2008). "Variscan tectonics". In: *The Geology of Central Europe: Volume 1: Precambrian and Palaeozoic*. Ed. by McCann, T. Geological Society of London. DOI: 10.1144/CEV1P.11.

Krzywiec, P., H. Kiersnowski, and T. Peryt (2019). "Fault-controlled Permian sedimentation in the central Polish Basin (Bydgoszcz–Szubin area) – Insights from well and seismic data". en. In: *Zeitschrift der Deutschen Gesellschaft für Geowissenschaften* 170.3-4, pp. 255–272. DOI: 10.1127/zdgg/2019/0198.

Kucha, H. and A. Piestrzynski (1995). "Excursion guide: Polish Kupferschiefer Deposits Soc". In: *Econ. Geol*, pp. 1–23.

Kutek, J. (2001). "The Polish permo-mesozoic rift basin". In: *Mémoires du Muséum national d'histoire naturelle (1993)* 186, pp. 213–236.

Legler, B. and J. W. Schneider (2008). "Marine ingressions into the Middle/Late Permian saline lake of the Southern Permian Basin (Rotliegend, Northern Germany) possibly linked to sea-level highstands in the Arctic rift system". en. In: *Palaeogeography, Palaeoclimatology, Palaeoecology* 267.1-2, pp. 102–114. DOI: 10.1016/j.palaeo.2008.06.009.

Maliszewska, A., E. Jackowicz, M. Kuberska, and H. Kiersnowski (2016). "Skały permu dolnego (czerwonego spągowca) zachodniej Polski: monografia petrograficzna". In: *Prace Państwowego Instytutu Geologicznego* 204.

Mazur, S., P. Aleksandrowski, K. Turniak, L. Krzemiński, K. Mastalerz, A. Górecka-Nowak, L. Kurowski, P. Krzywiec, A. Żelaźniewicz, and M. Fanning (2010). "Uplift and late orogenic deformation of the Central European Variscan belt as revealed by sediment provenance and structural record in the Carboniferous foreland basin of western Poland". In: *International Journal of Earth Sciences* 99, pp. 47–64. DOI: 10.1007/s00531-008-0367-3.

McCann, T. (1998a). "Sandstone composition and provenance of the Rotliegend of the NE German Basin". en. In: *Sedimentary Geology* 116.3, pp. 177–198. DOI: 10.1016/S0037-0738(97)00106-1.

– (1998b). "The Rotliegend of the NE German Basin; background and prospectivity". en. In: *Petroleum Geoscience* 4.1, pp. 17–27. DOI: 10.1144/petgeo.4.1.17.

Menning, M. (1995). "A Numerical Time Scale for the Permian and Triassic Periods: An Integrated Time Analysis". en. In: *The Permian of Northern Pangea*. Ed. by Scholle, P. A., Peryt, T. M., and Ulmer-Scholle, D. S. Berlin, Heidelberg: Springer Berlin Heidelberg, pp. 77–97. DOI: 10.1007/978-3-642-78593-1_6.

Menning, M., J. Glodny, J. Boy, R. Gast, G. Kowalczyk, T. Martens, R. Rößler, T. Schindler, V. von Seckendorff, and S. Voigt (2022). "The Rotliegend in the stratigraphic table of Germany 2016 (STG 2016)". In: *Zeitschrift der Deutschen Gesellschaft für Geowissenschaften* 173, pp. 3–139. DOI: 10.1127/zdgg/2022/0311.

Murphy, B. P., J. P. L. Johnson, N. M. Gasparini, and L. S. Sklar (2016). "Chemical weathering as a mechanism for the climatic control of bedrock river incision". en. In: *Nature* 532.7598, pp. 223–227. DOI: 10.1038/nature17449.

Nádaskay, R., J. Žák, J. Sláma, T. Sidorinová, and J. Valečka (2019). "Deciphering the Late Paleozoic to Mesozoic tectono sedimentary evolution of the northern Bohemian Massif from detrital zircon geochronology and heavy mineral provenance". en. In: *International Journal of Earth Sciences* 108.8, pp. 2653–2681. DOI: 10.1007/s00531-019-01781-z.

Naldrett, A. J. (2013). *Magmatic sulfide deposits: geology, geochemistry and exploration*. Springer Science & Business Media. DOI: ISBN:10.1007/978-3-662-08444-1.

Nawrocki, J. and P. Poprawa (2006). "Development of trans-European Suture Zone in Poland: from Ediacaran rifting to early Palaeozoic accretion". In: *Geological Quarterly* 50.1, pp. 59–76.

Neumann, E.-R., E. Dunworth, B. Sundvoll, and J. Tollefsrud (2002). "B1 basaltic lavas in Vestfold–Jeløya area, central Oslo rift: derivation from initial melts formed by progressive partial melting of an enriched mantle source". In: *Lithos* 61.1-2, pp. 21–53. DOI: 10.1016/S0024-4937(02)00068-3.

Oszczepalski, S. (1986). "On the Zechstein copper shale lithofacies and palaeoenvironments in SW Poland". In: *Geological Society, London, Special Publications* 22.1, pp. 171–182. DOI: 10.1144/GSL.SP.1986.022.01.16.

Oszczepalski, S., S. Speczik, K. Zieliński, and A. Chmielewski (2019). "The Kupferschiefer Deposits and Prospects in SW Poland: Past, Present and Future". en. In: *Minerals* 9.10, p. 592. DOI: 10.3390/min9100592.

Paul, J., K. Wemmer, and H. Ahrendt (2008). "Provenance of siliciclastic sediments (Permian to Jurassic) in the Central European Basin". In: *Zeitschrift der Deutschen Gesellschaft fur Geowissenschaften* 159.4, p. 641. DOI: 10.1127/1860-1804/2008/0159-0641.

Peryt, T. M. (1978). "Sedimentology and paleoecology of the Zechstein Limestone (Upper Permian) in the Fore-Sudetic area (western Poland)". In: *Sedimentary Geology* 20, pp. 217–243. DOI: 10.1016/0037-0738(78)90055-6.

Pharaoh, T. C., M. Dusar, M. C. Geluk, F. Kockel, C. M. Krawczyk, P. Krzywiec, M. Scheck-Wenderoth, H. Thybo, O. V. Vejbæk, and J. Van Wees (2010). "Tectonic Evolution". English. In: *Petroleum Geological Atlas of the Southern Permian Basin Area*. Ed. by Doornenbal, J. C. and Stevenson, A. G. EAGE Publications b.v. (Houten), pp. 25–57. DOI: ISBN978-90-73781-61-0.

Pharaoh, T. C., J. A. Winchester, J. Verniers, A. Lassen, and A. Seghedi (2006). "The Western Accretionary Margin of the East European Craton: an overview". en. In: *Geological Society, London, Memoirs* 32.1, pp. 291–311. DOI: 10.1144/GSL.MEM.2006.032.01.17.

Poprawa, P. (2019). "Geological setting and Ediacaran–Palaeozoic evolution of the western slope of the East European Craton and adjacent regions". In: *Annales Societatis Geologorum Poloniae*. DOI: 10.14241/asgp.2019.23.

Pożaryski, W. (1990). "The Middle Europe Caledonides-wrenching orogen composed of terranes". In: *Przegląd Geologiczny* 38.1, pp. 1–9.

Rey, P., J.-P. Burg, and M. Casey (1997). "The Scandinavian Caledonides and their relationship to the Variscan belt". en. In: *Geological Society, London, Special Publications* 121.1, pp. 179–200. DOI: 10.1144/GSL.SP.1997.121.01.08.

Rey, P., O. Vanderhaeghe, and C. Teyssier (2001). "Gravitational collapse of the continental crust: definition, regimes and modes". en. In: *Tectonophysics* 342.3-4, pp. 435–449. DOI: 10.1016/S0040-1951(01)00174-3.

Salles, T. (2016). "Badlands: A parallel basin and landscape dynamics model". en. In: *SoftwareX* 5, pp. 195–202. DOI: 10.1016/j.softx.2016.08.005.

Salles, T., X. Ding, and G. Brocard (2018). "pyBadlands: A framework to simulate sediment transport, landscape dynamics and basin stratigraphic evolution through space and time". en. In: *PLOS ONE* 13.4. Ed. by Borazjani, I., e0195557. DOI: 10.1371/journal.pone.0195557.

Salles, T., L. Husson, P. Rey, C. Mallard, S. Zahirovic, B. H. Boggiani, N. Coltice, and M. Arnould (2023). "Hundred million years of landscape dynamics from catchment to global scale". en. In: *Science* 379.6635, pp. 918–923. DOI: 10.1126/science.add2541.

Salles, T., C. Mallard, and S. Zahirovic (2020). "gospl: Global Scalable Paleo Landscape Evolution". In: *Journal of Open Source Software* 5.56, p. 2804. DOI: 10.21105/joss.02804.

Scheck, M. and U. Bayer (1999). "Evolution of the Northeast German Basin — inferences from a 3D structural model and subsidence analysis". In: *Tectonophysics* 313.1, pp. 145–169. DOI: 10.1016/S0040-1951(99)00194-8.

Scheck-Wenderoth, M. and J. Lamarche (2005). "Crustal memory and basin evolution in the Central European Basin System—new insights from a 3D structural model". en. In: *Tectonophysics* 397.1-2, pp. 143–165. DOI: 10.1016/j.tecto.2004.10.007.

Scotese, C. R. and N. Wright (2018). "PALEOMAP Paleodigital Elevation Models (PaleoDEMS) for the Phaerozoic". In: *PALEOMAP Proj.*

Sillitoe, R. H. (2010). "Porphyry copper systems". In: *Economic geology* 105.1, pp. 3–41. DOI: 10.2113/gsecongeo.105.1.3.

Smith, D. B. (1979). "Rapid marine transgressions and regressions of the Upper Permian Zechstein Sea". en. In: *Journal of the Geological Society* 136.2, pp. 155–156. DOI: 10.1144/gsjgs.136.2.0155.

Sok, T., C. Oeurng, I. Ich, S. Sauvage, and J. Miguel Sánchez-Pérez (2020). "Assessment of hydrology and sediment yield in the Mekong River Basin using SWAT model". In: *Water* 12.12, p. 3503. DOI: 10.3390/w12123503.

Stampfli, G. and G. Borel (2002). "A plate tectonic model for the Paleozoic and Mesozoic constrained by dynamic plate boundaries and restored synthetic oceanic isochrons". en. In: *Earth and Planetary Science Letters* 196.1-2, pp. 17–33. DOI: 10.1016/S0012-821X(01)00588-X.

Tomaszewski, J. B. (1978). "Budowa geologiczna okolic Lubina i Sieroszowic (Dolny Śląsk)". In: *Geologia Sudetica* 13.2, pp. 85–128.

Vacek, F. and J. Žák (2019). "A lifetime of the Variscan orogenic plateau from uplift to collapse as recorded by the Prague Basin, Bohemian Massif". en. In: *Geological Magazine* 156.3, pp. 485–509. DOI: 10.1017/S0016756817000875.

Valdes, P. J., C. R. Scotese, and D. J. Lunt (2020). "Deep ocean temperatures through time". In: *Climate of the Past Discussions* 2020. Publisher: Göttingen, Germany, pp. 1–37. DOI: 10.5194/cp-17-1483-2021.

Vaughan, D., M. Sweeney, G. Friedrich, R. Diedel, and C. Haranczyk (1989). "The Kupferschiefer; an overview with an appraisal of the different types of mineralization". In: *Economic Geology* 84.5, pp. 1003–1027. DOI: 10.2113/gsecongeo.84.5.1003.

Villaseñor, G., E. J. Catlos, I. Broska, M. Kohút, L. Hraško, K. Aguilera, T. M. Etzel, J. R. Kyle, and D. F. Stockli (2021). "Evidence for widespread mid-Permian mag-

matic activity related to rifting following the Variscan orogeny (Western Carpathians)". In: *Lithos* 390-391, p. 106083. DOI: 10.1016/j.lithos.2021.106083.

Wees, J.-D. van, R. Stephenson, P. Ziegler, U. Bayer, T. McCann, R. Dadlez, R. Gaupp, M. Narkiewicz, F. Bitzer, and M. Scheck (2000). "On the origin of the Southern Permian Basin, Central Europe". en. In: *Marine and Petroleum Geology* 17.1, pp. 43–59. DOI: 10.1016/S0264-8172(99)00052-5.

Wilson, M., E.-R. Neumann, G. R. Davies, M. J. Timmerman, M. Heeremans, and B. T. Larsen (2004). "Permo-Carboniferous magmatism and rifting in Europe: introduction". en. In: *Geological Society, London, Special Publications* 223.1, pp. 1–10. DOI: 10.1144/GSL.SP.2004.223.01.01.

Zieger, J., M. Zieger-Hofmann, A. Gärtner, and U. Linnemann (2023). "Variscan zircons everywhere? Multi-stage sedimentary recycling in Central Europe". In: *Geological Society, London, Special Publications* 542.1. Publisher: The Geological Society of London, SP542–2022–348. DOI: 10.1144/SP542-2022-348.

Ziegler, P. A., M. E. Schumacher, P. Dèzes, J.-D. Van Wees, and S. Cloetingh (2004). "Post-Variscan evolution of the lithosphere in the Rhine Graben area: constraints from subsidence modelling". In: *Geological Society, London, Special Publications* 223.1. Publisher: The Geological Society of London, pp. 289–317. DOI: 10.1144/GSL.SP.2004.223.01.13.

Ziegler, P. A. (1990). *Evolution of Laurussia*. en. Dordrecht: Springer Netherlands. DOI: 10.1007/978-94-009-0469-9.

4| ARTICLE 3
The roles of surface processes in porphyry copper deposits preservation

Beatriz Hadler Boggiani[1], Claire Mallard[2], Tristan Salles[1], Nicholas Atwood[3]

[1]School of Geosciences, The University of Sydney, Sydney, Australia
[2]BHP Metal Global Endowment Team, BHP, Brisbane, QLD, Australia
[3]BHP Metal Global Endowment Team, BHP, Tucson, Arizona, USA

- We use a new-generation global landscape evolution model that combines paleo-reconstructions of elevation and precipitation, at global scale for the past 100 Myr;
- We propose a novel approach to assess exhumation rates and emplacement depths of porphyry copper deposits;
- The dataset provided by our simulation effectively replicate calculations of emplacement depths on a global scale, with roughly 50% of the values ranging from 1 to 5 km depth;
- We identify inconsistencies between modeled data and independent data (e.g. fission track, thermochronology) that we relate to the resolution of our initial dataset as well as simplifications inherent to our model;
- Our study offers a new way to evaluate and quantify the accuracy of paleo-precipitations and paleo-elevation models when compared against independent data.

Earth Surf. Dynam., 13, 683–704, 2025
https://doi.org/10.5194/esurf-13-683-2025
© Author(s) 2025. This work is distributed under
the Creative Commons Attribution 4.0 License.

Earth Surface Dynamics
Open Access
EGU

The roles of surface processes in porphyry copper deposit preservation

Beatriz Hadler Boggiani[1], Tristan Salles[1], Claire Mallard[1], and Nicholas Atwood[2]

[1]School of Geosciences, The University of Sydney, Sydney, Australia
[2]BHP Exploration, Tucson, Arizona, USA

Correspondence: Beatriz Hadler Boggiani (beatriz.boggiani@sydney.edu.au)

Received: 20 June 2024 – Discussion started: 22 August 2024
Revised: 12 May 2025 – Accepted: 13 May 2025 – Published: 7 August 2025

Abstract. Porphyry copper deposits typically originate within subduction zones at 2–5 km depths. These deposits are exhumed due to the influence of tectonic forces and climate-driven erosion. Porphyry copper deposits are currently only mineable at relatively shallow depths, and their prospectivity relies on a balance between the rate of exhumation and preservation. In this study, we evaluate the impact of surface processes on the preservation or exhumation of porphyry copper deposits. To do so, we rely on a global-scale numerical model (*goSPL*), which simulates landscape dynamics and associated erosion and deposition patterns over geological timescales. High-resolution Cenozoic simulations incorporate published open-source global paleo-climate and paleo-elevation datasets and have been fine-tuned using contemporary data. We then calculate exhumation rates by comparing the ages of known porphyry copper deposits and their simulated emplacement depths based on modeled erosion–deposition values. Obtained average exhumation rates vary from 10^{-2} to 10^{-1} km Myr^{-1}, with an overall difference of 0.04 mm yr^{-1} when compared to independent erosion rate estimates available from published studies. The predicted global mean emplacement depths range from 1 to 3 km. To highlight the influence of paleo-reconstructions on exhumation rate estimates, we analyze simulated erosion rates across the Andean region using two distinct paleo-climate models and find significant spatial and temporal differences across the Central Andes. While our landscape evolution model successfully predicts the known emplacement depths for the North and South Andean deposits younger than 20 Myr, it also predicts depths exceeding 6 km for Central Andean deposits older than 60 Myr. We attribute these mismatches to a combination of limitations related to model assumptions and inputs resolutions. Our results show the intricate connection between deposit preservation and surface processes. Our method offers an addition to the traditional porphyry copper exploration toolkit that links geological observations to plate tectonics dynamics and paleo-climatic reconstructions.

1 Introduction

The association between porphyry copper deposits (PCDs) and alkaline/calc-alkaline magmatic arcs has been well established for at least 50 years (Sillitoe, 1972). These deposits most commonly originate from the combination of (i) rapid convergence rates (around 100 km Myr^{-1}) (Butterworth et al., 2016), (ii) subduction obliquity (around 15°) (Butterworth et al., 2016), (iii) subducting plate age (between 25–70 Myr) (Butterworth et al., 2016; Sillitoe, 2010), (iv) distance from the subducting trench boundary (> 2000 km) (Butterworth et al., 2016), and (v) a thick crust (> 45 km) (Lee and Tang, 2020).

Assuming the aforementioned conditions are fulfilled, the porphyry bodies are emplaced at a certain depth, with the emplacement depth (ED) referring to the depth at which magmatic fluids encounter a favorable environment within the Earth's crust (Lee and Tang, 2020; Sillitoe, 2010), characterized by optimal pressure, temperature, and salinity conditions (Richards, 2022; Sillitoe, 2010). Predictions regarding the depth of emplacement are inferred from fluid inclusion analysis or age temperature data (McInnes et al., 2005;

Landtwing et al., 2005; Noury and Calmus, 2021) and typically range between 1–5 km, with lower magmatic temperatures typically associated with shallower intrusions, while higher temperatures correspond to greater depths (Richards, 2022). It is common for economic porphyry deposits to have emplacement depths between 4–5 km (Zhao et al., 2022). Exceptional cases exist where deposits have been emplaced at depths greater than 5 km. For example, the Middle Paleocene (60.5 Ma) Butte body in Montana (USA) is believed to have been emplaced at an unusual depth between 5–9 km (Rusk et al., 2008). On the other hand, other deposits such as the 3.5 Ma Panguna in Papua New Guinea have been emplaced between 2–3 km (Eastoe, 1978; Cooke et al., 2005).

The exhumation trajectory and preservation of porphyry copper deposits are primarily influenced by climate-driven erosion and tectonic uplift. Exhumation rates (ERs) are strongly tied to precipitation history, substrate erodibility, slope angles, and direction of propagation of the deformation (Stalder et al., 2020). Whilst ERs between 0.1–1.0 $\mathrm{km\,Myr^{-1}}$ are considered typical for a moderately active mountain belt (Montgomery and Brandon, 2002), these rates can vary significantly at regional scale due to tectonic and climatic forces. For example, hyper-arid climates such as the Central Andes (Stern, 2004) have ERs that do not exceed 0.25 $\mathrm{km\,Myr^{-1}}$ (Stalder et al., 2020). Comparatively, regions such as Papua New Guinea, known for their young PCDs, elevated precipitation rates, and rapid plate convergence creating high uplift rates, exhibit some of the highest ERs, greater than 10 $\mathrm{km\,Myr^{-1}}$ (Baldwin et al., 2004).

Yanites and Kesler (2015) calculated the exhumation rates of 314 Cenozoic PCDs distributed globally and reported values ranging from 0.03 to 1.4 $\mathrm{km\,Myr^{-1}}$ by assuming uniform emplacement depth of 2 km for all their PCDs and extrapolating present-day climatic conditions for the entire Cenozoic. This reveals a pattern where younger deposits in wetter regions experienced rapid exhumation, while older deposits are more prevalent in arid regions. Apart from Yanites and Kesler (2015) and despite the critical role that climate plays on landscape evolution, its implication for PCD preservation has been overlooked in recent studies (Butterworth et al., 2016; Diaz-Rodriguez et al., 2021). Butterworth et al. (2016) and Diaz-Rodriguez et al. (2021) employed machine learning algorithms to predict the prospectivity of porphyry copper districts in the Americas. Both studies largely ignored the impact of climate and paleo-topographic variations on PCD exhumation and preservation. This study challenges the assumption of singular emplacement depth as well as static climatic and paleo-topographic conditions over geological time using a series of time-evolving databases (Valdes et al., 2020; Li et al., 2022; Stern, 2004) over the past 65 Myr (see Sect. 3.2).

Here, we leverage global-scale surface process simulations to estimate global rates of exhumation and emplacement depths of known PCDs and assess their preservation prospects. To do so, we use the refined paleo-elevation dataset produced in Salles et al. (2023), applying the *goSPL* model (Salles et al., 2020), and estimate exhumation rates and emplacement depths of the same 314 deposits presented in Yanites and Kesler (2015). We then compare exhumation rate and emplacement depth values obtained from the landscape evolution model with data obtained via independent published methods (e.g., fission track analysis). We explore discrepancies and their potential causes, such as factors related to the paleo-reconstructions or limitations inherent to the numerical approach.

2 Global paleo-elevation reconstruction

2.1 Landscape evolution model

To estimate exhumation rates and emplacement depths at global scale, we use *goSPL* (Salles et al., 2020), an open-source scalable parallel numerical model. *goSPL* accounts for river incision and soil creep, processes which are considered to be the main drivers of landscape changes over geological timescale (Bonetti and Porporato, 2017). Additional capabilities (e.g., multi-lithology sediment tracking, deposition in marine environments, sediment compaction, stratigraphic record) are not considered in this study, and we evaluate the impact of surface processes on landscape dynamics (Salles et al., 2023) by imposing a series of spatially and temporally varying topographic and climatic histories. Flexural responses due to erosional unloading and depositional loading influence long-term drainage evolution, landscape rejuvenation, and sedimentation, reflecting lithospheric strength and mantle buoyancy (Sacek, 2014). While goSPL does not explicitly model these processes, the assimilation method implicitly accounts for them by aligning modeled elevations with paleo-elevation reconstructions (Salles et al., 2023). As an example, the approach captures subsidence patterns near large deltaic systems (e.g., Amazon, Bengal fans, Pelotas Basin).

In *goSPL*, erosion occurring in upstream catchments is linked to basin sedimentation via a multiple flow direction algorithm that routes both water and sediment flux towards multiple downstream nodes, preventing the locking of erosion pathways along a single direction and allowing the distribution of the corresponding flux in downstream regions. The model's main equation, the continuity of mass, has the following common form:

$$\frac{\partial z}{\partial t} = U_i + \kappa \nabla^2 z_i + \epsilon P_i^d Q_i^m \nabla z_i^n, \tag{1}$$

where the flow discharge Q_i in cell i is given by

$$Q_i = P_i A_i + \sum_{j \in \mathrm{up}} Q_j, \tag{2}$$

where the changes in surface elevation (z in meters) with time (t in years) are dependent on the tectonic forcing U_i ($\mathrm{m\,yr^{-1}}$); on a diffusion equation used to simulate hillslope

processes, with the diffusion coefficient κ set to $0.5\,m^2\,yr^{-1}$ (Salles et al., 2018); and on the stream power law to evaluate the impact of fluvial processes by quantifying the rate of incision from local slope and amount of water passing through a cell. We set m to 0.5 and n to 1 (dimensionless empirical constants, Salles et al., 2023). The precipitation-independent component of erodibility ϵ (set to $4.0 \times 10^{-7}\,yr^{-1}$) is constant throughout the simulation time and is tied to the choice of m. The erodibility coefficient is scalable with local mean annual precipitation rate (P_i), which is a positive exponent (d) obtained from field-based relationships (Murphy et al., 2016) and set to 0.42. It is worth noting that d is incorporated in the formulation for enhancing the weathering impact of precipitation and its response in river incisions (Salles et al., 2018, 2023).

The flow discharge (Q_i) accounts for the upstream total area (A_i) and local precipitation (P_i) that combines to form the water flux ($P_i A_i$) with added upstream flow discharge (Q_j, in Eq. 2). To solve the flow discharge globally, we use a parallel implicit drainage area (IDA) method (Richardson et al., 2014; Salles et al., 2019) in a Eulerian reference frame, expressed in the form of a sparse matrix composed of diagonal terms set to unity and off-diagonal terms corresponding to the immediate neighbors of each vertex composing the spherical mesh. A similar technique is used to solve sediment transport and continental erosion. We use the Richardson solver with block Jacobian preconditioning to solve the IDA algorithm using the PETSc library (Balay et al., 2012) following the approach described in Richardson et al. (2014). Although Eq. (1) does not account for deposition in alluvial plains or along gentle slopes, it simulates continental deposition in depressions and endorheic basins.

2.2 Paleo-elevation and paleo-precipitation forcings

Here we use the global-scale simulations from Salles et al. (2023), which are based on the PALEOMAP Paleogeographic Atlas (Scotese and Wright, 2018). The PALEOMAP paleo-elevation maps are structured regular grids with a resolution equivalent to 10 km cell length at the Equator ($0.1° \times 0.1°$) defined at 5 Myr intervals. The paleo-elevation reconstructions are based on lithofacies and paleo-environmental datasets, supplemented and updated with regional paleogeographic atlases (Scotese and Schettino, 2017; Scotese and Wright, 2018) over the course of more than 40 years (Ziegler et al., 1985). Our choice for the PALEOMAP atlas as the foundational dataset was driven by its unique availability as a global open-source option with a resolution (0.1° or finer) appropriate for landscape evolution modeling. However, alternative datasets (e.g. Markwick and Valdes, 2004; Vérard et al., 2015; Straume et al., 2019) could equivalently be used.

To predict erosion–deposition rates, Salles et al. (2023) rely on the paleo-precipitation simulations from HadCM3BL-M2.1aD29, which is a variant derived from the coupled atmosphere–ocean–vegetation Hadley Centre model (Valdes et al., 2020) (resolution of $3.75° \times 2.5°$) and has been built using the PALEOMAP Paleogeographic Atlas (Scotese and Wright, 2018). For each time interval, this climate model has been run for at least 5000 model years to reach a dynamic equilibrium of the deep ocean (Valdes et al., 2020). The climate model is established under two time-dependent boundary conditions: the solar constant and the atmospheric CO_2 concentrations. We use the workflow set out in Salles et al. (2023) that adopted the CO_2 local weighted regression curve from Foster et al. (2017) based on their choice of HadCM3 climate simulations for the paleo-precipitation maps.

The input files for *goSPL* are composed of an icosahedral mesh with more than 10 million nodes and 21 million cells. They are generated by resampling the global temporal grids into this mesh. The average resolution of each cell is about 5 km, corresponding to 0.05° resolution at the Equator. The design approach (Salles et al., 2023, 2020) aims to achieve dynamic equilibrium between erosion rates balanced by tectonics under a steady boundary condition (rainfall, tectonic uplift, and erodibility) (Eq. 1 and Fig. 1). For each individual time slice, two sets of simulations were run over 168 CPU (Salles et al., 2023). From there, we estimate physiographic characteristics and associated water and sediment dynamics.

An initial simulation is performed over 2 Myr to appraise landscape evolution, water discharge, and sediment transport, using selected topographical and precipitation scenarios (Salles et al., 2023). This first simulation does not account for tectonic processes, resulting in an excessive fingerprint on the reconstructed landscape from surface processes, leading to a lowering of major long-lived orogenic belts and upland areas as well as creating extensive floodplains (Fig. 1a and b). Using a filtering approach that removes high amplitude short wavelength variations, we ensure that these morphological features are not accounted for in the correction step, resulting in minimal changes in hypsometry ($\leq 0.5\,\%$, Fig. 1c). Consequently, the final elevations were corrected by assimilating paleo-elevation information. The resultant paleo-elevation model integrates the surface process features from the initial simulation, recreating more detail when compared to the initial paleo-elevation, where canyons, incised channels, and basins can be identified (Fig. 1a and b). By calculating the regional differences between the paleo-elevation data and the modified enhanced paleo-elevation, we derive a vertical tectonic forcing map delineating uplift and subsidence rates.

The second and final round of simulations are run considering the same initial input files, however with the computed tectonic forcing, added to it (Salles et al., 2023) (Fig. 1). The tectonic forcing is computed from the mismatch between the model predictions and a geologically reconstructed target location. The mismatch indicates either that surface processes parameters (erodibility) need to be tuned or that other forcings such as dynamic uplift or subsidence need to be considered. If the second is decided, a new tectonic forc-

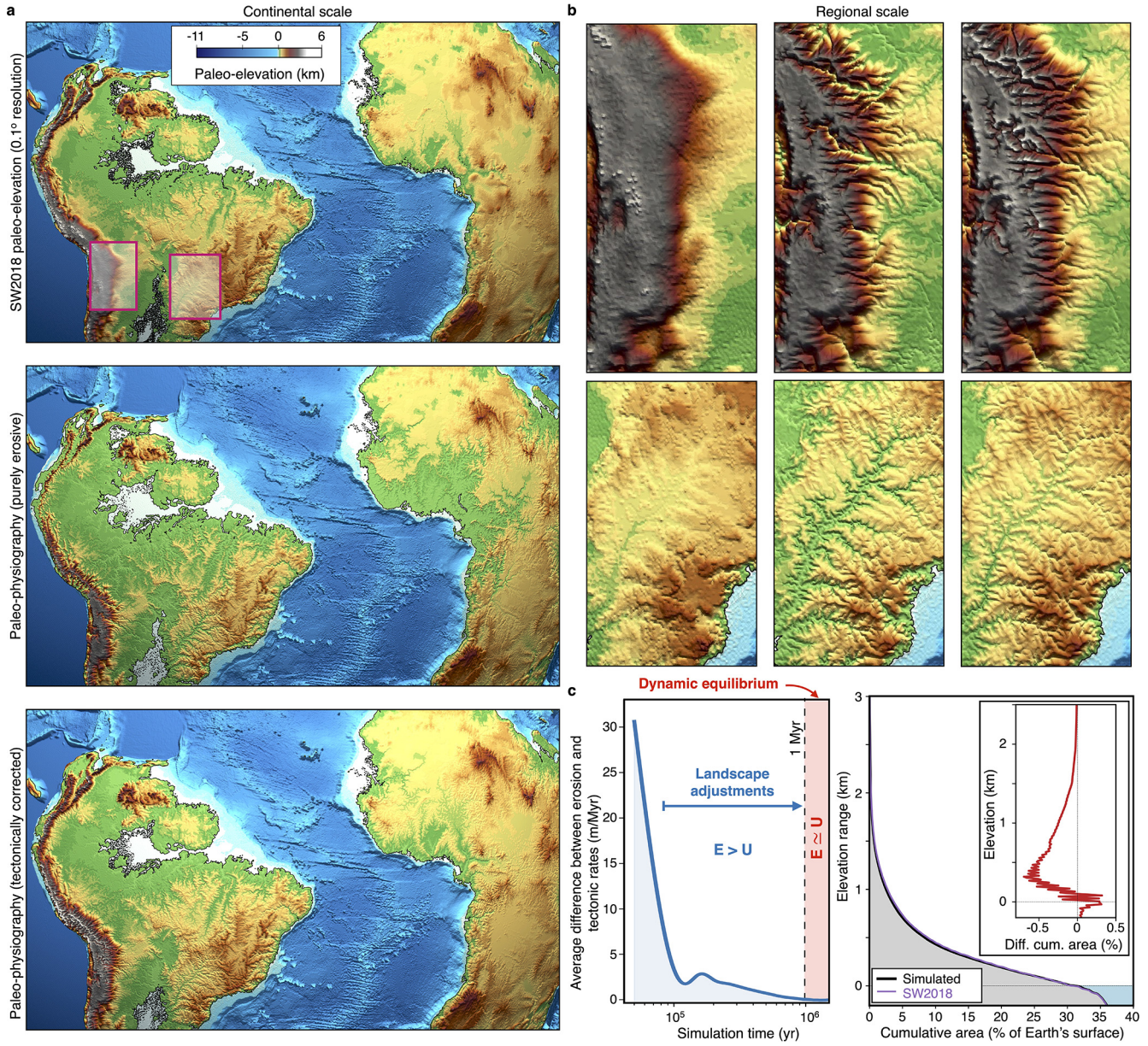

Figure 1. Comparison between predicted enhanced paleo-elevation and corresponding paleo-elevation map. **(a)** The top panel shows the input elevation conditions for 50 Ma at 0.1° resolution (SW2018 Scotese and Wright, 2018), and the bottom two represent model outputs after the first and second simulation steps (0.05° resolution), highlighting the geomorphological imprints induced by surface processes on the landscape. **(b)** Regional-scale elevations for the two domains highlighted in **(a)**, with the initial paleo-elevation SW2018 (Scotese and Wright, 2018) on the left, the resulting enhanced paleo-elevation under purely erosive scenario (center), and after applying the tectonic correction and reaching dynamic equilibrium (right). **(c)** Temporal change between imposed tectonic rates from corrected topography and erosion rates at 50 Ma (blue curve). This curve is used to estimate when dynamic equilibrium conditions have been reached. Corresponding continental hypsometric curves for the given paleo-elevation at 50 Ma (purple) and simulated enhanced paleo-elevation (black). Red curve in the inset shows the differences between the two hypsometric curves.

ing, based on the filtered mismatch map, which only considers long wavelengths and short amplitudes, is imposed. Mismatch percentages and correlation coefficients guide the calibration of the paleo-elevation maps. The simulation runs until it achieves dynamic equilibrium (i.e., erosion rates compensate tectonic ones), which usually occurs within the initial million years of landscape evolution (Fig. 1c) (Salles et al., 2023). From the output of this second simulation, it is possible to evaluate water and sediment flux for the time slice, as well as catchment characteristics, such as river network,

drainage areas, erosion, and deposition rates (Figs. 2 and 3a and d).

Using the outputs from the second simulation, Eq. (1) is then calibrated for the present day (i) based on estimates of suspended sediment flux, which is equivalent to $12.8\,\mathrm{Gt\,yr^{-1}}$ (from the BQART model Syvitski and Milliman, 2007; Peucker-Ehrenbrink, 2009), and (ii) with modern estimates of average global erosion rates (Willenbring et al., 2013), where the mean value is $63\,\mathrm{m\,Myr^{-1}}$ with a standard deviation of $15\,\mathrm{m\,Myr^{-1}}$ (Fig. 3b). The average present-day global modeled erosion rate is $73\,\mathrm{m\,Myr^{-1}}$, with a modeled sediment flux of $12.15\,\mathrm{Gt\,yr^{-1}}$ (assuming an average density of $2.7\,\mathrm{g\,cmr^{-3}}$) (Salles et al., 2023). Using the IDA algorithm (Richardson et al., 2014), basin characteristics and locations for the largest sediment flux and water discharge are extracted (Fig. 3d).

The model accurately accounts for the discharge–area scaling relationship between water and sediment flux for the major rivers for the present day (Whipple and Tucker, 1999). For example, the predictions from the Amazon River discharge and sediment flux lie well between estimates from the Land2Sea database (Peucker-Ehrenbrink, 2009) (6591–$7570\,\mathrm{km^3\,yr^{-1}}$) and are $\sim 4\,\%$ below the sediment production rate when compared with cosmogenic nuclide analysis ($\sim 610\,\mathrm{Mt\,yr^{-1}}$) (Wittmann et al., 2011; Salles et al., 2023). The parameterization from present-day suspended sediment flux and global erosion rates is then extrapolated into the past, enabling the computation of temporal trends in global sediment fluxes, which can be linked to changes in continental elevation and precipitation patterns (Salles et al., 2023) (Figs. 2 and 3a). The predicted trends of sediment fluxes produce reasonable records during the Meso-Cenozoic and are comparable with observations for other time periods (Wilkinson and McElroy, 2007) (Fig. 3a). Furthermore, multiple spikes in erosion flux align with major orogenic events, overlaying the trend observed throughout the Cenozoic (Salles et al., 2023) (Fig. 2a).

2.3 Landscape evolution model outputs extraction

The data produced in the simulation are processed with open-source workflows provided in GitHub repositories: https://github.com/Geodels/gospl-global-workflows (last access: 5 August 2025) and https://github.com/Geodels/gospl/ (last access: 5 August 2025) (Salles et al., 2020). All the notebooks are written in Python programming language and supported by a wide range of libraries, of which the most employed are Numpy (Oliphant, 2006), Pandas (McKinney, 2011), XArray (Hoyer and Hamman, 2017), pyGPlates (Mather et al., 2023), and PyGMT (Uieda et al., 2021).

The output files created with *goSPL* are exported to netCDF grids containing, for each time step, the following variables: elevation (m), cumulative erosion/deposition (m), water flux discharge accounting for lakes ($\mathrm{m^3\,yr^{-1}}$), water flux in rivers excluding lakes ($\mathrm{m^3\,yr^{-1}}$), sediment flux in rivers ($\mathrm{m^3\,yr^{-1}}$), and rainfall ($\mathrm{m\,yr^{-1}}$).

To access the information for a desired region over time, in our case the porphyry copper deposit location and its immediate surrounding region (i.e., within 25 km), it is necessary to track the region's position through tectonic plate reconstruction. This is achieved using the associated tectonic plate rotation file and its geometries (PALEOMAP Paleogeographic Atlas from Scotese and Wright, 2018). By determining the region's position over time, we then extract the relevant variables at each time step.

In our scenario, we used the cumulative erosion/deposition values over time to estimate erosion rates ($\mathrm{m\,yr^{-1}}$), which will correspond to exhumation rates ($\mathrm{km\,Myr^{-1}}$) over longer periods of time. With this information and the predicted ages of PCDs (Singer et al., 2008), we then infer the initial depth of emplacement.

3 Reconstructing exhumation history for porphyry copper deposits

We conducted an analysis of 314 porphyry copper deposits distributed globally and available from Yanites and Kesler (2015). These deposits range in age from the Paleocene to the Pleistocene (66–1 Ma) (Fig. 4).

3.1 Tectonic settings and deposits

We first categorized the deposits within three geodynamic regions/settings: the Alpine–Himalayan Orogeny, the Western Cordillera–Andean Belt, and the West Pacific Orogenic Belt.

The Western Cordillera and the Andean Belt belong to distinct subduction zones, active at different times, yet they share a similar geotectonic context, characteristic of continental margin settings (Ramos, 2009). The Western Cordillera (also known as the North American Cordillera) can be traced back to the breakup of Rodinia (Monger and Price, 2002; Clennett et al., 2020) and has been primarily shaped by the interactions between the North American plate and the surrounding oceanic lithospheres (Monger and Price, 2002). In Early Jurassic times, the convergence of the North American plate with continuous subduction zones led to the accretion of back-arc basins and offshore arcs that formed continental margins and new continental arcs (Monger and Price, 2002). By the Late Cretaceous, the newly formed Western Cordillera was located near its present-day position (Monger and Price, 2002).

The Western Cordillera can be subdivided into Canadian Cordillera and the Laramide Orogen (USA). In the Canadian Cordillera, the porphyry copper deposits were emplaced post-orogeny accretion from the Late Cretaceous to the Eocene (100–33 Ma) (McMillan et al., 1996; Leveille and Stegen, 2012). Conversely, in the Laramide Orogen, their formation is associated with magmatism and compressional

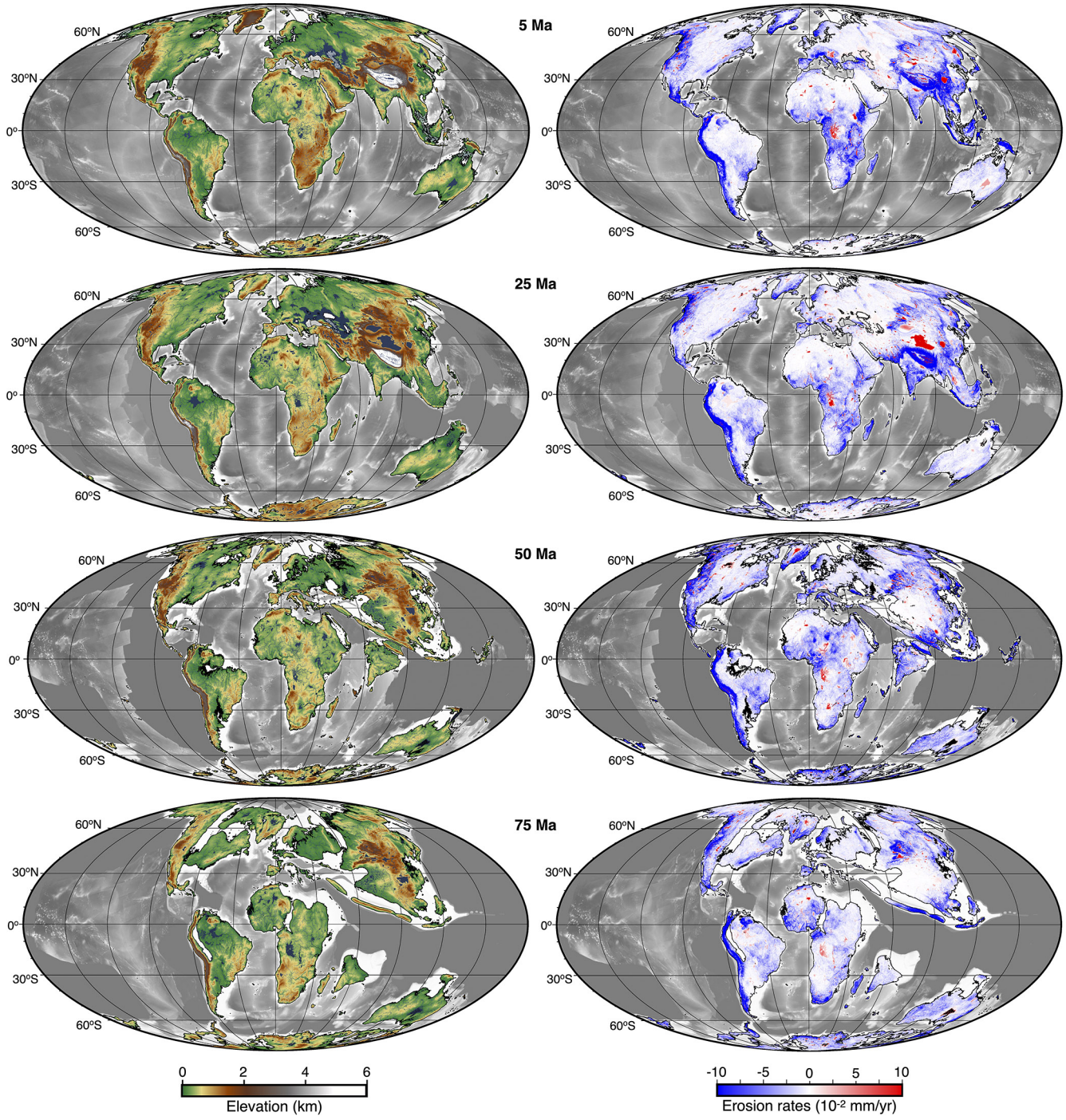

Figure 2. Global-scale landscape evolution model from the Cretaceous to present-day. Left panels represent simulated elevations for four time slices accounting for surface processes impact and highlighting continental topography and associated river networks (dark blue). Right panels show associated erosion/deposition rates (blue/red respectively) for the considered time slices.

deformation between 80–40 Ma (McLemore, 2008; Leveille and Stegen, 2012).

The Andean Belt results from the subduction of the Nazca Plate beneath the South American Plate; its formation began in the Middle Jurassic and is still active today (Ramos, 2009). The Andean Belt is subdivided into three sections, each characterized by different geodynamic events. The northern portion represents the major collision phases during the Paleogene, involving the accretion of oceanic crust due to the collision of oceanic terrains (Ramos, 2009). The central portion

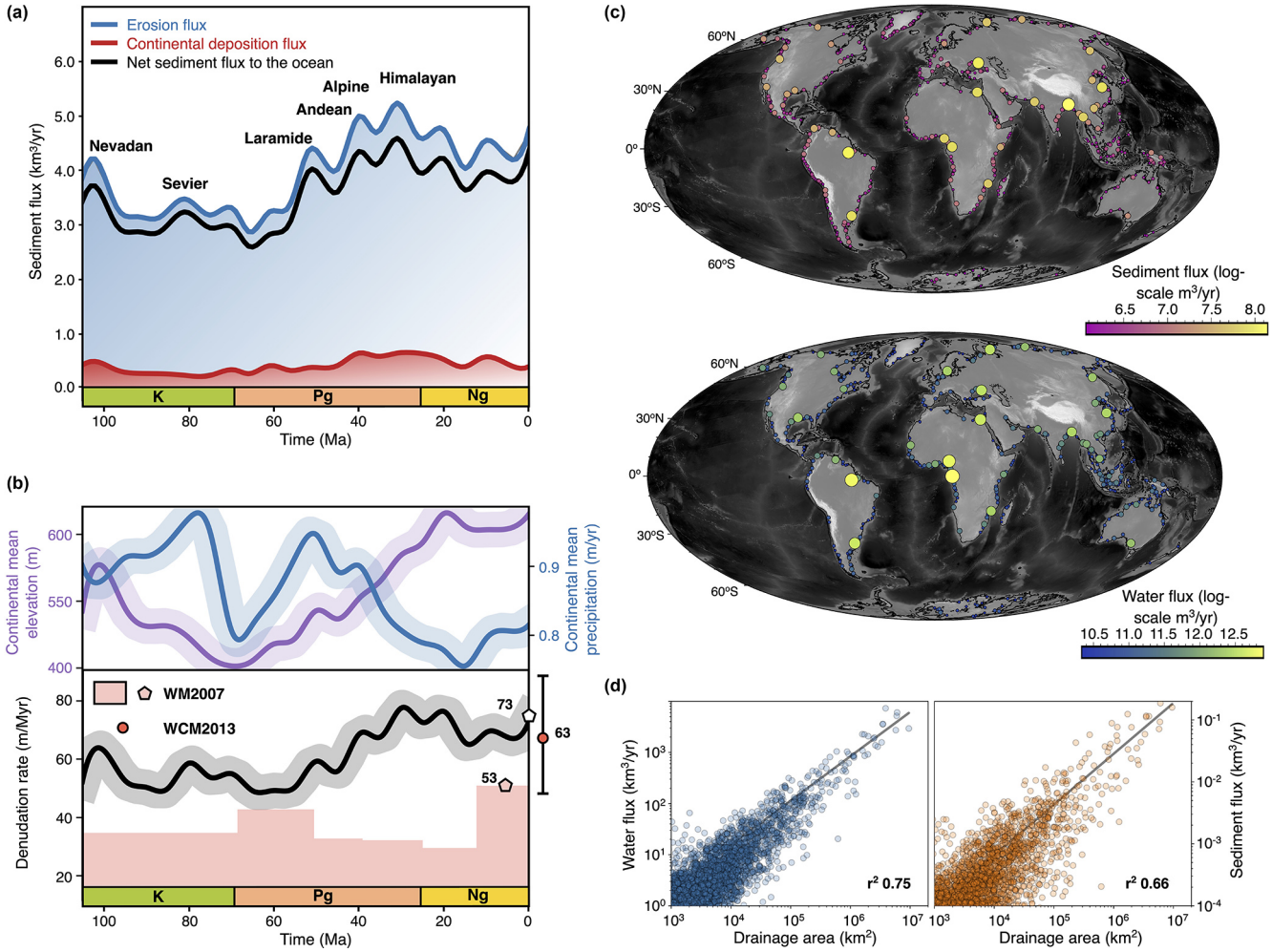

Figure 3. Reconstructed sediment fluxes and continental sedimentary basin evolution. **(a)** Simulated global average trends in erosion rate, net sediment flux delivered to the ocean, and cumulative deposition areas for the Phanerozoic with major orogenic episodes over the past 100 Myr. **(b)** Global changes in continental paleo-precipitation (Valdes et al., 2020) and paleo-elevation (Scotese and Wright, 2018) (top panel) and comparison of predicted long-term mean denudation rate with estimates from preserved sediments (WM2007 Wilkinson and McElroy, 2007) and recent rates compiled in WCM2013 (Willenbring et al., 2013) **(c)** Distribution of the 500th largest rivers water and sediment flux at 0 Ma. **(d)** Log–log plots representing the distribution of modeled water discharge and sediment flux against basin drainage area (blue and orange circles respectively). Relationship between the two variables is calculated with a power law curve fitting and is represented by the black lines.

has experienced more active subduction in the Late Neogene and is characterized by thermal uplift (Ramos, 2009). In the southern part, the uplift is associated with ridge collision, which is a result of the closure of back-arc oceanic basins (Ramos, 2009).

The Western Cordillera and Andean Belt host together the world's largest concentration of porphyry copper deposits, 177 in total (Fig. 4). Among these, the majority have an Eocene–Oligocene age (82 deposits), followed by Miocene to Pliocene (49 deposits) and Paleocene ages (46 deposits). Emphasis is given later to the Andean Belt, as it holds most of the known deposits.

The West Pacific Orogenic Belt, considered a polycyclic orogeny, has undergone repeated tectonic activity and magmatism since Late Precambrian (Matsumoto, 1977). The subduction of the Pacific Plate beneath the Eurasian continent resulted in the formation of island arcs that migrated toward the Pacific Ocean (Aubouin, 1990; Izosov et al., 2020). These collision events occurred between the Middle Paleogene and Neogene and are responsible for a major regional plate reorganization and contributed to the present-day configuration of the magmatic arcs (Hedenquist et al., 2012). The development of porphyry copper deposits within the West Pacific Orogenic Belt is associated with the reorganization of tectonic plates during the Early to Middle Miocene (Hedenquist et al., 2012).

The West Pacific Orogenic Belt encompasses a total of 66 known porphyry copper deposits, with the majority be-

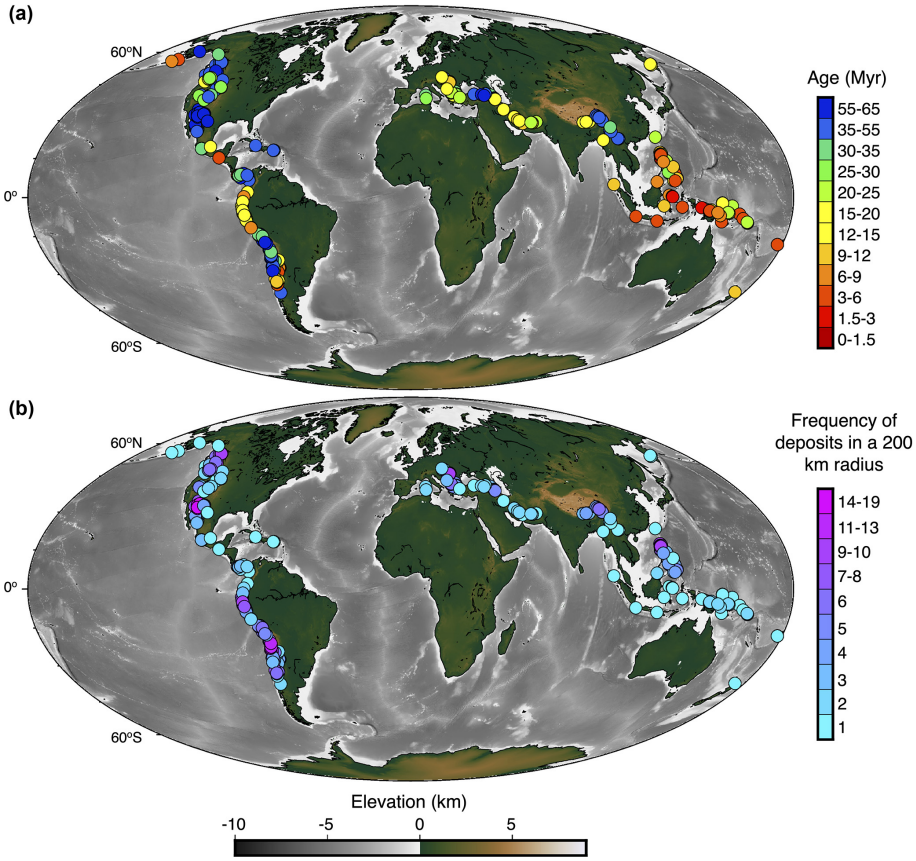

Figure 4. Distribution of Cenozoic porphyry copper deposit ages and deposit frequency. Panel **(a)** shows the deposit ages with warm colors representing young ages, whereas cool colors represent old ages (Singer et al., 2008). Panel **(b)** highlights the Cenozoic porphyry copper deposits counted within a 200 km radius of each central deposit. Warm colors represent high frequency, whereas cool colors represent fewer deposits (Yanites and Kesler, 2015).

ing of Miocene to Pliocene age (55 deposits). The remaining 11 deposits of Eocene–Oligocene ages are principally found in Papua New Guinea and in the Philippines.

The development of the Alpine–Himalayan Orogeny results from a transpressive tectonic regime where the African, Arabian, and Indian tectonic plates underthrust the Eurasian continental plate (Storetvedt, 1990). This following collisional process commenced in the Late Cretaceous (Stefanini and Williams-Jones, 1996; Perello et al., 2008), leading to the closure of the Tethys Ocean and to major phases of mountain building, forming the Alpine belt during the Paleocene (Storetvedt, 1990; Handy et al., 2015). In the Asian portion of the orogeny, the Himalayan Belt rose rapidly between the Middle Eocene and the Late Miocene due to the breakoff of the Neo-Tethyan slab (Ji et al., 2020, 2016).

The Alpine–Himalayan Orogeny encompasses a total of 71 known porphyry copper deposits. The two oldest deposits, dating back to the Paleocene, are located in the older section of this orogeny, namely the Alpine Orogeny. This deformation belt also contains a higher number of Eocene to Pleistocene deposits (44 ore bodies) when compared to the ones found on the Himalayan Mountain range (25 ore bodies).

3.2 Paleoclimatic evolution

We analyzed the paleo-precipitation reconstructions from Valdes et al. (2017) to evaluate variations in precipitation conditions through time for each of the three tectonic regions of interest.

The northern part of the Western Cordillera, where deposits do not exceed 64 Myr (Yanites and Kesler, 2015) of age, initially experienced humid conditions with mean precipitation levels around $5\,\mathrm{m\,yr^{-1}}$ (Valdes et al., 2017). The region then gradually becomes drier, with present-day precipitation values reaching $\sim 3\,\mathrm{m\,yr^{-1}}$ (Fig. A1) (Valdes et al., 2017). The central portion of the Cordillera (Laramide Orogeny) started as a dry environment with precipitation rates as low as $0.1\,\mathrm{m\,yr^{-1}}$ at the time of the formation of the first deposits, followed by an increase of up to $3\,\mathrm{m\,yr^{-1}}$ in recent times (Fig. A1). A similar pattern can be observed for the deposits found in Alaska. In contrast, the southern regions of the Western Cordillera, encompassing Mexico and

Central America, have experienced three main paleo-climatic conditions. During the early Cenozoic, these regions were characterized by a wet tropical climate with precipitation rates of up to 7 m yr^{-1}. From 20 to 10 Ma, these regions became drier, with precipitation of the order of 1 m yr^{-1}. For the last 10 Ma, the precipitation increased reaching up to 6 m yr^{-1} (Fig. A1).

In the central part of the Andean Belt, where the oldest deposits (64 Ma) are concentrated, we note a slow increase in rainfall since their emplacement, from 1 m yr^{-1} to nearly 2 m yr^{-1} around 10 Ma (see Fig. A1). From this point forward, the paleo-climate reconstructions show a wetter regime with rainfall reaching up to 3 m yr^{-1} at present-day. The younger deposits, in the southern portion of the Andean Belt, experienced a decrease in rainfall since their emplacement (22 Ma), with precipitation varying from 2 to 1 m yr^{-1}. In the northern Andean Belt, where the deposits are mainly from the Neogene, we note an overall high precipitation regime, where the rainfall fluctuates from 6 m yr^{-1} at 20 Ma to slightly drier conditions at 5 Ma (4 m yr^{-1}) and up to 8 m yr^{-1} in the present day (Fig. A1).

In the Alpine–Himalayan Orogeny, the oldest deposits in the Alps have transitioned from a predominantly dry climate to sporadic episodes of enhanced precipitation. The Eocene to Neogene Alpine deposits have generally remained under relatively dry conditions (1 m yr^{-1} at 40 Ma), with the exception of the last 5 Myr, where we note an increase of up to 4 m yr^{-1} precipitation (Fig. A1). For the deposits in the Himalayas, which date back no further than 46 Ma, there has been an overall increase in precipitation regimes that varied from 1 m yr^{-1} at 50 Ma to up to 6 m yr^{-1} in the present day (Fig. A1).

In the West Pacific Orogenic Belt, the deposits are no older than 31 Ma. Except for porphyry bodies of Oligocene age, all the younger deposits were emplaced in regions under tropical climatic conditions, where precipitation levels reached up to 8 m yr^{-1} and remained under stable precipitation forcing for the past 25 Ma (Fig. A1). As for the older deposits, we can track back their evolution to locations with lower precipitation rates. As an example, the deposits in Papua New Guinea, between 20–10 Ma, experienced fluctuations in precipitation ranging from 1 to 4 m yr^{-1}.

3.3 Global evaluation of predicted porphyry copper emplacement depths

Based on temporal variations of tectonics and climate forcings, we calculate exhumation rates and estimate emplacement depths for the 314 deposits described in Yanites and Kesler (2015). Our analysis utilizes the predicted erosion rates extracted from the simulation performed with *goSPL* (see Sect. 2) (Fig. 5). An emplacement depth of 2 km was assumed in Yanites and Kesler (2015), combined with known ages of the porphyry deposits, to estimate exhumation rates that were then benchmarked against independent measurements for 30 of these deposits (Singer et al., 2008). Their findings revealed a mean difference of 0.062 mm yr^{-1}. Predicted exhumation rates from landscape evolution simulation for the same deposit sites show a comparable mean difference of 0.04 mm yr^{-1} with Singer et al. (2008) measurements (Fig. 5a). These results indicate that the findings obtained from both approaches have the same order of magnitude, indicating a high level of similarity and comparability.

In our approach, exhumation rates and emplacement depths are calculated at the location of each of the 314 deposits as well as their surrounding area (within a 25 km diameter). Measuring the surrounding area mitigates potential distortion arising from low-resolution data (Fig. 5b and c). Mean simulated exhumation rates range from 0.002 to 0.620 km Myr^{-1}, with a normal centered distribution around 0.1 km Myr^{-1} (Fig. 5b). The distribution pattern of these rates is consistent with the exhumation rates extrapolated by Yanites and Kesler (2015), which were inferred based on the chronological record of the deposits (illustrated in Fig. 5d). Additionally, a latitudinal analysis of the deposits suggests a correlation between geographic location, reflective of climatic conditions, and both exhumation rates and emplacement depths (Fig. 5d). Of the 36 deposits with exhumation rates exceeding 0.3 km Myr^{-1}, the majority (25) are situated within the southern tropical belt (0–15° S-band). For the remaining ones, none of them are found outside 16° N and 17° S latitudes. Exhumation rates smaller than 0.3 km Myr^{-1} are evenly distributed across latitudes (Fig. 5d).

As expected, we find a relation between the ages of deposits and their exhumation rates (Fig. 5e). The older the deposits are, the smaller the rates tend to be, a trend that is aligned with previous findings (Yanites and Kesler, 2015). Also, within similar emplacement depths, older deposits tend to have smaller exhumation rates (Fig. 5e), conformable with literature data (Yanites and Kesler, 2015; Singer et al., 2008). Yet, climate exerts a strong influence on the exhumation patterns. The largest calculated exhumation rate (0.6 km Myr^{-1}) is seen in Ecuador, for a deposit of 20 Myr old. This contrasts with a neighboring deposit of 15 Myr old with an exhumation rate of 0.5 km Myr^{-1}.

We found that the simulated emplacement depths from the landscape evolution model are typically at 2 km or shallower (Fig. 5c), which is consistent with values proposed in the literature (Richards, 2022; Sillitoe, 2010; Yanites and Kesler, 2015). Although we note that the deepest calculated emplacement depths occur between 0–30° S (Fig. 5d), no strong correlation between the distribution in latitudinal bands (indicative of prevailing climate) and calculated emplacement depth is observed, as expected. While our analysis reveals relevant impact of climate on these calculations, it is important to emphasize that climatic factors alone do not solely dictate these estimations.

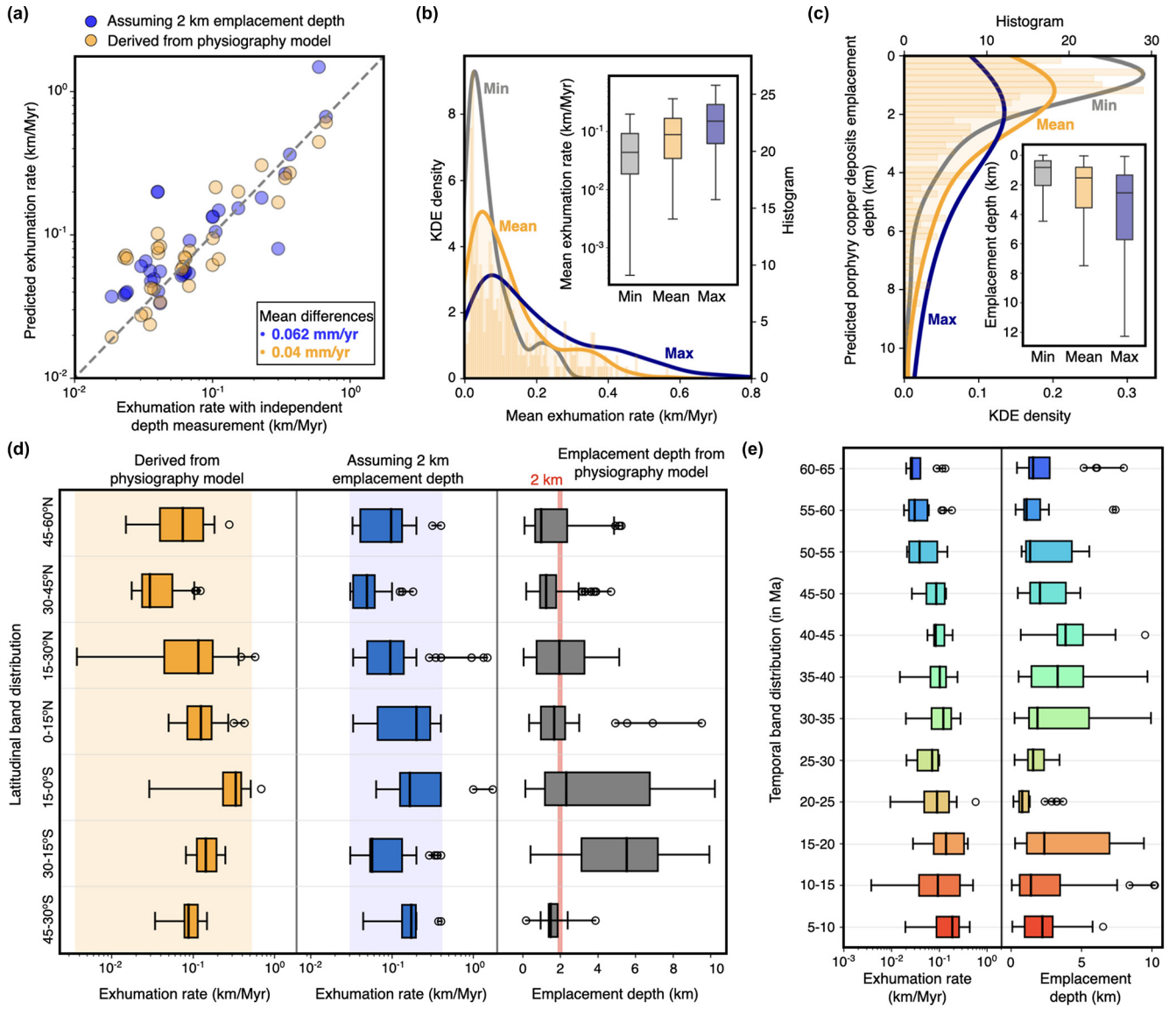

Figure 5. Global evaluation of exhumation rates and emplacement depths of porphyry copper deposits. **(a)** Comparison between exhumation rates using the independent depth estimate for 30 samples (Yanites and Kesler, 2015) and predicted rates assuming a 2.0 km emplacement depth and obtained from the enhanced paleo-elevation model. **(b)** Distribution of the predicted mean exhumation rates from the porphyry copper deposits (Singer et al., 2008) assuming a 25 km surrounding area for each site. **(c)** Calculated porphyry copper deposit emplacement depth distribution from the mean exhumation rates calculated in **(b)**. Box-and-whisker plots of exhumation rate distributions in 15° bands with the associated emplacement depths **(d)** and temporal distributions based on deposit ages (Singer et al., 2008) using 5 Myr bands (**e**).

4 Discussion

4.1 Exhumation rate (ER) and emplacement depth (ED)

Approximately 50 % of the averaged values for calculated exhumation rate and emplacement depths align with independent data published in the literature (Yanites and Kesler, 2015; Singer et al., 2008). However, discrepancies arise when comparing individual deposit data.

For instance, the lowest simulated exhumation rates are for deposits in the westernmost part of Pakistan (Reko Diq complex) and Iran, with values ranging from 0.002 to 0.007 km Myr^{-1} and ages varying between 11–21 Ma. In the literature, the ER values obtained based on the thermal history for the Reko Diq complex range between 0.20–0.79 km Myr^{-1} (Fu et al., 2005). Another example is the world's youngest giant porphyry Cu–Au deposit, Ok Tedi in Papua New Guinea (dated at 1.4 Ma, van Dongen et al., 2010), which has calculated exhumation rates of 0.3 km Myr^{-1}. In contrast, the exhumation rate derived from SHRIMP age data is between 3–5 km Myr^{-1} (van Dongen

et al., 2007). It is important to mention that both aforementioned examples are of deposits situated in highly active tectonic regions.

The emplacement depths of deposits like Butte (Rusk et al., 2008) in Montana (USA) and Panguna (Eastoe, 1978) (eastern Papua New Guinea), obtained from fluid inclusion, vary from 5 to 9 km and 2 to 3 km, respectively. The predicted emplacement depth from the landscape evolution model for Butte deposit is 1.8 km and for Panguna 0.9 km. In Sect. 2, we discussed several assumptions and simplifications from the landscape evolution model. Moreover, the model carries inherent uncertainties from the initial input data (paleo-elevation and paleo-precipitation) and assumes that all deposits are exposed at the surface and have experienced minimal erosion.

The Andean Belt per se concentrates 90 of the studied porphyry copper deposits. Their distribution can be associated with the presence of the morphostructural volcanic zones, which are mainly controlled by the absence of flat-slab subduction for at least the past 12 Myr (Ramos, 2009). The absence of PCDs in some latitudinal bands along the Andean Belt (e.g., between 10–13° S – Fig. 6a) coincides with the presence of flat-slab subduction in the past 12 Ma to present and the presence of aseismic ridges, like the one formed by the Nazca Plate collision (Ramos, 2009).

Remarkably, nearly all the highest exhumation rates were calculated within the Andean Belt, which is consistent with high precipitation rates described for the region (see Sect. 3.2). Additionally, all inferred emplacement depths exceeding 5 km were exclusively found within this region (Fig. 6a). When contrasting exhumation rate values obtained from Yanites and Kesler (2015) with those derived from our study for the three specific sites depicted in Fig. 6a, the results indicate that our model yields slightly lower exhumation rate values (Fig. 6b and c). Despite this difference in exhumation rate, the projected emplacement depth for these sites lies between 2–3 km (Fig. 6c).

4.2 Paleo-elevation

We acknowledge that the paleo-elevation model provided in the Scotese and Wright (2018) PALEOMAP dataset is associated with non-quantified uncertainties, which can also drastically influence our results. As no other continuous open-source global paleo-elevation model exists for the period of interest, we evaluate differences between Scotese and Wright (2018) and Boschman (2021) paleo-elevation models in South America. The study by Boschman (2021) reconstructs the paleo-elevation of the Andes for the last 80 Myr. Their reconstruction is derived from a compilation of paleo-elevation estimates collected from various sources in the literature (e.g., palynology, stable isotopes, thermochronology, fossil).

The comparison between Boschman (2021) and Scotese and Wright (2018) (Fig. A2) shows that the further back in time, the more discrepancies arise, with differences of up to 3000 m in elevation. For deposits located towards the north of 15° S, the differences tend to decrease in the last 15 Ma (see Fig. A2a and b). South of 15° S (see Fig. A2c), we note that between 20–5 Ma, elevation values from Scotese and Wright (2018) tend to underestimate elevations proposed by Boschman (2021), with differences of nearly 2000 m. Aside from the complex geology in and within these regions as will be discussed in Sect. 4.5, the differences in elevation calculations are attributed to the varying levels of detail in global (Scotese and Wright, 2018) vs. regional (Boschman, 2021) models. Considering that the landscape evolution model resolution is 5 km, a difference of 2000 m from different datasets is not negligible. In addition, changes in elevation can also imply differences in slope, which are likely to impact the resulting erosion rates.

Another method to interpret topography consists in describing its morphological features in the form of wavelengths signals (basic land surface parameters) (Olaya, 2009). The impact of tectonics (e.g., mountain building or collapsing) on the landscape can be associated with long-wavelength signals and therefore more likely to be represented in a global reconstruction. However, short wavelengths are comparable to smaller-scale events that shape the relief (e.g., canyons or incised channels, Richards et al., 2020), and those tend to be absent in global reconstructions. An example of oversimplification inherent to the global model resolution is reflected in the final calculation of the copper province Reko Diq complex in Pakistan. This landscape is shaped by complex tectonic processes, such as collision, post-collision extension, and back-arc rifting, resulting in 26 magmatic belts (Zürcher et al., 2019). The exhumation rate derived from our model for this region (0.007 km Myr^{-1}) is 2 orders of magnitudes smaller than that observed in the literature (Fu et al., 2005). This discrepancy can be attributed to the lack of detail in the paleo-elevation database, contributing to a likely inaccuracy in exhumation rate estimate.

In terms of initial elevation, we followed the assumptions proposed in Yanites and Kesler (2015), which state that present-day porphyry bodies encountered at the surface suffered negligible erosion since their emplacement. However, blind porphyry copper deposits, e.g., the Paleogene Resolution Deposit in Arizona (USA), demonstrate that this assumption is incorrect and not insignificant for all deposits. The Resolution Deposit was found beneath 2 km of postmineral cover (Hedenquist et al., 2012) and therefore theoretically not at the surface yet. Similarly, other deposits may have been eroded away, presenting only the remaining few kilometers of the porphyry body. These mistaken assumptions have implications in the final calculations of exhumation rate. For instance, for the Resolution Deposit, the lack of an extra 2 km sediment cover could reflect in an increased exhumation rate calculation from the model.

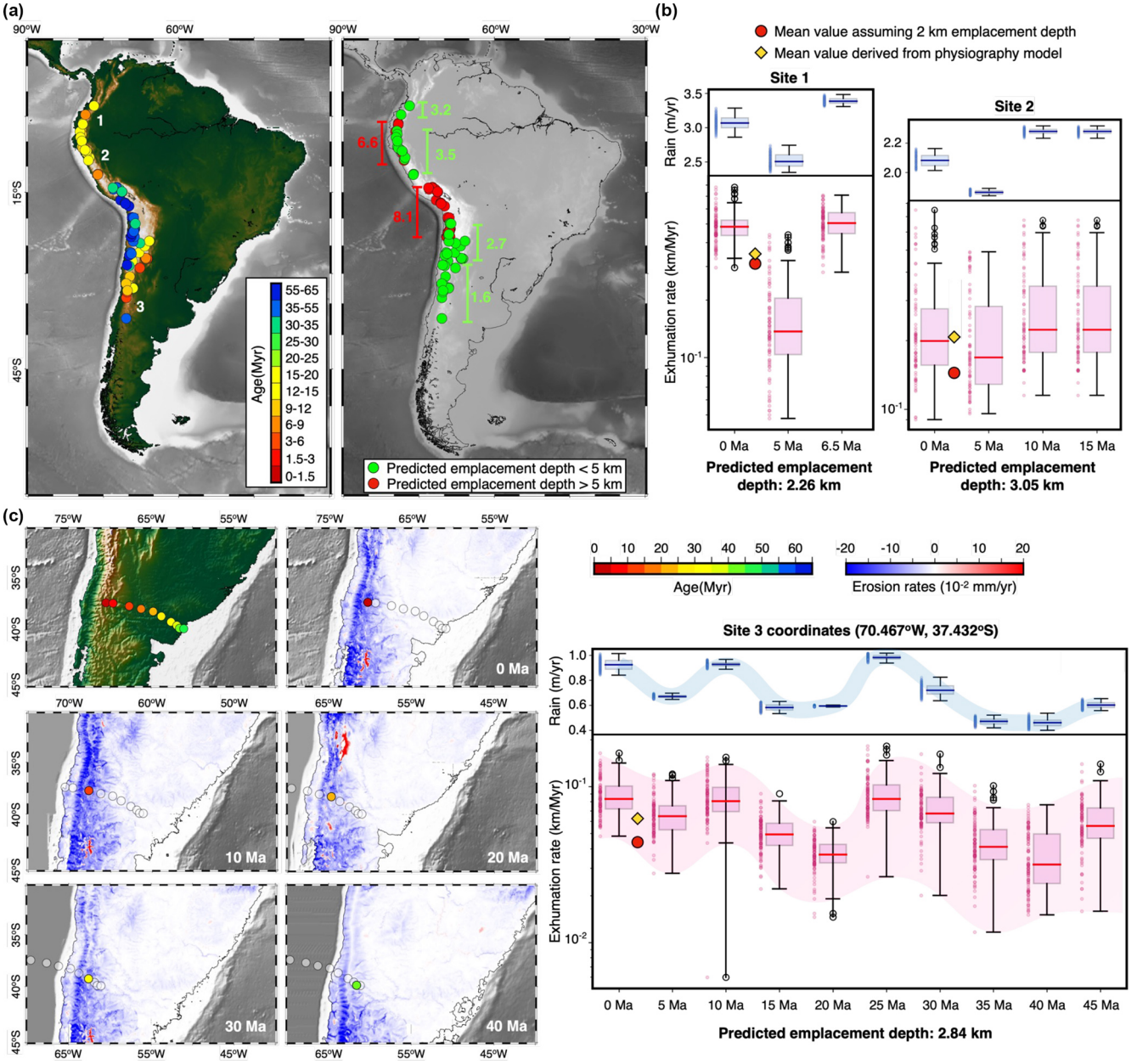

Figure 6. Evaluation of South America porphyry copper deposits exhumation histories and emplacement depths. **(a)** South America copper deposits formation ages (Singer et al., 2008; Yanites and Kesler, 2015) and predicted emplacement depths from the exhumation rates modeled with the enhanced paleo-elevation simulation. **(b)** Histories of exhumation induced by the surface processes action forced by paleo-precipitation (Valdes et al., 2020) and paleo-elevation (Scotese and Wright, 2018) for porphyry copper deposit sites 1 and 2 (defined in **b**). **(c)** Reconstructed positions of site 3 (defined in **a**) over time based on deposit age and the plate reconstruction rotations (PALEOMAP Scotese and Wright, 2018), showing the evolution of erosion and deposition rates (blue and red respectively). Right panel shows box-and-whisker plots of simulated precipitation (Valdes et al., 2020) and exhumation rates within a 25 km radius around the deposit site.

4.3 Paleo-climate data

The presented exhumation rates and emplacements depths have been calculated considering the paleo-elevation derived from Scotese and Wright (2018) and associated global paleo-climate model (HadCM3BL-M2.1aD Valdes et al., 2020). The modeling approach presented here depends on data resolution of the paleo-reconstruction models used and the differences that exist between different simulations (Valdes et al., 2020; Li et al., 2022). We acknowledge that rainfall highly impacts the evolution of physiography/paleo-elevation and therefore impacts the presented results.

To better understand the uncertainties associated with the imposed rainfall conditions, we analyzed an additional simulation that considers the paleo-climate reconstruction from Li et al. (2022) and compared the results with those obtained using Valdes et al. (2020) simulation (Fig. A3). Overall, the model by Li et al. (2022) shows higher precipitation than in Valdes et al. (2020).

For regions where PCDs are present, the difference in precipitation reaches up to $4\,\mathrm{m\,yr^{-1}}$, e.g., in the northern portion of South America (Fig. A3), which results in a mismatch in erosion/deposition rates between -1 to $2\,\mathrm{mm\,yr^{-1}}$ (Fig. A4). When taken into account since estimated deposit ages, these variations can lead to discrepancies of up to 1 km of erosion or deposition for every million years.

Rainfall values obtained from global models for specific regions also contrast. For instance, precipitation values for deposits formed in the Laramide Orogeny (e.g., Butte deposit) obtained from the global model from Valdes et al. (2020) vary from 0 to $3\,\mathrm{m\,yr^{-1}}$ (as seen in Sect. 3.2). However, higher-resolution precipitation obtained only for the Laramide Orogeny shows values from 0.5 to $1.7\,\mathrm{m\,yr^{-1}}$, between 0–40 Ma (Retallack, 2007). As a result, our approach considers a paleo-precipitation value that is doubled compared to higher-resolution data (Retallack, 2007). These discrepancies in input data reflect on how the emplacement depths might diverge depending on the chosen climatic forcing. Other regions, such as the Alpine Orogeny, also show discrepancies in precipitation data used in the model (Valdes et al., 2020) and data acquired specifically for the region (Bruch et al., 2011).

4.4 Erodibility

While *goSPL* (Salles et al., 2020) is capable of incorporating spatially variable erodibility values, the data resolution for lithologies in most orogenic belts remains insufficient, especially when exploring deeper time periods. Therefore, our approach accounts for a single erodibility component (ϵ) ($4.0 \times 10^{-7}\,\mathrm{yr^{-1}}$), which implies a single and global type of rock coverage.

Even though PCDs are often present in similar tectonic environments and lithologies, considering a single erodibility component is an oversimplification, which, propagated over simulation time, leads to significant discrepancies. Moosdorf et al. (2018), for instance, introduce a global erodibility index where six distinct erodibility values are classified for the present day. Their index is determined by the slopes distributed across lithology classes and their comparison to slopes relative to acid plutonics. Essentially, the lower the average slope of a lithological unit compared to that of acid plutonics, the higher the erodibility index.

In the Central Andean Belt, we identify at least four different rock types varying between granitic, rhyolitic, andesitic, and volcano-sedimentary (Geological Map of South America – 1 : 5 000 000, Gómez et al., 2019). According to Moosdorf et al. (2018), six erodibility indexes were classified in this region, in contrast to the single one applied in the model. In Sect. 4.1, we show that all the emplacement depths that exceed 5 km occur within the Central Andean Belt. This suggests that the erodibility value (ϵ) applied for the region is probably too high, predicting deeper emplacement depths. Upon availability, adding refined lithology maps into the simulation could improve some of these identified mismatches.

4.5 Volcano-sedimentary re-burial

All the calculated emplacement depths exceeding 5 km are found within the Central Volcanic Zone (Ramos, 2009) (14–27° S) in the Central Andes, except for one deposit in the Northern Volcanic Zone in Northern Andes (Ramos, 2009). The Central Volcanic Zone is well known for its complex tectonic evolution (Ramos, 2018; Nocquet et al., 2014) associated with hyper-arid climatic conditions since the Late Miocene (Nocquet et al., 2014; Stern, 2004; Reich et al., 2009), leading to low sediment supply (Stern, 2004). The crust of the Central Volcanic Zone is older than its surroundings, exceeding 70 km in thickness (Montgomery and Brandon, 2002; Stern, 2004; Portner et al., 2020), and is delimited from the Northern and Southern Andes by volcanic gaps (Nur and Ben-Avraham, 1983). These volcanic gaps are linked with the Peruvian and Pampean flat slabs (Portner et al., 2020), whilst the Central Volcanic Zone is marked by the normal subduction of the Nazca Ridge (Portner et al., 2020), leading to significant volcanism in the region. Moving southwards from the Pampean flat slab (27–33° S) is the Southern Volcanic Zone (33–46° S), which is geologically similar to the Central Volcanic Zone (Stern, 2004; Ramos, 2009).

The volcanism in the Central Volcanic Zone is marked by a significant volume of lava and ignimbrite that has erupted since at least the Early Miocene (ca. 20 Ma) and reaching up to 12×10^3 km^3 (Baker and Francis, 1978). Similarly, the Southern Volcanic Zone has had expressive volcanism from the Late Miocene to Early Pliocene, covering up to $40\,000\,\mathrm{km^2}$ (Hernando et al., 2019). The re-burial process associated with the overlaying of volcaniclastic rock is not accounted for in our study (Salles et al., 2023). Therefore, the model accounts for less sedimentation than what has been deposited, suggesting overestimated emplacement depth estimations. On the other hand, for the deposits younger than 20 Myr in the Pampean flat slab, where volcanic activity is limited, we find emplacement depths that coincide with the smallest depth calculations for South America (< 2 km, Fig. 5d).

Re-burial processes can also initiate flexural responses, which are implicitly accounted for in the model. These processes are particularly significant in the Northern Andes, where the interplay between flexural isostasy and surface processes helps explain the drainage reversal of the Amazon River (Sacek, 2014). The isostatic effect of volcanic loading can induce local subsidence, which, if not taken into account,

may lead to overestimation of the final exhumation rates. Conversely, neglecting flexural isostasy associated with sediment unloading can result in an underestimation of exhumation rates.

5 Conclusions and future work

Understanding the influence of surface processes on porphyry copper deposit preservation is essential for determining how these deposits can be exhumed to mineable depths or be eroded away altogether. Several studies using machine learning attempted to predict the fertility of a porphyry copper province based on geological, metallogenic and statistical analyses (e.g. Keykhay-Hosseinpoor et al., 2020; Diaz-Rodriguez et al., 2021; Nathwani et al., 2022; Jafrasteh et al., 2018; Abbaszadeh et al., 2021), neglecting the strong effects of climate on deposit exhumation and preservation. Here, we have demonstrated how slight changes in climate impact the exhumation of porphyry copper deposits. We aim to inspire future research in the field of machine learning to consider the role of climatic contributions in deposit preservation and secondary supergene enrichment of copper near the surface.

The landscape evolution model proposed in this study is innovative as it is the first to globally incorporate both paleo-elevation and paleo-precipitation reconstructions in assessing exhumation rates and emplacement depths of porphyry copper deposits. This new approach not only provides a comprehensive global understanding of the correlation between climate history and the existence of the major porphyry copper provinces but also shows how this technique can be more efficiently applied for regional porphyry copper exploration given better spatial resolution in the input datasets.

We have shown that the approach effectively replicates calculations of emplacement depths on a global scale, with approximately 50 % of the values falling within the anticipated ranges of emplacement depth. In addition, our approach allows for quantifying the complex relationships between climate, tectonics, physiography, and porphyry copper preservation and could be extrapolated as an exploration tool for assessing the probability of undiscovered porphyry copper deposit preservation.

Inherent to any numerical model are simplifications and assumptions. In this case, factors such as erodibility, reburial, initial depth of deposit, and surface rock lithologies are recognized as oversimplified. We also highlight how minor variations in a dataset can contribute to disparities in final predictions and potentially misleading interpretations, underscoring that uncertainties are influenced by model assumptions and dataset resolution. Due to such simplifications and uncertainties, some of our calculated values for exhumation rates and emplacement depths do not match data found in the literature. Nevertheless, we have established workflows that enable us to test and quantify the differences between different paleo-datasets (either paleo-climate or paleo-elevation). By identifying which dataset (paleo-elevation or paleo-rainfall) or simplifications most affect the model, we aim to target future directions for model improvements.

Appendix A

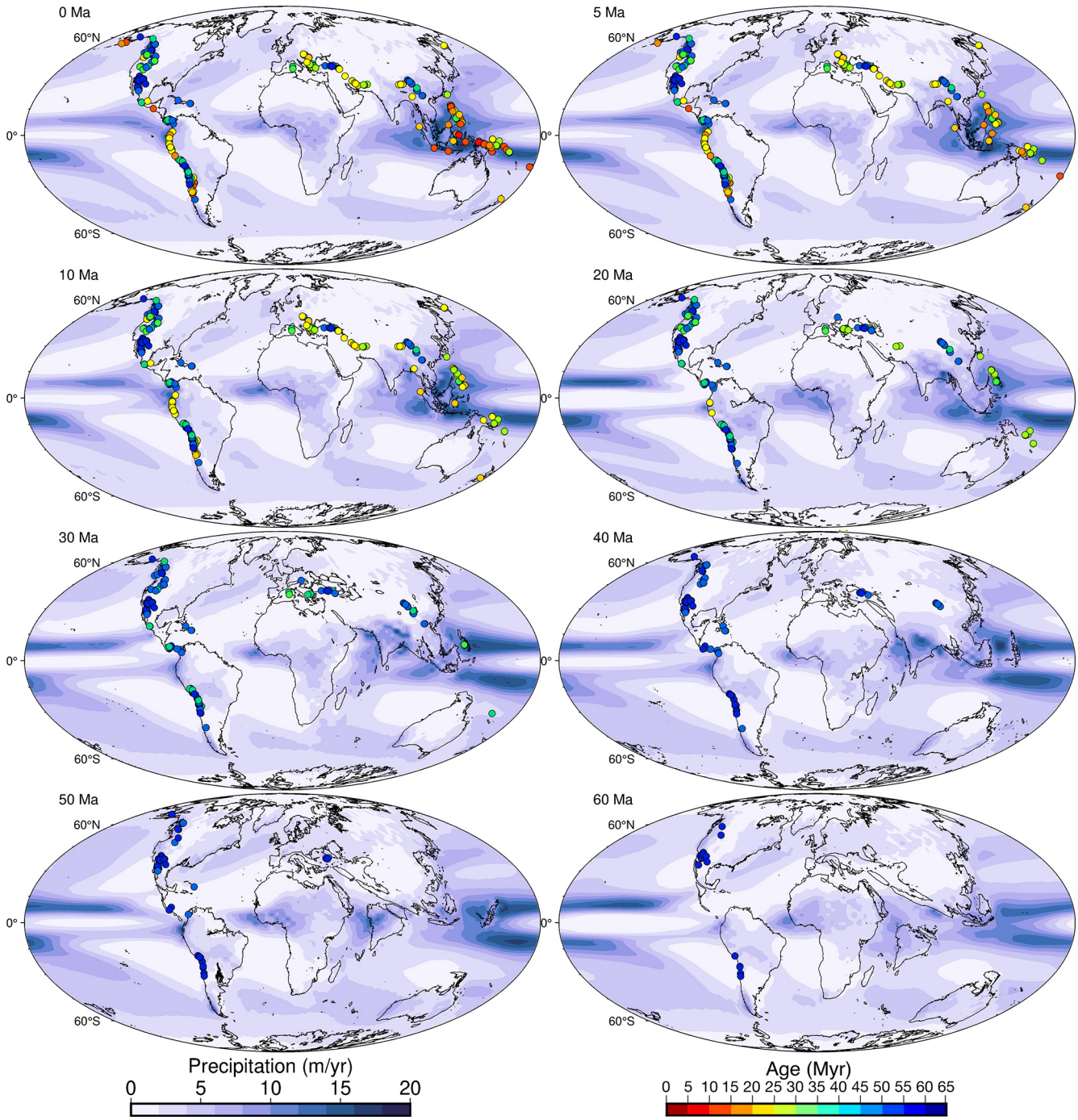

Figure A1. Global paleo-precipitation maps over the past 60 Ma. Darker blues represent higher precipitation, which is usually recurrent over the equatorial region. White patches depict dry regions. The location of each PCD is projected on the maps as from their age of emplacement.

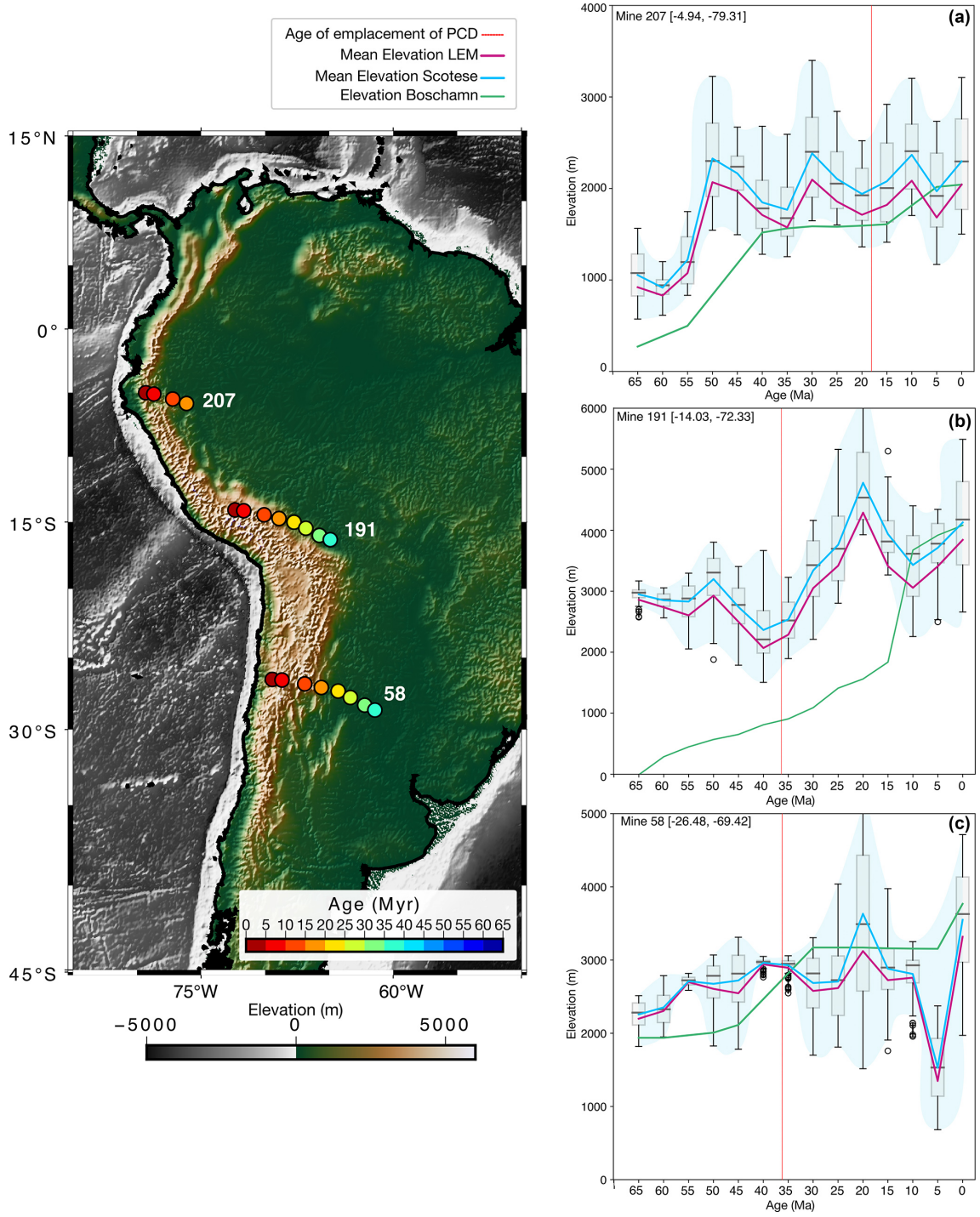

Figure A2. Mean elevations around 25 km radius from a point over time (left) considering the different datasets: Scotese and Wright (2018) PALEOMAP, *goSPL* Salles et al. (2023), and Boschman (2021) The whisker plots and the blue line refer to the dataset from PALEOMAP (Scotese and Wright, 2018). The green line shows the elevation values from Boschman (2021) model. The pink line is the mean elevation from the landscape evolution model from Salles et al. (2023). The red line shows the age of emplacement of the porphyry copper deposit related to the depicted location.

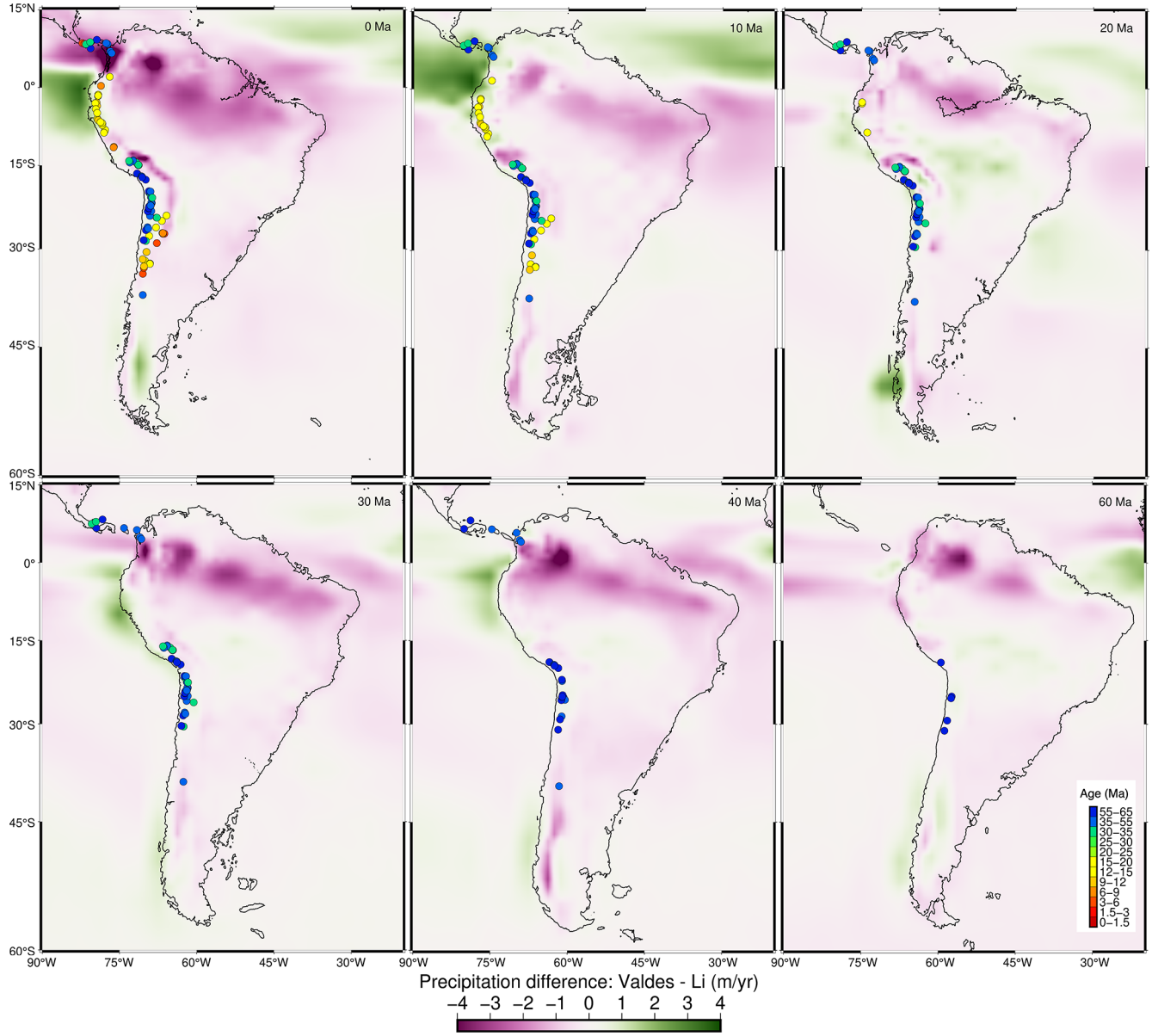

Figure A3. Differences in precipitation over time between paleo-climate models. Negative values (purple) represent precipitation conditions from Li et al. (2022), which are larger than the ones predicted by Valdes et al. (2020) (positive ones are shown in green).

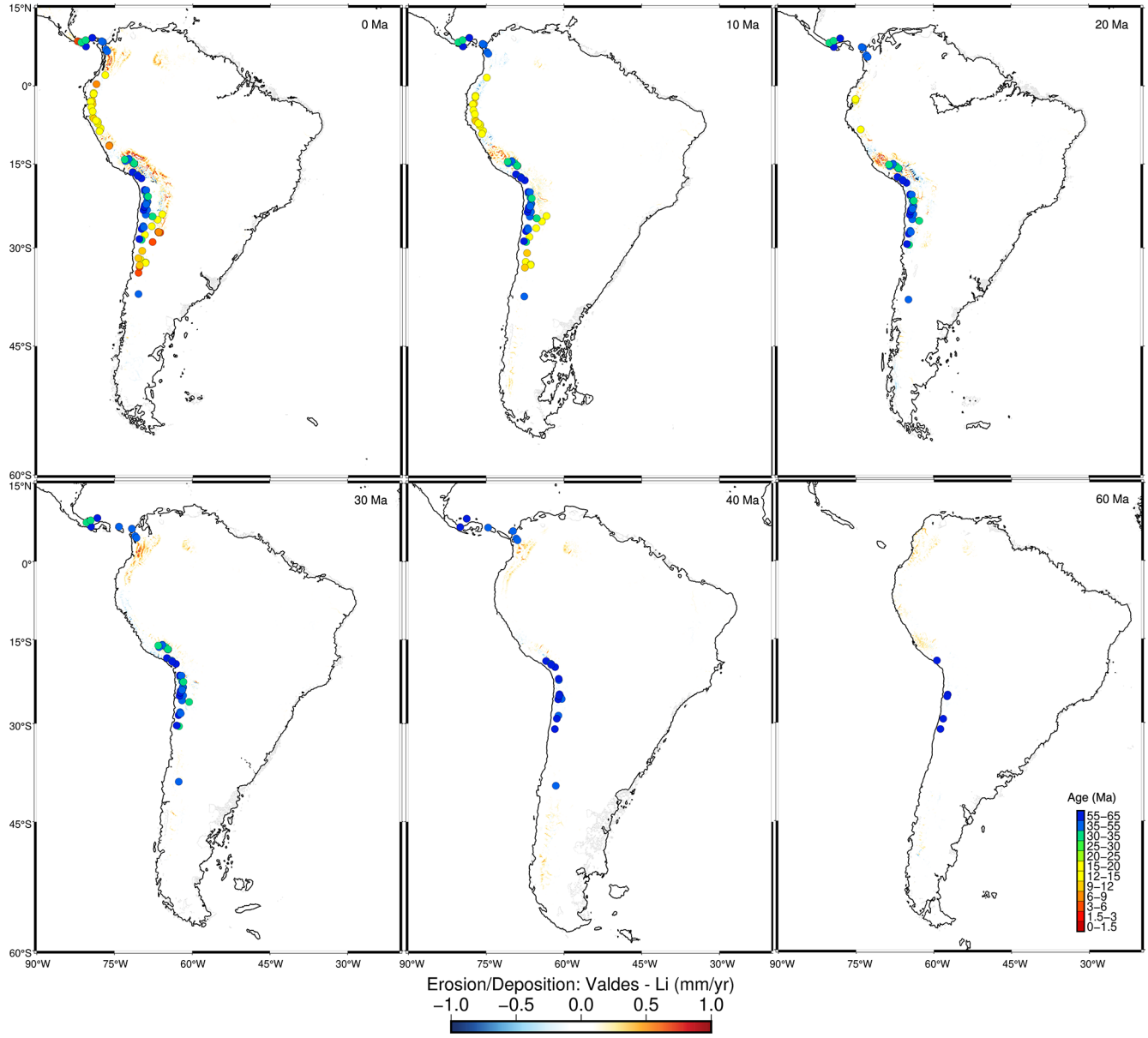

Figure A4. Differences in erosion/sedimentation through time between Valdes et al. (2020) and Li et al. (2022). Negative values represent where the precipitation from Li et al. (2022) is larger than that considered in Valdes et al. (2020) and positive ones the other way around.

Code availability. The scientific software used in this study, *goSPL* (Salles et al., 2020), is available from https://github.com/Geodels/gospl, and the software documentation can be found at https://gospl.readthedocs.io (last access: 5 August 2025). We also provide a series of Jupyter notebooks (https://doi.org/10.5281/zenodo.11239057, Hadler Boggiani et al., 2024) used for processing the datasets and model outputs that can be followed to reproduce some of the figures presented in the paper and can be accessed from https://github.com/Geodels/paleoPhysiography (Salles et al., 2022) and https://github.com/biahadler/porphyry-data (Hadler Boggiani et al., 2025).

Data availability. The PALEOMAP paleo-elevation reconstruction and related GPlates rotation and geometry files can be downloaded from https://doi.org/10.5281/zenodo.5460860 (Scotese and Wright, 2018). Paleo-precipitation maps from the HadCM3BL-M2.1aD model (Valdes et al., 2020) are available from the Bristol Research Initiative for the Dynamic Global Environment (BRIDGE) website https://www.paleo.bristol.ac.uk/ummodel/scripts/papers/Valdes_et_al_2017.html?utm_source=chatgpt.com (Valdes et al., 2017). All the maps with enhanced paleo-elevation reconstruction for the Phanerozoic are available from HydroShare: http://www.hydroshare.org/resource/0106c156507c4861b4cfd404022f9580 Salles et al., 2022. The

paleo-elevation reconstruction from Boschman (2021) is available from https://data.mendeley.com/datasets/h2w7pshz44/1. Paleoclimate simulations from Li et al. (2022) are available in the original article and can be accessed at https://figshare.com/articles/dataset/A_high-resolution_climate_simulation_dataset_for_the_past_540_million_years/19920662/1 (Boschman, 2021). The dataset containing the 314 studied mines in this project can be found within the Supplement of Yanites and Kesler (2015). We provide data as netCDF files for a few examples of mines that were used to produce Fig. A2 and the rotation file utilized in that as well, available at https://doi.org/10.5281/zenodo.11239057 (Hadler Boggiani et al., 2024).

Author contributions. BHB and TS conceived the study and conducted the numerical experiments, BHB, TS, and CM analyzed the exhumation rates. BHB wrote the initial draft, and all co-authors reviewed the manuscript.

Competing interests. The contact author has declared that none of the authors has any competing interests.

Disclaimer. Publisher's note: Copernicus Publications remains neutral with regard to jurisdictional claims made in the text, published maps, institutional affiliations, or any other geographical representation in this paper. While Copernicus Publications makes every effort to include appropriate place names, the final responsibility lies with the authors.

Acknowledgements. This work was undertaken through STELLAR (Spatio-temporal exploration for resources) industry collaboration supported by BHP. This research was undertaken with the assistance of resources from the National Computational Infrastructure (NCI), which is supported by the Australian Government, and from the Artemis HPC Grand Challenge, supported by the Sydney Informatics Hub at the University of Sydney.

Financial support. This research has been supported by the BHP (STELLAR Project) and the National Computational Infrastructure (Artemis HPC Grand Challenge).

Review statement. This paper was edited by Valier Galy and reviewed by Victor Sacek and one anonymous referee.

References

Abbaszadeh, M., Ehteram, M., Ahmed, A. N., Singh, V. P., and Elshafie, A.: The copper grade estimation of porphyry deposits using machine learning algorithms and Henry gas solubility optimization, Earth Sci. Inform., 14, 2049–2075, https://doi.org/10.1007/s12145-021-00667-6, 2021.

Aubouin, J.: The west Pacific geodynamic model, Tectonophysics, 183, 1–7, https://doi.org/10.1016/0040-1951(90)90185-B, 1990.

Baker, M. C. W. and Francis, P. W.: Upper Cenozoic volcanism in the Central Andes – ages and volumes, Earth Planet. Sc. Lett., 41, 175–187, https://doi.org/10.1016/0012-821X(78)90008-0, 1978.

Balay, S., Brown, J., Buschelman, K., Gropp, W. D., Kaushik, D., Knepley, M. G., McInnes, L. C., Smith, B. F., and Zhang, H.: Argonne national laboratory, PETSc, Web page, http://www.mcs.anl.gov/petsc (last access: 5 August 2025), 2012.

Baldwin, S. L., Monteleone, B. D., Webb, L. E., Fitzgerald, P. G., Grove, M., and June Hill, E.: Pliocene eclogite exhumation at plate tectonic rates in eastern Papua New Guinea, Nature, 431, 263–267, https://doi.org/10.1038/nature02846, 2004.

Bonetti, S. and Porporato, A.: On the dynamic smoothing of mountains, Geophys. Res. Lett., 44, 5531–5539, https://doi.org/10.1002/2017GL073095, 2017.

Boschman, L. M.: Andean mountain building since the Late Cretaceous: a paleoelevation reconstruction, Earth-Sci. Rev., 220, 103640, https://doi.org/10.1016/j.earscirev.2021.103640, 2021 (data available at: https://data.mendeley.com/datasets/h2w7pshz44/1 (last access: 21 May 2024).

Bruch, A. A., Utescher, T., and Mosbrugger, V.: Precipitation patterns in the Miocene of Central Europe and the development of continentality, Palaeogeogr. Palaeocl., 304, 202–211, https://doi.org/10.1016/j.palaeo.2010.10.002, 2011.

Butterworth, N., Steinberg, D., Müller, R. D., Williams, S., Merdith, A. S., and Hardy, S.: Tectonic environments of South American porphyry copper magmatism through time revealed by spatiotemporal data mining, Tectonics, 35, 2847–2862, https://doi.org/10.1002/2016TC004289, 2016.

Clennett, E. J., Sigloch, K., Mihalynuk, M. G., Seton, M., Henderson, M. A., Hosseini, K., Mohammadzaheri, A., Johnston, S. T., and Müller, R. D.: A quantitative tomotectonic plate reconstruction of Western North America and the Eastern Pacific Basin, Geochem. Geophy. Geosy., 21, e2020GC009117, https://doi.org/10.1029/2020GC009117, 2020.

Cooke, D. R., Hollings, P., and Walshe, J. L.: Giant porphyry deposits: characteristics, distribution, and tectonic controls, Econ. Geol., 100, 801–818, https://doi.org/10.2113/gsecongeo.100.5.801, 2005.

Diaz-Rodriguez, J., Müller, R. D., and Chandra, R.: Predicting the emplacement of Cordilleran porphyry copper systems using a spatio-temporal machine learning model, Ore Geol. Rev., 137, 104300, https://doi.org/10.1016/j.oregeorev.2021.104300, 2021.

Eastoe, C. J.: A fluid inclusion study of the Panguna porphyry copper deposit, Bougainville, Papua New Guinea, Econ. Geol., 73, 721–748, https://doi.org/10.2113/gsecongeo.73.5.721, 1978.

Foster, G. L., Royer, D. L., and Lunt, D. J.: Future climate forcing potentially without precedent in the last 420 million years, Nat. Commun., 8, 14845, https://doi.org/10.1038/ncomms14845, 2017.

Fu, F. Q., McInnes, B. I. A., Evans, N. J., Davies, P. J., Schloderer, J., Griffin, W. L., and Saeed, A.: Thermal and exhumation history of the Parra Koh porphyry CU-AU deposit, Pakistan: inverse numerical modeling of U-PB-HE data, Salt Lake City Annual Meeting, 16–19 October 2005, https://gsa.confex.com/gsa/2005AM/webprogram/Paper94905.html (last access: 5 August 2025), 2005.

Gómez, J., Schobbenhaus, C., and Montes Ramírez, N. E.: Geological Map Of South America At a Scale of 1: 5M, Tech. rep., Servicio Geológico Colombiano, https://doi.org/10.32685/10.143.2019.929, 2019.

Hadler Boggiani, B.: biahadler/porphyry-data: Porphyry Copper Workflows (PophyryCopper), Zenodo [code], https://doi.org/10.5281/zenodo.15400584, 2025.

Hadler Boggiani, B., Salles, T., Mallard, C. A., and Atwood, N.: Porphyry Copper Data, Zenodo [data set], https://doi.org/10.5281/zenodo.11239057, 2024.

Handy, M. R., Ustaszewski, K., and Kissling, E.: Reconstructing the Alps–Carpathians–Dinarides as a key to understanding switches in subduction polarity, slab gaps and surface motion, Int. J. Earth Sci., 104, 1–26, https://doi.org/10.1007/s00531-014-1060-3, 2015.

Hedenquist, J. W., Harris, M., and Camus, F.: Geology and Genesis of Major Copper Deposits and Districts of the World: A Tribute to Richard H. Sillitoe, Society of Economic Geologists, https://doi.org/10.5382/SP.16, 2012.

Hernando, I. R., Petrinovic, I. A., Gutiérrez, D. A., Bucher, J., Fuentes, T. G., and Aragón, E.: The caldera-forming eruption of the quaternary Payún Matrú volcano, Andean back-arc of the southern volcanic zone, J. Volcanol. Geoth. Res., 384, 15–30, https://doi.org/10.1016/j.jvolgeores.2019.07.003, 2019.

Hoyer, S. and Hamman, J.: xarray: ND labeled arrays and datasets in Python, Journal of Open Research Software, 5, 10, https://doi.org/10.5334/jors.148 2017.

Izosov, L. A., Petrishchevsky, A. M., Emel'yanova, T. A., Chuprynin, V. I., Lee, N. S., and Vasilyeva, M. A.: The model of formation of the Western Pacific Marginal Seas: vortex geodynamics, seismicity, and mantle upwelling, J. Volcanol. Seismol.+, 14, 44–57, https://doi.org/10.1134/S0742046320010029, 2020.

Jafrasteh, B., Fathianpour, N., and Suárez, A.: Comparison of machine learning methods for copper ore grade estimation, Computat. Geosci., 22, 1371–1388, https://doi.org/10.1007/s10596-018-9758-0, 2018.

Ji, W.-Q., Wu, F.-Y., Chung, S.-L., Wang, X.-C., Liu, C.-Z., Li, Q.-L., Liu, Z.-C., Liu, X.-C., and Wang, J.-G.: Eocene Neo-Tethyan slab breakoff constrained by 45 Ma oceanic island basalt–type magmatism in southern Tibet, Geology, 44, 283–286, https://doi.org/10.1130/G37612.1, 2016.

Ji, W.-Q., Wu, F.-Y., Wang, J.-M., Liu, X.-C., Liu, Z.-C., Zhang, Z., Cao, W., Wang, J.-G., and Zhang, C.: Early evolution of Himalayan orogenic belt and generation of middle eocene magmatism: constraint from Haweng granodiorite porphyry in the Tethyan Himalaya, Front. Earth Sci., 8, 236, https://doi.org/10.3389/feart.2020.00236, 2020.

Keykhay-Hosseinpoor, M., Kohsary, A.-H., Hossein-Morshedy, A., and Porwal, A.: A machine learning-based approach to exploration targeting of porphyry Cu-Au deposits in the Dehsalm district, eastern Iran, Ore Geol. Rev., 116, 103234, https://doi.org/10.1016/j.oregeorev.2019.103234, 2020.

Landtwing, M. R., Pettke, T., Halter, W. E., Heinrich, C. A., Redmond, P. B., Einaudi, M. T., and Kunze, K.: Copper deposition during quartz dissolution by cooling magmatic–hydrothermal fluids: the Bingham porphyry, Earth Planet. Sc. Lett., 235, 229–243, https://doi.org/10.1016/j.epsl.2005.02.046, 2005.

Lee, C.-T. A. and Tang, M.: How to make porphyry copper deposits, Earth Planet. Sc. Lett., 529, 115868, https://doi.org/10.1016/j.epsl.2019.115868, 2020.

Leveille, R. A. and Stegen, R. J.: The Southwestern North America Porphyry Copper Province, in: Geology and Genesis of Major Copper Deposits and Districts of the World: A Tribute to Richard H. Sillitoe, Society of Economic Geologists, https://doi.org/10.5382/SP.16.15, 2012.

Li, X., Hu, Y., Guo, J., Lan, J., Lin, Q., Bao, X., Yuan, S., Wei, M., Li, Z., Man, K., Yin, Z., Han, J., Zhang, J., Zhu, C., Zhao, Z., Liu, Y., Yang, J., and Nie, J.: A high-resolution climate simulation dataset for the past 540 million years, Scientific Data, 9, 371, https://doi.org/10.1038/s41597-022-01490-4, 2022 (data available at: https://figshare.com/articles/dataset/A_high-resolution_climate_simulation_dataset_for_the_past_540_million_years/19920662/1, last access: 21 May 2024).

Markwick, P. J. and Valdes, P. J.: Palaeo-digital elevation models for use as boundary conditions in coupled ocean–atmosphere GCM experiments: a Maastrichtian (late Cretaceous) example, Palaeogeogr. Palaeocl., 213, 37–63, 2004.

Mather, B. R., Müller, R. D., Zahirovic, S., Cannon, J., Chin, M., Ilano, L., Wright, N. M., Alfonso, C., Williams, S., Tetley, M., and Merdith, A.: Deep time spatio-temporal data analysis using pyGPlates with PlateTectonicTools and GPlately, Geosci. Data J., 10, 1–8, https://doi.org/10.1002/gdj3.185, 2023.

Matsumoto, T.: Timing of geological events in the circum-Pacific region, Can. J. Earth Sci., 14, 551–561, https://doi.org/10.1139/e77-057, 1977.

McInnes, B., Evans, N., Fu, F., Garwin, S., Belousova, E., Griffin, W., Bertens, A., Sukarna, D., Permanadewi, S., Andrew, R., and Deckart, K.: Thermal History Analysis of Selected Chilean, Indonesian and Iranian Porphyry Cu-Mo-Au Deposits, vol. 1, PGC Publishing, 1st edn., ISBN 0958057427, 2005.

McKinney, W.: pandas: a foundational Python library for data analysis and statistics, Python for High Performance and Scientific Computing, 14, 1–9, 2011.

McLemore, V. T.: Potential for Laramide porphyry copper deposits in southwestern New Mexico, in: Geology of the Gila Wilderness-Silver City area, New Mexico Geological Society, https://doi.org/10.56577/FFC-59.141, 141–149, 2008.

McMillan, W., Thompson, J. F. H., Hart, C., and Johnston, S.: Porphyry deposits of the Canadian Cordillera, Geosci. Can., 23, 125–134, 1996.

Monger, J. and Price, R.: The Canadian Cordillera: geology and tectonic evolution, CSEG Recorder, 27, 17–36, 2002.

Montgomery, D. R. and Brandon, M. T.: Topographic controls on erosion rates in tectonically active mountain ranges, Earth Planet. Sc. Lett., 201, 481–489, https://doi.org/10.1016/S0012-821X(02)00725-2, 2002.

Moosdorf, N., Cohen, S., and Von Hagke, C.: A global erodibility index to represent sediment production potential of different rock types, Appl. Geogr., 101, 36–44, https://doi.org/10.1016/j.apgeog.2018.10.010, 2018.

Murphy, B. P., Johnson, J. P. L., Gasparini, N. M., and Sklar, L. S.: Chemical weathering as a mechanism for the climatic control of bedrock river incision, Nature, 532, 223–227, https://doi.org/10.1038/nature17449, 2016.

Nathwani, C. L., Wilkinson, J. J., Fry, G., Armstrong, R. N., Smith, D. J., and Ihlenfeld, C.: Machine learning for geochem-

ical exploration: classifying metallogenic fertility in arc magmas and insights into porphyry copper deposit formation, Miner. Deposita, 57, 1143–1166, https://doi.org/10.1007/s00126-021-01086-9, 2022.

Nocquet, J.-M., Villegas-Lanza, J. C., Chlieh, M., Mothes, P. A., Rolandone, F., Jarrin, P., Cisneros, D., Alvarado, A., Audin, L., Bondoux, F., Martin, X., Font, Y., Régnier, M., Vallée, M., Tran, T., Beauval, C., Maguiña Mendoza, J. M., Martinez, W., Tavera, H., and Yepes, H.: Motion of continental slivers and creeping subduction in the northern Andes, Nat. Geosci., 7, 287–291, https://doi.org/10.1038/ngeo2099, 2014.

Noury, M. and Calmus, T.: Exhumation history of the La Caridad and Suaqui Verde porphyry copper deposits in the eastern Basin and Range province of Sonora: insights from thermobarometry and apatite thermochronology, J. S. Am. Earth Sci., 105, 102893, https://doi.org/10.1016/j.jsames.2020.102893, 2021.

Nur, A. and Ben-Avraham, Z.: Volcanic gaps due to oblique consumption of aseismic ridges, Tectonophysics, 99, 355–362, https://doi.org/10.1016/0040-1951(83)90112-9, 1983.

Olaya, V.: Chapter 6 Basic Land-Surface Parameters, in: Geomorphometry, edited by: Hengl, T. and Reuter, H. I., Developments in Soil Science, vol. 33, Elsevier, https://doi.org/10.1016/S0166-2481(08)00006-8, 141–169, 2009.

Oliphant, T. E.: Guide to Numpy, vol. 1, Trelgol Publishing USA, Identifier NumPyBook, 2006.

Perello, J., Razique, A., Schloderer, J., and Asad-ur-Rehman: The Chagai porphyry copper belt, Baluchistan Province, Pakistan, Econ. Geol., 103, 1583–1612, https://doi.org/10.2113/gsecongeo.103.8.1583, 2008.

Peucker-Ehrenbrink, B.: Land2Sea database of river drainage basin sizes, annual water discharges, and suspended sediment fluxes, Geochem. Geophy. Geosy., 10, Q06014, https://doi.org/10.1029/2008GC002356, 2009.

Portner, D. E., Rodríguez, E. E., Beck, S., Zandt, G., Scire, A., Rocha, M. P., Bianchi, M. B., Ruiz, M., França, G. S., Condori, C., and Alvarado, P.: Detailed structure of the subducted Nazca slab into the lower mantle derived from continent-scale teleseismic P wave tomography, J. Geophys. Res.-Sol. Ea., 125, e2019JB017884, https://doi.org/10.1029/2019JB017884, 2020.

Ramos, V. A.: Anatomy and global context of the Andes: Main geologic features and the Andean orogenic cycle, in: Backbone of the Americas: Shallow Subduction, Plateau Uplift, and Ridge and Terrane Collision, Geological Society of America, https://doi.org/10.1130/2009.1204(02), 2009.

Ramos, V. A.: Tectonic evolution of the central Andes: From terrane accretion to crustal delamination, AAPG Special Volumes, ISBN 978-0891813972, 2018.

Reich, M., Palacios, C., Vargas, G., Luo, S., Cameron, E. M., Leybourne, M. I., Parada, M. A., Zúñiga, A., and You, C.-F.: Supergene enrichment of copper deposits since the onset of modern hyperaridity in the Atacama Desert, Chile, Miner. Deposita, 44, 497–504, https://doi.org/10.1007/s00126-009-0229-3, 2009.

Retallack, G.: Cenozoic paleoclimate on land in North America, J. Geol., 115, 271–294, https://doi.org/10.1086/512753, 2007.

Richards, F. D., Hoggard, M. J., White, N., and Ghelichkhan, S.: Quantifying the relationship between short wavelength dynamic topography and thermomechanical structure of the upper mantle using calibrated parameterization of anelasticity, J. Geophys. Res.-Sol. Ea., 125, e2019JB019062, https://doi.org/10.1029/2019JB019062, 2020.

Richards, J. P.: Porphyry copper deposit formation in arcs: What are the odds?, Geosphere, 18, 130–155, https://doi.org/10.1130/GES02086.1, 2022.

Richardson, A., Hill, C. N., and Perron, J. T.: IDA: an implicit, parallelizable method for calculating drainage area, Water Resour. Res., 50, 4110–4130, https://doi.org/10.1002/2013WR014326, 2014.

Rusk, B. G., Reed, M. H., and Dilles, J. H.: Fluid inclusion evidence for magmatic-hydrothermal fluid evolution in the porphyry copper-molybdenum deposit at Butte, Montana, Econ. Geol., 103, 307–334, https://doi.org/10.2113/gsecongeo.103.2.307, 2008.

Sacek, V.: Drainage reversal of the Amazon River due to the coupling of surface and lithospheric processes, Earth Planet. Sc. Lett., 401, 301–312, 2014.

Salles, T., Ding, X., and Brocard, G.: pyBadlands: a framework to simulate sediment transport, landscape dynamics and basin stratigraphic evolution through space and time, PLoS One, 13, e0195557, https://doi.org/10.1371/journal.pone.0195557, 2018.

Salles, T., Rey, P., and Bertuzzo, E.: Mapping landscape connectivity as a driver of species richness under tectonic and climatic forcing, Earth Surf. Dynam., 7, 895–910, https://doi.org/10.5194/esurf-7-895-2019, 2019.

Salles, T., Mallard, C., and Zahirovic, S.: gospl: Global Scalable Paleo Landscape Evolution, Journal of Open Source Software, 5, 2804, https://doi.org/10.21105/joss.02804, 2020 (data available at: https://github.com/Geodels/gospl, last access: 5 August 2025).

Salles, T., Husson, L., Lorcery, M., and Hadler Boggiani, B.: Paleo-Physiography Project, HydroShare [data set, code], https://www.hydroshare.org/resource/0106c156507c4861b4cfd404022f9580/ (last access: 5 August 2025), 2022.

Salles, T., Husson, L., Rey, P., Mallard, C., Zahirovic, S., Boggiani, B. H., Coltice, N., and Arnould, M.: Hundred million years of landscape dynamics from catchment to global scale, Science, 379, 918–923, https://doi.org/10.1126/science.add2541, 2023.

Scotese, C. and Schettino, A.: Late Permian-Early Jurassic paleogeography of western Tethys and the world, in: Permo-Triassic Salt Provinces of Europe, North Africa and the Atlantic margins, Elsevier, 57–95, https://doi.org/10.1016/B978-0-12-809417-4.00004-5, 2017.

Scotese, C. R. and Wright, N.: PALEOMAP Paleodigital Elevation Models (PaleoDEMS) for the Phaerozoic, PALEOMAP Proj, Zenodo [data set], https://doi.org/10.5281/zenodo.5460860, 2018.

Sillitoe, R. H.: A plate tectonic model for the origin of porphyry copper deposits, Econ. Geol., 67, 184–197, https://doi.org/10.2113/gsecongeo.67.2.184, 1972.

Sillitoe, R. H.: Porphyry copper systems, Econ. Geol., 105, 3–41, https://doi.org/10.2113/gsecongeo.105.1.3, 2010.

Singer, D. A., Berger, V. I., and Moring, B. C.: Porphyry Copper Deposits of the World: Database and Grade and Tonnage Models, Open-File Report, Report No. 2008–1155 US Geological Survey, series: Open-File Report, https://doi.org/10.3133/ofr20081155, 2008.

Stalder, N. F., Herman, F., Fellin, M. G., Coutand, I., Aguilar, G., Reiners, P. W., and Fox, M.: The relationships between tecton-

ics, climate and exhumation in the Central Andes (18–36°S): evidence from low-temperature thermochronology, Earth-Sci. Rev., 210, 103276, https://doi.org/10.1016/j.earscirev.2020.103276, 2020.

Stefanini, B. and Williams-Jones, A. E.: Hydrothermal evolution in the Calabona porphyry copper system (Sardinia, Italy); the path to an uneconomic deposit, Econ. Geol., 91, 774–791, https://doi.org/10.2113/gsecongeo.91.4.774, 1996.

Stern, C. R.: Active Andean volcanism: its geologic and tectonic setting, Rev. Geol. Chile, 31, 161–206, https://doi.org/10.4067/S0716-02082004000200001, 2004.

Storetvedt, K.: The Tethys Sea and the Alpine-Himalayan orogenic belt; mega-elements in a new global tectonic system, Physics of the Earth and Planetary Interiors, 62, 141–184, https://doi.org/10.1016/0031-9201(90)90198-7, 1990.

Straume, E. O., Gaina, C., Medvedev, S., Hochmuth, K., Gohl, K., Whittaker, J. M., Abdul Fattah, R., Doornenbal, J. C., and Hopper, J. R.: Globsed: updated total sediment thickness in the world's oceans, Geochem. Geophy. Geosy., 20, 1756–1772, https://doi.org/10.1029/2018GC008115, 2019.

Syvitski, J. P. and Milliman, J. D.: Geology, geography, and humans battle for dominance over the delivery of fluvial sediment to the coastal ocean, J. Geol., 115, 1–19, 2007.

Uieda, L., Tian, D., Leong, W. J., Toney, L., Schlitzer, W., Grund, M., Newton, D., Ziebarth, M., Jones, M., and Wessel, P.: PyGMT: A Python interface for the generic mapping tools, Zenodo [code], https://doi.org/10.5281/zenodo.4592991, 2021.

Valdes, P. J., Armstrong, E., Badger, M. P. S., Bradshaw, C. D., Bragg, F., Crucifix, M., Davies-Barnard, T., Day, J. J., Farnsworth, A., Gordon, C., Hopcroft, P. O., Kennedy, A. T., Lord, N. S., Lunt, D. J., Marzocchi, A., Parry, L. M., Pope, V., Roberts, W. H. G., Stone, E. J., Tourte, G. J. L., and Williams, J. H. T.: The BRIDGE HadCM3 family of climate models: HadCM3@Bristol v1.0, Geosci. Model Dev., 10, 3715–3743, https://doi.org/10.5194/gmd-10-3715-2017, 2017 (data available at: https://www.paleo.bristol.ac.uk/ummodel/scripts/papers/Valdes_et_al_2017.html?utm_source=chatgpt.com, last access: 5 August 2025).

Valdes, P. J., Scotese, C. R., and Lunt, D. J.: Deep ocean temperatures through time, Clim. Past, 17, 1483–1506, https://doi.org/10.5194/cp-17-1483-2021, 2021.

van Dongen, M., Weinberg, R., Tomkins, A., and Armstrong, R.: Ancient crust in the world's youngest giant porphyry Cu-Au deposit, Ok Tedi, Papua New Guinea, Conference, AGU Fall Meeting, 2007AGUFMV33F.07V, 2007, V33F–07, 9–14 December 2007 in San Francisco, Calif., https://ui.adsabs.harvard.edu/abs/2007AGUFM.V33F..07V, 2007.

van Dongen, M., Weinberg, R. F., Tomkins, A. G., Armstrong, R. A., and Woodhead, J. D.: Recycling of Proterozoic crust in Pleistocene juvenile magma and rapid formation of the Ok Tedi porphyry Cu–Au deposit, Papua New Guinea, Lithos, 114, 282–292, https://doi.org/10.1016/j.lithos.2009.09.003, 2010.

Vérard, C., Hochard, C., Baumgartner, P. O., Stampfli, G. M., and Liu, M.: 3D palaeogeographic reconstructions of the Phanerozoic versus sea-level and Sr-ratio variations, Journal of Palaeogeography, 4, 64–84, https://doi.org/10.3724/SP.~J.1261.2015.00068, 2015.

Whipple, K. X. and Tucker, G. E.: Dynamics of the stream power river incision model: Implications for height limits of mountain ranges, landscape response timescales, and research needs, J. Geophys. Res.-Sol. Ea., 104, 17661–17674, 1999.

Wilkinson, B. H. and McElroy, B. J.: The impact of humans on continental erosion and sedimentation, Geol. Soc. Am. Bull., 119, 140–156, https://doi.org/10.1130/B25899.1, 2007.

Willenbring, J. K., Codilean, A. T., and McElroy, B.: Earth is (mostly) flat: apportionment of the flux of continental sediment over millennial time scales, Geology, 41, 343–346, https://doi.org/10.1130/G33918.1, 2013.

Wittmann, H., von Blanckenburg, F., Maurice, L., Guyot, J.-L., Filizola, N., and Kubik, P. W.: Sediment production and delivery in the Amazon River basin quantified by in situ–produced cosmogenic nuclides and recent river loads, Geol. Soc. Am. Bull., 123, 934–950, 2011.

Yanites, B. J. and Kesler, S. E.: A climate signal in exhumation patterns revealed by porphyry copper deposits, Nat. Geosci., 8, 462–465, https://doi.org/10.1038/ngeo2429, 2015.

Zhao, H., Wang, Q., Li, W., Shu, Q., Sun, X., and Deng, J.: The roles of emplacement depth, magma volume and local geologic conditions in the formation of the giant Yulong copper deposit, Eastern Tibet, Ore Geol. Rev., 145, 104877, https://doi.org/10.1016/j.oregeorev.2022.104877, 2022.

Ziegler, A., Rowley, D. B., Lottes, A. L., Sahagian, D. L., Hulver, M. L., and Gierlowski, T. C.: Paleogeographic interpretation: with an example from the Mid-Cretaceous, Annu. Rev. Earth Pl. Sc., 13, 385–428, 1985.

Zürcher, L., Bookstrom, A., Hammarstrom, J., Mars, J., Ludington, S., Zientek, M., Dunlap, P., and Wallis, J.: Tectonomagmatic evolution of porphyry belts in the central Tethys region of Turkey, the Caucasus, Iran, western Pakistan, and southern Afghanistan, Ore Geol. Rev., 111, 102849, https://doi.org/10.1016/j.oregeorev.2019.02.034, 2019.

5 | Discussion

5.1 Imprints of forcing conditions in LEMs

Geomorphology and landscape evolution have been central to Geosciences since the late 19th century. Initially driven more by qualitative and theoretical insights, the field transitioned to quantitative methodologies around the 1960s. This shift led to the development of landscape evolution models (LEMs) that are grounded in the conservation of mass principle. Modern LEMs incorporate process-based representations of surface dynamics, such as hillslope diffusion, runoff, erosion, and sediment transport, to simulate elevation change through time. Historically, the computational demands of these models posed significant challenges. However, advances in computing have enabled the integration of large, high-resolution datasets into standardized modeling workflows. This progress has opened new avenues for exploratory analysis, allowing for the quantitative evaluation of how initial conditions and forcing parameters shape source-to-sink sediment systems.

This Thesis studies how the effects of varying parameters of the conservation of mass equation (e.g., erodibility, diffusion coefficients, slope) and initial and temporal input conditions (elevation, precipitation, sea level) affect the source-to-sink systems in local (Chapters 2 and 3) and global scales (Chapters 4, Appendices A, and B). By comparing model scenarios with published data, it identifies the best-fitting configurations. It then, presents new methods to evaluate the outputs of these LEMs in the context of basin analysis, stratigraphy, and, increasingly, in mineral exploration (Chapters 3 and 4).

Chapter 2 explored various parameter combinations within the *goSPL* model applied to high resolution datasets from different authors (GBDS, Xu et al. 2017; Snedden and Galloway 2019; Galloway et al. 2011) to reconstruct Mid-Miocene sedimentation patterns in the Gulf of Mexico. After accurately reconstructing the sedimentation history in the Gulf, sensitivity tests performed within this Chapter demonstrated how the marine sedimentation is affected by changes in diffusion, slope and erodibility (Chapter 2, Figure C1). Expectedly, increased erodibility coefficient led to higher sediment accumulation in the basin, although the spatial distribution of these sediments depended on the number and geometry of clinoform slopes.

Beyond model parameters, initial forcing conditions (especially paleo-elevation and paleo-climate) were also varied in Chapters 2 and 3. Two complementary approaches were used to quantify how these variations affect erosion and sediment transport. In Chapter 2, continental erosion and deposition were assessed under different elevation, tectonic, and precipitation scenarios. Expectantly, the results indicate that

increased precipitation or tectonics leads to measurable changes in erosion. However, the degree of impact is strongly tied to initial topographic relief: while elevated areas are generally less responsive to such changes, this is not a universal rule (Chapter 2, Figs. 10 and F1). In contrast, Chapter 3 focused on the Polish Basin, analyzing sedimentation resulting from the erosion of surrounding watersheds. For under constrained regions, such as the Permian Polish Trough, where the reliability of available data is diminished by temporal distance, climate interpretations were guided by known relationships (such as orographic rain), though these inherently involve trade-offs. The sensitivity analysis (Chapter 3, Figs. 6 and 7) revealed that, in this case, the subsidence history within the basin played a more dominant role in controlling sedimentation than changes in the surrounding terrain. These findings emphasize the importance of evaluating local geomorphic and tectonic contexts when interpreting model outputs. Tackling such problems of paleoelevation and paleoclimatic calibrations in these two chapters helps understanding how the variations in forcing conditions affect and imprint the landscape evolution history.

In a global perspective, Chapter 4 compared various paleoelevation datasets Scotese and Wright (2018), Boschman (2021), Salles et al. (2023b) and paleoclimate models Valdes et al. (2017), Li et al. (2022). These datasets show significant differences, up to 3 km in elevation while precipitation rates vary up to 4 m/year between models (Chapter 4, Figs. A2 and A3). Such discrepancies directly affect derived quantities like exhumation rates, for example, the same location may vary in elevation by up to 3 km depending on the dataset used, with substantial consequences for computed sediment fluxes.

Given that the LEMs used here simulate long time spans (3 to 65 million years) with spatial resolutions between 2.5 and 5 km, it is unsurprising that results are highly sensitive to initial conditions, slope and tectonic forcing, in which the last is typically represented as time-varying paleoelevation. Similarly, different climatic forcings imprint distinct erosion and sediment routing patterns. A key insight from this work is that quantitative source-to-sink modeling allows for the explicit measurement of the landscape sensitivity to specific forcing conditions and input datasets. This opens the door for validation of LEM outputs against modern sediment fluxes and loads by supplying measured sediment and water flux data in previously data poor regions.

In summary, the increasing availability of global-scale paleogeographic and paleoclimatic reconstructions enables more detailed and realistic simulations of landscape evolution. However, the variability across datasets highlights the need for careful calibration and validation. The work presented here demonstrates how LEMs, when combined with sensitivity analysis, can reveal the imprint of environmental forcings on landscape dynamics, advancing their application in stratigraphy, basin analysis, and mineral exploration.

5.2 A quantitative framework for provenance analysis

Traditional provenance studies rely on physical sampling of sediments, often centered on mineralogical and geochemical analysis of detrital grains (Weltje and Eynatten 2004; Liedel et al. 2024). While such approaches provide valuable insights, they are inherently constrained by sampling biases and issues of mineral preser-

vation, with zircon being a long lived mineral usually over-represented in detrital records, and apatite is less stable over time and therefore under-represented. These biases raise fundamental questions: how representative are traditional provenance datasets? And to what extent do they reflect true sediment sources? How can their results be reliably extrapolated to the scale of entire catchments?

This Thesis addresses these uncertainties by leveraging landscape evolution models (LEMs) as a foundation for spatially comprehensive coverage quantitative provenance analysis. Chapter 2 and 3 investigate how initial forcing conditions (e.g., elevation, precipitation, tectonics) influence sediment flux and deposition patterns across time and space. These chapters effectively redefine provenance studies as full source-to-sink analyses, using quantitative models to trace sediment pathways from erosion in the hinterland to final deposition in sedimentary basins.

In both case studies, provenance interpretations based on LEM outputs complemented those derived from traditional methods. For the Gulf of Mexico, provenance estimations were compared with Xu et al. (2022) who used detrital zircon data to infer sediment sources. In contrast, provenance in the Polish Basin was interpreted qualitatively from stratigraphic (paleocurrents) and lithological (petrography) associations by McCann (1998), Kiersnowski et al. (2010), Kiersnowski (2013), and Bachmann et al. (2008).

While all the provenance areas proposed by the authors for both regions could be recognized in the provenance analysis from the LEMs, the LEMs also revealed additional, previously unrecognized sediment pathways and provenance domains. Comparing the quantitative results from Xu et al. (2022) with those from the LEMs in the Gulf of Mexico, it is noticeable the under-representativeness of older sources in traditional methods, due to preservation biases or limited sampling coverage. This mismatch illustrates a core limitation of conventional provenance tools and highlights the value of model-driven approaches that integrate erosion, transport, and deposition dynamics over geological timescales. Quantitative source-to-sink modeling provides a more holistic framework, that not only captures these complexities but also enables reproducible, scenario-based testing of geological hypotheses.

Overall, this Thesis proposes that LEMs offer a powerful and standardized tool for provenance analysis, overcoming many of the limitations associated with sample-based methods. By explicitly simulating landscape dynamics and sediment routing through time, LEMs provide a more complete and bias-resistant view of sediment provenance, especially in regions with recycled sediments, complex tectonic histories, or incomplete stratigraphic records.

5.3 LEMs in frontier copper system exploration

Similarly to traditional provenance analysis techniques, mineral deposit exploration has long depended on physical sampling. Geochemical analyses of collected samples, alongside structural and stratigraphic data acquired through field campaigns, geophysics and drilling, are integrated into numerical models that reconstruct the present-day state of mineralized systems. Although effective, these methods are expensive and inherently qualitative limited data, as they often capture only a snapshot of the system's history, typically ignoring its earlier burial, exhumation and/or

preservation phases.

Landscape evolution models (LEMs) offer a forward-modeling alternative capable of simulating the continuous surface evolution of the Earth over geological time. By incorporating climatic and tectonic forcings, LEMs provide a framework to investigate mechanisms and magnitude of mineral system responses to erosion, sedimentation, and topography change. This dynamic perspective allows for the reconstruction of transient phases in mineral system development, which are phases often missed in static models.

While several recent studies have explored machine learning approaches to improve porphyry copper exploration (Butterworth et al. 2016; Diaz-Rodriguez et al. 2021; Alfonso et al. 2024), none have explicitly considered the role of climate in the preservation or exhumation of mineral bodies. Chapter 4 introduces this novel dimension by analyzing how climate influences the exposure history of porphyry copper systems from emplacement through to exhumation. The global models used in that chapter predict emplacement depths and exhumation histories that align with empirical datasets in approximately 50% of the cases (Fig. 5, Chapter 4). These results highlight both the potential and the limitations of current LEM resolutions, and suggest that refinement at regional scales, particularly where high-resolution datasets are available, could significantly enhance predictive accuracy. Advancing new and automated methods for estimating paleoelevation and paleoclimate is essential. In this way, LEMs can support mineral exploration by guiding spatial targeting and eliminating geologically implausible areas, thus reducing false positives.

Beyond magmatic arc copper systems, Chapter 3 demonstrates how LEMs can be applied to sediment-hosted copper deposits. This chapter applies a quantitative provenance workflow to assess the plausibility of the hypothesis that red bed sediments served as the source of copper found in overlying shale-hosted deposits (Hitzman et al. 2010), such as the Kupferschiefer, and in evaporite-associated systems like those of the Central African Copperbelt. Protolith rocks that could be identified as favorable for copper sourcing were combined to produce a paleolithology map for the Permian in the Southern Permian Basins. Volumes of sediment derived from these source regions are quantified, then combined with sediment porosity (available from the LEMs reproduced with *goSPL*) and used to estimate potential copper masses. This technique is not only replicable but also adaptable to other deposit types where surface processes are key to ore concentration, such as supergene and placer deposits.

Importantly, the methods developed in Chapters 2 and 3 can be integrated with those from Chapter 4 to build a more complete picture of copper system evolution, from primary magmatic emplacement to sedimentary redistribution. Such an integrated LEM-based approach may prove especially useful in identifying new targets in underexplored or buried frontier basins. By retrofitting LEM outputs as exploration progresses, this methodology brings open-source workflows (Hadler Boggiani 2024; Hadler Boggiani et al. 2024; Boggiani 2025) to enable early-stage targeting and adaptive refinement of mineral potential maps based on evolving geological understanding.

5.4 Limitations

Like all numerical approaches, landscape evolution models (LEMs) involve a series of simplifications and assumptions that introduce limitations to the accuracy and scope of their predictions. While earlier sections have emphasized how uncertainties in initial conditions (elevation, climate, and tectonic settings) affect the final outputs of simulations, it is also important to acknowledge limitations specific to the capabilities and structure of the modeling framework itself, particularly *goSPL*.

A key simplification in *goSPL* is the treatment of erodibility. The model allows for a maximum of two erodibility values within a simulation, whereas more comprehensive global assessments, such as those presented by Moosdorf et al. (2018), identify at least five distinct categories to represent surface erodibility. This limited classification reduces the model's ability to resolve spatial variations in lithological resistance, potentially skewing sediment fluxes and biasing the delineation of provenance areas. Consequently, sediment volumes derived from specific source regions may be under or overestimated, affecting downstream interpretations of sediment routing and deposition.

goSPL simulates sediment transport using a single grain size class. This excludes complex sorting processes and consequently alters the porosity of deposited sediment packages, which affects predictions of sediment volume and tonnage. Additionally, the model currently simplifies the effects of sediment compaction and porosity reduction over time, potentially leading to overestimation of sediment thickness and volume, especially in deeper sections of the basins.

The model focus exclusively on sediment transport via fluvial processes, omitting gravity-driven sediment transfer mechanisms such as landslides, slumps, debris flows, turbidity currents, and aeolian transport, and volcaniclastics deposition. These processes are often dominant in steep or tectonically active regions and strongly influence basin fill and stratigraphy. Their omission can cause underestimation of sediment volume, oversimplification of landscape evolution, and incomplete basin dynamic representations.

For example, the exclusion of volcaniclastics not only limits the representation of key sediment inputs in volcanic terrains but also has implications for mineral systems, as is the case of the results presented in Chapter 3. Volcaniclastics often contribute to copper enrichment processes and play a role in generating the subsidence patterns observed in forearc or intra-arc basins due to their influence on lithospheric loading. Their absence thus reduces the precision of LEM outputs for scenarios involving volcanic contributions to copper systems, particularly when modeling basin-scale flexural responses and sediment-hosted mineralization. Although incorporating lithospheric flexure is important for modeling basin subsidence and sediment accommodation, it considerably increases computational demand, which constrains model resolution and runtime.

Chemical weathering and soil formation processes, which influence surface erodibility and vertical mass transfer within sedimentary sequences, are also omitted in *goSPL*. These processes are highly relevant to mineral system development and supergene enrichment but remain unrepresented.

While *goSPL* offers a powerful tool for modeling large-scale surface processes, its

simplified treatment of surface erodibility and exclusion of key sedimentary processes highlight the need for cautious interpretation. Future iterations of LEMs aiming to support mineral exploration could benefit from incorporating a broader suite of erosion, transport, and deposition mechanisms, along with more refined lithological parameterizations, to better approximate real-world source-to-sink dynamics.

5.5 Significance

The results presented in this Thesis represent a significant advancement in sedimentology and mineral exploration through the integration of landscape evolution modeling. By offering the first quantitative framework for provenance analysis based on forward modeling, this work addresses long-standing limitations in traditional provenance methods, particularly those related to sampling bias and mineral preservation. The developed methodology effectively estimates source rock contributions and sediment flux histories, enabling more robust reconstructions of source-to-sink systems.

Moreover, this Thesis introduces novel approaches for analyzing sediment distribution, water and sediment fluxes, and catchment evolution through time, and its relationship with mineralization processes, especially copper accumulation, providing a valuable tool for mineral exploration. These techniques not only support the re-evaluation of existing copper prospects but also contribute to the generation of prospectivity maps that can inform and refine future drilling campaigns.

In addition to applications in resource exploration, the landscape evolution models developed here (and those produced by other recent efforts with varying spatial and temporal resolutions) yield physiographic reconstructions that serve as crucial proxies for understanding paleo-landscapes. These outputs have broad interdisciplinary value, offering insights into paleogeographic controls on biodiversity dispersal across both regional and global scales (Salles et al. 2023b; Salles et al. 2023a; Husson et al. 2022; Salles et al. 2024; Cohen et al. 2022).

5.6 Future work

The research presented in this Thesis highlights several promising avenues for future developments in Landscape Evolution Modeling (LEM).

A primary direction involves expanding the LEM framework to incorporate the effects of vegetation cover and regolith formation on sediment production. These processes provide important feedbacks to chemical weathering derived from soil formation. Including them would allow for more realistic simulations of soil development and landscape response, as well as a dynamic representation of how surface erodibility evolves through time. Implementation of water table variations over time would also be beneficial, particularly for modeling supergene deposit formation. Accounting for hydrological factors such as water table depth would improve simulations of subsurface weathering and the mobilization of sediments and metals, which are crucial processes for refining mineral prospectivity predictions.

Additionally, integrating sediments from volcanic eruptions and extrusive volcanic deposits into the LEM framework is essential for mineral exploration applications.

These materials are important sources of industrial minerals and often influence basin architecture and sediment routing. Accounting for their contribution would refine predictive models of sedimentary provenance and enhance targeting in resource exploration. Furthermore, LEMs could benefit from incorporating thermochronology data within validation and calibration workflows, improving constraints on paleoelevation and reducing error propagation through model simulations.

A more fundamental challenge lies in the limited ability of surface process models to represent geodynamic forces at depth. The surface expression of many geological phenomena is intrinsically linked to lithospheric-scale processes such as flexural isostasy, dynamic topography, and crustal deformation. While preliminary efforts have been made to couple LEMs with lithospheric models (Rodriguez-Corcho 2023), such approaches remain computationally expensive and technically complex. Future research should focus on developing streamlined coupling strategies that enable more efficient integration of deep Earth processes into long-term surface evolution models. This would enable a more comprehensive understanding of landscape dynamics, particularly in tectonically active or rapidly evolving settings.

Taken together, these advancements would significantly expand the scope and applicability of LEMs across geosciences disciplines, from mineral exploration to Earth system modeling.

References

Alfonso, C. P., R. D. Müller, B. Mather, and M. Anthony (2024). "Spatio-temporal copper prospectivity in the American Cordillera predicted by positive-unlabeled machine learning". In: *GSA Bulletin* 137.1-2, pp. 702–711. DOI: 10.1130/B37614.1.

Bachmann, G., T. Voigt, U. Bayer, H. von Eynatten, B. Legler, and R. Littke (2008). "Depositional history and sedimentary cycles in the Central European Basin System". In: *Dynamics of Complex Intracontinental Basins: the Example of the Central European Basin System*. Springer, pp. 156–172.

Boggiani, B. H. (2025). *biahadler/porphyry-data: Porphyry Copper Workflows*. DOI: 10.5281/zenodo.15400584.

Boschman, L. M. (2021). "Andean mountain building since the Late Cretaceous: A paleoelevation reconstruction". en. In: *Earth-Science Reviews* 220, p. 103640. DOI: 10.1016/j.earscirev.2021.103640.

Butterworth, N., D. Steinberg, R. D. Müller, S. Williams, A. S. Merdith, and S. Hardy (2016). "Tectonic environments of South American porphyry copper magmatism through time revealed by spatiotemporal data mining: Tectonics of South American Porphyries". en. In: *Tectonics* 35.12, pp. 2847–2862. DOI: 10.1002/2016TC004289.

Cohen, A. S., C. J. Campisano, J. R. Arrowsmith, A. Asrat, C. C. Beck, A. K. Behrensmeyer, A. L. Deino, C. S. Feibel, V. Foerster, J. D. Kingston, H. F. Lamb, T. K. Lowenstein, R. L. Lupien, V. Muiruri, D. O. Olago, R. B. Owen, R. Potts, J. M. Russell, F. Schaebitz, J. R. Stone, M. H. Trauth, and C. L. Yost (2022). "Reconstructing the Environmental Context of Human Origins in Eastern Africa Through Scientific Drilling". en. In: *Annual Review of Earth and Plane-*

tary Sciences 50.Volume 50, 2022. Publisher: Annual Reviews, pp. 451–476. DOI: 10.1146/annurev-earth-031920-081947.

Diaz-Rodriguez, J., R. D. Müller, and R. Chandra (2021). "Predicting the emplacement of Cordilleran porphyry copper systems using a spatio-temporal machine learning model". In: *Ore Geology Reviews* 137, p. 104300. DOI: 10.1016/j.oregeorev.2021.104300.

Galloway, W. E., T. L. Whiteaker, and P. Ganey-Curry (2011). "History of Cenozoic North American drainage basin evolution, sediment yield, and accumulation in the Gulf of Mexico basin". en. In: *Geosphere* 7.4, pp. 938–973. DOI: 10.1130/GES00647.1.

Hadler Boggiani, B. (2024). "Polish Rotliegend Basin". In: Publisher: Zenodo. DOI: 10.5281/ZENODO.14126215.

Hadler Boggiani, B., T. Salles, C. A. Mallard, and N. Atwood (2024). *Porphyry Copper Data*. en. DOI: 10.5281/ZENODO.11239057.

Hitzman, M. W., D. Selley, and S. Bull (2010). "Formation of Sedimentary Rock-Hosted Stratiform Copper Deposits through Earth History". en. In: *Economic Geology* 105.3, pp. 627–639. DOI: 10.2113/gsecongeo.105.3.627.

Husson, L., T. Salles, A.-E. Lebatard, S. Zerathe, R. Braucher, S. Noerwidi, S. Aribowo, C. Mallard, J. Carcaillet, D. H. Natawidjaja, D. Bourlès, ASTER team, G. Aumaitre, D. Bourlès, and K. Keddadouche (2022). "Javanese Homo erectus on the move in SE Asia circa 1.8 Ma". en. In: *Scientific Reports* 12.1, p. 19012. DOI: 10.1038/s41598-022-23206-9.

Kiersnowski, H. (2013). "Late Permian aeolian sand seas from the Polish Upper Rotliegend Basin in the context of palaeoclimatic periodicity". In: *Geological Society, London, Special Publications* 376.1. Publisher: The Geological Society of London, pp. 431–456. DOI: 10.1144/SP376.20.

Kiersnowski, H., T. M. Peryt, A. Buniak, and Z. Mikołajewski (2010). "From the intra-desert ridges to the marine carbonate island chain: middle to late Permian (Upper Rotliegend–Lower Zechstein) of the Wolsztyn–Pogorzela high, west Poland". en. In: *Geological Journal* 45.2-3, pp. 319–335. DOI: 10.1002/gj.1189.

Li, X., Y. Hu, J. Guo, J. Lan, Q. Lin, X. Bao, S. Yuan, M. Wei, Z. Li, K. Man, Z. Yin, J. Han, J. Zhang, C. Zhu, Z. Zhao, Y. Liu, J. Yang, and J. Nie (2022). "A high-resolution climate simulation dataset for the past 540 million years". en. In: *Scientific Data* 9.1, p. 371. DOI: 10.1038/s41597-022-01490-4.

Liedel, S., L. Caracciolo, J. C. Restrepo, G. J. Weltje, F. Lucà, A. Beltrán-Triviño, and J. D. Restrepo Ángel (2024). "A Quantitative Provenance Analysis (QPA) Approach to Quantify Controls on Sediment Generation and Sediment Flux in the Upper Reaches of the Magdalena River (Colombia): 1. Natural and Anthropic Controls on the Sand Fraction". en. In: *Journal of Geophysical Research: Earth Surface* 129.5, e2023JF007369. DOI: 10.1029/2023JF007369.

McCann, T. (1998). "Sandstone composition and provenance of the Rotliegend of the NE German Basin". en. In: *Sedimentary Geology* 116.3, pp. 177–198. DOI: 10.1016/S0037-0738(97)00106-1.

Moosdorf, N., S. Cohen, and C. Von Hagke (2018). "A global erodibility index to represent sediment production potential of different rock types". en. In: *Applied Geography* 101, pp. 36–44. DOI: 10.1016/j.apgeog.2018.10.010.

Rodriguez-Corcho, A. (2023). "The Role of Lithospheric–Deep Mantle Interactions in the Evolution and Subduction Dynamics of Arc–Continent Collision Settings". Minerva Access. PhD thesis. University of Melbourne.

Salles, T., L. Husson, M. Lorcery, and B. Hadler Boggiani (2023a). "Landscape dynamics and the Phanerozoic diversification of the biosphere". en. In: *Nature* 624.7990, pp. 115–121. DOI: 10.1038/s41586-023-06777-z.

Salles, T., L. Husson, P. Rey, C. Mallard, S. Zahirovic, B. H. Boggiani, N. Coltice, and M. Arnould (2023b). "Hundred million years of landscape dynamics from catchment to global scale". en. In: *Science* 379.6635, pp. 918–923. DOI: 10.1126/science.add2541.

Salles, T., R. Joannes-Boyau, I. Moffat, L. Husson, and M. Lorcery (2024). "Physiography, foraging mobility, and the first peopling of Sahul". en. In: *Nature Communications* 15.1. Publisher: Nature Publishing Group, p. 3430. DOI: 10.1038/s41467-024-47662-1.

Scotese, C. R. and N. Wright (2018). "PALEOMAP Paleodigital Elevation Models (PaleoDEMS) for the Phaerozoic". In: *PALEOMAP Proj.*

Snedden, J. W. and W. E. Galloway (2019). *The Gulf of Mexico Sedimentary Basin: Depositional Evolution and Petroleum Applications*. en. 1st ed. Cambridge University Press. DOI: 10.1017/9781108292795.

Valdes, P. J., E. Armstrong, M. P. S. Badger, C. D. Bradshaw, F. Bragg, T. Davies-Barnard, J. J. Day, A. Farnsworth, P. O. Hopcroft, A. T. Kennedy, N. S. Lord, D. J. Lunt, A. Marzocchi, L. M. Parry, W. H. G. Roberts, E. J. Stone, G. J. L. Tourte, and J. H. T. Williams (2017). *The BRIDGE HadCM3 family of climate models:HadCM3@Bristol v1.0*. preprint. Climate and Earth System Modeling. DOI: 10.5194/gmd-2017-16.

Weltje, G. J. and H. von Eynatten (2004). "Quantitative provenance analysis of sediments: review and outlook". In: *Sedimentary Geology*. Quantitative Provenance Analysis of Sediments 171.1, pp. 1–11. DOI: 10.1016/j.sedgeo.2004.05.007.

Xu, J., J. W. Snedden, C. S. Fulthorpe, D. F. Stockli, W. E. Galloway, and Z. T. Sickmann (2022). "Quantifying the relative contributions of Miocene rivers to the deep Gulf of Mexico using detrital zircon geochronology: Implications for the evolution of Gulf Basin circulation and regional drainage". en. In: *Basin Research* 34.3, pp. 1143–1163. DOI: 10.1111/bre.12653.

Xu, J., D. F. Stockli, and J. W. Snedden (2017). "Enhanced provenance interpretation using combined U–Pb and (U–Th)/He double dating of detrital zircon grains from lower Miocene strata, proximal Gulf of Mexico Basin, North America". In: *Earth and Planetary Science Letters* 475, pp. 44–57. DOI: 10.1016/j.epsl.2017.07.024.

6 | Conclusion

This thesis advances the use of landscape evolution models (LEMs) across multiple spatial and temporal scales to quantify sediment provenance and support mineral exploration strategies. By integrating dynamic Earth surface processes like climate, sea-level change, topographic evolution, and sediment transport within a unified modeling framework using *goSPL*, this research bridges a critical gap between traditional provenance methods and process-based simulation approaches by unraveling quantitative data. The findings demonstrate the value of LEMs not only in complementing conventional provenance techniques, but also in improving our understanding of source-to-sink systems and enhance the spatial and temporal prediction of copper deposit formation and preservation.

Demonstrating the predictive capacity of this approach, a series of *goSPL* simulations were developed for the Miocene Gulf of Mexico (GoM) and the Permian red beds of the Polish Trough. These models successfully reproduced first-order sediment accumulation patterns, onshore and offshore, that align with available observed data. In the Gulf of Mexico, sensitivity analyses between simulations revealed that climatic forcing tends to exerted a greater influence on sediment distribution in higher elevated regions when compared to the effects of tectonic forcing. In the Polish Trough, varying subsidence styles produced distinct sedimentation histories. Source contributions were quantitatively assessed in both cases. For the GoM, comparisons with conventional provenance methods (e.g. apatite fission track and detrital zircon) indicated that traditional methods may underestimate the contribution from older sources while overestimating younger ones. In the Polish Trough, paleolithology maps were used to attribute copper potential to sediment transported and accumulated, enabling a new assessment of copper-bearing sediment contributions, providing new insights into critical mineral potential in red bed systems.

At global scale, this thesis pioneered the use of LEM outputs to assess the preservation, emplacement depth, and exhumation of porphyry copper deposits during the Cenozoic. Despite the strong interdependence between input datasets (*e.g.* paleoelevation and paleo-climate) and final outputs, the model reproduced patterns that matched approximately 50% of the global porphyry deposit dataset, underscoring the promise of LEMs for large-scale mineral systems analysis, and has already inspired further research projects employing similar approaches.

Throughout the course of this research, several model limitations were identified that influence predictive accuracy, but also guided developments in the LEM. These include reliance on a maximum of two erodibility values, reburial processes, lack of dynamic coupling between surface and deep Earth processes, simplified emplacement

depth data, the absence of gravity-dominated transport mechanisms, volcaniclastic contributions, and vegetation effects. Such limitations can affect sediment load computations and estimates of copper contributions.

Despite these limitations, the frameworks developed in this thesis are equivalently adaptable for studying basin evolution across diverse geologic settings and time spans, and for exploring critical metals with similar genetic pathways (e.g., lithium, rare earth elements), thereby broadening their impact beyond copper exploration.

Overall, this thesis presents a novel framework for integrating landscape evolution modeling with sediment provenance analysis to support predictive mineral exploration. It emphasizes advances in our ability to quantitatively simulate the coupled interactions between geological, climatic, and geomorphic processes in dynamic Earth surface systems. This approach paves the way for next-generation tools with enhanced capacity to track sediment and metal transport from source to sink, with significant implications not only for mineral exploration but also for fields such as biogeography, landscape ecology and archaeology. By bridging these disciplines, this research contributes to a better understanding of surface processes shaping environments across spatial and temporal scales.

A| APPENDIX

Hundred million years of landscape dynamics from catchment to global scale

Salles, T., Husson, L., Rey, P., Mallard, C., Zahirovic, S., Boggiani, B.H., Coltice, N. and Arnould, M., 2023. Hundred million years of landscape dynamics from catchment to global scale. *Science*, 379(6635), pp.918–923. DOI: 10.1126/science.add2541.

LANDSCAPE DYNAMICS

Hundred million years of landscape dynamics from catchment to global scale

Tristan Salles[1]*, Laurent Husson[2], Patrice Rey[1], Claire Mallard[1], Sabin Zahirovic[1], Beatriz Hadler Boggiani[1], Nicolas Coltice[3], Maëlis Arnould[4]

Our capability to reconstruct past landscapes and the processes that shape them underpins our understanding of paleo-Earth. We take advantage of a global-scale landscape evolution model assimilating paleoelevation and paleoclimate reconstructions over the past 100 million years. This model provides continuous quantifications of metrics critical to the understanding of the Earth system, from global physiography to sediment flux and stratigraphic architectures. We reappraise the role played by surface processes in controlling sediment delivery to the oceans and find stable sedimentation rates throughout the Cenozoic with distinct phases of sediment transfer from terrestrial to marine basins. Our simulation provides a tool for identifying inconsistencies in previous interpretations of the geological record as preserved in sedimentary strata, and in available paleoelevation and paleoclimatic reconstructions.

Landscapes are the expression of the interplay between tectono-geodynamic processes that deform and modify Earth's surface and its climate, which acts to transfer sediments from sources to sinks, through drainage networks that incise and dissect the landscape into high-frequency elevation patterns. Earth's physiography acts as a key evolving boundary condition for a plethora of geological, climatic, and biological processes and models (*1*–*4*). Traditionally, sedimentology, geochemistry, and paleontological studies have been used to decode Earth's paleoelevation. However, available observations from the geological record remain sparse, providing only a low-resolution, spatially and temporally fragmented representation of past physiography and are, to our knowledge, unable to account for past drainage networks, making it difficult to reconstruct the partitioning and distribution of sedimentary basins, geochemical cycles, the flux of nutrients from continents to oceans, and the evolution of global atmospheric and oceanic circulation. To unlock these constraints, we must be able to model—with high levels of detail—the evolution of the Earth's physiography at the global scale and through geological time.

We present a prediction of the past physiography of the Earth at a global scale, at fine resolution [10 km spatially, 1 million years (Myr) in time]. We simulate landscape evolution resulting from erosion and deposition, adjusting the physiography over time by assimilating a long-wavelength paleoelevation reconstruction derived from the geological record and paleontological archives (*5*) and paleoclimatic data from a general circulation model (*3*). Our results are first calibrated using a series of present-day observations. We then extract an ensemble of predictions that we compare with well-documented natural examples of sediments and water fluxes, stratigraphic architecture of sedimentary basins, and estimates of sediment volumes trapped in terrestrial sinks. Our numerical framework integrates the physics of surface processes and provides 100 Myr of high-spatial and temporal resolution physiography and sediment accumulation maps, fundamental in interpreting and modeling Earth's past environmental and biological conditions.

[1]School of Geosciences, The University of Sydney, Sydney, Australia. [2]CNRS, ISTerre, Université Grenoble-Alpes, Grenoble, France. [3]ENS, PSL Research University, CNRS UMR 8538, Paris, France. [4]Université Lyon 1, LGL-TPE, Villeurbanne, France.
*Corresponding author. Email: tristan.salles@sydney.edu.au

A global landscape and sediment transport geomodel

We developed a modeling framework accounting for geodynamic, tectonic, climatic, and surface processes to perform paleolandscape reconstructions at a global scale. Based on the recently released global landscape evolution model goSPL (*6*), landscape dynamics are forced with a state-of-the-art paleoelevation reconstruction tied to its plate tectonic model (*5*), and a series of paleoprecipitation maps (*3*). We implement a stepwise matching approach (see SM) to assimilate the paleoelevation dataset and estimate uplift rates over time. In this scheme, the envelope of the reconstructed landscape targets the long-wavelength pattern of the paleoelevation reconstruction model. Predictive model outputs from our paleolandscape reconstructions allow us to build high-resolution (~10 km) maps of the physiography and drainage network organization at the global scale (Fig. 1A), making it possible to simulate past sediment and fluvial paleofluxes across drainage networks (Fig. 1B), to estimate both continental and marine sediment accumulations, and to build global three-dimensional (3D) compacted stratigraphic architectures (Fig. 1C).

First, we calibrate our model (table S1) using modern estimates of suspended and bedload transport from the land to the ocean corresponding to ~20 gigatonnes (GT) per year (Fig. 2A) and contributing to >70% of the global sediment flux (*1*). These global values are similar to those of the Land2Sea database (*7*), which contain present-day estimates

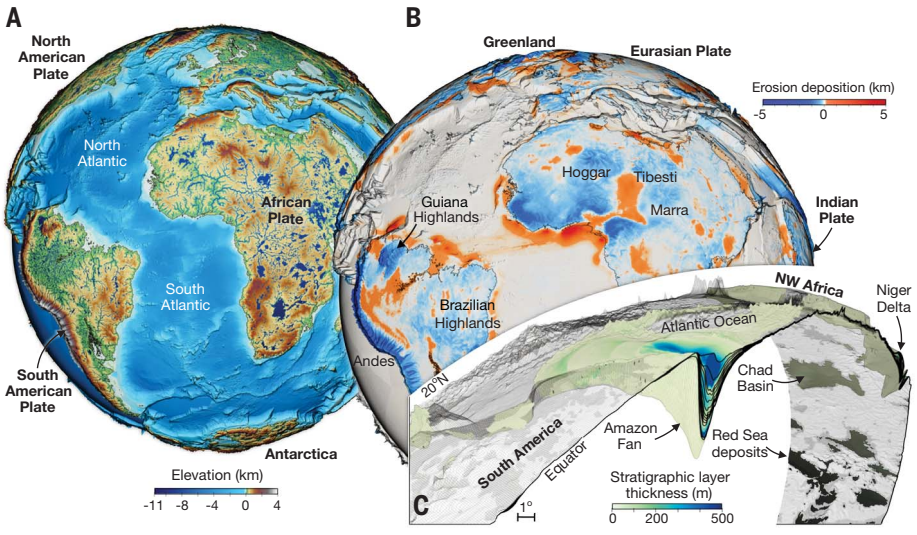

Fig. 1. Landscape evolution simulation. (**A**) Global physiography and major rivers at 50 Ma, after assimilating paleoelevation (*5*) and paleoclimatic (*3*) reconstructions. (**B**) 50 Myr of cumulative erosion and sedimentation highlighting erosion over mountain ranges (Andes) and topographic highs (Brazilian and Guiana highlands, Hoggar, Tibesti, and Marra) and major sediment accumulations along continental shelves (Atlantic margins) and endorheic basins (Amazonian watershed). (**C**) Perspective view of a stripe 20° wide featuring the relief and stratigraphy after 100 Myr of evolution; the architecture of the Amazon Fan and other sedimentary basins prominently appear.

Downloaded from https://www.science.org at University of Sydney on June 21, 2023

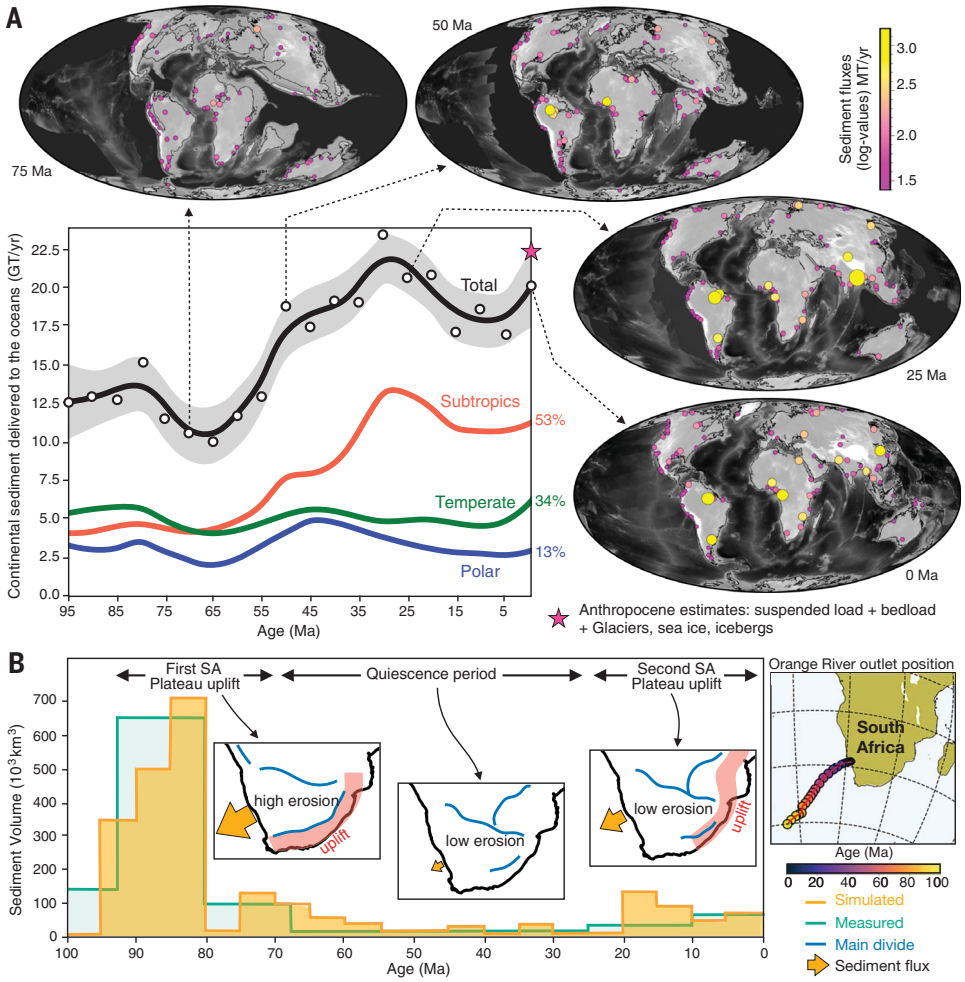

Fig. 2. Sediment flux over time. (**A**) Map view (pink and yellow circles) of the 100 highest river sediment fluxes at specific times caused by riverine and hillslope processes activated by the interplay between tectonic and climatic forcings. Latitudinal dependence of the sediment fluxes at specific times (circles) and averaged over time (Lowess regression, shaded area corresponds to confidence intervals) (subtropics: from 30°S to 30°N; temperate: 30° to 60°; and polar: above 60°). Stars show the modern estimates of sediment flux to the ocean used for model calibration in magenta (*1*) and values from the Land2Sea database in pink (*7*). (**B**) Computed (orange area) and observed (teal line) sediment fluxes in the Orange River, southern Africa over the past 100 Ma. Inset sketches show the erosion-sedimentation evolution from (*29*). Map on the right shows the Orange River mouth position reconstructed from the plate motion model (*5*).

for suspended sediment flux average to 18.6 GT per year based on 1519 exorheic river drainage basins (*7*). Latitudinal sediment flux distribution shows predominant contributions from subtropical regions corresponding to 53% of the total flux. This strong correlation between sediment flux and climate matches estimates from the global terrestrial sink catchment database (*8*) and organic carbon flux studies (*9*). From the multiple flow drainage method used to integrate runoff over the upstream drainage basin area (*6*), simulated major river positions and associated watersheds conform with those of the real world (Fig. 3A). As an example, the simulated catchment area for the Paraná Basin at the present day, after 100 Myr of simulation, has a similar shape and is only 8% smaller than the actual Paraná catchment (model resolution impedes reconstructing the highest frequencies of river sinuosity). The output also compares well with observed magnitude of discharge for the largest modern rivers (Fig. 3B) and accounts for the discharge-area scaling relationship (exponent close to 1.0 from curve fitting analysis) (*10*).

The positions of the rivers and their associated catchments are not fixed and evolve over time (Fig. 3A and fig. S6). At the catchment scale, our simulation can be used to further evaluate the transient geomorphic response of individual catchments to tectonic and climatic forcing (*11*, *12*). As an example, the main tributaries for the Paraná Basin (Grande, Paraguay, Salado, and Uruguay rivers) and their confluence positions are also well-reproduced in the simulation (Fig. 3C). From the longitudinal profiles, we identify several knickzones (Fig. 3C), the amplitudes and positions of which follow observations (*13*, *14*)—particularly for the simulated Uruguay River, which reproduces two knickzones between 1200 and 2000 km (at ~400 and 600 m elevation) similar to the present-day river profile.

Finally, our simulation also reproduces the first-order distribution of the main depocenters for the past 100 Myr (Fig. 1, B and C, Fig. 4, and fig. S10). Comparison with present-day total marine sediment thickness grid GlobSed (*15*) shows that our simulation underpredicts global thickness by 1.5 km (fig. S7, A and C), which is expected as the cumulative depositional record from this dataset spans a much longer period than ours. However, we find a better match in subtropical regions (0.8 km) where many of the largest modern oceanic sedimentary basins formed over the past 100 Myr. As an example, it predicts a maximum accumulation under the outer Pakistan shelf of up to 7.5 km in the Indus Fan (fig. S7B) that compares well with the global depocenter observed from subsurface observations (*16*). Likewise, the predicted accumulation of sediments in the post-Paleocene Bengal Fan (up to 10.3 km fig. S7B) conforms to the geological record (*17*). Similar observations can be made for the Niger Delta that accumulates in our simulation—up to 9.5 km of sediments, which can readily be compared with the 8.5-km estimate from sediment budgets (*18*) or the Eromanga Basin in central Australia with a predicted broad 1.2-km thick deposit, also within the range of observed values since the Late Cretaceous (Fig. 5B) (*19*). For the Amazon Fan (Fig. 1A), we obtain a deposit that extends up to 600 km seaward and records a 13-km thick accumulation that here again matches observations (*20*).

Water and sediment flux through space and time

The transfer of eroded sediments from the mountains to the oceans is a proxy for long-term

Downloaded from https://www.science.org at University of Sydney on June 21, 2023

physical weathering and plays a central role in modulating ocean chemistry, and more generally in geochemical cycles over geological time scales (*1*, *8*, *21*, *22*). We extracted the top hundred largest sediment fluxes (Fig. 2A) and monitored water discharges over the past 100 Myr (Fig. 3A). The distribution of the water discharge, whether dominated by a few major catchments or many smaller watersheds (Fig. 3A and S6), depends on the size of the river catchments and the amount of rainfall they receive. Typically, the highest sediment fluxes correspond to the largest river discharges. However, this relationship does not always hold because the local physiography

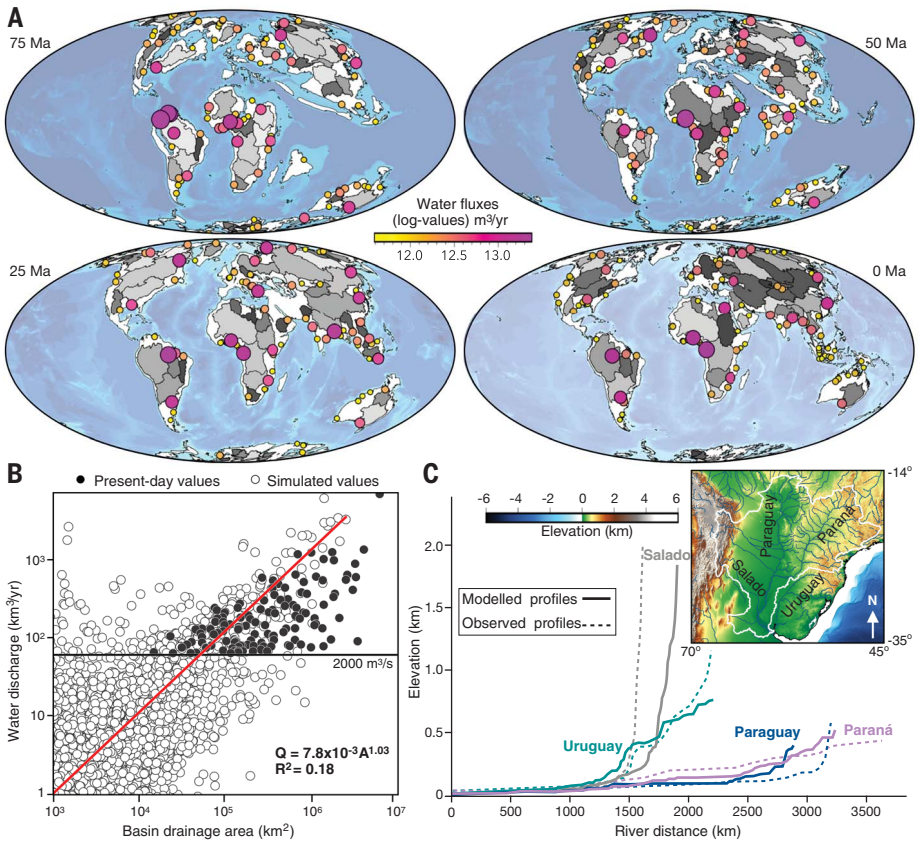

Fig. 3. Water discharges and catchment dynamics. (**A**) Map view of the 100 largest annual river discharges (circle sizes and colors scale with water flux) and 50 largest drainage basins (gray shading). (**B**) Modeled water discharge against basin drainage area (white circles) at present day (log scales). Red line, power law curve fitting. Black circles correspond to observed river fluxes at the present day for rivers whose discharge is <2000 m^3 per s (horizontal line at ~63 km^3 per yr) (*1*). Paraná drainage basin and tributaries. Simulated longitudinal main rivers profiles (solid curves) and corresponding actual river profiles (dashed, downsampled at 10 km resolution from 90 m SRTM database) (*14*). (**C**) Teal lines show identified kickzones for the Uruguay River.

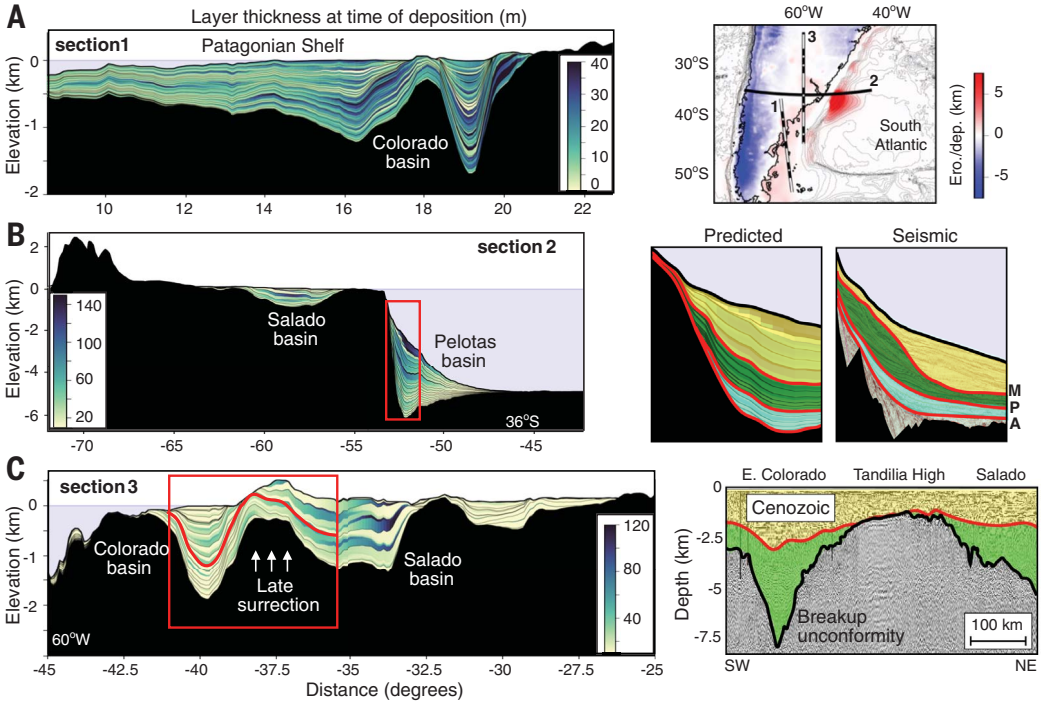

Fig. 4. Stratigraphic predictions. (**A**) Cumulative erosion/deposition (top right) at the present day, sliced with three cross sections. Simulated stratigraphy sampled every 1 Myr are displayed and colored by sediment accumulation rates (meters per million years) for each cross section. (**B**) Predicted stratigraphy for section 2 after 100 Myr of simulation (left) and focus on the Pelotas Basin (right) where comparison with megasequences from 2D seismic sections are presented (*34*). Red lines in the predicted and interpreted seismic defines the Albian (A ~100 Ma), Paleocene (P ~59 Ma), and Miocene (M ~23 Ma) transitions. (**C**) Cross section across the Salado and Colorado basins (left) compared with depth-converted interpreted seismic (*36*). Red line corresponds to the top Cretaceous horizon (~66 Ma) in both panels.

Downloaded from https://www.science.org at University of Sydney on June 21, 2023

plays a crucial role in modulating sediment flux (*21*). For example, small catchments adjacent to high mountain ranges, such as on the western side of the Andes, have low water discharges but deliver a large volume of sediments to the ocean (*8*, *21*). Conversely, the northern part of South America or Central Africa at 75 Ma or Southeast Asia at 25 Ma (Fig. 3A) demonstrate that large water flux does not necessarily convey large sediment flux (Fig. 2A). This can either be attributed to high precipitation rates over relatively flat landscapes or to the storage of sediments in upstream depocenters (Fig. 5A).

Both water and sediment fluxes over time mirror several phases of continental scale drainage reorganizations. For example, our reconstruction at 75 Ma suggests that drainage networks in the upper part of the Amazon Basin were feeding an epicontinental sea at the foot of the northern Andes (Figs. 2A and 3A). In our simulation, rearrangement of these fragmented catchments into an Amazon basin that resembles the modern one occurs first around 50 Ma (fig. S9 and movie S3), followed by periods of intermittent flooding and shallow-water sedimentation in mega lakes covering the central part of the basin (movie S3). The complete drainage reversal of the Amazon River, driven by the paleoelevation reconstruction (*5*), happens during the past 20 Myr in agreement with the geological record that suggests the drying up of the Pebas system due to dynamic uplift during the Miocene epoch (*23*, *24*).

At the catchment scale we evaluate the temporal evolution of the Orange River drainage basin in southern Africa (Fig. 2B). The surface uplift history of this cratonic interior region has been attributed to mantle processes (*25*). Such regional settings, distant from plate boundaries and with negligible effects from crustal tectonics, comprise most continental areas. However, the mechanisms driving their long-term denudation patterns as well as their contributions to global sediment flux are unclear (*26*, *27*). The modeled sediment flux shows good agreement with observations (*28*, *29*); specifically, the simulation reproduces the magnitude and timing of phases of high sedimentation rates during the Late Cretaceous (93.5 to 81 Ma) and from the Oligocene to the present day (*29*).

The simulation predicts an almost twofold increase in bulk detrital flux to the oceans during the Cenozoic (Fig. 2A). The main sediment contribution comes from subtropical rivers with a threefold increase from 5 to 15 GT per year between 60 and 30 Ma. This increase is associated with the rise of the Himalayas and Tibetan plateau and to the early rearrangement of the Amazon paleobasin. Similar conclusions have been drawn when interpreting the general increase in seawater strontium isotopic composition over the past 100 Myr, with the Late Cenozoic rise of the Himalayas as its paroxysmal expression (*30*). Our results also show an increase in sediment flux delivered to the oceans over the past 15 Myr mainly from rivers in temperate regions (Fig. 2A). This increase has already been documented (*22*, *27*) but its origin remains unclear as the cooling climate during the Late Cenozoic should result in decreasing erosion rates as wetter and warmer climates accelerate mechanical rock weathering (*31*). Under these conditions, enhanced Pleistocene glacial erosion has been invoked as a major driver (*27*, *32*). Our model does not account for glacial erosion and therefore the simulated increase represents the lower range of sediment flux estimates. It shows a net positive contribution from riverine processes during the past 10 Myr (~2 GT per year representing a ~10% increase in incoming flux) that must be considered when assessing global long-term erosion rates. However, this late increase is relatively limited and the average flux over the Neogene remains relatively stable (~18.5 GT per year).

Our method offers an independent alternative to existing approaches evaluating sediment flux and long-term trends in erosion rates (*22*, *27*) such as Be isotope ratios or thermochronometric data. Similar to these approaches, our results suggest that sediment flux were higher than what they seem from the preserved sediment record (likely induced by observational biases, also known as the Sadler effect) and provide limited evidence for any major changes in worldwide erosion rates over the Late Cenozoic (*26*, *27*).

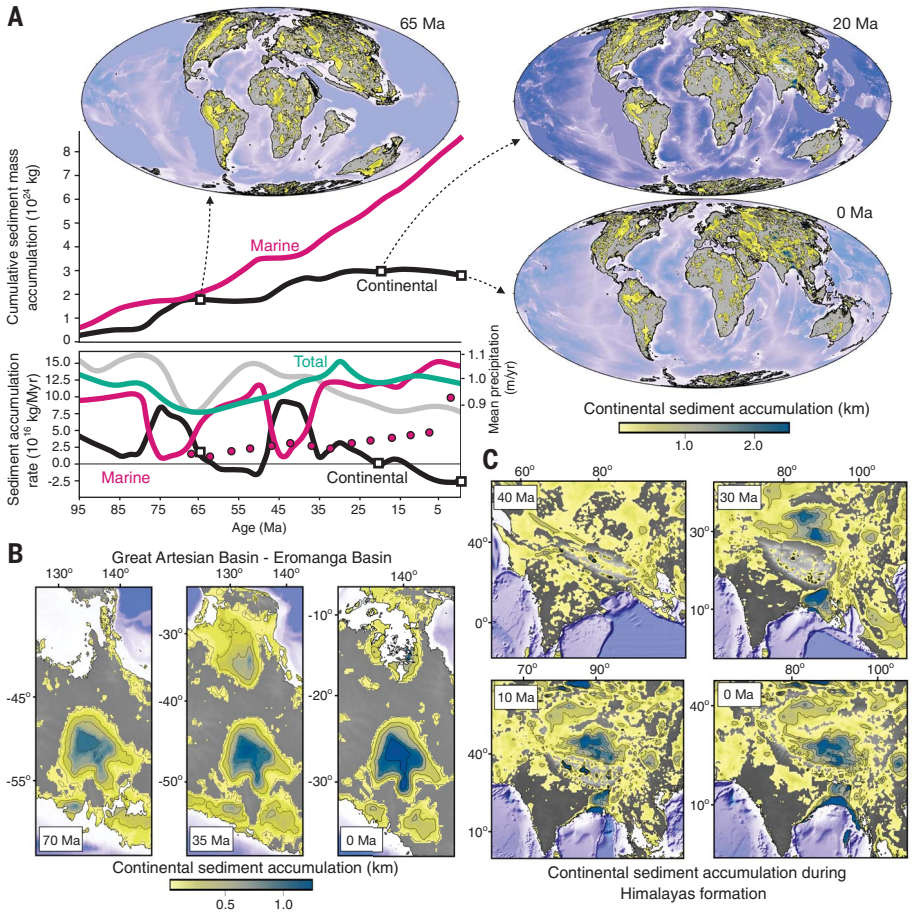

Fig. 5. Continental sediment cover temporal evolution. (**A**) Predicted temporal evolution of marine (magenta line) and continental (black line) cumulative sediment mass accumulation (top) and rate (bottom) assuming an average grain density of 2.7 g/cm^3 (total rate in teal). Magenta circles indicate estimated global values for ocean basins (*26*). The gray curve shows the average precipitation from the paleoclimate reconstruction (*3*). Maps show distribution of continental depocenters at 65, 20, and 0 Ma. (**B**) Predicted sediment accumulation in the Eromanga Basin (central Australia) showing up to 1.5 km of sediments underlying the endorheic Lake Eyre basin. (**C**) Predicted sediment accumulation in, during, and after the India-Eurasia collision. Note the formation of the Himalayan foreland basin in the south (between the Himalayan belt and the Indian continental shield) and the filling of the Tarim and Qaidam basins along the northern margin of the Tibetan plateau.

Downloaded from https://www.science.org at University of Sydney on June 21, 2023

Oceanic and continental sedimentary basins

Our framework captures, at first order, the details of sedimentary basin architectures. Here, we focus again on South America (Fig. 4) and compare cross sections of the predicted stratigraphy and sediment accumulation maps with post-rift sediment thicknesses imaged by seismic data. Section 1 crosses the Colorado Basin on its northern side where the model records up to 1.8 km of sediment accumulation followed by continuous and relatively thin layers extending across the Patagonian Shelf (Fig. 4A). The simulated stratigraphic architecture of the shelf agrees with large-scale elongated stratigraphy imaged by seismic data (*33*). For section 2, the main deposits are characterized by a seaward thickening sedimentary wedge, with two depocenters that match the location, thickness, and stratigraphic record of the Salado and Pelotas basins (*34*, *35*) (Fig. 4B). Section 3 cuts through the large alluvial plain of the Paraná Basin on its northern side, where it predicts ~250 m of post-rift sediment accumulation, before entering first the Salado then the Colorado basins. In addition, our simulation predicts an early connection (up to 45 Ma) between these basins and a late tectonic forcing that uplifted the southern side of the Salado Basin by 500 m. This, however, is partly at odds with the current understanding of the tectonic and sedimentary evolution of the region (*34*, *36*). This mismatch corroborates identified inconsistencies in Late Cretaceous paleoelevation reconstructions when compared with fossil collections (*37*, *38*). It illustrates how quantitative metrics extracted from our approach could be used to test existing paleogeographic reconstructions. To adjust the paleoelevation reconstruction, one option consists of extending eastward the orographic belt of the Tandilia System during the early stages of the simulation until the predicted stratigraphic record matches the subsurface archive (*37*).

Continental sediments modulate the geological carbon cycle through weathering (*39*). As such, investigating the spatial and temporal evolution of terrestrial sinks is crucial to refining our understanding of Earth's paleoclimate variability. In contrast to marine deposits on continental margins, for which overall net deposition and good stratigraphic control exist (*15*), terrestrial sedimentary basins are typically less complete due to sedimentary erosion and hiatuses and are much harder to correlate between basins (*8*). From our simulation, we estimate the temporal evolution of endorheic (internally drained) and exorheic (coastal) continental sinks (Fig. 5A) and find that terrestrial deposits store some 28% of the total sedimentary yield over the past 100 Myr. We predict a two-stage increase, first between 80 and 60 Ma during the drying of the North America interior seaway (*5*), partial sedimentary filling of Andean retroarc foreland basins (*40*), and to a lesser extent, the transition from marine to fluvial lacustrine environments of the epicontinental Eromanga Sea (*19*) (Fig. 5B). The second, between 50 and 25 Ma, is triggered by the Himalayan orogeny and the development of extensive foreland basins (*16*, *17*) and the filling of large endorheic basins north of the Tibetan plateau (Fig. 5C). We find that global sediment accumulation rates are relatively constant over the past 100 Myr with an average value of 11.5×10^{16} kg per Myr (ranging between 7.6 and 15.0×10^{16} kg per Myr, Fig. 5A). It supports the null hypothesis (*27*) that suggests a limited impact of global climate change and mountain building events on the long-term global sedimentation rate (*41*). Despite its overall global stability, the analysis of individual contribution from either marine or continental regions tells a more complex history related to the fine balance between physiography development, sediment transport, and deposition (Fig. 5A). Over the Late Cenozoic (from 30 Ma), we predict a long-term decrease in preserved continental sediment volume. Negative rates in Fig. 5A represent erosive periods (particularly along continental margins) that translate into stratigraphic hiatuses and explain the observed mismatch between estimated and simulated sediment accumulation rates (Fig. 5A). We first relate this long-term continental decrease to limited accommodation space in major endorheic basins due to rapid infilling by sustained erosion before the Oligocene-Eocene transition. This infill is concomitant with the development of major continental-scale drainage systems throughout the Miocene (such as the Amazon, Ganges-Brahmaputra, or Indus river basins Figs. 3A, 5C, and fig. S7B) that wash out sediments from the surface of continents. In addition, the Oligocene-Eocene transition marks the emergence of continental shelves which become prone to continental erosion and increase sediment transfer to the marine environment (*41*). Our results not only highlight the critical role played by the sediment routing systems in modulating long-term sediment fluxes at the global scale but also offer a new perspective on the apparent discrepancy between Late Cenozoic stability of global erosion rates (*27*) and the observed increase in marine sedimentation (*22*, *30*).

Conclusion

We have built a quantitative and integrated exploratory modeling framework that provides global predictions of physiographic changes at 10 km and 1 Myr resolution. This time-lapse view of the Earth's landscapes is tightly linked to its associated global stratigraphy for the past 100 Myr. Our simulations yield suites of continuous, high-resolution global elevation and erosion/deposition accumulation maps, as well as water and sediment fluxes and stratigraphic information that form the basis for estimating the rates at which the global landscape changes. This dataset permits testing of the responses of the Earth's surface to different hypotheses related to climate, tectonics, and paleogeography. In addition, our model reproduces the key components of source-to-sink systems from catchment dynamics depicting river networks over time, to marine and continental sedimentary basin evolution under various forcing conditions. This analysis permits better quantification of the role that the constantly evolving physiography of the Earth has played in modulating the transport of sediments from mountain tops to ocean basins, ultimately regulating the carbon cycle and Earth's climate fluctuations through deep time. Exploring these results in tandem with the geological record will permit testing of long-standing hypotheses regarding first order features of the Earth system, such as biogeochemical cycles or biological evolution. The approach can also help to identify inconsistencies in our understanding of the origin and evolution of particular sedimentary strata and to pose alternative hypothesis that could be tested with, for example, new thermochronological or stratigraphic data in certain model-highlighted locations.

REFERENCES AND NOTES

1. J. P. Syvitski, S. D. Peckham, R. Hilberman, T. Mulder, *Sediment. Geol.* **162**, 5–24 (2003).
2. E. Straume, C. Gaina, S. Medvedev, K. Nisancioglu, *Gondwana Res.* **86**, 126–143 (2020).
3. P. Valdes, C. Scotese, D. Lunt, *Clim. Past* **17**, 1483–1506 (2021).
4. O. Hagen *et al.*, *J. Biogeogr.* **46**, 1792–1807 (2019).
5. C. Scotese, N. Wright, PALEOMAP Paleodigital Elevation Models for the Phaerozoic (2018); https://www.earthbyte.org/webdav/ftp/Data_Collections/Scotese_Wright_2018_PaleoDEM/Scotese_Wright2018_PALEOMAP_PaleoDEMs.pdf.
6. T. Salles, C. Mallard, S. Zahirovic, *J. Open Source Softw.* **5**, 2804 (2020).
7. B. Peucker-Ehrenbrink, *Geochem. Geophys. Geosyst.* **10**, 6 (2009).
8. B. Nyberg, R. Gawthorpe, W. Helland-Hansen, *Geomorphology* **316**, 1–23 (2018).
9. W. Ludwig, J.-L. Probst, S. Kempe, *Global Biogeochem. Cycles* **10**, 23–41 (1996).
10. K. Whipple, G. Tucker, *J. Geophys. Res.* **104**, 17661–17674 (1999).
11. J. Perron, L. Royden, *Earth Surf. Process. Landf.* **38**, 570–576 (2013).
12. B. A. Adams, K. X. Whipple, A. M. Forte, A. M. Heimsath, K. V. Hodges, *Sci. Adv.* **6**, eaaz3166 (2020).
13. A. G. Lima, A. L. Binda, *J. S. Am. Earth Sci.* **48**, 262–270 (2013).
14. V. Rodríguez Tribaldos, N. J. White, G. G. Roberts, M. J. Hoggard, *Geochem. Geophys. Geosyst.* **18**, 2321–2353 (2017).
15. E. O. Straume *et al.*, *Geochem. Geophys. Geosyst.* **20**, 1756–1772 (2019).
16. P. Clift, *Prog. Earth Planet. Sci.* **4**, 39 (2017).
17. M. Blum *et al.*, *Sci. Rep.* **8**, 7973 (2018).
18. J.-L. Grimaud, D. Rouby, D. Chardon, A. Beauvais, *Basin Res.* **30**, 169–186 (2018).
19. C. Braz *et al.*, *Basin Res.* **33**, 3378–3405 (2021).
20. M. Rodger, A. Watts, C. Greenroyd, C. Peirce, R. Hobbs, *Geology* **34**, 1081–1084 (2006).
21. J. D. Milliman, J. P. M. Syvitski, *J. Geol.* **100**, 525–544 (1992).
22. P. Molnar, *Annu. Rev. Earth Planet. Sci.* **32**, 67–89 (2004).

Downloaded from https://www.science.org at University of Sydney on June 21, 2023

23. G. Shephard, L. Liu, D. Müller, M. Gurnis, *Gondwana Res.* **22**, 658–663 (2012).
24. N. Flament, M. Gurnis, D. Müller, D. Bower, L. Husson, *Earth Planet. Sci. Lett.* **430**, 9–18 (2015).
25. J. R. Stanley, R. M. Flowers, *Lithosphere* **12**, 74–87 (2020).
26. J. K. Willenbring, F. von Blanckenburg, *Nature* **465**, 211–214 (2010).
27. J. Willenbring, D. Jerolmack, *Terra Nova* **28**, 11–18 (2015).
28. J. Stanley *et al.*, *Journal of Geophysical Research: Solid Earth* **126**, e2020JB021243 (2021).
29. G. Baby, F. Guillocheau, J. Braun, C. Robin, M. Dall'Asta, *Terra Nova* **32**, 53–65 (2020).
30. J. M. Edmond, *Science* **258**, 1594–1597 (1992).
31. M. C. Eppes *et al.*, *Geophysical Research Letters*, **47**, 2020GL089062, (2020).
32. M. Koppes *et al.*, *Nature* **526**, 100–103 (2015).
33. J. Cavallotto, R. Violante, F. Hernández-Molina, *Biol. J. Linn. Soc.* **103**, 346–362 (2011).
34. B. Conti *et al.*, *Mar. Pet. Geol.* **83**, 1–25 (2017).
35. U. Schattner, F. J. Lobo, A. López-Ouirós, J. L. Nascimento, M. Mahiques, *Basin Res.* **32**, 293–301 (2019).
36. J. Lovecchio *et al.*, *Terra Nova* **30**, 359–368 (2018).
37. M. J. Arrouy *et al.*, *Sci. Rep.* **6**, 30590 (2016).
38. W. Cao *et al.*, *Biogeosciences* **14**, 5425–5439 (2017).
39. J. Krissansen-Totton, D. C. Catling, *Nat. Commun.* **8**, 15423 (2017).
40. M. C. Menegazzo, O. Catuneanu, H. K. Chang, *Mar. Pet. Geol.* **73**, 131–156 (2016).
41. R. Schumer, D. Jerolmack, *J. Geophys. Res.* **114**, F00A06 (2009).

ACKNOWLEDGMENTS

This research was undertaken with resources from the National Computational Infrastructure supported by the Australian Government and from Artemis HPC supported by the University of Sydney. We would also like to thank the two anonymous reviewers for their suggestions and comments. **Funding:** This work was supported by the following: Australian Research Council grant IC190100031 (to T.S.) and Australian Research Council grant DE210100084 (to S.Z.) **Author contributions:** Conceptualization: T.S. and L.H. Methodology: T.S. and L.H. Investigation: T.S. and L.H. Visualization: T.S. and L.H. Funding acquisition: T.S. and S.Z. Project administration: T.S. Supervision: T.S. Writing – original draft: T.S., L.H., P.R., N.C., and M.A. Writing – review and editing: T.S., L.H., P.R., N.C., M.A., S.Z., C.M., and B.H.B. **Competing interests:** Authors declare that they have no competing interests. **Data and materials availability:** The scientific software used in this study, goSPL (*13*), is available from https://github.com/Geodels/gospl and the software documentation can be found at https://gospl.readthedocs.io. We also provide a series of Jupyter notebooks used for pre-and post-processing model outputs and can be accessed at https://github.com/Geodels/gospl-global-workflows. The PALEOMAP paleoelevation reconstruction and related GPlates rotation and geometry files are downloaded from https://www.earthbyte.org/paleodem-resource-scotese-and-wright-2018. Paleoprecipitation maps from the HadCM3BL-M2.1aD model (*3*) are available at https://www.paleo.bristol.ac.uk. Simulation results provided as netcdf files containing four parameters: elevation, filled flow accumulation (rivers with lakes), flow accumulation (rivers only) and watershed (drainage basins) are available at 5 Myr interval from https://osf.io/5aek4/.
License information: Copyright © 2023 the authors, some rights reserved; exclusive licensee American Association for the Advancement of Science. No claim to original US government works. https://www.sciencemag.org/about/science-licenses-journal-article-reuse

SUPPLEMENTARY MATERIALS

science.org/doi/10.1126/science.add2541
Materials and Methods
Figs. S1 to S11
Table S1
Movies S1 to S3
References (*42*–*72*)

Submitted 2 June 2022; accepted 12 January 2023
10.1126/science.add2541

Downloaded from https://www.science.org at University of Sydney on June 21, 2023

Science
AAAS

Hundred million years of landscape dynamics from catchment to global scale

Tristan Salles, Laurent Husson, Patrice Rey, Claire Mallard, Sabin Zahirovic, Beatriz Hadler Boggiani, Nicolas Coltice, and Malis Arnould

Science, **379** (6635), .
DOI: 10.1126/science.add2541

Shaping Earth's surface

How has sediment transfer and accumulation from lands to oceans affected Earth's geomorphology? Salles *et al*. present results from a high-resolution model of surface physiography, validated by independent observations from the geological record, which simulates landscape evolution caused by erosion and deposition over the past 100 million years (see the Perspective by Ehlers). Their results should help us better understand the apparent contradiction between the observed Late Cenozoic pulse in marine sedimentation and the constancy of the global weathering flux. —HJS

View the article online
https://www.science.org/doi/10.1126/science.add2541
Permissions
https://www.science.org/help/reprints-and-permissions

Use of this article is subject to the Terms of service

Science (ISSN) is published by the American Association for the Advancement of Science. 1200 New York Avenue NW, Washington, DC 20005. The title *Science* is a registered trademark of AAAS.
Copyright © 2023 The Authors, some rights reserved; exclusive licensee American Association for the Advancement of Science. No claim to original U.S. Government Works

Downloaded from https://www.science.org at University of Sydney on June 21, 2023

B| APPENDIX

Landscape dynamics and the Phanerozoic diversification of the biosphere

Salles, T., Husson, L., Lorcery, M. and Hadler Boggiani, B., 2023. Landscape dynamics and the Phanerozoic diversification of the biosphere. *Nature*, 624(7990), pp.115–121. DOI: 10.1038/s41586-023-06777-z.

Article

Landscape dynamics and the Phanerozoic diversification of the biosphere

https://doi.org/10.1038/s41586-023-06777-z

Received: 21 April 2023

Accepted: 23 October 2023

Published online: 29 November 2023

Open access

Check for updates

Tristan Salles[1,3]✉, Laurent Husson[2,3]✉, Manon Lorcery[1,2] & Beatriz Hadler Boggiani[1]

The long-term diversification of the biosphere responds to changes in the physical environment. Yet, over the continents, the nearly monotonic expansion of life started later in the early part of the Phanerozoic eon[1] than the expansion in the marine realm, where instead the number of genera waxed and waned over time[2]. A comprehensive evaluation of the changes in the geodynamic and climatic forcing fails to provide a unified theory for the long-term pattern of evolution of life on Earth. Here we couple climate and plate tectonics models to numerically reconstruct the evolution of the Earth's landscape over the entire Phanerozoic eon, which we then compare to palaeodiversity datasets from marine animal and land plant genera. Our results indicate that biodiversity is strongly reliant on landscape dynamics, which at all times determine the carrying capacity of both the continental domain and the oceanic domain. In the oceans, diversity closely adjusted to the riverine sedimentary flux that provides nutrients for primary production. On land, plant expansion was hampered by poor edaphic conditions until widespread endorheic basins resurfaced continents with a sedimentary cover that facilitated the development of soil-dependent rooted flora, and the increasing variety of the landscape additionally promoted their development.

The diversity of marine and terrestrial life was assembled over the Phanerozoic eon through complex interplays between biotic controls and abiotic controls[3,4] that are still unclear, although biodiversity patterns over time are fairly well identified from the fossil record[2,5] and mounting evidence from phylogenetics[6,7]. Although both continents and oceans, in the most recent stages of the Phanerozoic, host more species than ever, the monotonic increase of diversity over time in the terrestrial realm[1] contrasts with the more complex evolution of diversity in the oceans[8]. Besides the 'big five' mass extinctions[9], turning points in their progressions also became iconic: Darwin referred to the advent of flowering plants in continents as an abominable mystery; Vermeij[10] coined the term Cenozoic marine revolution. Another enduring puzzle is the late expansion of land plants compared to marine life that rapidly diversified 100 million years earlier. Although the joint effects of biotic and abiotic factors are probably required to explain the biodiversity patterns in time[3] and space[11], a wealth of possible mechanisms have been examined independently. Within this variety, truly independent potential abiotic forcings might have been overlooked, although they are not many and ultimately refer to the physical environment, which couples climatic or geological forcings, suggesting that biodiversity trends could be more comparable for marine and terrestrial life.

Continental drift sets the distribution of landmasses at the surface of the Earth during the Phanerozoic. The changing palaeogeography in turns influences the atmospheric circulation. Both plate tectonics and climate are critical to the development of marine and terrestrial life, by setting the latitude and hours of daylight, temperatures or hydrological cycles. Although these processes are undoubtedly primordial, they do not account for the dynamic evolution of the surface of the Earth, which should not be regarded as a series of stationary configurations. Reliefs are changing over time and mass transfers are crucial to the expansion of life: both on the continents and in the oceans, nutrient availability is determined by landscape dynamics. Understanding the impact of nutrient fluxes thus requires a comprehensive quantitative approach that we develop herein, leaving aside the role of truly biotic processes.

Here we propose a new method to quantify the global-scale physiographic changes over the Phanerozoic eon, applying the landscape evolution model goSPL[12,13] to a series of global-scale palaeo-elevation reconstructions, consistently tied to a plate tectonic model[14] and to a series of palaeoclimatic reconstructions[15] (Fig. 1). Our approach allows us to jointly quantify the tectonic uplift at long wavelengths and the high-resolution dissection of the landscape (Methods and Extended Data Figs. 1 and 2). Model outputs, including high-resolution topography, continental erosion and sedimentation rates, drainage networks and sediment and freshwater yields to the oceans (all datasets released online[16]), allow estimation of the impacts of surface processes on the physiography of the Earth throughout the entire Phanerozoic (Fig. 1). Sensitivity tests using alternative climatic and tectonic models (Methods) point to spatial variations and differences in the magnitude of erosion rates although global temporal trends remain mostly insensitive (Extended Data Fig. 6a,c).

Reconstructing sediment flux dynamics

Surface processes are first calibrated using modern estimates of average global erosion rates[17,18] and suspended sediment flux[19,20] (Methods). Then, propagating this parameterization in past times yields temporal

[1]School of Geosciences, The University of Sydney, Sydney, New South Wales, Australia. [2]CNRS, ISTerre, Université Grenoble-Alpes, Grenoble, France. [3]These authors contributed equally: Tristan Salles, Laurent Husson. ✉e-mail: tristan.salles@sydney.edu.au; laurent.husson@univ-grenoble-alpes.fr

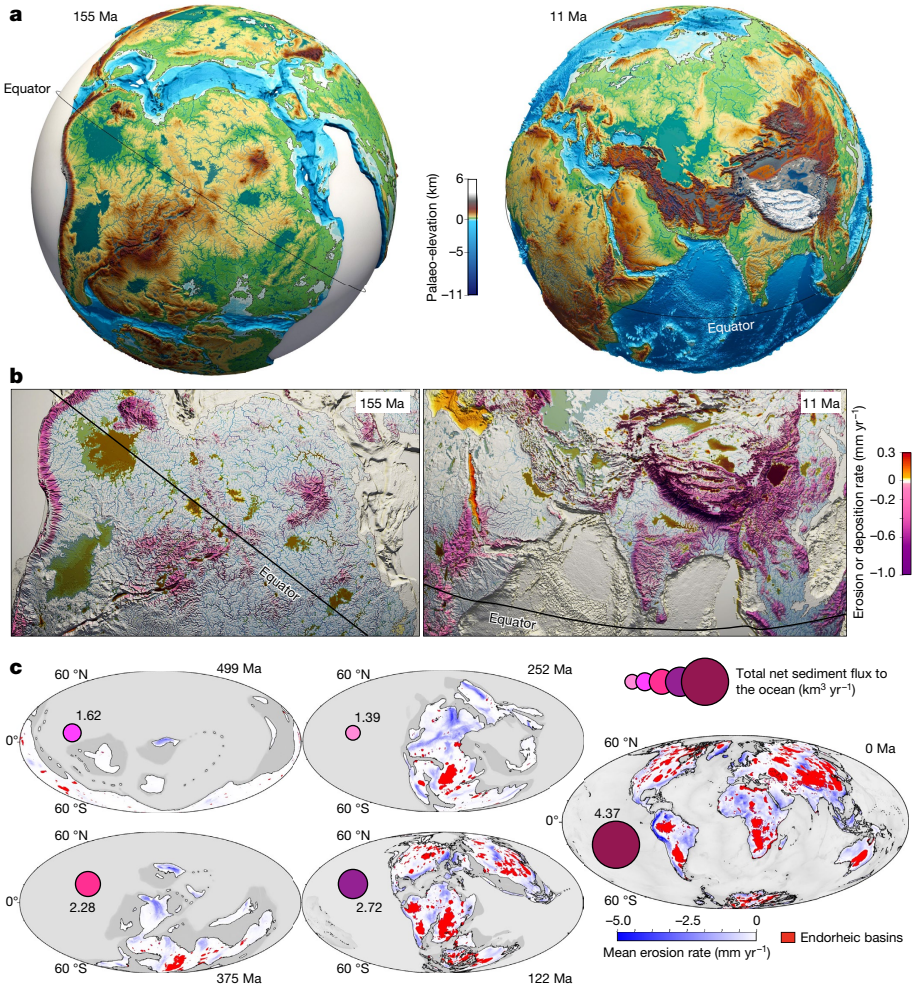

Fig. 1 | Physiographic evolution and associated patterns of erosion–deposition across the Phanerozoic. a, goSPL[12,13] simulations showing high-resolution palaeo-landscape, heterogeneous landforms and drainage networks, under the influence of surface processes, at 155 Ma and 11 Ma. **b**, Erosion and sedimentation rates; positive values correspond to deposition in endorheic basins and depressions, and negative ones to erosion across mountain ranges and along major river upstream channels, at 155 Ma and 11 Ma. **c**, Total endorheic sediment coverage since 540 Ma (in red) with cumulative mean erosion rates on continents (blue), and instantaneous global net sediment flux to the ocean for specific time intervals (purple).

trends in bulk sediment transfer (Fig. 2a) that can be tied to continental elevations and surface runoff (that is, precipitation minus evapotranspiration; Extended Data Fig. 6a). Two phases of sustained fast erosion separated by a quieter period mark the long-term Phanerozoic evolution. The Palaeozoic phase relates to an increase in continental runoff from the Silurian period to the Carboniferous period, and to higher reliefs until the assembly of Pangaea during Permian times. Lower continental elevations and more arid conditions prevailed until Pangaea breakup after the Triassic period. During this period, up to 30% of eroded materials were trapped in the terrestrial domain (Fig. 2a). The Meso-Cenozoic phase of erosion, from the Jurassic period onwards, is marked by a more than twofold increase in erosion flux, fostered by higher runoff and by the rising reliefs of the Cenozoic mountain belts. During that phase, most of the sediments are directly transferred to the ocean (continental deposition decreases to about 13% of the erosion flux). Several peaks in erosion flux, coinciding with major orogenic episodes, overprint the low-frequency Phanerozoic trend (Fig. 2a).

By redistributing sediments eroded from the continental reliefs to the oceans, rivers are crucial players in biochemical cycles. However, before extrapolating the model results towards such considerations in deep time, we confront our model predictions with available independent data. First, the geography of model-predicted modern river outlets and watersheds conforms with actual ones (Extended Data Fig. 3). Likewise, the predicted water discharge and sediment yield for the largest modern rivers compare to current ones[13]. As an example, our predictions of the Amazon River discharge and sediment flux are respectively well within the estimated range (6,591 to 7,570 km^3 yr^{-1})[20] and only about 4% below the sediment production rate inferred from cosmogenic nuclide analysis (about 610 Mt yr^{-1})[21]. Our model faithfully accounts for the discharge–area scaling relationship between water and sediment flux at the present day[22], and throughout the entire Phanerozoic (Extended Data Fig. 3). Predicted trends of sediment flux compare reasonably well with observations[17], although more closely during the Meso-Cenozoic for which the record is more accurate (Extended Data Fig. 6c). Water and sedimentary fluxes are remarkably anticorrelated over time to the average area of the watersheds (Extended Data Fig. 3c), indicating that large sediment yields are primarily due to small basins characteristic of the heterogeneous landscapes found in tectonically dynamic regions. This is well exemplified by the sharp increase in average drainage basin areas about 240 million years ago (Ma) related to the development of the low-relief landmasses of Pangaea, which closely matches a major decrease in sediment and water flux. Following Pangaea breakup after 200 Ma, water and sediment flux resume owing to wetter climates

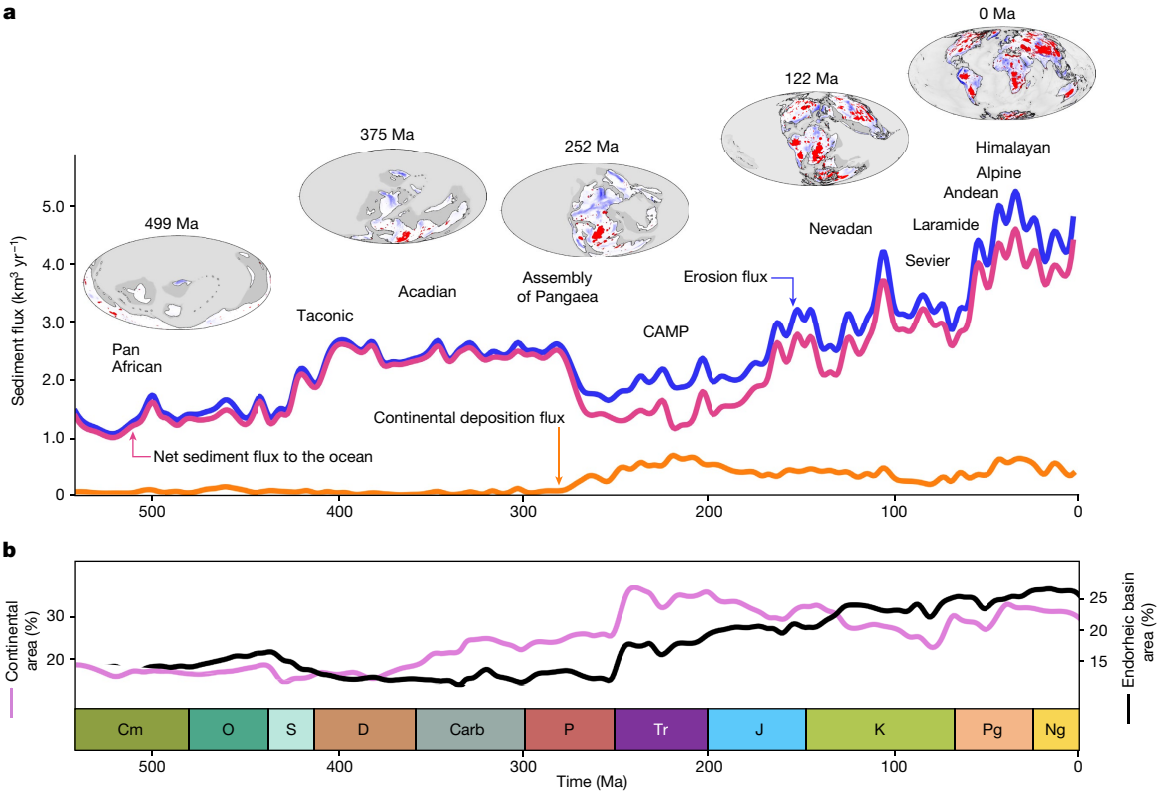

Fig. 2 | Reconstructed sediment flux and continental sedimentary basin evolution. a, Simulated global erosion flux, net sediment flux delivered to the ocean and endorheic sedimentation flux; and major orogenic episodes for the Phanerozoic (CAMP, Central Atlantic Magmatic Province). **b**, Global changes in total continental area, and in modelled endorheic basin area. Cm, Cambrian; O, Ordovician; S, Silurian; D, Devonian; Carb, Carboniferous; P, Permian; Tr, Triassic; J, Jurassic; K, Cretaceous; Pg, Palaeogene; Ng, Neogene.

and an overall increase in mean elevation range under renewed plate tectonic activity. We also predict that about 25% of the surface of present-day landmasses is covered by endorheic catchments (Fig. 2b), in agreement with earlier estimates[23]. Additionally, we corroborate the model-predicted sediment flux using the strontium isotopic ratio of seawater for the Phanerozoic, and with a sensitivity analysis based on different palaeo-elevation and palaeoclimate reconstructions (Methods).

Phanerozoic marine biodiversification

Owing to their quantitative nature, our model predictions provide unprecedented tools to assess the role that physiographic changes might have played in the long-term evolution of the biosphere. During the Phanerozoic, the evolution of the marine biodiversity, derived from palaeontological data[2,5,24], exhibits three major phases (Fig. 3). Following the emergence of the primitive Cambrian fauna, an initial phase of rapid diversification of the Palaeozoic fauna (between the Ordovician and Silurian periods) plateaued up to the Permian period. After a period of lower diversity over the Triassic, marine faunas monotonically diversified and radiated (Extended Data Fig. 10a).

Among the forcings that control the biodiversity, nutrient availability is regarded as one of the most influential environmental drivers because it directly acts on primary productivity within the trophic zone required to sustain marine life[4,24,25] and diversity[26,27]. As nutrient intake by the oceans is primarily related to river runoff, higher erosion rates during orogenic episodes have been proposed as a crucial extrinsic forcing[24,25,28]. Yet inferences between nutrient flux and erosion are to our knowledge only qualitatively assessed, either from the geochemical trends—often matching marine genera to the equivocal $^{87}Sr/^{86}Sr$ isotopic ratio of seawater—or by deriving first-order empirical relationships between mountain elevations and sediment flux from major rivers. Our direct quantification of these fluxes over time permits us to alleviate the biases associated with the interpretation of the $^{87}Sr/^{86}Sr$ ratio of seawater (see Methods) or caused by the default assumption[23] of a linear transfer function between elevation and sediment transport. For example, downstream sediment storage in endorheic basins or reduced precipitation due to orographic shadowing curbs the sediment yield to the oceans, and conversely, small exorheic basins might enhance transport in mid-elevation regions[29].

The reconstructed net sediment flux to the ocean and the total number of marine families are strongly correlated (Pearson coefficient 0.88) and sediment flux variation markedly matches the three main phases that span the Phanerozoic eon (Fig. 3 and Extended Data Fig. 10a). This suggests that nutrient availability is a prime control on marine diversity, providing an explanation for the observed Palaeozoic plateau—as opposed to a continuous increase—and for the Mesozoic marine revolution[10] that sparked biodiversification until the present day, but also for the low-diversity period of Pangaea, when endorheic basins suddenly sequestered a vast amount of sediments over the continents, depriving oceans of about 30% of the nutrient source (Figs. 1c and 2a). The time lag between the Great Ordovician Biodiversification Event and the predicted increase in Palaeozoic sediment fluxes (Fig. 3) could be explained either by uncertainties in the reconstructions of the climate and tectonics, or by the overwhelming effect of climate cooling[30].

Mass extinctions are inescapable attributes of the marine diversity curve[9], which can also be partially matched to the high-frequency variations in the predicted sediment yield to the oceans. Among the big five extinction events, the most pronounced one, during the end-Permian, is associated with the largest drop in sediment flux (Fig. 3).

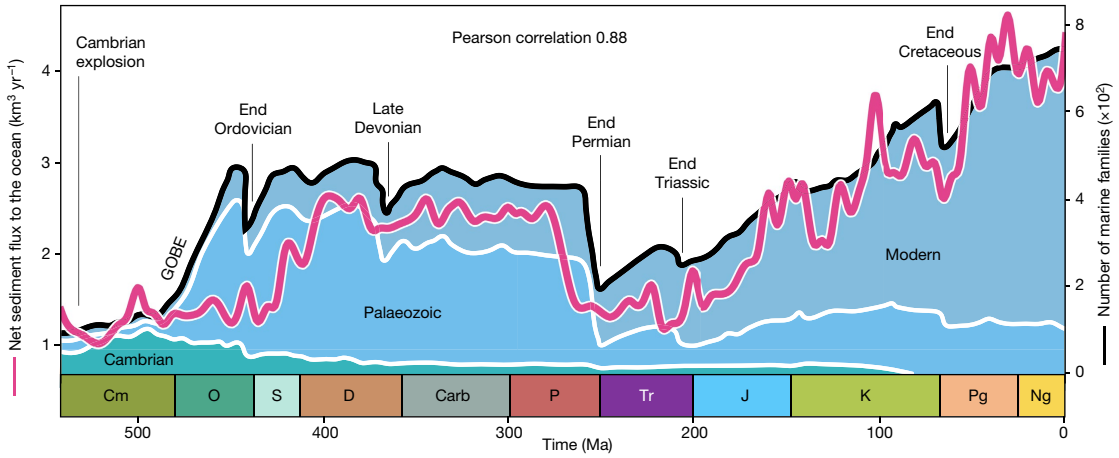

Fig. 3 | Sediment flux to the oceans and diversity of marine animal families during the Phanerozoic. Predicted trend in net sediment flux to the ocean (purple curve) and diversity of Cambrian, Palaeozoic and modern marine families (black line indicates total marine families, and Cambrian, Palaeozoic and modern faunas are delimited by white lines, all derived from Sepkoski's compendium[2]; http://strata.geology.wisc.edu/jack/). The Pearson coefficient of 0.88 indicates a strong positive correlation between the two variables. The Cambrian explosion and Great Ordovician Biodiversification Event (GOBE), as well as the big five mass extinction events[9], are indicated.

Besides the end-Ordovician and end-Triassic crises, mass extinction events occurred in the aftermath (about 2 to 15 Myr) of important reductions in the net sediment flux (Fig. 3), caused by either major declines in precipitation rates (Late Devonian) or elevation and palaeogeography (end-Permian), or both (end-Cretaceous; Extended Data Fig. 6a). Conversely, intensified hydrological conditions and weathering, and increases in nutrient discharge, are often considered as major drivers of oceanic anoxia[31] and possibly extinction[32]. Although some congruences between specific Mesozoic anoxic events[33] and peaks in predicted net sediment flux to the ocean can be found in our model, here instead, we posit that sediment shortage—and not excess—more efficiently acts as an essential undermining mechanism before the impact of the compounding processes that ultimately triggered the episodes of mass extinctions (for example, sea-level fluctuations, rapid climatic changes, volcanism and bolide impacts) during Phanerozoic history, as referred to in the press-pulse framework[34].

The identified relationship between marine biodiversity and predicted ocean sedimentary flux could be a direct consequence of the incompleteness and spatial heterogeneity of the fossil record. Many have already raised the issue of preservation bias in the marine palaeobiological record[8,35,36]. If so, the calculated strong correlation would represent an original tool to deconstruct biodiversity curves[37], and computed sediment flux could be used to find under-explored regions with high preservation potentials from the spatiotemporal distribution of simulated palaeo-rivers (Extended Data Fig. 9a). While acknowledging the possibilities for biases in the fossil record[2,5,24], we suggest that the carrying capacity for biodiversity of the oceans is extensively contingent on sedimentary flux and, therefore, on the physiographic evolution of continents. This supports earlier claims that abiotic factors (either environmental[38,39] or related to continental fragmentation and reassembly[40,41]) control speciation and extinction rates. The recently proposed diversity hotspots hypothesis[11] posits that stability in environmental conditions and high continental fragmentation drove the global marine diversity to levels rarely approaching ecological saturation. Our results accordingly support the idea that tectonically driven shifts in palaeogeographies (that is, creation and destruction of geological barriers) and global ocean–atmospheric circulation ultimately affect sediment transport, which in turn modulates the carrying capacity for marine diversity. Our method offers an independent alternative to existing approaches evaluating long-term trends in nutrient flux[24,25,28]; a natural avenue will be to account for the variable lithologies of eroded continental rocks over time and space (for example, large igneous provinces, and continental and volcanic arcs) to precisely quantify the chemical nature of the transferred nutrients (such as silica or phosphorus) that may foster or hinder the development of certain species and trigger evolutionary innovations.

Phanerozoic terrestrial diversification

Along the same lines, we reappraise the diversification of terrestrial life during the Phanerozoic eon, except that we focus on land plants whose role as primary producers limits the impact of uncontrolled feedback interactions within the trophic chain. For that purpose, we test the possible impact of physiographic changes on vascular plants, by taking as predictors the sedimentary flux onto continents, the gradual spreading of the sediment cover over landmasses and the physiographic diversity of the landscape (Methods).

At first order, the diversification of land plants[1] shows a roughly monotonic increase in the number of species from the Carboniferous onwards (Fig. 4a). Our model results indicate that the sediments accumulated in endorheic basins but that the flux was uneven through time. Owing to the model integration period, the sediment cover is null when the simulation starts, but this does not suggest that no sediment accumulated before the Cambrian period. We however reason that former soft sediments would have turned into barren hard rocks by 450 Ma owing to the limited sediment storage on continents during the Palaeozoic era (Fig. 2a). Sediment flux rapidly rose during the Mesozoic and Cenozoic eras. The good correlation between the sediment flux on continents and the bulk diversity of terrestrial plants (Pearson coefficient 0.67) already suggests that diversification is limited by sediment availability at any time. Moreover, endorheic sediments were mostly preserved after their deposition, thereby increasing the total continental surface covered by sediments (Figs. 1c and 4a). The correlation markedly improves (Pearson coefficient 0.91 (Fig. 4a) and up to 0.96 when limited to the gymnosperms and angiosperms (Extended Data Fig. 10b)) when considering instead that it is the spatial coverage of sediments cumulated over time that limits diversification, by replacing the bare rocks of the substratum with a soil that provides nutrients and moisture to the more specialized plant species that develop over time. Sediment cover is a necessary but non-unique condition for the development of terrestrial plants[42], and for soil and sediment cover to have an effect of diversification, life is required to co-evolve[6,42]. However, after the inception of life, our results suggest that it is the sediment cover that sets the carrying capacity.

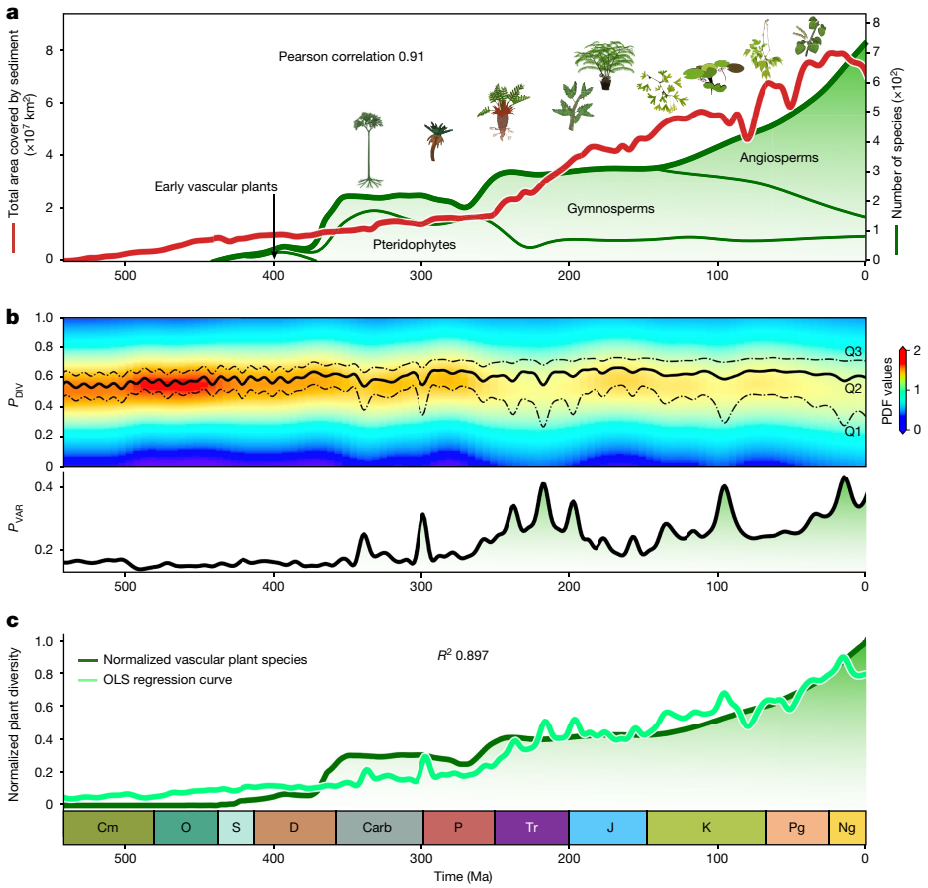

Fig. 4 | Continental sediment deposition and physiographic complexity, and diversity of vascular plants, during the Phanerozoic. a, Predicted cumulative area covered by sediments (red curve) and diversity of tracheophyte species throughout the Phanerozoic[1] (green curves). The Pearson coefficient of 0.91 indicates a strong positive correlation between the two main curves. **b**, Top: temporal distribution of the physiographic diversity index (P_{DIV}; Methods) with lower (Q1; 25%), median (Q2) and upper (Q3; 75%) quartiles. Probability density function (PDF) is used to estimate the likelihood of having a specific P_{DIV} for each time interval. Bottom: temporal evolution of the physiographic variety index (P_{VAR} given by the interquartile range of P_{DIV} ($Q3–Q1$). **c**, Multivariate regression analysis (ordinary least squares (OLS) regression curve) carried out on normalized cumulative area covered by sediments (S_{COV}) and physiographic variety (P_{VAR}) gives a strong statistically significant relationship (P value $< 2.2 \times 10^{-16}$). The resulting regression equation is defined by $0.019 + 0.27P_{VAR} + 0.61S_{COV}$. Analysis of variance shows a high dependence of plant diversity dynamics on these abiotic parameters ($R^2 \approx 0.9$). Botanical icons by Rebecca Horwitt, available at full size and open access from https://sites.psu.edu/rhorwitt/.

A further incentive to diversification comes from the increasing physiographic variety of the landscape (Fig. 4b) since the Carboniferous. Whereas the mean physiographic diversity (P_{DIV}; Methods) varies only moderately throughout the Phanerozoic eon, the physiographic variety (P_{VAR}; Methods) varies strongly. From the Triassic to the Cretaceous period, and during the Cretaceous and Cenozoic, the variety of the landscape increases at times when the overall rate of diversification accordingly increased (Fig. 4). By offering new habitats, periods of increased topographic heterogeneity have been identified as drivers of diversification at the regional scale[43,44]; our results qualify this observation and indicate that the impact is in fact global, but also that it is the variety of the landscape—from low and high diversity—that promotes the overall diversification of terrestrial plants (Fig. 4c).

More insights can be gained by scrutinizing the evolution at genus level (Fig. 4a). During the early Palaeozoic era, continents covered less than 20% of the Earth surface with restricted endorheic basins (about 17% of emerged lands; Fig. 2b) and sparse continental deposition, hampering both soil production by physical and chemical weathering and preservation. Irrespective of climatic or biological factors, these poor edaphic conditions are suitable only for non-vascular plants that inhabit a variety of substrates (including bare rock) and access nutrients directly from meteoric waters and leachate[4,7]. Early vascular plants radiated during the Devonian period, with the development of arborescent species and seed plants[4,6]. Our reconstructions show that at that time, the increased global sediment flux (Fig. 2a) was not stored in endorheic basins (Fig. 4a), and that the physiographic variety was low (Fig. 4b). The low diversification of early vascular plants on land was thus driven only by species adaptation and climatic forcing rather than by geomorphological changes[45,46]. This is corroborated by the increasing tolerance of plants to water stress and seasonality[47] associated with the colonization of diverse environments[6,48] at that time, feeding back on the landforms they live on[6].

The diversity of land plants steeply increased only during the Late Devonian epoch with the rapid rise of pteridophytes and gymnosperms, but diversity quickly plateaued until the mid-Permian. As the total sediment coverage of landmasses stalled during that period (Fig. 4a) despite sustained erosion flux (Fig. 2a), we suggest that the diversity of terrestrial plants was further hampered by the limited expanse of favourable edaphic conditions.

Over the Permian and Triassic, pteridophytes were superseded by gymnosperms that further radiated (Fig. 4a). At that time, the Pangaea supercontinent gathered more emerged lands than at any other time in the Phanerozoic (Fig. 2b). Sediment-covered surface areas also rapidly increased owing to the development of large endorheic basins (up to 20% of the continental surface; Fig. 2b), fed by a sustained flux of

sediments from the high relief of the widespread circum-Pangaean orogenies[49] (Fig. 4a). The massive development of these reliefs is also associated with an increase of physiographic variety (Fig. 4b). The emergence of these conditions, which would favour the diversification of deep-rooting plants across a diverse range of physiographic environments, coincided with the development of gymnosperms (Fig. 4) that dominated terrestrial floras by the end of the Triassic[4].

Gymnosperm diversity continued to rise during the early phases of Pangaea breakup before levelling off during the Jurassic and Cretaceous, along with a decrease in both continental deposition flux (Fig. 2a) and physiographic variety (Fig. 4b), as well as a relatively steady sediment coverage (Fig. 4a), which all restrained the favourable rejuvenation of continental surfaces. Gymnosperms were superseded by angiosperms that diversified at unprecedented rates at least from the Cretaceous onwards (Fig. 4a and Extended Data Fig. 10b), although the timing remains largely controversial[50,51]. Common explanations invoke their efficient cross-pollination strategies and high growth rates[52,53]. Yet the period was also marked by extensive orogenic phases in North and South America and Eurasia (Fig. 2a). At that time, erosion resumed in the reliefs along with renewed endorheic deposition in the lowlands, and the overall physiographic variety further increased (Fig. 4b). The new diverse niches that developed in this heterogeneous topography, along with quickly expanding, nutrient-rich continental surfaces, could have promoted the fast radiation of angiosperms.

Conclusion

Our study shows a remarkable congruence between the Phanerozoic landscape dynamics and the diversification of both marine life and terrestrial life. Earlier work already identified elements of this, but the analyses remained fragmentary[25,53–56], considering isolated pieces of the environmental puzzle: climatic, geological or biotic. Here we suggest that the evolution of continental physiography—as set by the interplay between the geosphere and the atmosphere—determines nutrient availability, and that it is a crucial limiting factor in both the marine realm and terrestrial realm, as important as intrinsic biotic processes[9,10,53], or extrinsic processes such as the climatic control[46] or plate tectonics[41]. In the oceans, riverine sedimentary flux directly sets nutrient availability for primary productivity. In continents, nutrient availability is tuned by endorheism, by rerouting the sedimentary flux and gradually varnishing their surfaces with a sedimentary cover, which facilitates the development of more specialized species. The relative effects of physiographic diversity and erosion rates on diversification are difficult to discriminate, but we suggest that the variety of the physiography further adjusts the effect of endorheism by tessellating the landscape.

The modality of sediment routing implies that diversification is simultaneously detachment limited (the sediment flux should be enough to sustain diversification) and transport limited (sediment storage in continents may, in an extreme case, starve marine life while instead feeding terrestrial life, or vice versa). The Phanerozoic trends of marine and terrestrial diversity highlight these regimes: marine diversity directly scales with sediment flux and is thus dominantly detachment limited. Land plant diversity is instead transport limited: its onset occurred much later than that of marine diversity and exploded only once endorheism efficiently resurfaced continents with sediments. Overall, physiographic changes determine the carrying capacity of both the oceans and the continents.

We anticipate that these findings, together with the released sets of physiographic descriptors at a high spatial resolution for the past 540 Myr (ref. 16), will invite more quantitative reappraisal of the interactions between the solid Earth and the atmosphere, hydrosphere and biosphere. For instance, our current approach conveniently reduced the problem to the temporal dimension by extracting spatially averaged metrics but ignores the spatialization of diversification events. A thorough palaeogeographical analysis of diversification events[56] in both continents and oceans is now permitted thanks to these reconstructions. Sensitivity tests, which illustrate how denudation rates scale with climate reconstructions and endorheic sediment storage is chiefly controlled by palaeo-elevation reconstructions, will allow further testing of our hypothesis.

Online content

Any methods, additional references, Nature Portfolio reporting summaries, source data, extended data, supplementary information, acknowledgements, peer review information; details of author contributions and competing interests; and statements of data and code availability are available at https://doi.org/10.1038/s41586-023-06777-z.

1. Niklas, K. J., Tiffney, B. H. & Knoll, A. H. Patterns in vascular land plants diversification. *Nature* **303**, 614–616 (1983).
2. Sepkoski, J. J. A compendium of fossil marine animal genera. *Bull. Am. Paleontol.* **363**, 1–560 (2002).
3. Benton, M. J. The Red Queen and the Court Jester: species diversity and the role of biotic and abiotic factors through time. *Science* **323**, 728–732 (2009).
4. Martin, R. E. & Servais, T. Did the evolution of the phytoplankton fuel the diversification of the marine biosphere? *Lethaia* **53**, 5–31 (2020).
5. Rohde, R. A. & Muller, R. A. Cycles in fossil diversity. *Nature* **434**, 208–210 (2005).
6. Gibling, M. & Davies, N. Paleozoic landscapes shaped by plant evolution. *Nat. Geosci.* **5**, 99–105 (2012).
7. Morris, J. et al. The timescale of early land plant evolution. *Proc. Natl Acad. Sci. USA* **115**, 201719588 (2018).
8. Sepkoski, J. J. A factor analytic description of the Phanerozoic marine fossil record. *Paleobiology* **7**, 36–53 (1981).
9. Sepkoski, J. J. A kinetic model of phanerozoic taxonomic diversity. III. Post-paleozoic families and mass extinctions. *Paleobiology* **10**, 246–267 (1984).
10. Vermeij, G. J. The Mesozoic marine revolution: evidence from snails, predators and grazers. *Paleobiology* **3**, 245–258 (1977).
11. Cermeño, P. et al. Post-extinction recovery of the phanerozoic oceans and biodiversity hotspots. *Nature* **607**, 507–511 (2022).
12. Salles, T., Mallard, C. & Zahirovic, S. goSPL: Global Scalable Paleo Landscape Evolution. *J. Open Source Softw.* **5**, 2804 (2020).
13. Salles, T. et al. Hundred million years of landscape dynamics from catchment to global scale. *Science* **379**, 918–923 (2023).
14. Scotese, C. & Wright, N. PALEOMAP Paleodigital Elevation Models (PaleoDEMS) for the Phanerozoic PALEOMAP Project. *zenodo* https://doi.org/10.5281/zenodo.53484911 (2018).
15. Valdes, P., Scotese, C. & Lunt, D. Deep ocean temperatures through time. *Clim. Past* **17**, 1483–1506 (2021).
16. Salles, T., Husson, L., Lorcery, M. & Halder Boggiani, B. Paleo-Physiography Project. *HydroShare* http://www.hydroshare.org/resource/0106c156507c4861b4cfd40402 2f9580 (2022).
17. Wilkinson, B. & McElroy, B. The impact of humans on continental erosion and sedimentation. *Geol. Soc. Am. Bull.* **119**, 140–156 (2007).
18. Willenbring, J., Codilean, A. & McElroy, B. Earth is (mostly) flat: apportionment of the flux of continental sediment over millennial time scales. *Geology* **41**, 343–346 (2013).
19. Syvitski, J. P. M. & Milliman, J. D. Geology, geography, and humans battle for dominance over the delivery of fluvial sediment to the coastal ocean. *J. Geol.* **115**, 1–19 (2007).
20. Peucker-Ehrenbrink, B. Land2sea database of river drainage basin sizes, annual water discharges, and suspended sediment fluxes. *Geochem. Geophys. Geosyst.* **10**, Q06014 (2009).
21. Wittmann, H. et al. Sediment production and delivery in the Amazon River basin quantified by in situ–produced cosmogenic nuclides and recent river loads. *GSA Bull.* **123**, 934–950 (2011).
22. Whipple, K. X. & Tucker, G. E. Dynamics of the stream-power river incision model: implications for height limits of mountain ranges, landscape response timescales, and research needs. *J. Geophys. Res. Solid Earth* **104**, 17661–17674 (1999).
23. Nyberg, B., Gawthorpe, R. & Helland-Hansen, W. The distribution of rivers to terrestrial sinks: implications for sediment routing systems. *Geomorphology* https://doi.org/10.1016/j.geomorph.2018.05.007 (2018).
24. Cárdenas, A. L. & Harries, P. J. Effect of nutrient availability on marine origination rates throughout the Phanerozoic eon. *Nat. Geosci.* **3**, 430–434 (2010).
25. Martin, R. & Cárdenas, A. Terrestrial forcing of marine biodiversification. *Sci. Rep.* **12**, 8309 (2022).
26. Duffy, J., Godwin, C. & Cardinale, B. Biodiversity effects in the wild are common and as strong as key drivers of productivity. *Nature* **549**, 261–264 (2017).
27. Cardinale, B., Bennett, D., Nelson, C. & Gross, K. Does species diversity drive productivity or vice versa? A test of the multivariate productivity–diversity hypothesis in streams. *Ecology* **90**, 1227–1241 (2009).
28. Sharoni, S. & Halevy, I. Rates of seafloor and continental weathering govern Phanerozoic marine phosphate levels. *Nat. Geosci.* **16**, 75–81 (2023).
29. Milliman, J. D. & Syvitski, J. P. M. Geomorphic tectonic control of sediment discharge to the ocean - the importance of small mountainous rivers. *J. Geol.* **100**, 525–544 (1992).
30. Trotter, J., Williams, I., Barnes, C., Lécuyer, C. & Nicoll, R. Did cooling oceans trigger Ordovician biodiversification? Evidence from conodont thermometry. *Science* **321**, 550–554 (2008).

31. Watson, A. Oceans on the edge of anoxia. *Science* **354**, 1529–1530 (2016).
32. Ernst, R. E. & Youbi, N. How large igneous provinces affect global climate, sometimes cause mass extinctions, and represent natural markers in the geological record. *Palaeogeogr. Palaeoclimatol. Palaeoecol.* **478**, 30–52 (2017).
33. Jenkyns, H. C. Geochemistry of oceanic anoxic events. *Geochem. Geophys. Geosyst.* https://doi.org/10.1029/2009GC002788 (2010).
34. Arens, N. & West, I. Press-pulse: a general theory of mass extinction? *Paleobiology* **34**, 456–471 (2008).
35. Donovan, S. & Paul, C. *The Adequacy of the Fossil Record* (Wiley, 1998).
36. Alroy, J. et al. Phanerozoic trends in the global diversity of marine invertebrates. *Science* **321**, 97–100 (2008).
37. Harper, D. A., Cascales-Miñana, B., Kroeck, D. M. & Servais, T. The palaeogeographical impact on the biodiversity of marine faunas during the Ordovician radiations. *Glob. Planet. Chang.* **207**, 103665 (2021).
38. Stanley, S. An analysis of the history of marine animal diversity. *Paleobiology* **33**, 1–55 (2007).
39. Hannisdal, B. & Peters, S. Phanerozoic earth system evolution and marine biodiversity. *Science* **334**, 1121–1124 (2011).
40. Valentine, J. & Moores, E. Plate-tectonic regulation of faunal diversity and sea level: a model. *Nature* **228**, 657–659 (1970).
41. Zaffos, A., Finnegan, S. & Peters, S. E. Plate tectonic regulation of global marine animal diversity. *Proc. Natl Acad. Sci. USA* **114**, 5653–5658 (2017).
42. Matthaeus, W. et al. A systems approach to understanding how plants transformed Earth's environment in deep time. *Annu. Rev. Earth Planet. Sci.* **51**, 551–580 (2023).
43. Badgley, C. et al. Biodiversity and topographic complexity: modern and geohistorical perspectives. *Trends Ecol. Evol.* **32**, 211–226 (2017).
44. Antonelli, A. et al. Geological and climatic influences on mountain biodiversity. *Nat. Geosci.* https://doi.org/10.1038/s41561-018-0236-z (2018).
45. Boyce, C. K. & Lee, J.-E. Plant evolution and climate over geological timescales. *Annu. Rev. Earth Planet.y Sci.* **45**, 61–87 (2017).
46. Gurung, K. et al. Climate windows of opportunity for plant expansion during the phanerozoic. *Nat. Commun.* https://doi.org/10.1038/s41467-022-32077-7 (2022).
47. Dahl, T. W. & Arens, S. K. The impacts of land plant evolution on Earth's climate and oxygenation state – an interdisciplinary review. *Chem. Geol.* **547**, 119665 (2020).
48. Thomas, B. & Cleal, C. Distinguishing Pennsylvanian-age lowland, extra-basinal and upland vegetation. *Palaeobiodivers. Palaeoenviron.* **97**, 273–293 (2017).
49. Guillaume, B., Pochat, S., Monteux, J., Husson, L. & Choblet, G. Can eustatic charts go beyond first order? Insights from the Permian–Triassic. *Lithosphere* **8**, 505–518 (2016).
50. van der Kooi, C. J. & Ollerton, J. The origins of flowering plants and pollinators. *Science* **368**, 1306–1308 (2020).
51. Silvestro, D. et al. Fossil data support a pre-Cretaceous origin of flowering plants. *Nat. Ecol. Evol.* **5**, 449–457 (2021).
52. Katz, O. Extending the scope of Darwin's 'abominable mystery': integrative approaches to understanding angiosperm origins and species richness. *Ann. Bot.* **121**, 1–8 (2017).
53. Benton, M. J., Wilf, P. & Sauquet, H. The angiosperm terrestrial revolution and the origins of modern biodiversity. *New Phytol.* **233**, 2017–2035 (2022).
54. Falkowski, P. et al. The evolution of modern eukaryotic phytoplankton? *Science* **305**, 354–360 (2004).
55. Martin, R. E. Secular increase in nutrient levels through the Phanerozoic; implications for productivity, biomass, and diversity of the marine biosphere. *PALAIOS* **11**, 209–219 (1996).
56. Chaboureau, A.-C., Sepulchre, P., Donnadieu, Y. & Franc, A. Tectonic-driven climate change and the diversification of angiosperms. *Proc. Natl Acad. Sci. USA* **111**, 14066–14070 (2014).

Publisher's note Springer Nature remains neutral with regard to jurisdictional claims in published maps and institutional affiliations.

Open Access This article is licensed under a Creative Commons Attribution 4.0 International License, which permits use, sharing, adaptation, distribution and reproduction in any medium or format, as long as you give appropriate credit to the original author(s) and the source, provide a link to the Creative Commons licence, and indicate if changes were made. The images or other third party material in this article are included in the article's Creative Commons licence, unless indicated otherwise in a credit line to the material. If material is not included in the article's Creative Commons licence and your intended use is not permitted by statutory regulation or exceeds the permitted use, you will need to obtain permission directly from the copyright holder. To view a copy of this licence, visit http://creativecommons.org/licenses/by/4.0/.

© The Author(s) 2023

Methods

Global landscape model

Here we use goSPL[12,13], an open-source scalable parallel numerical model that simulates landscape and sedimentary basin evolution at the global scale (resolution about 5 km). It accounts for river incision and soil creep, both considered as the main drivers of long-term physiographic changes. goSPL also tracks eroded sediments from source to sink considering alluvial and marine deposition, sediment compaction and porosity change, and could be used to reconstruct basin stratigraphic records. To evaluate these processes on landscape dynamics, different forcing conditions could be imposed from spatially and temporally varying tectonics (both horizontal and vertical displacements) to multiple climatic histories (for example, precipitation patterns and sea-level fluctuations). The model's main equation, the continuity of mass, has the following common form:

$$\frac{\partial z}{\partial t} = U + \kappa \nabla^2 z + \epsilon P^d (PA)^m \nabla z^n \quad (1)$$

for which changes in surface elevation z with time t depend on tectonic forcing U (rock uplift rate, in metres per year), hillslope processes for which κ is the diffusion coefficient (set to 0.5 m^2 yr^{-1})[57] and fluvial processes defined using the stream power law. m and n are dimensionless empirical constants (set to 0.5 and 1), ε is a precipitation-independent component of erodibility (set to 4.0×10^{-7} yr^{-1} on the basis of the choice of m), and PA is the water flux combining upstream total area (A) and local runoff (P) obtained from palaeoclimate mean annual precipitation minus evapotranspiration[57]. In our formulation, the weathering impact of runoff and its role on river incision enhancement is incorporated by scaling the erodibility coefficient with local mean annual runoff rate with a prefactor d (a positive exponent estimated from field-based relationships[58] and set to 0.42). It follows from equation (1) that deposition in flat plains or along gentle slopes is null. However, it simulates continental deposition in depressions and endorheic basins.

In goSPL, erosion occurring in upstream catchments is linked to basin sedimentation through a multiple-flow-direction algorithm that routes both water and sediment flux towards multiple downstream nodes, preventing the locking of erosion pathways along a single direction and helping the distribution of the corresponding flux in downstream regions. To solve the flow discharge globally (PA), we use a parallel implicit drainage area (IDA) method[59,60] in a Eulerian reference frame, expressed in the form of a sparse matrix composed of diagonal terms set to unity and off-diagonal terms corresponding to the immediate neighbours of each vertex composing the spherical mesh. The solution of the IDA algorithm is obtained using the Richardson solver with block Jacobian preconditioning[59], both available in PETSc[61]. Continental erosion and sediment transport solutions follow a similar approach[60]. Some of the main advantages of goSPL lie in its design of implicit and parallel solutions of its constitutive equations[60], making it possible to increase the model stability even with large time steps, and to scale the simulation run time over hundreds of CPUs.

Palaeo-elevation and precipitation forcing. To reconstruct the past physiography, goSPL relies on time-evolving boundary conditions—climatic and palaeogeographic—that are used to compute the interplay between the solid Earth and the climate. To reconstruct high-resolution palaeo-elevations throughout the Phanerozoic, we use a series of 108 maps from the PALEOMAP palaeogeographic atlas[14] ranging from the Holocene epoch to the Cambrian–Precambrian boundary (541 Ma). These palaeo-maps are defined at approximately 5-Myr intervals, and each of them is represented as a regular grid with a resolution of 0.1° × 0.1° (approximately 10-km cell width at the Equator). These palaeogeographic maps were initially based on information related to lithofacies and palaeoenvironmental datasets[62] and supplemented and refined for more than 40 years with regional palaeogeographic atlases[14,63]. We acknowledge that these maps bear some uncertainties and controversial aspects. For example, the very early Andean rise to their modern elevations consequently precociously lowers the predicted bulk sediment flux during the Neogene period while diversification continues to increase (Figs. 3 and 4). It is worth noting that even though the PALEOMAP dataset forms the basis of this study, from a methodology standpoint, other datasets[64–66] could be used.

To simulate riverine processes, the palaeo-precipitation dataset used was generated using a variant, HadCM3BL-M2.1aD (ref. 15), of the coupled atmosphere–ocean–vegetation Hadley Centre model. This climate model also uses the PALEOMAP Atlas[67] but at a lower resolution (3.75° × 2.5°). The reconstructed palaeo-precipitation regimes are obtained for each individual palaeo-elevation map after running the climate model for at least 5,000 model years to reach a dynamic equilibrium of the deep ocean[15]. In addition to palaeo-elevation grids, there are two additional time-dependent boundary conditions that were set in the climate model: the solar constant; and the atmospheric CO_2 concentrations. Regarding the last condition, two alternative CO_2 estimates are proposed[15] and we chose the palaeo-precipitation and evapotranspiration maps generated from the set of HadCM3 climate simulations using the CO_2 local weighted regression curve from ref. 68.

From the palaeo-elevation and palaeo-runoff maps, we generate the input files for goSPL by resampling the global temporal grids on an icosahedral mesh composed of more than 10 million nodes and 21 million cells (corresponding to an averaged resolution of about 5 km globally—about 0.05° resolution at the Equator). Inspired by techniques used in palaeoclimate modelling[15,67], we designed an approach to achieve a dynamic equilibrium (erosion rates balance tectonics; equation (1) and Extended Data Fig. 2) under steady boundary conditions (rainfall, tectonic uplift and erodibility). For each individual time slice, we run two sets of simulations over 168 CPUs to estimate their corresponding physiographic characteristics and associated water and sediment dynamics (Extended Data Fig. 1). A first simulation is carried out over an interval of 2 Myr under prescribed elevation and runoff conditions and simulates landscape evolution and associated water discharge and sediment flux assuming no other forcing. Under this setting, the role of surface processes is not counterbalanced by tectonics, and they excessively erode the reconstructed elevation, trimming part of the major long-lived orogenic belts and upland areas, and causing extensive floodplains. The resulting elevations are then corrected by assimilating the palaeo-elevation information[13]. Model predictions account for landscape evolution, and at this stage already contain a more detailed representation of terrestrial landforms (for example, canyons, valleys, incised channels and basins to cite a few) than the initial palaeo-elevation (Extended Data Fig. 2a). To preserve these morphological features during the correction step, high-amplitude and high-frequency structures are removed using a combination of moving average windows (ranging from 0.5° to 2°) that conserves the global distribution of the initial palaeo-elevation with minimal change of its hypsometry (≤0.5%; Extended Data Fig. 2c). We then derive a tectonic map (uplift and subsidence rates) by computing the local differences between the palaeo-elevation values and the adjusted ones.

A second simulation starts with previous palaeo-elevation and runoff conditions and additionally accounts for tectonic forcing. This simulation runs until dynamic equilibrium is reached (that is, erosion rates compensate tectonic uplift rates) within the first million years of landscape evolution (Extended Data Fig. 2c). The outputs of this second simulation are then used to evaluate water and sediment flux for the considered time slice, as well as the major catchment characteristics (river networks, drainage areas, and erosion and deposition rates).

The parametrization of equation (1) is obtained by calibrating its variables with modern estimates of average global erosion rates[18] (mean value of 63 m Myr^{-1} with a standard deviation of 15 m Myr^{-1}; Extended Data Fig. 6c) and of suspended sediment flux from the BQART model[19,20]

(corresponding to 12.8 Gt yr^{-1}). Following calibration, we predict an average present-day global erosion rate of 71 m Myr^{-1}, and a sediment flux of 12.15 Gt yr^{-1} (assuming an average density of 2.7 g cm^{-3}). On the basis of the multiple-flow IDA approach used to integrate runoff over upstream catchments[59] (IDA algorithm), we also extract the spatial distribution of the largest water discharges and sediment flux (Extended Data Fig. 3a) and their respective basin characteristics.

Sr isotopic variations from mantle origin

We use the geochemical archive of oceanic sediments to test the validity of the model predictions. The $^{87}Sr/^{86}Sr$ isotopic ratio of seawater (Extended Data Fig. 4) reflects the balance between continental weathering and mantle dynamics (hydrothermalism at mid-ocean ridges and weathering of island arcs and oceanic islands)[69,70], making it a classic proxy to diagnose the relative importance of geodynamic and climatic forcings through time[71,72].

From the measured isotopic budget of the ocean (O), present-day low $^{87}Sr/^{86}Sr$ ratios (about 0.703) are produced from mantle sources (M), whereas high ratios (about 0.713) come from continental runoff (CR, measured from main rivers worldwide)[69]. As a result, the strontium isotope oceanic mass balance has the following form:

$$\left[\frac{^{87}Sr}{^{86}Sr}\right]_O = \xi\left[\frac{^{87}Sr}{^{86}Sr}\right]_M + (1-\xi)\left[\frac{^{87}Sr}{^{86}Sr}\right]_{CR}$$
$$\left[\frac{^{87}Sr}{^{86}Sr}\right]_M \approx 0.703; \quad \left[\frac{^{87}Sr}{^{86}Sr}\right]_{CR} \approx 0.713 \tag{2}$$

in which ξ represents the mass fraction of the Sr coming from the mantle ($Q_M/(Q_M + Q_S)$ with Q_S being the predicted net sediment flux to the ocean derived from our simulation) and the flux of mantle origin (Q_M). At the present day, Q^0_M is given by the percentages defined above:

$$Q^0_M = rQ^0_S \quad r = 0.41/0.59 \tag{3}$$

Assuming that weathering scales with erosion rates, our reconstructed global net sediment flux to the ocean (Q_S) offers an independent alternative to existing approaches evaluating Sr flux from tectonic origin and could be used to infer past tectonic activity[73–76]. Under this assumption, differences ($\Delta(^{87}Sr/^{86}Sr)$) between our predicted Sr ratio and the one from the geological record[39] would reflect the dynamics of the Earth's exogenic system, with positive $\Delta(^{87}Sr/^{86}Sr)$ values corresponding to periods of higher tectonic activities relative to the present day and negative ones coinciding with more quiescent periods. We then use the isotope oceanic mass balance to independently derive the mantle contribution to the $^{87}Sr/^{86}Sr$ ratio, relying on our estimates of terrigenous flux and on the observed $^{87}Sr/^{86}Sr$ ratio of seawater. We crudely use the Sr isotope oceanic mass balance to estimate the Sr flux of mantellic origin (Q_M; Extended Data Fig. 4) in the mass fraction ξ:

$$Q_M = Q_S \frac{\left[\frac{^{87}Sr}{^{86}Sr}\right]_{CR} - \left[\frac{^{87}Sr}{^{86}Sr}\right]_O}{\left[\frac{^{87}Sr}{^{86}Sr}\right]_O - \left[\frac{^{87}Sr}{^{86}Sr}\right]_M} \tag{4}$$

Note that we assume that the isotopic ratios $\left[\frac{^{87}Sr}{^{86}Sr}\right]_{CR}$ and $\left[\frac{^{87}Sr}{^{86}Sr}\right]_M$ remained equivalent to those of the present day. Whereas the Sr ratio from the mantle budget might change marginally ($^{87}Sr/^{86}Sr$ about 0.703 for mid-ocean ridge hydrothermal and about 0.7035 for island arcs and oceanic islands[69]), the contribution of the continental crust to the Sr ratio is highly dependent on the type of weathered materials[70] ($^{87}Sr/^{86}Sr$ about 0.708 for limestones, compared to about 0.721 for silicates[69]).

We find that the contributions of mantle and terrigenous sources relative to those of the present day covary at long wavelengths, with two periods of reinforced influx from both sources separated by a quieter period during Pangaea. This trend mirrors the Wilson cycle. It indicates that the periods of high erosion, coinciding with periods of continental aggregation and contraction, increased elevation and wetter climates, also match periods of reinforced tectonic activity. Seafloor expansion is faster during periods of continental dispersal, and the total length of ridges increases during breakup[77]. As the mantle input to the $^{87}Sr/^{86}Sr$ ratio of seawater is partially driven by seafloor kinematics, we find several similarities between the predicted mantle Sr flux and subduction rates[72,74,76] that can be taken as a proxy for oceanic spreading rates; Extended Data Fig. 4). Notably, over the past 250 Ma, we deduce that mantle fluxes were low during Pangaea, and subsequently increased during Pangaea breakup; flux decreased during the late Palaeogene, mirroring the decrease in crustal production rates in the Atlantic and Pacific oceans[78] and the consumption of the East Pacific ridge.

Our model predictions of sediment flux compare at first order to the observed increase in the $^{87}Sr/^{86}Sr$ ratio of seawater over the past 150 Myr (Extended Data Fig. 4). Assuming that weathering scales with erosion rates, it corroborates the first-order impact of Cenozoic orogenesis[79] on the Sr ratio. Likewise, over the entire Phanerozoic, short-lived (20–40 Myr) increases in predicted erosion flux can explain the increase in the $^{87}Sr/^{86}Sr$ record during major orogenic phases[80], whereas the long-term variations of the record can be at first order explained by the coevolution of the terrigenous and mantle sources during the Wilson cycle. These results indirectly substantiate our model predictions of sediment flux to the oceans.

Limitations and sensitivity

In goSPL[12], erosion is defined using a first-order parametrization of the physics at play (equation (1)), which captures the long-term, large-scale landscape evolution[22,57,81]. More sophisticated treatments directly linked to sediment transport theory and incorporating different erosional behaviours have been proposed (for example, by accounting for mobile sediment and bed resistance to erosion, or using different formulations of sediment transport based on transport-limited equations)[82–84].

In addition, the erodibility parameter does not consider spatiotemporal variations that could be induced by environmental (for example, temperature gradients and seasonal precipitation), geological (for example, soil composition and fault-induced bedrock weakening) or biological (for example, plant root growth and soil microbial activity) mechanisms[6,85–89]. Instead, we assume uniform erodibility across all continents. Accounting for variable lithologies in model space could be achieved by assigning an erodibility prefactor depending on the surface rock composition in the stream power law term of equation (1) by an erodibility prefactor depending on the type of surficial lithology classes (typically with values ranging between 1.0 and 3.2; ref. 90). However, this approach would require global palaeo-lithological surficial cover data that are difficult to obtain when looking into deep geological times. Although we do not account for seasonality variations, the weathering impact of precipitation and its role on river incision enhancement is incorporated by scaling the erodibility coefficient with the local mean net annual precipitation rate[58]. One could also incorporate the effect of temperature on weathering of rocks according to rock composition by scaling the erodibility coefficient using the palaeoclimate temperature distribution. Such refinement possibilities are many, and although in principle desirable to better reproduce observations, adding those would necessarily add poorly controlled degrees of freedom in the parameterization, and lead to illusory enhanced predictive capabilities.

By design, our simulation is sensitive to both the climatic and palaeoelevation reconstructions. Although other palaeogeography reconstructions exist[62,64–66], many are restricted to specific geological intervals

and, to our knowledge, are not tied to a series of palaeo-precipitation maps for the entire Phanerozoic. Consequently, we chose to evaluate model sensitivity on palaeo-elevation using a single time slice (Aptian period about 120 Ma) by comparing our predicted sediment flux with a different set of palaeogeography and palaeoclimate reconstructions[91]. The results highlight several differences at the regional scale (Extended Data Fig. 5). For instance, a more humid equatorial climatic zone in the second reconstruction[92] induces higher erosion rates on the northern and central part of Gondwana. The palaeo-elevation differences also redefine the drainage network and the volumes of sediment transported to the oceans or stored in continental basins. This is the case in Antarctica and on the eastern part of Eurasia where we note higher erosion rates or an increase in terrestrial sediment accumulation depending on the considered palaeogeography. Despite these local variations, those disparities become more tenuous when evaluating the global response. As an example, the percentage of endorheic basins varies from 24 to 26.5% between the two simulations and the net sediment flux to the ocean changes from 2.72 to 2.26 $km^3\ yr^{-1}$ (Extended Data Fig. 5). This suggests that although regional differences exist and if the imposed forcing conditions are not too dissimilar (both in terms of palaeoclimates and palaeogeographies), the reported global evolution and global trends that are presented in the study should remain relatively unchanged between reconstructions.

To evaluate the model sensitivity to palaeo-runoff, we ran a full series of simulations throughout the Phanerozoic. The palaeoclimate reconstructions from ref. 15 have been carried out with two different CO_2 conditions (the atmospheric concentrations from ref. 68 and a smoothed curve), but the mean global continental runoff remains very similar in both cases; Extended Data Fig. 6a) and should only very marginally change our results. Instead, we opted for the recent Phanerozoic palaeo-precipitation reconstruction from ref. 93 that was run at 10-Myr intervals using the PALEOMAP palaeogeographic atlas[14] with a much higher resolution (1°) than those of ref. 15. The release from ref. 93 does not contain the evapotranspiration time slices, and we could therefore use the total palaeo-precipitation only as a proxy for runoff. Global mean continental runoff from ref. 93 exhibits a similar temporal trend to the ones from ref. 15 but, because evapotranspiration could not be accounted for, with higher values (about 0.3 m yr^{-1} on average over the Phanerozoic; Extended Data Fig. 6a). As erosion scales with runoff (equation (1)), this inflated runoff directly affects the global net sediment flux to the ocean (about 0.84 $km^3\ yr^{-1}$ on average) and to a lesser extent the continental deposition flux (<0.1 $km^3\ yr^{-1}$ on average; Extended Data Fig. 6b). The spatial distributions of these two runoff scenarios and their relative impact on denudation rates show substantial spatial differences over time (Extended Data Fig. 7). At the continental scale, the higher resolution in ref. 93 should better account for the control of topography on the spatial variability in precipitation. For example, we note at 40 Ma (Extended Data Fig. 7) the orographic control of the Himalayas on the regional rainfall regime with its implications on erosion and deposition.

The sensitivity analysis provides two important pieces of information. First, both simulations show similar responses in terms of global sediment flux and denudation rates (Pearson correlations of 0.94 and 0.92, respectively). This suggests that irrespectively of the chosen palaeoclimatic reconstruction, our interpretation of the relationships between predicted sedimentary flux and biodiversity still holds. Second, the runoff has a stronger effect on the amplitudes in net sediment flux to the ocean and denudation rates when considering similar palaeo-elevation reconstruction (Extended Data Fig. 6b). Instead, differences in palaeo-elevations affect continental sediment cover and sediment accumulation in endorheic basins (Extended Data Fig. 5).

Another limitation of our approach is to propose a hypothesis by comparing time series of mean model outputs with independent variables, but similar trends could possibly be expected for any model that accounts for plate tectonics—with essentially two cycles of continental aggregation and dispersal over the Phanerozoic eon—and subsequent climate reconstructions. The highly relevant correlations that we found can be however advocated to hierarchize these studies. As plate tectonics—and the breakup of Pangaea in particular—form the cornerstone of such studies[11,40,41], we thus compared continental fragmentation[41] with Phanerozoic marine diversity, which yields only moderate correlations (Pearson coefficients of 0.46 with number of marine families[2]; 0.54 to 0.58 with the number of genera[2,5]; Extended Data Fig. 8).

Physiographic diversity and variety

To evaluate the relationships between physiography and the Phanerozoic climate and tectonics, we define a unique continuous variable (named the physiographic diversity index) that encapsulates several of the reconstructed morphometric attributes. Simulation outputs are first interpolated from the icosahedral mesh on a regular 0.05° grid (open-access online release, HydroShare[16]).

First, we quantify palaeo-landforms by calculating the topographic position index on each cell i (TPI_i) that measures the relative relief[94]:

$$TPI_i = z_i - \sum_{k=1}^{n} z_k / nTPI_S = 100 \times (TPI - \overline{TPI})/\sigma_{TPI} \quad (5)$$

in which z_i is the considered elevation at cell i and z_k is the mean of its surrounding cells (z_k), with n being the number of cells contained inside an annulus neighbourhood. Topographic position is an inherently scale-dependent calculation[95]. To circumvent this problem, TPI is computed considering two scales of observation, a fine one ranging between 0.05° and 0.15° and a coarser one from 0.25° to 0.5°. As elevation is generally spatially autocorrelated, TPI values increases with scale, making it difficult to compare both scales of observation directly. To overcome this issue, we calculate a standardized TPI_S (equation (5)), in which $\overline{TPI}$ is the mean over the entire grid and σ_{TPI} is its standard deviation[96] (top map in Extended Data Fig. 9a).

We also extract the slope and water discharge for each time slice (bottom maps in Extended Data Fig. 9a). Note that we selected these three variables—TPI, slope and discharge—as morphometric indicators of the physiographic diversity but other ones such as aspect (that is, the direction of maximum gradient), and erosion and deposition rates could equally be added[97]. From these continuous variables, we then derive categorical variables by defining seven categories from the slope, five from the water flux and ten from the TPI_S (Extended Data Fig. 9a,b and Supplementary Table 1; ref. 98).

From the categorical variables, we quantify the physiographic diversity index P_{DIV} (Supplementary Fig. 1a,b) using Shannon's equitability (continuous variable [0,1]), which is calculated by normalizing the Shannon–Weaver diversity index (d_{SW}):

$$d_{SW} = -\sum_{k=1}^{\mathcal{C}} p_k \ln(p_k)\ P_{DIV} = d_{SW}/\ln(\mathcal{C}) \quad (6)$$

with p_k being the proportion of observations of type k in each neighbourhood and $\mathcal{C}$ being the number of categorical variables (here $\mathcal{C} = 3$). The physiographic diversity index is calculated at each location for the 108 reconstructed time slices spanning the Phanerozoic (Supplementary Fig. 1c). The variations of P_{DIV} can be described either spatially for a given period (Supplementary Fig. 1c) or across time (Supplementary Fig. 2). As it characterizes how landscape complexity evolves over the geological timescale[99], this index can be used to infer the role physiography, and changes thereof, might have played on species migration, dispersal or isolation at both global and continental scales. Biodiversity richness emerges from many abiotic and biotic interactions; however, the role physiography might have played has often been overlooked[100]. The high-resolution global maps generated from our simulation could be used as an additional palaeoenvironmental layer in mechanistic eco-evolutionary models[101,102].

To compare the temporal evolution of physiographic diversity with biotic[2,5] or abiotic geochemical and geophysical proxies, the mean value of P_{DIV} is insufficient, as it ignores the variety of landforms, which is better accounted for by the probability density function: the probability density function can be usefully reduced to a unique scalar—physiographic variety—given by the interquartile range $P_{VAR} = Q_3 - Q_1$ (that is, the range between the first quartile (Q_1; 25%) and the third quartile (Q_3;75%); Supplementary Fig. 2c).

As an example, we observe an increase in physiographic diversity of South America from the Upper Cretaceous to the Palaeocene related to the Andean mountain building period (Supplementary Fig. 2b,c) and concomitant with microflora diversity patterns in northern South America[103] and plant diversification in Patagonia[104]. We also note periods of low P_{VAR} values around 50 Ma and 28 Ma related to the intermittent development of internal seas or lakes in the central part of the Amazon basin. Periods of increasing P_{VAR} follow each of these episodes, suggesting that the Pebas basin could have acted as a permeable biogeographical system favouring biotic exchange and adaptation in the region[105].

Reporting summary

Further information on research design is available in the Nature Portfolio Reporting Summary linked to this article.

Data availability

The PALEOMAP Paleodigital Elevation Models for the Phanerozoic from ref. 14 can be downloaded from https://doi.org/10.5281/zenodo.5460860 (last accessed 3 October 2023). Palaeoclimatic maps from the HadCM3BL-M2.1aD model[15] are available from the Bristol Research Initiative for the Dynamic Global Environment website at https://www.paleo.bristol.ac.uk/resources/simulations/. Palaeoclimate simulations from ref. 93 are made available in the original article, as referenced. All palaeo-elevation reconstruction maps[16] for the Phanerozoic generated in this study are available from HydroShare: http://www.hydroshare.org/resource/0106c156507c4861b4cfd404022f9580.

Code availability

The scientific software used in this study, goSPL[12], is available from https://github.com/Geodels/gospl and the software documentation can be found at https://gospl.readthedocs.io. We also provide a series of Jupyter notebooks used for processing the datasets and model outputs that can be followed to reproduce some of the figures presented in the paper, which can be accessed from https://github.com/Geodels/paleoPhysiography. The open-source python interface for the Generic Mapping Tools (https://www.pygmt.org) was used for global two-dimensional map visualization and the three-dimensional global maps in Fig. 1 were created with the open-source Paraview software (https://www.paraview.org).

57. Salles, T., Ding, X. & Brocard, G. pyBadlands: a framework to simulate sediment transport, landscape dynamics and basin stratigraphic evolution through space and time. *PLoS ONE* **13**, e0195557 (2018).
58. Murphy, B., Johnson, J., Gasparini, N. & Sklar, L. S. Chemical weathering as a mechanism for the climatic control of bedrock river incision. *Nature* **532**, 223–227 (2016).
59. Richardson, A., Hill, C. N. & Perron, J. T. IDA: an implicit, parallelizable method for calculating drainage area. *Water Resour. Res.* **50**, 4110–4130 (2014).
60. Salles, T. eSCAPE: regional to global scale landscape evolution model v2.0. *Geosci. Model Dev.* **12**, 4165–4184 (2019).
61. Balay, S. et al. *PETSc Users Manual* (Argonne National Laboratory, 2012).
62. Ziegler, A. et al. Paleogeographic interpretation: with an example from the mid-Cretaceous. *Annu. Rev. Earth Planet. Sci.* **13**, 385–428 (1985).
63. Scotese, C. & Schettino, A. in *Permo-Triassic Salt Provinces of Europe, North Africa and the Atlantic Margins* (eds Soto, J. I. et al.) 57–95 (Elsevier, 2017).
64. Markwick, P. & Valdes, P. Palaeo-digital elevation models for use as boundary conditions in coupled ocean - atmosphere GCM experiments: a Maastrichtian (late Cretaceous) example. *Palaeogeogr. Palaeoclimatol. Palaeoecol.* **213**, 37–63 (2004).
65. Vérard, C., Hochard, C., Baumgartner, P. O., Stampfli, G. M. & Liu, M. 3D palaeogeographic reconstructions of the Phanerozoic versus sea-level and Sr-ratio variations. *J. Palaeogeogr.* **4**, 64–84 (2015).
66. Straume, E., Gaina, C., Medvedev, S. & Nisancioglu, K. Global Cenozoic Paleobathymetry with a focus on the Northern Hemisphere oceanic gateways. *Gondwana Res.* https://doi.org/10.1016/j.gr.2020.05.011 (2020).
67. Valdes, P. et al. The BRIDGE HadCM3 family of climate models: HadCM3@Bristol v1.0. *Geosci. Model Dev.* **10**, 3715–3743 (2017).
68. Foster, G., Royer, D. & Lunt, D. Future climate forcing potentially without precedent in the last 420 million years. *Nat. Commun.* **8**, 14845 (2017).
69. Allègre, C. J. et al. The fundamental role of island arc weathering in the oceanic Sr isotope budget. *Earth Planet. Sci. Lett.* **292**, 51–56 (2010).
70. Vollstaedt, H. et al. The Phanerozoic $\delta^{88/86}$Sr record of seawater: new constraints on past changes in oceanic carbonate fluxes. *Geochim. Cosmochim. Acta* **128**, 249–265 (2014).
71. van der Meer, D. et al. Reconstructing first-order changes in sea level during the Phanerozoic and Neoproterozoic using strontium isotopes. *Gondwana Res.* **44**, 22–34 (2017).
72. Mills, B., Scotese, C., Walding, N., Shields, G. & Lenton, T. Elevated CO_2 degassing rates prevented the return of Snowball Earth during the Phanerozoic. *Nat. Commun.* https://doi.org/10.1038/s41467-017-01456-w (2017).
73. Merdith, A. S., Atkins, S. E. & Tetley, M. G. Tectonic controls on carbon and serpentinite storage in subducted upper oceanic lithosphere for the past 320 Ma. *Front. Earth Sci.* https://doi.org/10.3389/feart.2019.00332 (2019).
74. East, M., Müller, D., Williams, S., Zahirovic, S. & Heine, C. Subduction history reveals Cretaceous slab superflux as a possible cause for the mid-Cretaceous plume pulse and superswell events. *Gondwana Res.* **79**, 125–139 (2020).
75. Mills, B. J. et al. Modelling the long-term carbon cycle, atmospheric CO_2, and Earth surface temperature from late Neoproterozoic to present day. *Gondwana Res.* **67**, 172–186 (2019).
76. Müller, D. et al. Evolution of Earth's tectonic carbon conveyor belt. *Nature* **605**, 629–639 (2022).
77. Coltice, N., Husson, L., Faccenna, C. & Arnould, M. What drives tectonic plates. *Sci. Adv.* **5**, eaax4295 (2019).
78. Herbert, T. D. et al. Tectonic degassing drove global temperature trends since 20 Ma. *Science* **377**, 116–119 (2022).
79. Goddéris, Y. & François, L. The Cenozoic evolution of the strontium and carbon cycles: relative importance of continental erosion and mantle exchanges. *Chem. Geol.* **126**, 169–190 (1995).
80. Peucker-Ehrenbrink, B. & Fiske, G. J. A continental perspective of the seawater ^{87}Sr/^{86}Sr record: a review. *Chem. Geol.* **510**, 140–165 (2019).
81. Tucker, G. & Hancock, G. Modeling landscape evolution. *Earth Surf. Process. Landf.* **35**, 28–50 (2010).
82. Adams, J. et al. The Landlab v1.0 OverlandFlow component: a Python tool for computing shallow-water flow across watersheds. *Geosci. Model Dev.* **10**, 1645–1663 (2017).
83. Salles, T. et al. A unified framework for modelling sediment fate from source to sink and its interactions with reef systems over geological times. *Sci. Rep.* https://doi.org/10.1038/s41598-018-23519-8 (2018).
84. Yuan, X. et al. Linking continental erosion to marine sediment transport and deposition: a new implicit and O(N) method for inverse analysis. *Earth Planet. Sci. Lett.* **524**, 115728 (2019).
85. Ferrier, K., Huppert, K. & Perron, J. Climatic control of bedrock river incision. *Nature* **496**, 206–209 (2013).
86. Perron, J. T. Climate and the pace of erosional landscape evolution. *Annu. Rev. Earth Planet. Sci.* **45**, 561–591 (2017).
87. Eppes, M. C. et al. Warmer, wetter climates accelerate mechanical weathering in field data, independent of stress loading. *Geophys. Res. Lett.* **47**, 2020GL089062 (2020).
88. Meurer, K. et al. A framework for modelling soil structure dynamics induced by biological activity. *Glob. Chang. Biol.* **26**, 5382–5403 (2020).
89. Adams, B., Whipple, K., Forte, A. & Heimsath, A. Climate controls on erosion in tectonically active landscapes. *Sci. Adv.* https://doi.org/10.1126/sciadv.aaz3166 (2020).
90. Moosdorf, N., Cohen, S. & von Hagke, C. A global erodibility index to represent sediment production potential of different rock types. *Appl. Geogr.* **101**, 36–44 (2018).
91. Laugié, M. et al. Stripping back the modern to reveal the Cenomanian–Turonian climate and temperature gradient underneath. *Clim. Past* **16**, 953–971 (2020).
92. Sepulchre, P. et al. IPSL-CM5A2 – an Earth system model designed for multi-millennial climate simulations. *Geosci. Model Dev.* **13**, 3011–3053 (2020).
93. Li, X. et al. A high-resolution climate simulation dataset for the past 540 million years. *Sci. Data* **9**, 371 (2022).
94. Theobald, D., Harrison-Atlas, D., Monahan, W. & Albano, C. Ecologically-relevant maps of landforms and physiographic diversity for climate adaptation planning. *PLoS ONE* **10**, e0143619 (2015).
95. Newman, D., Lindsay, J. & Cockburn, J. Evaluating metrics of local topographic position for multiscale geomorphometric analysis. *Geomorphology* https://doi.org/10.1016/j.geomorph.2018.04.003 (2018).
96. De Reu, J. et al. Application of the topographic position index to heterogeneous landscapes. *Geomorphology* **186**, 39–49 (2013).
97. Husson, L. et al. Javanese *Homo erectus* on the move in SE Asia circa 1.8 Ma. *Sci. Rep.* **12**, 19012 (2022).
98. Weiss, A. Topographic position and landforms analysis. In *Proc. ESRI Users Conference* (ESRI, 2001).
99. Salles, T., Rey, P. & Bertuzzo, E. Mapping landscape connectivity as a driver of species richness under tectonic and climatic forcing. *Earth Surf. Dyn.* **7**, 895–910 (2019).
100. Salles, T. et al. Quaternary landscape dynamics boosted species dispersal across Southeast Asia. *Commun. Earth Environ.* https://doi.org/10.1038/s43247-021-00311-7 (2021).
101. Hagen, O. et al. Mountain building, climate cooling and the richness of cold-adapted plants in the Northern Hemisphere. *J. Biogeogr.* https://doi.org/10.1111/jbi.13653 (2019).

102. Hagen, O. Coupling eco-evolutionary mechanisms with deep-time environmental dynamics to understand biodiversity patterns. *Ecography* https://doi.org/10.1111/ecog.06132 (2022).
103. Jaramillo, C. A. & Dilcher, D. L. Microfloral diversity patterns of the late Paleocene–Eocene interval in Colombia, northern South America. *Geology* **28**, 815–818 (2000).
104. Wilf, P. et al. High plant diversity in Eocene South America: evidence from Patagonia. *Science* **300**, 122–125 (2003).
105. Hoorn, C., Boschman, L. M., Kukla, T., Sciumbata, M. & Val, P. The Miocene wetland of western Amazonia and its role in Neotropical biogeography. *Bot. J. Linn. Soc.* **199**, 25–35 (2022).

Acknowledgements This work was principally supported by the Australian Research Council DARE Centre grant IC190100031. This research was undertaken with the assistance of resources from the National Computational Infrastructure, which is supported by the Australian Government, and from Artemis HPC Grand Challenge supported by the Sydney Informatics Hub at the University of Sydney. In addition, we acknowledge C. Nielsen, M. Laugié and A. Lettéron for providing the Aptian palaeo-elevation and palaeo-precipitation grids used in Extended Data Fig. 5c. The manuscript was improved by the reviews and suggestions of R. Martin and A. Pohl.

Author contributions T.S. and L.H. contributed equally to this work; they conceived the study and conducted the numerical experiments. M.L. and T.S. worked on the physiography index definition and interpretations. L.H. and T.S. derived the strontium budget. All authors analysed the endorheic basin evolution. L.H. and T.S. wrote the initial draft and all authors reviewed the manuscript.

Competing interests The authors declare no competing interests.

Additional information

Supplementary information The online version contains supplementary material available at https://doi.org/10.1038/s41586-023-06777-z.

Correspondence and requests for materials should be addressed to Tristan Salles or Laurent Husson.

Peer review information *Nature* thanks Ronald Martin, Alexandre Pohl and the other, anonymous, reviewer(s) for their contribution to the peer review of this work. Peer reviewer reports are available.

Reprints and permissions information is available at http://www.nature.com/reprints.

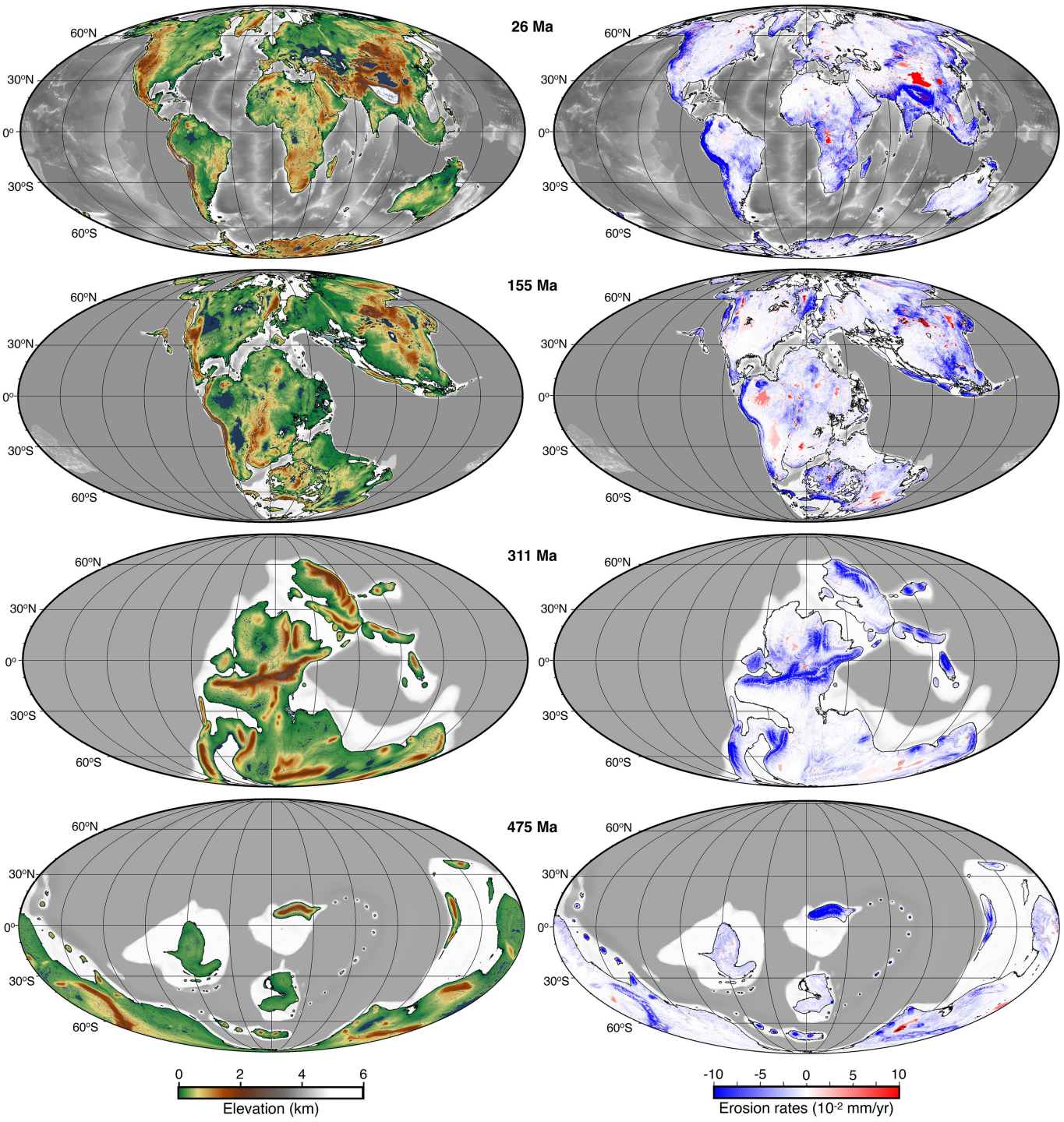

Extended Data Fig. 1 | Global scale Phanerozoic landscape evolution model. Left panels represent simulated physiographies for 4 time-slices accounting for surface processes impact and highlighting continental topography and associated river networks (dark blue). Right panels show associated erosion/deposition rates (blue/red respectively) for the considered time-slices.

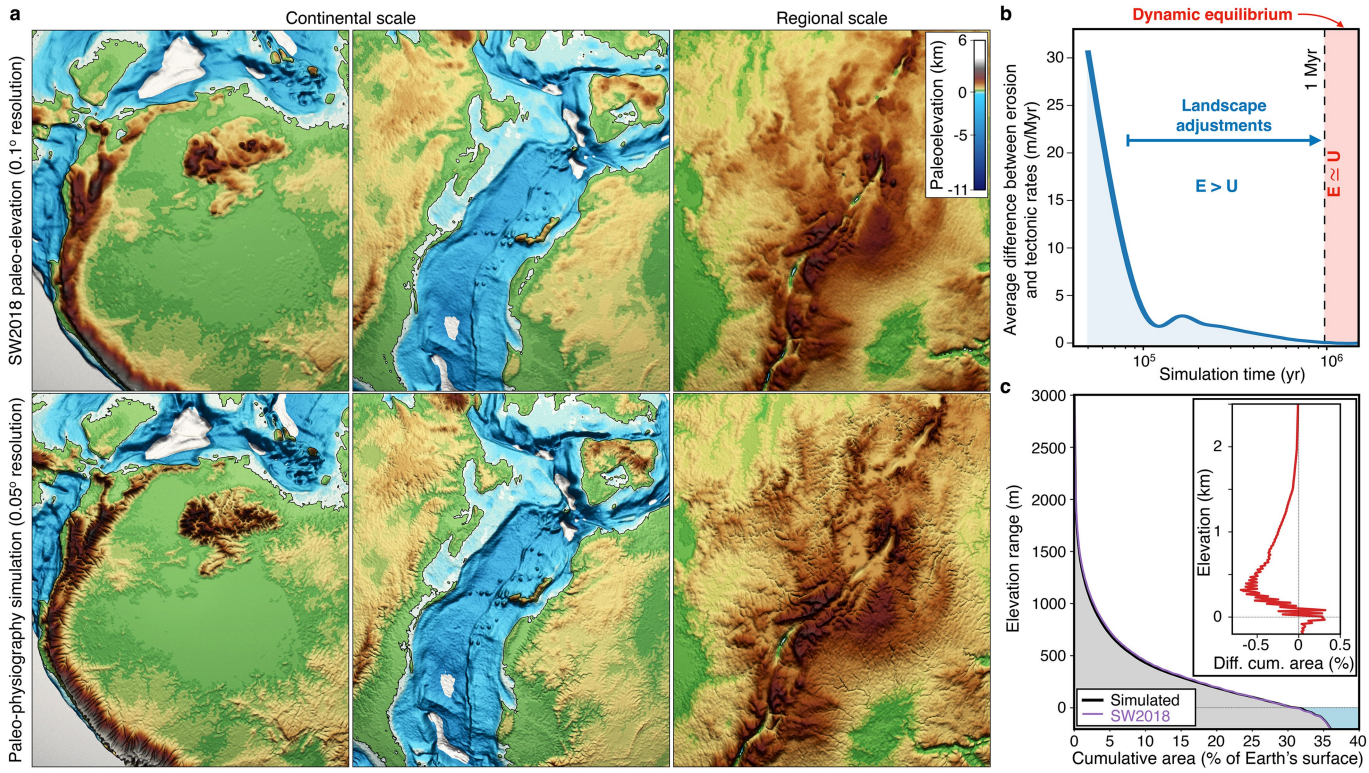

Extended Data Fig. 2 | Comparisons between predicted elevations and corresponding paleo-elevation map. a. Top 3 panels show the input elevation conditions for 155 Ma at 0.1° resolution (SW2018[14]) and bottom ones represent model outputs (0.05° resolution), highlighting the geomorphological imprints of surface processes on the landscape. **b**. Temporal change between imposed tectonic rates from corrected topography and erosion rates at 155 Ma (blue curve). This curve is used to estimate when dynamic equilibrium conditions have been reached. **c**. Corresponding continental hypsometric curves for the given paleo-elevation at 155 Ma (purple) and simulated one (black). Red curve in the inset shows the differences between the two hypsometric curves.

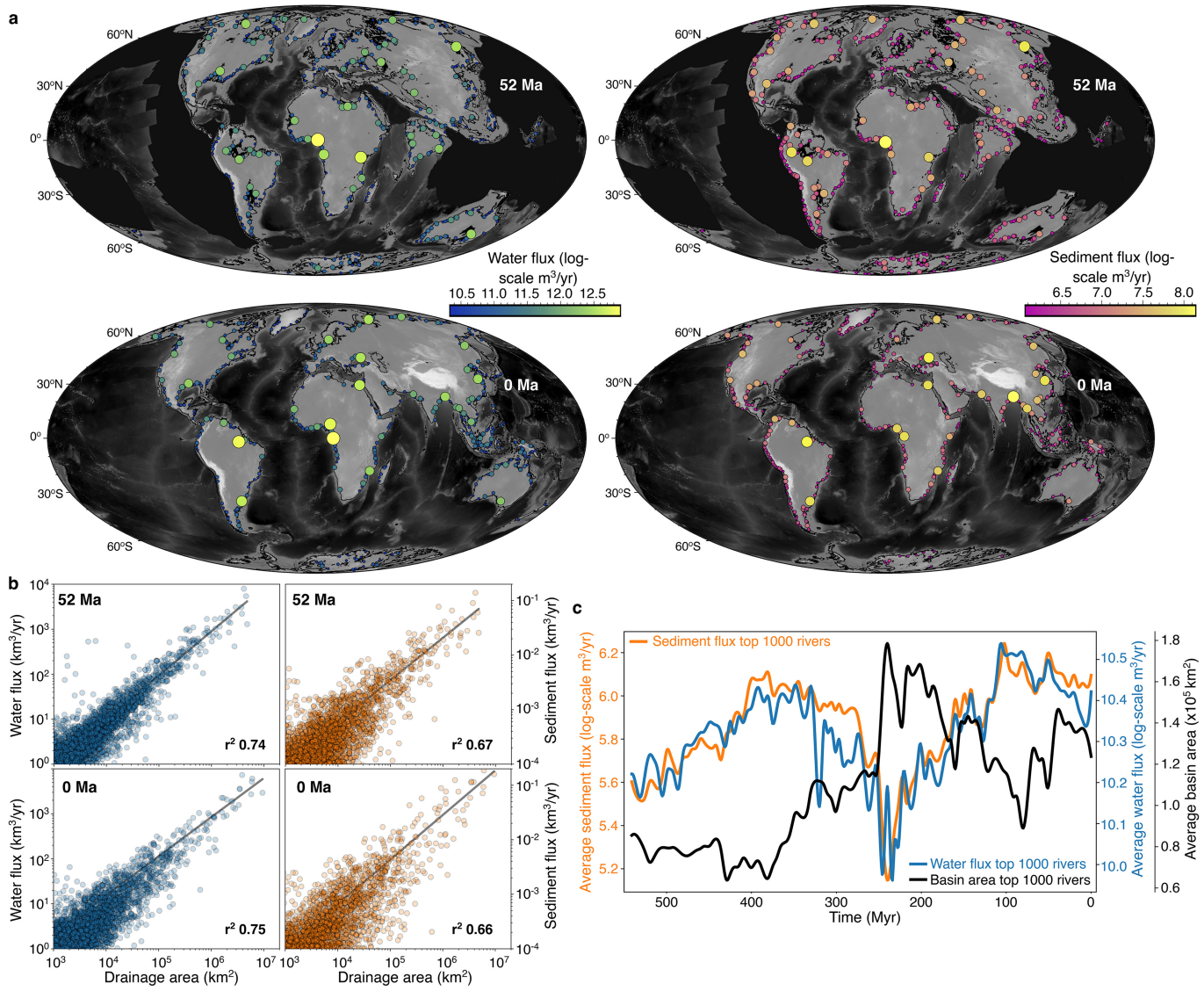

Extended Data Fig. 3 | Drainage patterns evolution at catchment scale. **a**. Distribution of water and sediment flux for the 500th largest rivers at 52 and 0 Ma. **b**. Log-log plots of modelled water discharge and sediment flux against basin drainage area (blue and orange circles respectively). Power law curve fitting and is represented by the black lines. **c**. Phanerozoic evolution of average water discharges (blue), sediment flux (orange) and basin areas (black) for the top 1000th largest rivers.

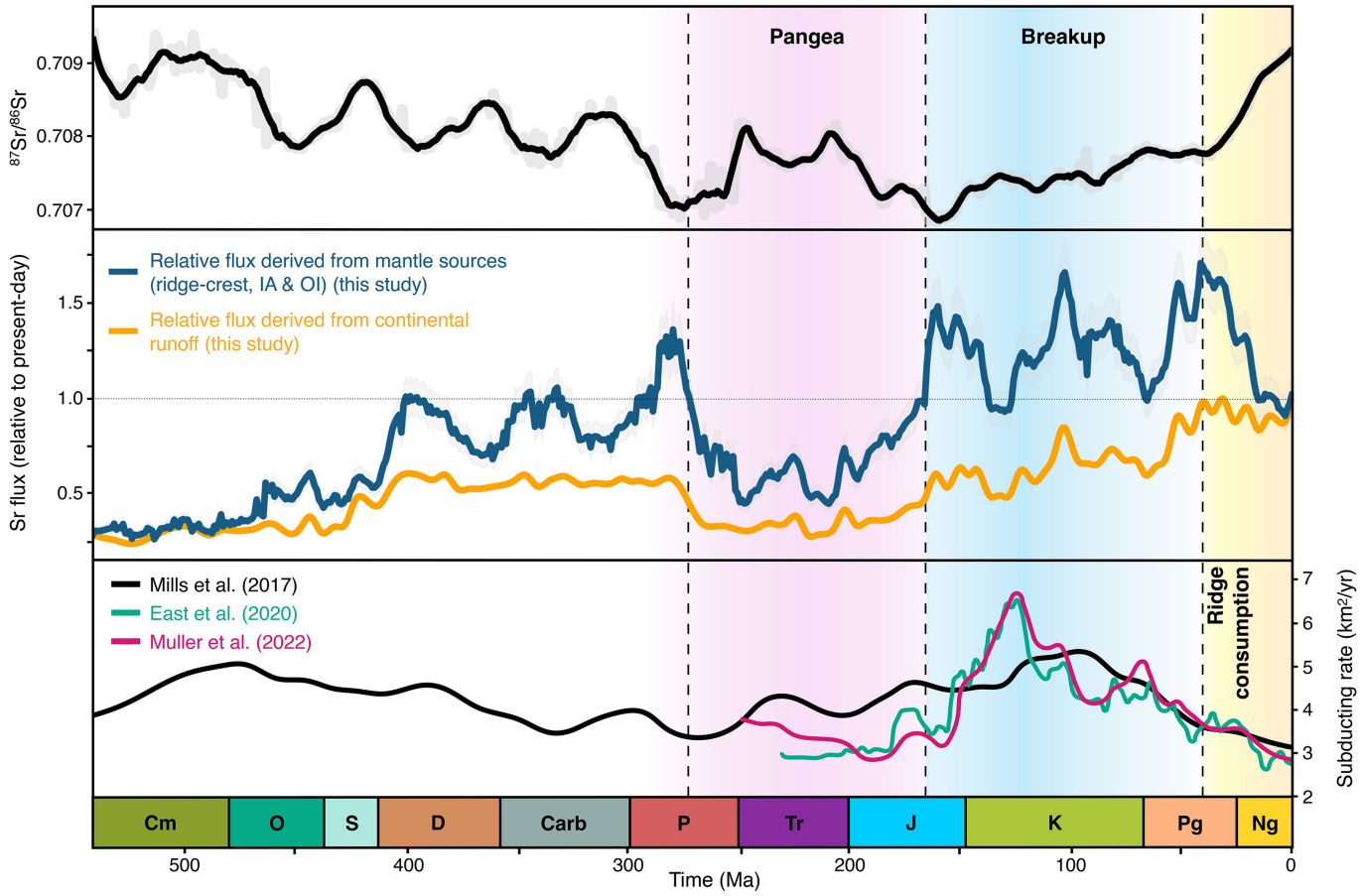

Extended Data Fig. 4 | Strontium signal from mantellic source and continental runoff. Top panel shows Strontium isotopic ratio of seawater for the Phanerozoic[39] (grey line represents the data from[39] and the black line shows the corresponding least square regression using SciPy Savitzky-Golay filter). From the oceanic Strontium mass balance (Methods) and using present-day weighted average inputs[69] (i.e., 0.7136 ± 0.0002 from continental crust and 0.7029 ± 0.0003 from mantle sources), the relative strontium mantle budget is derived. The mantellic flux associated to ridge-crest, island arcs (IA) and oceanic islands (OI) underground alteration is predicted in the second panel based on the flux obtained from continental runoff (grey area shows the extent of the flux based on the range ±0.0003 from[69]). Reconstructions of mean crustal destruction rates from recent studies[72,74,76] are presented in the bottom panel.

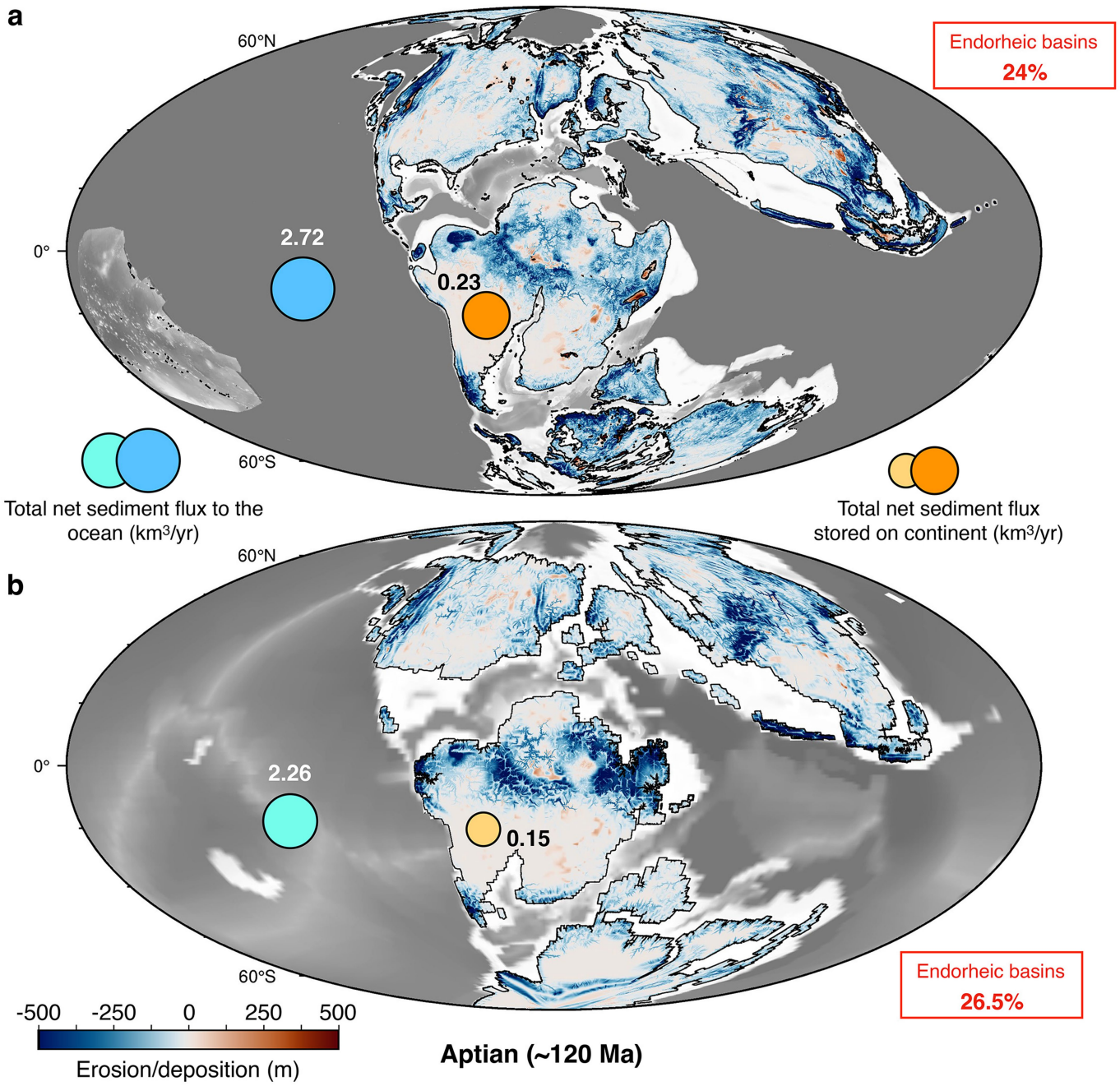

Extended Data Fig. 5 | Impact of paleogeographies and paleoclimates on sediment flux dynamic for the Aptian period (~120 Ma). Predicted continental erosion and deposition maps computed using the paleo-elevation of Scotese & Wright[14] and its associated paleo-precipitation from Valdes et al.[15] in **a** and using the continental reconstruction and paleo-precipitation provided by Nielsen, Laugié and Lettéron and obtained from the IPSL-CM5A2 paleo-climate model from Sepulchre et al.[92] in **b**. Estimated sediment flux delivered to the ocean (blue gradients circles) and stored on continents (orange circles) are shown as well as the percentage of endorheic basin area for each simulation.

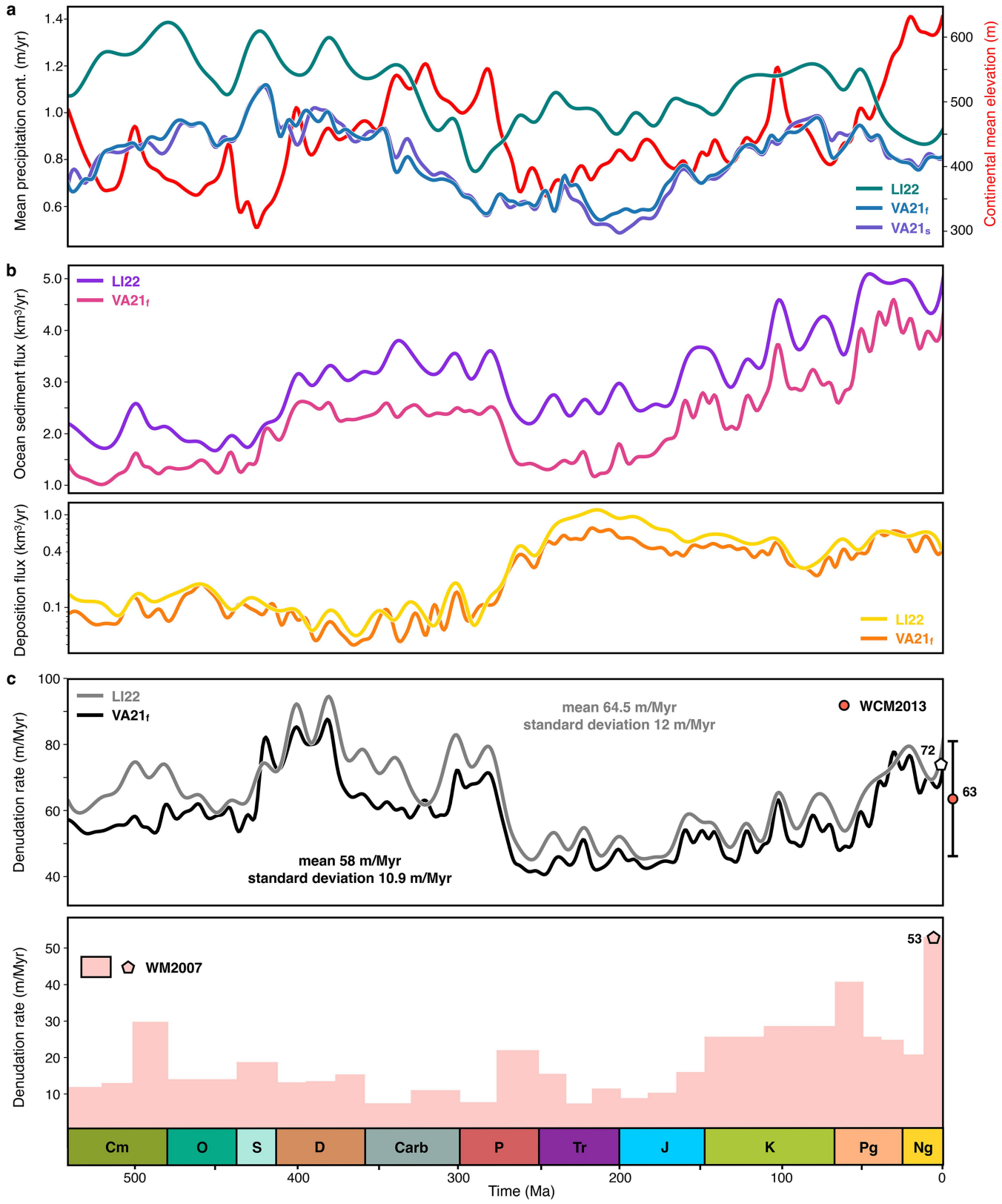

Extended Data Fig. 6 | Comparisons between paleo-precipitation scenarios and global sediment flux for the Phanerozoic. a. Evolution of continental paleo-precipitation for three scenarios (Li et al.[93] (LI22) in teal, Valdes et al.[15] using the CO_2 curve from Foster et al.[68] ($VA21_f$) in blue, and a smoothed CO_2 curve ($VA21_s$) in purple) and paleo-elevation[14] (red). **b**. Estimated net sediment flux to the ocean (fuchsia and magenta curves) and continental deposition flux (yellow and orange curves) for two climatic scenarios (LI22[93] and $VA21_f$[15] respectively). **c**. Global average denudation rates estimated for the simulated paleo-precipitations (LI22 and $VA21_f$ – grey and black curves) against estimated rates from preserved sediments (pink, WM2007[17]) and recent rates (red, WCM2013[18]).

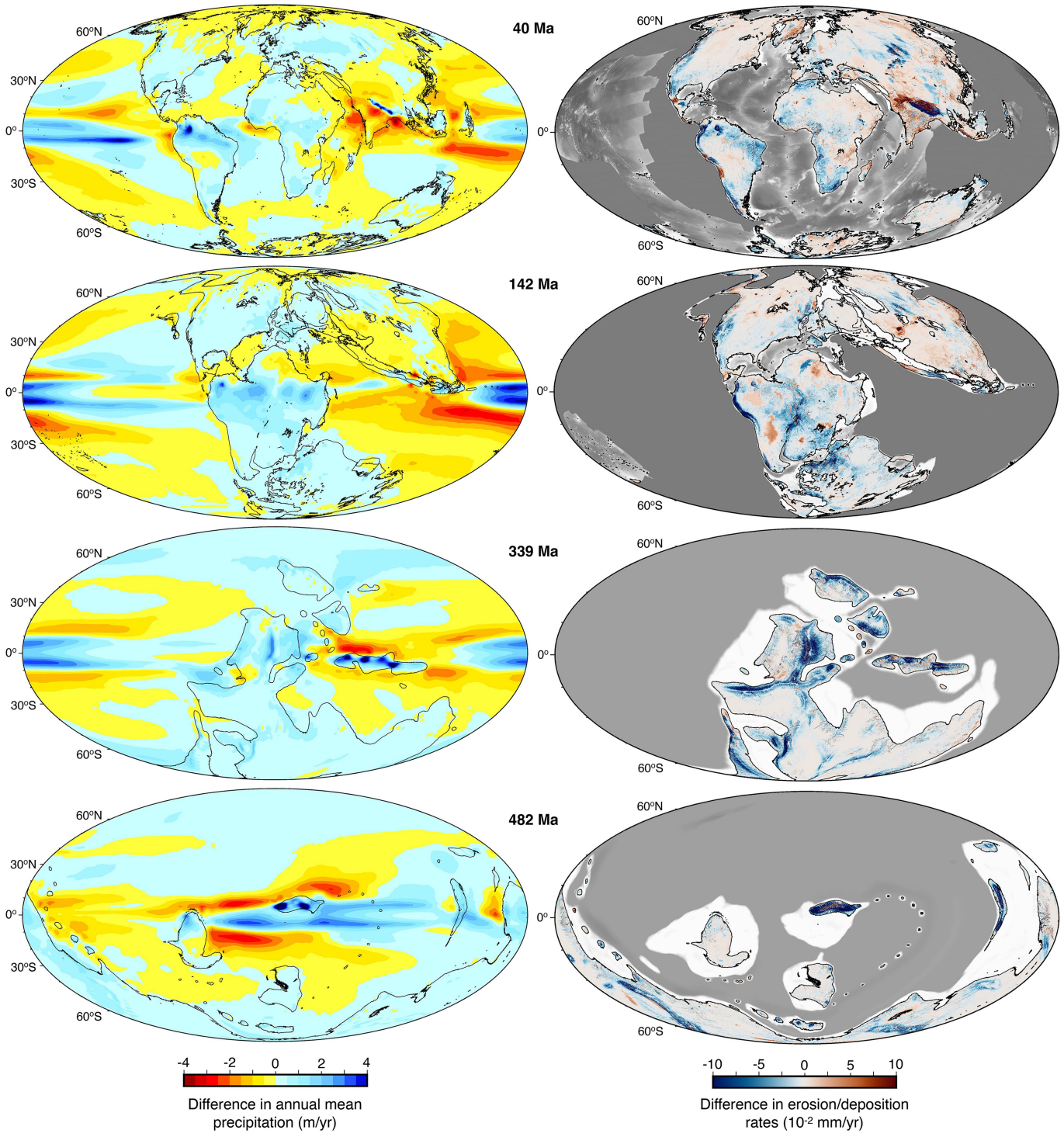

Extended Data Fig. 7 | Influence of paleo-precipitation scenarios on spatial distribution of denudation rates. Differences in annual mean precipitation between the Phanerozoic paleo-climate model of Li et al.[93] and the one from Valdes et al.[15] using the CO_2 curve from Foster et al.[68] are presented on the left (drier predictions in Li et al.[93] range from yellow to red and wetter ones from cyan to dark blue). Simulated differences in erosion and deposition rates between the two scenarios using goSPL[12] show higher erosion with the Li et al.[93] simulation in blue and higher deposition in red.

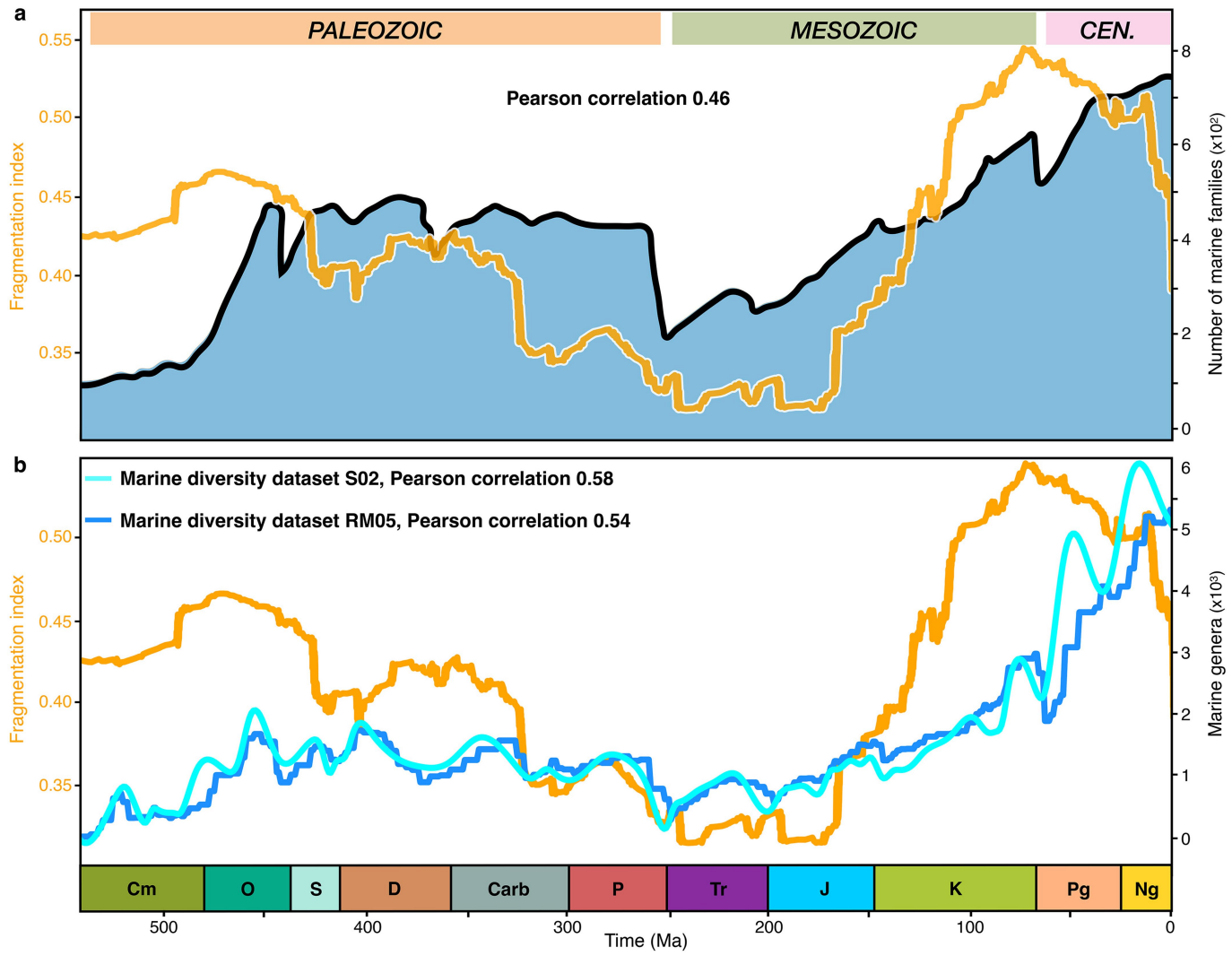

Extended Data Fig. 8 | Plate tectonics and the Phanerozoic marine biodiversity. a. The index of continental block fragmentation derived from Zaffos et al.[41] (orange curve) with value close to 1 indicating no plates are touching and a value of zero corresponding to contiguous continental blocks arranged in a single mass. Pearson correlation (0.46) indicates a positive but moderate relationship with the number of marine families (black line from Sepkoski's dataset[2]. **b.** Correlations between the fragmentation index and the total number of marine genera from Sepkoski[2] (SO2) and Rohde & Muller[5] (RM05) show a slightly stronger but still moderate positive trends (Pearson values of 0.58 and 0.54 respectively).

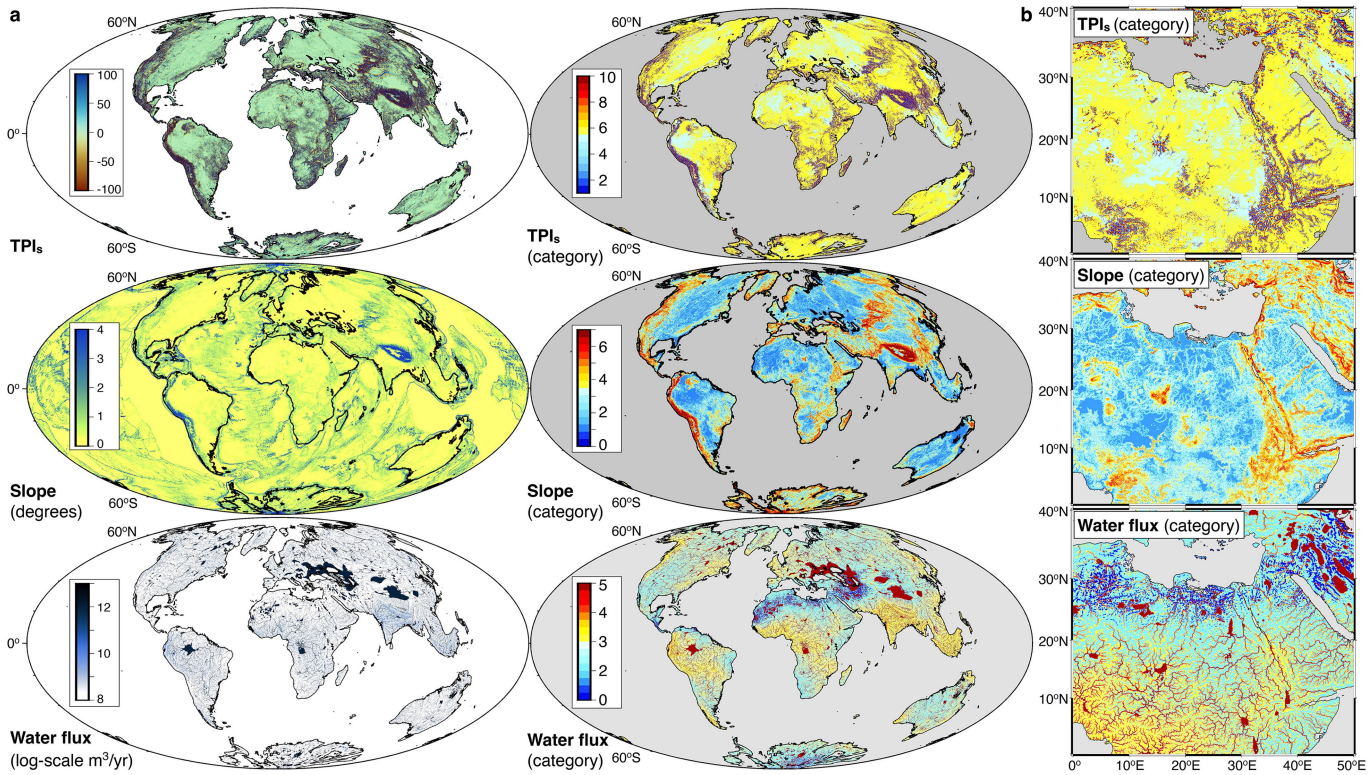

Extended Data Fig. 9 | Hierarchical classification of physiographic relevant morphometrics derived from model outputs. a. From standardized topographic position index (TPI_S), slopes calculated at 0.05° resolution, and reconstructed water flux, series of categories characterizing the physiography are produced at global scale (chosen example at 26 Ma). **b**. Zoomed-in maps of the physiographic categories for Northeast Africa.

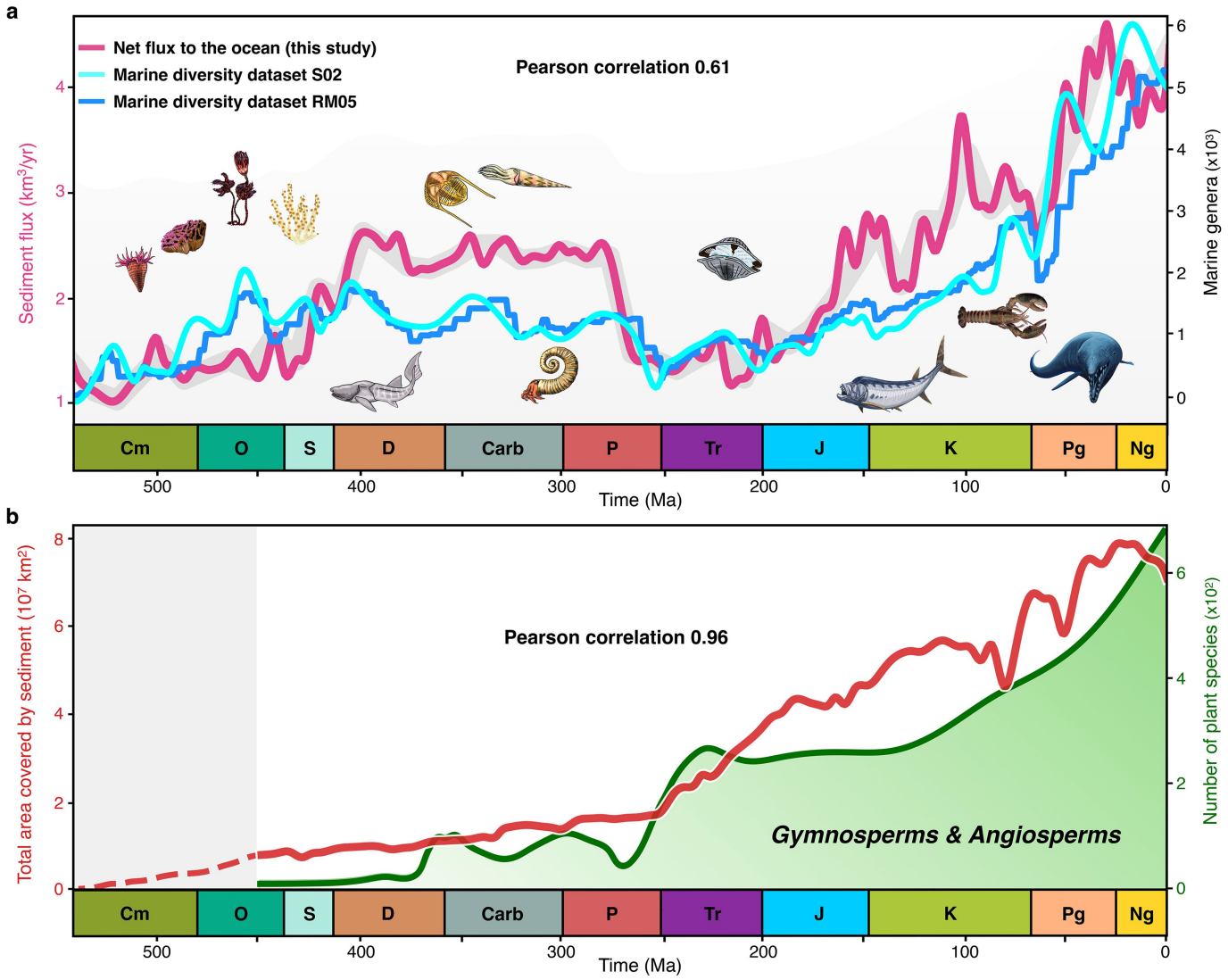

Extended Data Fig. 10 | Biodiversity and sediment flux through time. **a**. Predicted trend in net sediment flux to the ocean (purple line) and estimates of total number of marine genera from S02[2] and RM05[5]; Pearson correlation of 0.61. Sepkoski's dataset (S02) downloaded from http://strata.geology.wisc.edu/jack/. Paleo-marine life by Rebecca Horwitt, available at full size and open access from https://sites.psu.edu/rhorwitt/. The grey line shows the least square regression of the sediment flux to the ocean using SciPy Savitzky-Golay filter. **b**. Cumulative total area covered by sediments preserved over time (red line) and cumulative number of gymnosperm and angiosperm species[1] (green line) showing a strongly positive correlation (Pearson of 0.96).